Communauté
UNIVERSITÉ Grenoble Alpes

THÈSE

Pour obtenir le grade de

DOCTEUR DE LA COMMUNAUTE UNIVERSITE GRENOBLE ALPES

Spécialité : **Physique de la matière condensée et du rayonnement**

Arrêté ministériel : 25 mai 2016

Présentée par

Quentin FAURE

Thèse dirigée par **Virginie SIMONET, Directrice de recherche, Institut Néel**
et codirigée par **Béatrice GRENIER, Maître de conférences, Université Grenoble Alpes-INAC**

préparée au sein du **CNRS**, à **l'institut Néel** et de **l'Institut des NAnosciences et Cryogénie (INAC)** du **CEA-Grenoble**
dans **l'École Doctorale de Physique de Grenoble**

Transitions de phases quantiques dans le composé quasi-1D antiferromagnétique de type Ising $BaCo_2V_2O_8$

Quantum phase transitions in the quasi-1D Ising-like antiferromagnet $BaCo_2V_2O_8$

Thèse soutenue publiquement le **29 novembre 2018**,
devant le jury composé de :

M. Rafik BALLOU Directeur de recherche, Institut Néel, CNRS (Grenoble, France),	Président
M. Michel KENZELMANN Professeur, Paul Scherrer Institute (Villigen, Suisse),	Rapporteur
M. Nicolas LAFLORENCIE Chargé de recherche, Laboratoire de Physique Théorique, CNRS, (Toulouse, France),	Rapporteur
Mme Françoise DAMAY Directrice de recherche, Laboratoire Léon Brillouin, CNRS-CEA (Saclay, France),	Examinateur
M. Martin KLANJSEK Chercheur associé, Jožef Stefan Institute (Ljubljana, Slovénie),	Examinateur
M. Sylvain PETIT Ingénieur chercheur, Laboratoire Léon Brillouin, CNRS-CEA (Saclay, France),	Invité
M. Thierry GIAMARCHI Professeur, Université de Genève (Genève, Suisse)	Invité

Cette thèse est dédiée à mes parents.

"C'est ce que nous pensons déjà connaître qui nous empêche souvent d'apprendre."
Claude Bernard

ACKOWLEDGMENTS

C'est avec plaisir et émotion que j'aborde une partie de ce manuscrit, peut-être la plus agréable et facile à écrire, les remerciements. Ce travail est le fruit de nombreuses collaborations et rien de tout ceci n'aurait pu voir le jour sans de nombreuses rencontres qui m'ont guidé et poussé dans mes choix, spécialement celui de vouloir rentrer dans le monde "fou" (dans tous les sens du terme) qu'est la recherche scientifique. Je vais donc, tout en m'efforçant de n'en oublier aucunes (mes sincères excuses pour d'éventuels oublis), adresser mes remerciements aux personnes qui ont contribué à la réalisation de cette thèse.

I would like to start by thanking Rafik Ballou, Michel Kenzelmann, Nicolas Laflorencie, Françoise Damay, Martin Klanjšek, Sylvain Petit and Thierry Giamarchi for accepting to be part of my jury. Special thanks to Michel Kenlzmann and Nicolas Laflorencie for taking in charge the task to be the reviewers of this manuscript. Thanks for all the efforts and the interests that you have put in reading it. Let me emphasize that it was a real pleasure for me to expose my work to you all.

Souvent frustrante, tantôt excitante, et parfois jouissive, la thèse n'est pas un long fleuve tranquille. C'est bien ce que j'aurais appris au cours de ces trois années. Je me souviendrai toujours de ma première expérience de neutrons au bout de deux semaines sur ThALES... avec Sylvain que je rencontre pour la premiêre fois et qui me demande "Ben alors? Elles sont où les maps?" et moi, tout naif, qui répond "Des maps? C'est quoi une map?". Bien du temps a passé depuis et rien n'aurait été possible sans une ambiance de travail saine et un bon entourage. C'est pourquoi je voudrai maintenant remercier mes trois directeurs de thèse, essentiels moteurs de ce travail. J'ai emmagasiné un énorme bagage de connaissances grâce à vous. Merci infiniment pour votre patience et pour m'avoir accordé votre confiance. Merci aussi d'avoir accetpé de me prendre en thèse. Malgré la nécessité de vos récurrents et nécessaires coups de fouet, notre travail collectif aura été, pour ma part, très fructueux, plein de beaux résultats et de beaux papiers publiés, en cours et à venir. Laissons place à quelques commentaires un peu plus personnels.

Virginie Simonet: merci pour ta bienveillance, ta gentillesse et ton honnêteté, pour m'avoir dit aussi bien mes défauts que mes qualités. Tu m'as toujours soutenu dans les moments difficiles et de doutes, tout en me donnant beaucoup de tes sages conseils. Ta connaissance dans de nombreux sujets couplée à ton humilité m'ont toujours impressionné! Merci aussi pour ton dynamisme et ta bonne humeur exemplaires, travailler et discuter avec une personne telle que toi fut un réel plaisir.

Béatrice Grenier: Comme pour Virginie, je te remercie aussi pour ta bienveillance, ta gentillesse et ton honnêteté. Je me rends bien compte de tout le temps que t'as pris cette thèse. Jusqu'à la fin, tu as toujours été présente et tu as continué à m'encadrer

avec cette rigueur quasi-parfaite que tu appliques dans tout ce que tu entreprends. Pour ceci, merci infiniment. Bien qu'il était parfois difficile de suivre la cadence avec toi sur les expériences de neutrons, sache que tu m'auras énormément (et le mot est faible) appris sur la diffusion neutronique. De plus, j'ai beaucoup apprécié les temps post-manips ou post-confs passés ensemble, i.e. les apéros/ restaurants dans divers lieux (PSI, Berlin, San Francisco pour ne citer que ces trois là). C'était top et j'espère qu'on aura le temps de se reboire une bière un de ces quatre!

Sylvain Petit: Comme les deux "mémères" du dessus (comme tu aimes si bien les appeler), laisse moi te remercier pour ta bienveillance et ta gentillesse. Sache que d'un point de vue scientifique, tu es vraiment un exemple pour moi car tu es un véritable "touche à tout" (théorie, numérique, expérience). J'ai vraiment apprécié mes venues à Saclay pour avancer sur le sujet, parler de physique et même monter sur le ring de boxe avec Pfeuty. Mention spéciale au dernier trajet effectué en voiture en ta compagnie où on a du passer six heures à parler de $BaCo_2V_2O_8$ et de physique. C'etait mutuellement très enrichissant. J'espère qu'on se reverra à l'avenir sur Saclay ou sur Grenoble!

Merci infiniment à vous trois.

J'aimerai remercier grandement Thierry Giamarchi et Shintaro Takayoshi. Quelle aventure passée ensemble! C'était un réel plaisir de travailler avec vous sur ce sujet. J'ai beaucoup appris grâce à cette colaboration fructueuse, tant sur le plan analatyque que numérique. J'espère que notre collaboration ne s'arrêtera pas là.

Concernant les personnes de l'équipe MEM, j'aimerai remercier Eric Ressouche, Stéphane Raymond, Frédérique Bourdarot, Louis-Pierre Regnault et Ketty Beauvois. Eric, merci pour ta bonhomie et ta "coolitude", j'espère qu'on aura l'occasion de boire un jaune et de faire un boeuf entre guitaristes dans le futur! Stéphane, merci pour les mêmes qualités, pour ton aide sur IN12, et pour avoir partager ton amour du jazz avec moi. Louis-Pierre, je n'ai malheureusement pas eu beaucoup de temps pour discuter avec toi de physique mais j'aurai tout de même assister à ta dernière manip! Je te souhaite de profiter d'une retraite bien méritée! Ketty, c'était un plaisir d'être dans la même équipe que toi pour ma dernière année. Je te souhaite bon courage pour la fin du post-doc et pour la suite! Merci à tous pour votre bonhomie, les nombreux cafés et manips passés ensemble. C'était vraiment agréable de travailler avec vous à l'ILL! Merci aussi aux deux cryogénistes Bruno Vettard et Pascal Fouilloux pour leur sympathie et leur aide durant les expériences. Enfin, merci à Charles Picot et Marielle Perrier qui ont toujours réussi à faire les démarches admistratives pour mes missions malgré la lourdeur des procédures.

J'aimerai maintenant me tourner vers l'institut Néel. Tout d'abord merci à l'équipe MagSup. Merci à Elsa Lhotel, Julien Robert, Sophie Debrion, Mattéo Dastuto, Carley Paulsen et Rafik Ballou. Julien, merci pour les nombreuses discussions politico-sociales et scientifiques partagées ensemble. Merci aussi pour ton humilité et pour ton aide et ta présence à certains moments de la thèse. Sophie, je te remercie pour ta gentillesse et ta bonne humeur omniprésentes. Merci pour tes précieux conseils et ton aide. Rafik, merci infiniment pour ta sympathie et ta bienveillance à mon égard, pour avoir pris le temps de parler de physique avec moi alors que tu es débordé par l'administration (CNRS quand tu nous tiens). C'était un réel plaisir d'avoir échangé des conversations scientifiques avec toi et d'avoir partagé un peu de ton (immense/ incommensurable?) savoir. J'aimerai remercier Benjamin Canals pour son aide quant à l'élaboration du code numérique. Un

grand merci à Pascal Lejay pour les superbes échantillons que tu nous as fournis tout le long de cette thèse. Merci à Jérôme Debray pour m'avoir aidé à les orienter. Merci à Laurent Cagnon pour toutes les cigarettes passées ensemble après un bon café. Enfin, un grand merci à Arnaud Ralko. J'ai beaucoup apprécié nos conversations, tant musicales que scientifiques, et nos nombreux moments passés en conférences. C'était top! Merci aussi aux nombreux doctorants que j'ai vu défiler au cours de cette thèse: Karim Ferhat, Emilie Lefrançois, Ketty Beauvois, Yann Perrin, Alexis Wartelle, Olivier Dupré et Clément Godfrin. Bon courage aux deux nouveaux du bureau Yann Alexanian et Tristan Lugan.

Je voudrai aussi remercier les personnes de l'ILL. Merci beaucoup à Martin Boehm, Henry Fischer, Mark Johnson, Helmut Schober, et Navid Qureshi. Merci aussi à Brigitte Dubouloz et Anne Dale pour leur aide concernant l'admninistration. Merci à l'équipe technique et aux cryogénistes, en particulier Olivier Losserand à qui je souhaite un bel avenir de pilote d'avion! Enfin j'aimerai remercier les nombreux doctorants de l'ILL: Javier Lopez Garcia, Javier Rodriguez Murias, Marta Crisanti, Rafal Wawrzynczak, Maria Pedrosa Rivera, Irina Safiulina, Joao Ramos, Giuseppe Rosario Del Sorbo, Silvia Achilli, Loreto Misuraca, Stanislav Podchezertsev (my Russian Boy), Peter Mills, Francesca Caporaletti, Amélie Castel, Loïc Joly, Tim Birger, Tejsner, Aline Cissé, Simon Riberolles, Marco Grimaldo, Gaynor Lawrence, Lukáš Gajdoš Dominik Zumum, Diane Lançon, Bruno Tomasello, Ana Ţuţueanu (and her husband Radu), Tatania Renzi, Tatiana Lemishko, Umbertoluca Ranieri, Angel Fernandez Blanco and Lidia Mazzuca. Thanks to all of you for these years together shared between la Casa de España, beers and so forth. It was great and I wish you all a good continuation.

Je me tourne maintenant vers les personnes de l'équipe IMAPEC du CEA Grenoble: Daniel Braithwaite, Georg Knebel et Alexandre Pourret. Daniel, merci infiniment pour ta patience et ta bonhomie. J'ai beaucoup appris avec toi, spécialement le montage d'une cellule pression. C'était dur et j'ai failli craquer de nombreuses fois mais j'ai finalement réussi en faisant preuve de ténacité et grâce à ton aide. Merci pour tout. J'ai beaucoup apprécié les moments passés en votre compagnie au CEA.

Je vais maintenant remercier mes amis d'enfance qui ont fait le déplacement pour ma soutenance de thèse: Thierry Savanier, Thomas Lefort, Ludovic Sylvi, Pierre Bartoli et Aziz Mouffoki. Merci pour toutes ses années passées ensemble, pour votre présence et votre soutien sans faille. Même si la distance nous sépare, je suis certain que l'on continuera à se voir dans le futur!

Merci aussi à mes amis d'Orsay: Jean-François Lemaître, Anthony Laroque, Alexis Taine, Raphael Saiseau, Anaëlle Legros, Maud Glandier et Agathe Vatone. Je vous remercie pour toutes ces superbes années passées ensemble à l'université d'Orsay et à la résidence universitaire de la Pacaterie. À très bientôt sur Paris, Cadiz et Bruxelles!

J'aimerai remercier mes amis de Grenoble qui sont des amis de longue date: Victor Doebele, Alexis Walsh, Anthony Amisse, Quentin Peoc'h et Paul Michelet. Heureusement que vous étiez là ces trois années. On aura bien rigoler entre les tournois de coinches, les nombreuses conversations scientifiques autour d'une bière, les nombreux drak', les sessions de ski etc ... On aura partagé les bons moments mais aussi les galères et c'est aussi grâce

à vous que je suis allé jusqu'au bout. Merci à vous. Victor et Anthony, bon courage pour la fin de la thèse, tenez la barre, vous y êtes presque! Comptez sur moi pour venir voir votre défense!

Un grand merci à toute ma famille, et plus spécialement mes parents Dominique et Nathalie, et mon frère Nathan. Merci de m'avoir toujours soutenu dans ma démarche, d'avoir toujours été compréhensifs et disponibles en toutes circonstances. Merci pour votre présence et pour tous les moments passés que nous avons partagés.

Enfin, le meilleur pour la fin (et non je ne t'ai pas oublié), merci à toi Palmerina, de m'avoir soutenu et (sup)porté pendant ces 6 derniers mois, spécialement les deux derniers où tu me voyais revenir à minuit quasiment tous les jours. Merci pour l'amour (réciproque) que tu me portes. C'est à ton tour de finir ta thèse et sache que je serai là pour t'épauler quand le moment viendra!

Contents

INTRODUCTION

In the last decades, there has been an increasing focus on low-dimensional systems, in particular one-dimensional (1D) or quasi-one dimensional magnetic systems where the magnetic ions interact preferentially along a single direction in space. This interest is justified by the fact that the physics in one dimension leads to a very rich physics as the quantum effects are enhanced by the low-dimensionality. Moreover these systems can be described by models that have the particularity to be integrable, i.e. that are easily solvable analytically. Let us cite for instance the famous Bethe ansatz giving the exact solution of an antiferromagnetic (AF) 1D Heisenberg spin-1/2 chain, which was the first exact solution of a many-body quantum system. Therefore 1D magnetic systems allow a direct comparison with theoretical work.

Among all the quantum manifestations of matter, the quantum phase transitions, corresponding to an abrupt change of the ground state of a many body system due to quantum fluctuations by varying a physical parameter (e.g. a magnetic field or pressure), are particularly enhanced in 1D AF systems. Another interesting effect is the doping of spin-chains by non-magnetic impurities which strongly affects both the static and the dynamical properties of quantum spin-chains.

Neutron scattering experiments coupled to macroscopic measurements such as specific heat allow a comprehensive study of both static and dynamical properties of these quantum spin-chains, and therefore a better understanding of quantum phase transitions occurring in such systems.

The aim of this thesis was to study various quantum phase transitions in $BaCo_2V_2O_8$, a quasi-1D antiferromagnet which presents an Ising-like anisotropy. This system consists of weakly coupled chains of magnetic ions Co^{2+} carrying an effective spin $S = 1/2$. Therefore $BaCo_2V_2O_8$ can be mapped onto the 1D XXZ spin-1/2 model, largely studied theoretically with and without a magnetic field. Different quantum phase transitions are predicted in this model depending on the orientation of the magnetic field, i.e. whether the field is applied perpendicularly (transverse) or parallel (longitudinal) to the Ising z-axis. The former case, namely the Ising-chain in a transverse field, is well known to be a paradigm of quantum phase transition while in the latter case, it has been theoretically predicted that an Ising-like system enters in a gapless phase known as Tomonoga Luttinger liquid (TLL) phase. Actually, as we will see later, $BaCo_2V_2O_8$ unexpectedly exhibits a very original quantum phase transition when subjected to a transverse field different from the one of the Ising chain model in a transverse field. Both the static properties and the spin-dynamics of $BaCo_2V_2O_8$ for these field orientations have been investigated by means of neutron scattering during this thesis to understand the quantum phase transitions occurring in this compound. Moreover, heat capacity measurements under high pressure

and longitudinal magnetic field have been carried out in order to establish the (H, P, T) phase diagram of the system. Finally a study of the static and dynamical properties of $Ba(Co_{1-x}Mg_x)_2V_2O_8$ with $x = 2\%$ and 5% has been initiated to understand the effect of the substitution of magnetic ions Co^{2+} by non-magnetic impurities Mg^{2+}.

The manuscript is organized as follows:

- The **first chapter** will be devoted to generalities about quantum spin-chains, first by introducing the Heisenberg AF chain and the Haldane conjecture. Secondly I will explain the 1D XXZ spin-1/2 model and the various field-induced quantum phase transitions predicted for such a system. Then I will give an overview of some theoretical tools, namely the fermionization and the bosonization of quantum spin chains which will be useful to the understanding of our system. Finally I will present the state of the art of the results on $BaCo_2V_2O_8$ at zero-field.

- **Chapter 2** aims at describing the different experimental techniques that I have used during my PhD, namely neutron scattering and specific heat measurements under high pressure.

- **Chapter 3** presents the numerical code using exact diagonalization that I have built with the help of the Mathematica software in order to have a deeper understanding of our system.

- **Chapter 4** is dedicated to the study of $BaCo_2V_2O_8$ in a transverse magnetic field. The field evolution of both the static and the dynamical properties are reported. I will then show a comparison of the experimental results with numerical calculations and the quantum field theory associated to our system, enlightening the very non-trivial quantum phase transition occurring in this compound.

- **Chapter 5** reports the study of $BaCo_2V_2O_8$ under a longitudinal magnetic field, in particular the spin-dynamics above the critical field marking the onset of the TLL regime. I will then compare the experimental results with numerical calculations and discuss the nature of the spin-dynamics in this phase.

- **Chapter 6** is devoted to two ongoing studies. First I will present the specific heat measurements of $BaCo_2V_2O_8$ under high pressure and under a longitudinal magnetic field. Secondly, I will present briefly our preliminary neutron scattering results concerning the effect of the substitution of Co^{2+} magnetic ions by non-magnetic impurities.

Ces dernières années, un intérêt constant a été porté sur les systèmes de basses dimensions, en particulier les systèmes magnétiques unidimensionnels (1D) ou quasi-unidimensionnels, où les ions magnétiques interagissent préférentiellement selon une direction de l'espace. Cet intérêt est justifié par le fait qu'une physique très riche émerge des effets quantiques renforcés par la basse dimensionnalité et des petites valeurs de spins. De plus, ces systèmes peuvent être décrits par des modèles qui ont la particularité d'être intégrables, i.e. exactement solubles analytiquement.

Parmi toutes les manifestations quantiques de la matière, les transitions de phases quantiques (correspondant à un changement abrupt de l'état fondamental d'un système à plusieurs corps à température nulle dû aux fluctuations quantiques en appliquant un paramètre extérieur comme un champ magnétique ou une pression), sont particulièrement exacerbés dans les systèmes magnétiques 1D. Un autre exemple d'effet particulièrement intéressant est le dopage de chaînes de spins quantiques par des impuretés non magnétiques qui affectent à la fois leurs propriétés statiques et dynamiques.

Les expériences de diffusion de neutrons, couplées à des mesures macroscopiques, par exemple les mesures de chaleur spécifique, permettent une étude compréhensive des propriétés statiques et dynamiques des transitions de phases quantiques se produisant dans ces systèmes.

Le but de cette thèse a été d'étudier des transitions de phases quantiques dans $BaCo_2V_2O_8$, un système quasi-1D antiferromagnétique (AF) présentant une anisotropie de type Ising. Ce système est constitué de chaînes faiblement couplées d'ions magnétiques Co^{2+} portant un spin effectif $S = 1/2$. Par conséquent $BaCo_2V_2O_8$ peut être modélisé par le Hamiltonien 1D XXZ, largement étudié théoriquement avec et sans champ magnétique. Différentes transitions de phases quantiques sont prédites par ce modèle en fonction de l'orientation du champ magnétique: perpendiculaire (transverse) ou parallèle (longitudinal) à l'axe d'anisotropie de type Ising. Le premier cas, à savoir la chaîne de spins de type Ising en champ transverse, est bien connu pour être un paradigme de transition de phase quantique. Concernant le deuxième cas, il a été théoriquement montré qu'un système de type Ising entre dans une phase originale non-gappée connue sous le nom de liquide de Tomonoga Luttinger (TLL). Durant cette thèse, les propriétés statiques et dynamiques de $BaCo_2V_2O_8$ pour ces deux orientations du champ ont été étudiées à l'aide d'expériences de diffusion neutronique afin de mieux comprendre les transitions de phases se produisant dans ce système. De plus, des mesures de chaleur spécifique sous haute pression et champ magnétique longitudinal ont été effectuées afin d'établir le diagramme de phase (H, P, T) de ce système. Finalement, une étude des propriétés statiques et dynamiques de $Ba(Co_{1-x}Mg_x)_2V_2O_8$ avec $x = 2\%$ et $x = 5\%$ a été initiée afin de comprendre l'effet de subsitution des ions magnétiques Co^{2+} par des ions non magnétiques Mg^{2+}.

Chapter 1

One dimensional quantum magnetism and the model system $BaCo_2V_2O_8$

Sommaire

1.1 Summary

1.1.1 Abstract

The aim of this chapter is to introduce general concepts about one-dimensional (1D) systems. First, I will present the very general case of an antiferromagnetic (AF) spin-chain with isotropic, i.e. Heisenberg, interactions. I will then present the Haldane conjecture and the difference between integer spin and half integer spin chains. Then, anisotropic spin 1/2 chains and different quantum phases transitions will be introduced, followed by some useful theoretical tools to model these systems. Finally I will summarize the state of the art of the quasi-1D Ising-like antiferromagnet $BaCo_2V_2O_8$ in zero-field, the compound that I have studied during my PhD.

1.1.2 Résumé en français

Le premier chapitre est consacré à une introduction sur les chaînes de spins quantiques. Dans un premier temps, nous présentons la chaîne Heisenberg AF, puis nous expliquons la conjecture de Haldane qui postule que les chaînes de spins entiers et demi-entiers se comportent de façon totalement différentes. Nous nous intéressons particulièrement au cas des spins demi-entiers, qui correspond à $BaCo_2V_2O_8$. Les excitations magnétiques dans ce cas précis sont appelées des "spinons" et sont au coeur de ce sujet d'étude. Elles correspondent à des excitations fractionnaires créées par paires portant chacune un spin 1/2.

L'Hamiltonien XXZ est ensuite présenté. Celui-ci permet de décrire des chaînes de spins anisotropes, i.e. où les spins veulent s'aligner dans des directions particulières de l'espace, par exemple dans le plan perpendiculaire à l'axe z (anisotropie de type XY) ou encore lorsque le spin pointe dans une seule direction de l'espace (anisotropie de type Ising), ce dernier cas étant celui de $BaCo_2V_2O_8$. Les différentes transitions de phase quantiques prédites théoriquement pour diverses configurations du champ magnétique par rapport l'axe Ising sont alors introduites. Lorsque le champ est appliqué parallèlement à l'axe Ising (longitudinal), il a été montré que le système entre dans une phase non-gappée dite de liquide de Tomonaga Luttinger (TLL) alors que lorsqu'il est appliqué perpendiculairement (transverse), la transition de phase quantique attendue est celle d'une phase ordonnée à une phase désordonnée (transition AF-paramagnétique).

Plus loin, des outils théoriques tels que la fermionisation et la bosonisation, utiles à la compréhension de ces systèmes, sont présentés.

Enfin l'état de l'art de $BaCo_2V_2O_8$ à champ nul est exposé. Ce système consiste en des chaînes faiblement couplées d'ions magnétiques Co^{2+} portant un spin effectif 1/2. La structure magnétique à champ nul correspond à un ordre antiferromagnétique où les spins sont parallèlement alignés le long des chaînes et pointent selon l'axe z (anisotropie de type Ising). Le spectre des excitations à champ nul est alors présenté ainsi que les excitations magnétiques associées qui correspondent à des spinons confinés par l'interaction interchaîne.

1.2 Introduction: 3D vs 1D systems

Three-dimensional (3D) non frustrated magnetic systems show a well-established behavior. The moments interact with each other through an exchange interaction J which generally leads to a long-range ordering, for instance the Néel order shown in Fig. 1.1(a) for antiferromagnetic interactions. The associated excitations are spin waves, quantized as magnons that one can see semi-classically as the precession of the spins around their equilibrium position (see Fig. 1.1(b)). Spin waves both for AF and ferromagnets are only valid assuming an ordered state and for large values of the spins S (i.e. the semi-classical limit with $S \to +\infty$). Indeed, the precession of the spins induces a reduction of the total magnetic moment by 1 (for one magnon), 2 (for two magnons) and so forth. For instance, if we consider a ground state with spins $S = 7/2$, one magnon reduces one of the spins down to $S = 5/2$, and this reduction will spread along the system creating a spin-wave. The criteria of validation of the spin-wave theory is thus $n_b \leq 2S$ where n_b is the number of magnons (bosons) per site [1] [Aue94].

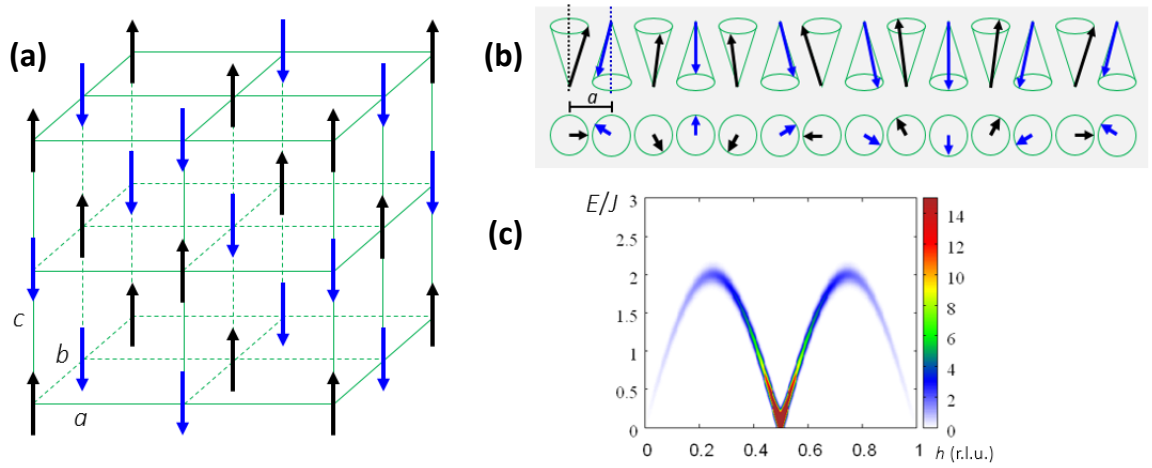

Figure 1.1: **3D conventional magnetism.** (a) Example of a Néel ordering in a 3D antiferromagnet. (b) Spin waves excitation in a 3D antiferromagnet corresponding to the precession of the spin around their equilibrium position. (c) The associated dispersion spectrum with a well defined branch emerging from the AF position $q = \pi$ (with q the wave vector).

Is it possible to go beyond the conventional behavior of 3D magnetic systems? How can we enhance quantum fluctuations to be able to produce quantum effects? Two ingredients allow us to do that: a small value of the spin (for example a spin $S = 1/2$) and a small dimensionality (for example $D = 1$). We will see in the following that the physics in low-dimensional systems is much more exotic compared to the conventional 3D case and leads to very peculiar ground states and excitations (for instance spinons) arising from pure quantum effects.

[1] One can ask the legitimate question: what about a spin $S = 1/2$? This case is the limit of the spin-wave theory as one magnon corresponds to a state where the spin has totally flipped.

1.3 Heisenberg antiferromagnetic spin-chains

In this section I will present some generalities on Heisenberg antiferromagnetic (AF) spin-chains and the Haldane conjecture which stipulates that half integer and integer spin chains show a totally different behavior.

1.3.1 Generalities

One simple model is the Heisenberg AF spin chain Hamiltonian. For instance, the $S = 1/2$ Heisenberg AF chain is the first many-body system solved analytically almost a century ago by Bethe through the famous Bethe ansatz [Bet31]. The general Hamiltonian of a 1D Heisenberg system writes as:

$$\begin{aligned} \mathscr{H}_{Heisenberg} &= J \sum_j \vec{S}_j \cdot \vec{S}_{j+1} \\ &= J \sum_j \left\{ S_j^x S_{j+1}^x + S_j^y S_{j+1}^y + S_j^z S_{j+1}^z \right\} \end{aligned} \tag{1.1}$$

where J is the intrachain interaction between first neighbor sites, j labels the sites along the chain, $\vec{S}_j$ is the spin on site j and S_j^α its component along α (with $\alpha = x, y, z$). In the convention used here, if $J > 0$, the system is AF while if $J < 0$, the system is ferromagnetic (FM). The scalar form of J means that the exchange interactions are isotropic (in other words $J_{xx} = J_{yy} = J_{zz} = J$, $J_{\alpha,\beta} = 0$ for $\alpha \neq \beta$ with α and $\beta = (x, y, z)$). This kind of chain is pictured in Fig. 1.2.

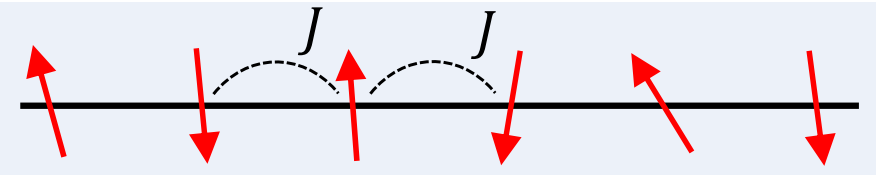

Figure 1.2: **Sketch of a AF Heisenberg spin chain.** Only the first neighbor interactions are taken into account here.

One of the first argument which evidences the relevance of the quantum effects in spin-chains is the Haldane conjecture [Hal83b; Hal83a] which predicts that half-integer spin and integer spin Heisenberg AF chains behave differently.

1.3.2 Haldane conjecture: Integer vs half integer spins

1.3.2.1 Haldane conjecture

To get an insight of the Haldane conjecture, a simple way is to deal with the set of coherent states [Hal83b; Hal83a]:

$$|n\rangle = e^{i\hat{S}^z\phi}e^{i\hat{S}^y\theta}\,|M_S, S\rangle \tag{1.2}$$

$$= e^{i\phi/2}\cos\frac{\theta}{2}\,|\uparrow\rangle + e^{-i\phi/2}\sin\frac{\phi}{2}\,|\downarrow\rangle \tag{1.3}$$

where $|M_S, S\rangle$ are states such that $\hat{S}^z\,|M_S, S\rangle = S\,|M_S, S\rangle$, and θ and ϕ are the polar and azimuthal angles describing the orientation of $|n\rangle$.

In the semi-classical limit, i.e. $S \to +\infty$, these states are a semi-classical representation of the spin and can be understood as a vector pointing on the Bloch sphere (in other words pointing the direction of the spin) as shown in Fig. 1.3.

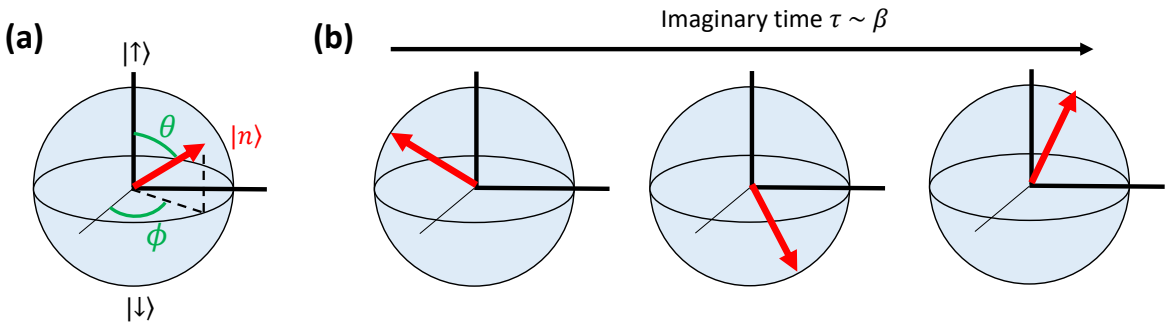

Figure 1.3: **Coherent states representation of the spin.** (a) Bloch sphere. The states $|\uparrow\rangle$ and $|\downarrow\rangle$ are the north and south poles of the Bloch sphere. (b) Qualitative imaginary time evolution of the coherent state.

The main idea behind the Haldane conjecture is to use the path integral [2] (i.e. the action) of these coherent states. One can show that the partition function Z and the path integral $\mathcal{S}$ are related through the following formula [Aue94; MK04]:

$$\begin{aligned} Z = Tr\left(e^{-\beta\mathscr{H}}\right) &= \int \mathscr{D}\vec{n}e^{-\int_0^\beta d\tau\{-\langle\partial_{d\tau}n|n\rangle+\mathscr{H}(\vec{n})\}} \\ &= \int \mathscr{D}\vec{n}e^{-\mathcal{S}(\vec{n})} \end{aligned} \tag{1.4}$$

where $\mathscr{H}$ is the Hamiltonian of the system, β the inverse temperature T defined as $\beta = 1/(k_BT)$, and $\tau = \hbar\beta$ the imaginary time (which is used to connect quantum mechanics with statistical physics). The integration $\int \mathscr{D}\vec{n}$ stands for the summation over all possible paths that $\vec{n}$ can take in a time τ. For an AF: $\vec{S}_j = S(-1)^j\vec{n}_j$ where $\vec{S}_j$ is the spin at site

[2] Let us consider a field $\psi(\vec{r}, t)$. The probability amplitude P associated with the realization of a given final configuration $\psi_f = \psi(\vec{r}_f, t_f)$ from an initial state $\psi_i = \psi(\vec{r}_i, t_i)$ writes as the path integral: $P = \langle\psi_i|e^{-i\int_{t_i}^{t_f} dt\mathscr{H}}|\psi_f\rangle = \int_{\psi_i\to\psi_f}\mathscr{D}\vec{r}(t)e^{i\mathcal{S}[\psi(\vec{r},t)]}$.

j, $\vec{n}_j$ the vector describing its orientation and S the value of the spin. It can be shown in this case that, in the continuous limit, the action $\mathcal{S}(\vec{n})$ writes as the sum of a kinetic term $\mathcal{S}_{kin}$ and a topological term (or Berry term) $\mathcal{S}_{top}$:

$$\begin{aligned}\mathcal{S}(\vec{n}) &= \mathcal{S}_{kin}(\vec{n}) + \mathcal{S}_{top}(\vec{n}) \\ &= \int d\tau dx \frac{1}{2g}\left\{(\partial_\tau \vec{n})^2 + (\partial_x \vec{n})^2\right\} + 2\pi S Q_{\tau,x}\end{aligned} \tag{1.5}$$

where $g = 2/S$ and $Q_{\tau,x}$ is a winding number ($Q_{\tau,x} \in \mathbb{Z}$) which counts the number of times the unit vectors $\vec{n}$ sweeps the unit sphere (this can be seen somehow as a Berry phase). This leads to the partition function:

$$Z = \sum_{Q_{\tau,x}} e^{-i2\pi S Q_{\tau,x}} \int \mathcal{D}\vec{n} e^{-\mathcal{S}_{kin}(\vec{n})} \tag{1.6}$$

This topological term (which has no classical analogue) is at the origin of the different behavior between half integer and integer spins. Indeed, for integer spins $\mathcal{S}_{top} = 2\pi n Q_{\tau,x}$ while for half integer spins $\mathcal{S}_{top} = (2n+1)\pi Q_{\tau,x}$ with $n \in \mathbb{N}$. Hence the latter will cause (non-trivial) quantum interference of configurations with different $Q_{\tau,x}$ in Eq. (1.6), which dramatically affects the ground state correlations and excitations. This is responsible for the fact that there is a gapless phase in spin-1/2 chains. One must be cautious that this Berry phase effect is actually a "conjecture". For more details, readers can refer to [MK04; Aue94].

Let us now discuss in more details the differences between integer and half integer spin chains.

1.3.2.2 Integer spins

For integer spin-chains and at zero-temparature, the ground state is a singlet state ($S = 0$) separated from the first triplet excited state ($S = 1$) by an energy gap Δ. This gap is related to the intrachain coupling J and to the value of the spin S through $\Delta \simeq JSe^{-\pi S}$ [WH93]. The ground state is described by a spin-liquid state called Haldane phase with short range correlations (the correlation length is about 6 spins for $S = 1$ and 50 for $S = 2$). Indeed the static spin-spin correlations decay exponentially with the distance between two spins at positions $\vec{0}$ and $\vec{r}$ and writes as:

$$\langle \vec{S}(\vec{0}, t=0) \cdot \vec{S}(\vec{r}, t=0) \rangle \simeq \frac{(-1)^r}{\sqrt{r}} e^{-r/\xi} \tag{1.7}$$

where ξ is the correlation length, and $r = ||\vec{r}||$.

Theoretically, the Haldane phase is explained through the valence bond solid (VBS) theory. This is rigourosly demonstrated by the AKLT (Affleck-Kennedy-Lieb-Tasaki) model [Aff+87], i.e. for a bilinear 1/3 biquadratic Hamiltonian [3]. The idea behind the VBS is to consider the ground state as a coherent superposition of all the possible configurations in which spins form valence bonds between first neighbors. In the case of the $S = 1$ spin chain, it consists in splitting the spin $S = 1$ into two fictitious spins $s = 1/2$ and to describe the system as a succession of pairs of spins $s = 1/2$ as shown in Fig. 1.4(a).

[3] This Hamiltonian writes as $\mathcal{H}_{AKLT} = \sum_j \left\{\vec{S}_j \cdot \vec{S}_{j+1} + \frac{1}{3}(\vec{S}_j \cdot \vec{S}_{j+1})^2\right\}$

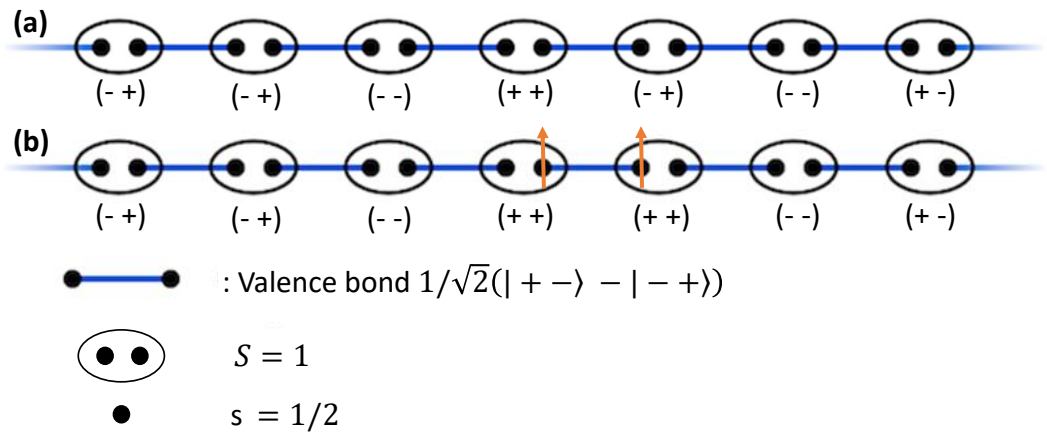

Figure 1.4: **AKLT model.** Sketch of the spin-1 Heisenberg chain: every spin $S = 1$ is decomposed into a pair of two fictitious spins $s = 1/2$. (a) Ground state where each spin $s = \pm 1/2$ forms a valence bond (blue line) with its first neighbor $s = \mp 1/2$ from the neighboring $S = 1$ state. (b) First excited state: one spin $s = -1/2$ has been flipped creating a triplet excitation pointed out by the two orange arrows.

There are three possible states for a spin $S = 1$ that we can decompose in two spins $s = 1/2$ which can have the (+) (spin up) or (-) (spin down) states:

$$\begin{aligned} S^z = +1 &\leftrightarrow |\uparrow\rangle = (++) \\ S^z = -1 &\leftrightarrow |\downarrow\rangle = (--) \\ S^z = 0 &\leftrightarrow (+-) \quad \text{or} \quad (-+) \end{aligned}$$

Then, a valence bond state consists in forming singlet states $(|+-\rangle - |-+\rangle)/\sqrt{2}$ by combining each spin $s = 1/2$ $|+\rangle$ with its first neighbor spin $s = -1/2$ $|-\rangle$ from the neighboring $S = 1$ state, yielding for example the possible configuration below:

$$(-+)(-+)(--)(++)(-+)(--)(+-)(+-)... = |00\downarrow\uparrow 0\downarrow 00...\rangle$$

The ground state consists in a succession of spin triplets $|\uparrow\rangle$ and $|\downarrow\rangle$ which can be separated by an arbitrary number of states $|0\rangle$. This kind of ground state is often called diluted antiferromagnet or "hidden" order [4].

The first excited state is a spin-triplet and such an excitation can be created by flipping one of the spins 1/2 of the singlet formed by two spins $+1/2$ and $-1/2$ tied through the valence bond (see Fig. 1.4(b)). At a wave-vector $k = \pi$, the energy gap Δ separates the ground state $S = 0$ from the first excited triplet $S = 1$ which is often referred to as a magnon (see Fig. 1.5(a)). At $k = 0$, the lowest energy excited state is a continuum of 2-particles (2 magnons) separated by a gap 2Δ. It is predicted theoretically that the one magnon excitation melts in the 2-magnons continuum at the critical wave-vector $k_c \simeq 0.23\pi$ [WA08].

[4] This denomination comes from the fact that the order parameter is non-local. Such an order parameter is called a "string" order parameter.

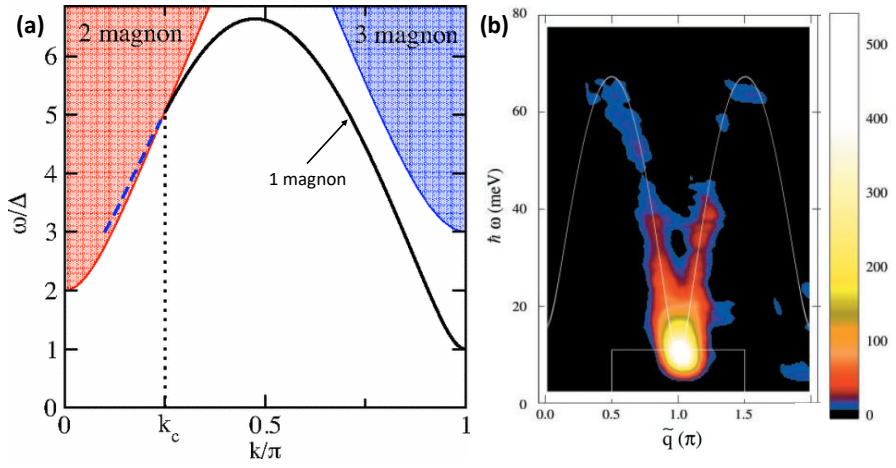

Figure 1.5: **Dispersion spectrum of a $S = 1$ Haldane chain.** (a) Theoretical prediction for the zero-field dispersion spectrum. Figure extracted from [WA08]. (b) Experimental dispersion spectrum obtained by inelastic neutron scattering in the Haldane chain $S = 1$ compound Y_2BaNiO_5. Figure extracted from [Xu+00].

1.3.2.3 Half integer spins

For half integer spin chains and at zero-temperature, the ground state is a singlet $S = 0$. While quantum fluctuations prevent any ordering in 1D systems, for a spin-1/2 AF spin chain, the static spin-spin correlations decay with the distance r between two spins with the power law [Bet31]:

$$\langle \vec{S}(\vec{0}, t = 0) \cdot \vec{S}(\vec{r}, t = 0) \rangle \simeq \frac{(-1)^r}{r} \tag{1.8}$$

It is then often named a "quasi" long range order and the ground state is called Tomonaga Luttinger liquid (TLL), which I will explain later.

Contrary to Haldane chains, half integer spin chains are gapless at zero-temperature. To describe the spin-dynamics of such chains, it is useful to rewrite the Heisenberg Hamiltonian of Eq. (1.1). For this purpose, let us consider the quantization axis along the z-axis.

$$\mathcal{H}_{Heisenberg} = J \sum_j S_j^z S_{j+1}^z + \frac{1}{2} \underbrace{\left(S_j^+ S_{j+1}^- + S_j^- S_{j+1}^+ \right)}_{\text{kinetic part}} \tag{1.9}$$

where the $S_j^+ = S_j^x + iS_j^y$ and $S_j^- = S_j^x - iS_j^y$ spin-flip operators at site j are introduced. To create an excitation in such a system, one has to flip one of the $S = 1/2$ spins. This leads to a triplet excitation $S = 1$. What is remarkable in spin-1/2 chains is that this bosonic excitation fractionalizes into two fermionic excitations each of them carrying a spin 1/2. These fractionalized excitations are called "spinons" and can propagate along the chain without any cost of energy through the kinetic part of the Hamiltonian. Therefore the spinons are "deconfined" and they can be seen as magnetic solitons [5]. This is well understood in the case of an Ising anisotropy where the spinons are equivalent to domain walls as shown in Fig. 1.6.

[5] A soliton is defined as a wave maintaining its shape while it propagates at constant velocity.

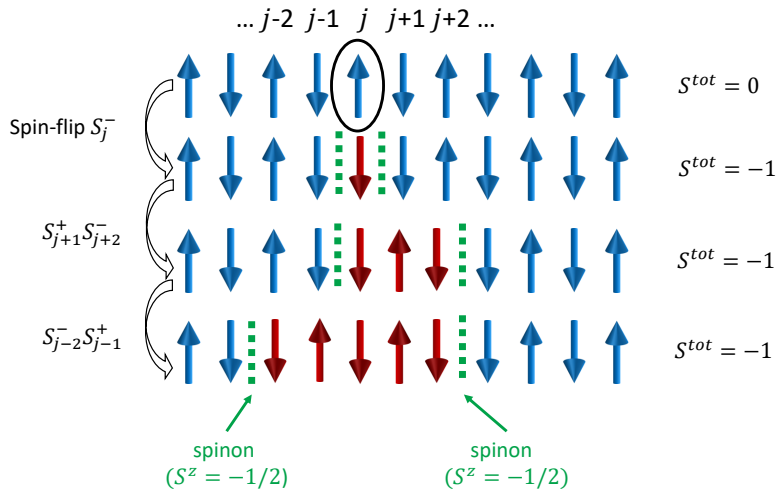

Figure 1.6: **Sketch of a two spinon excitation in a spin-1/2 chain.** One spin at site j in the ground state is flipped through S_j^-. This $S^{tot} = -1$ excitation fractionalizes into two spinons, each of them carrying a spin $S^z = -1/2$. The spinons can be seen as domain walls in the Ising case (dashed green lines) which can propagate freely along the chain through the kinetic part of the Hamiltonian (see Eq. (1.9)). Indeed, the kinetic part allows the spinons to hop by two sites and preserves the total magnetization S^{tot} of the system.

The fact that these excitations can propagate freely along the chain with no energy cost leads to an ungapped continuum of excitations, characteristic of quantum half integer spin chains. The lower bound of the dispersion spectrum has been calculated analytically by Des Cloizeaux and Pearson [CP62]. The dispersion spectrum is delimited by the two dispersion relations given by:

$$E_1(k) = \hbar\omega_1(k) = \frac{\pi J}{2}|\sin(k)|$$
$$E_2(k) = \hbar\omega_2(k) = \pi J\left|\sin\left(\frac{k}{2}\right)\right|$$

where E_1 and $E_2(k)$ are the energies of the lower and upper bounds of the dispersion spectrum respectively, and k is the wave-vector.

It is interesting to compare these excitations with the semi-classical limit ($S \to \infty$) described by the spin-wave theory. Indeed the dispersion relation of spin waves for a classical AF chain is given by $E_{SW} = \hbar\omega_{SW} = J|\sin k|$ and thus differs by a scaling factor $\pi/2$ with the lower bound of the 2-spinon continuum. The dispersion of the Heisenberg AF spin-1/2 chain is plotted in Fig. 1.7.

The spectral weight of these excitations is given by the Müller ansatz, giving theoretically the dynamical structure factor $S(k,\omega)$ (which can be measured in inelastic neutron scattering experiments) through the following formula [Mül+81]:

$$S(k,\omega) = \frac{A}{\sqrt{\omega_1(k)^2 - \omega(k)^2}}\Theta\left(\omega(k) - \omega_1(k)\right)\Theta\left(\omega(k) - \omega_2(k)\right) \tag{1.10}$$

where $\omega(k)$ is the energy of a given excitation, A is a constant, and Θ is the Heaviside function defined by $\Theta(x) = 0$ if $x < 0$ and $\Theta(x) = 1$ if $x \geq 1$. Therefore, $S(k, \omega)$ has a singularity at $E_1(k) = \hbar\omega_1(k)$ and a tail up to $E_2(k) = \hbar\omega_2(k)$. All the spectral weight is contained in the continuum with a maximum of intensity at $k = \pi$ (called the AF point of the Brillouin zone (BZ), in contrast with the points at $k = 2n\pi$ with $n \in \mathbb{Z}$ called zone center (ZC) points).

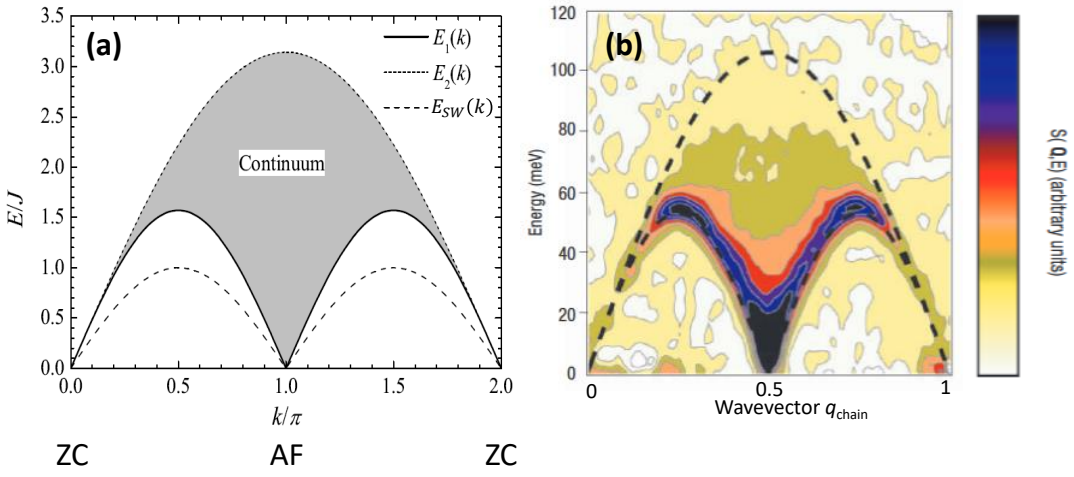

Figure 1.7: **2-spinon excitations.** (a) 2-spinon excitation spectrum predicted theoretically for a Heisenberg AF spin-1/2 chain [CP62; FT81; MK04]. The spectrum is contained between the lower and upper bounds $E_1(k)$ and $E_2(k)$ respectively and consists in a continuum of excitations. The dispersion relation of spin waves $E_{SW}(k)$ is also plotted for comparison. The AF and ZC points are pointed out. (b) Excitation spectrum of the quasi-1D Heisenberg antiferromagnet $KCuF_3$ obtained by inelastic neutron scattering at low temperature. Figure extracted from [Lak+05].

Many experimental studies, in particular neutron scattering experiments, have confirmed the existence of such a continuum, for instance in the AF Heisenberg spin-1/2 chain compounds $KCuF_3$ [Nag+91; Lak+05] (see Fig. 1.7(b)), $CuSO_4 \bullet 5D_2O$ [Mou+13] or CuPzN [Sto+03].

The question is now: what about systems with an anisotropic exchange interaction, thus breaking the rotational symmetry of Heisenberg systems?

1.4 Anisotropic AF spin-1/2 chains

1.4.1 XXZ Hamiltonian

The magnetic anisotropy refers to the fact that the magnetic moments prefer to point along given directions (thus reducing the number of degrees of freedom for the spin). It emerges from different effects such as the magneto-crystalline anisotropy. To modelize the influence of the anisotropy in quantum AF spin-chains, one can modify the Hamiltonian of Eq. (1.1) to the XXZ Hamiltonian:

$$\begin{aligned} \mathcal{H}_{\text{XXZ}} &= J \sum_j \left\{ S_j^x S_{j+1}^x + S_j^y S_{j+1}^y + \Delta S_j^z S_{j+1}^z \right\} \\ \text{or also} \quad &= J \sum_j \left\{ \varepsilon \left(S_j^x S_{j+1}^x + S_j^y S_{j+1}^y \right) + S_j^z S_{j+1}^z \right\} \end{aligned} \tag{1.11}$$

where Δ and $\varepsilon = 1/\Delta$ are the anisotropy parameters [6]. Therefore, we have:

- $\Delta = 1 \leftrightarrow \varepsilon = 1$ corresponds to the AF **Heisenberg** case where the orientation of the magnetic moment is **isotropic** (same Hamiltonian as in Eq. (1.1)). The spins have three degrees of freedom.

- $|\Delta| < 1 \leftrightarrow |\varepsilon| > 1$ corresponds to the **XY-like** case where the magnetic moments want to lie in the **plane** perpendicular to z. The limit $\Delta = 0^+ \leftrightarrow \epsilon \to +\infty$ corresponds to the pure AF XY case, where the spins have only two degrees of freedom.

- $|\Delta| > 1 \leftrightarrow |\varepsilon| < 1$ corresponds to the **Ising-like** case where the magnetic moments want to point along a **single direction**. The limit $\Delta \to +\infty \leftrightarrow \epsilon = 0^+$ corresponds to the pure AF Ising case, where the spins have a single degree of freedom.

These considerations are summarized in Fig. 1.8.

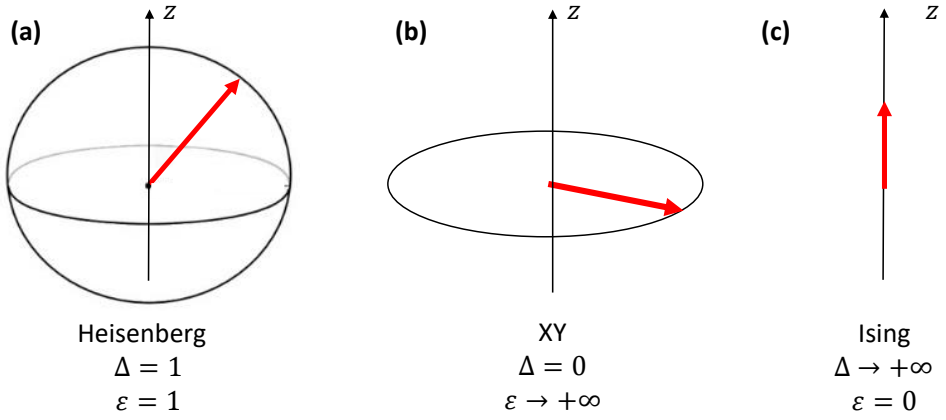

Figure 1.8: **Different anisotropies.** The red arrow indicates one orientation of the spin among all the possible ones (shown by the black sphere, circle or line). (a) Heisenberg case where the orientation of the spin is isotropic. (b) XY case where the spin lies in the plane perpendicular to z. (c) Ising case where the spin points along the z direction.

This Hamiltonian will be intensively used in the rest of this manuscript as we will see in the next chapters. Let us now examine the influence of a magnetic field on this model.

[6] Note that in the first expression J ($J > 0$) corresponds to $J_{xx} = J_{yy}$ and thus $J_{zz} = \Delta J$, while in the second expression J ($\text{sign}(J) = \text{sign}(\varepsilon)$) corresponds to J_{zz} and thus $J_{xx} = J_{yy} = \epsilon J$.

1.4.2 Quantum phase transitions in Ising-like spin-1/2 AF chains

1.4.2.1 Tomonaga Luttinger liquid phase and $H-\Delta$ phase diagram of spin-1/2 AF chains

Let us first consider a magnetic field along the z-axis. This yields the following Hamiltonian:

$$\mathcal{H} = J\sum_j \left\{S_j^x S_{j+1}^x + S_j^y S_{j+1}^y + \Delta S_j^z S_{j+1}^z\right\} - g_{zz}\mu_B H S_j^z \tag{1.12}$$

where g_{zz} is the component of the Landé tensor $\tilde{g}$ along z, μ_B is the Bohr magneton and H the applied magnetic field. The second term is the Zeeman Hamiltonian describing the interactions between the spins and the magnetic field. For the particular case of Ising-like systems (with z the Ising axis), such a direction of the field is called "longitudinal". This model is well known theoretically and has led to the $H-\Delta$ phase diagram of XXZ spin-1/2 AF chains [WH00b] shown in Fig. 1.9.

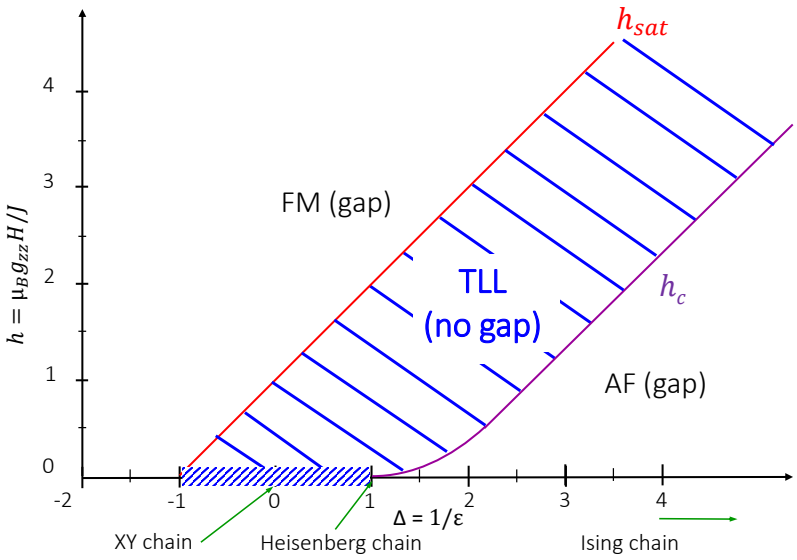

Figure 1.9: **$H-\Delta$ phase diagram of XXZ AF spin-1/2 chains.** Magnetic field $h = \mu_B g_{zz} H/J$ (in reduced units) applied along $\vec{z}$ vs the anisotropy parameter $\Delta = 1/\epsilon$. The TLL phase is delimited by a critical field h_c and a saturation field h_{sat}.

I will explain in more detail this phase diagram in Chap. 5. Nevertheless let me introduce the Tomonaga Luttinger liquid (TLL) theory.

The Fermi liquid theory is commonly used to understand 3D electronic systems by a renormalization of the parameters taking into account the interaction terms of the Hamiltonian. In 1D this theory breaks down and is replaced by the TLL theory (it can be seen somehow as the equivalent of the Fermi Liquid theory for 1D systems). This model describes interacting spinless fermions in 1D systems [GP04; ML94] and is obtained through bosonization techniques that I will briefly introduce later. This theory leads to the establishment of the TLL gapless phase for spin-1/2 chains.

At zero-field, this phase exists between $-1 < \Delta \leq 1$ (with in between the XY case $\Delta = 0$). For $\Delta > 1$, i.e. in the Ising-like case, the system is AF and gapped. However the TLL phase is shifted to larger values of Δ in a magnetic field and thus increasing the magnetic field above the critical field H_c at which the gap closes (due to the Zeeman splitting) brings the AF Ising-like systems into this TLL gapless phase.

So far, no chain compound with Ising-like anisotropy has been studied in this field-induced TLL phase by neutron scattering. During my PhD, I have studied $BaCo_2V_2O_8$ which has a moderate anisotropy $\Delta \simeq 2$ and thus a rather small critical field of $\mu_0 H_c \simeq 4$ T, allowing this system to be studied in the TLL phase under a longitudinal magnetic field. As we will see later, an interesting physics emerges for Ising-like systems in the TLL phase (see Chap. (5)).

1.4.2.2 Ising model in a transverse field, a paradigm for quantum phase transitions

Quantum phase transitions are defined by a change of the ground-state of a many-body system due to quantum fluctuations by varying a physical parameter such as a pressure or a magnetic field (which comes naturally in mind for magnetic systems) at $T = 0$ K [7].

The 1D Ising model in a transverse magnetic field, i.e. in a field applied perpendicularly to the easy-axis of magnetization [8], is perhaps the most studied theoretical paradigm for quantum phase transitions [Sac11]. Indeed this simple model can describe order-disorder transition in many systems (therefore these systems are said to belong to the universality class of the Ising model). Concerning the 1D case, it has been theoretically solved by Pfeuty fifty years ago [Pfe70] and experimentally evidenced only recently by neutron scattering in the strong Ising-like ferromagnet $CoNb_2O_6$ by Coldea et *al.* [Col+10].

Qualitatively, the transverse magnetic field competes with the Ising-axis. It will flip the spin state from $|\uparrow\rangle$ to $|\downarrow\rangle$ (and vice versa) and these fluctuations will "melt" (and thus destroy) the magnetic order at a critical field $\mu_0 H_c$ where the system enters in a paramagnetic phase (disordered phase). A phase diagram of such a transition is shown in Fig. 1.10.

At first sight, $BaCo_2V_2O_8$ was a very-good candidate to investigate this quantum phase transition for the AF case but as I will explain later in Chap. 4, our study led to a totally different phase transition of topological nature [Fau+18].

1.4.2.3 Topological phase transition

In the world of condensed matter, the understanding of phase transitions has been much improved by the Ginzburg-Landau theory [Lan+80]. This theory describes phase transitions by the concept of spontaneous symmetry breaking [9] where a physical invariant called "order parameter" is introduced to describe the physical quantity which breaks the symmetry under consideration. For instance the transition from a paramagnetic state to a ferromagnetic one when cooling down the temperature is an example of such spontaneous symmetry breaking where the order parameter is the local magnetization. P. Ehrenfest is the first one who tried to classify such transitions [Jae98]. The actual classification of

[7] In contrast, a classical phase transition is defined by a change of state driven by thermal fluctuations.

[8] The Hamiltonian in this case writes: $\mathcal{H} = J\sum_j S_j^z S_{j+1}^z - \sum_j g_{xx}\mu_B H S_j^x$ where g_{xx} is the Landé component of the tensor along the x-axis. Here $\vec{H} \parallel \vec{x}$.

[9] Thus violating the Curie principle which stands that "the symmetry of the causes are to be found in the effects", in other words that the final state is more symmetric than the initial one.

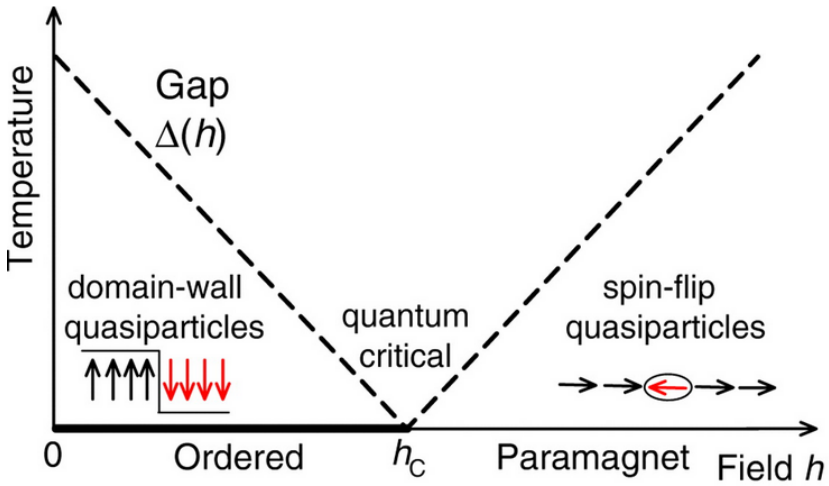

Figure 1.10: **Ising model in a transverse magnetic field.** $H-T$ phase diagram of the Ising FM chain in a transverse field. The dashed line shows the gap Δ as a function of the magnetic field h. By increasing the field, the gap closes at the critical field h_c where an order-disorder quantum phase transition occurs and then increasees again when h further increases. In the low-field phase, the excitations are spinons like in the AF case, already described above. In the high field phase, i.e. above h_c, the transverse field forces the spins to align along its direction. These ones can fluctuate and are called spin-flip particles [Cab+14]. Figure extracted from [Col+10]. This quantum phase transition is theoretically predicted to be the same for an AF Ising chain [Pfe70]

phase transitions is based on his work and stands that a "nth" order transition corresponds to a discontinuity in the "nth" derivative of the free energy of the system. Interestingly, it has been understood recently that some transitions are ∞-order phase transitions. They are continuous but do not break symmetries in the system. Such a transition is called "topological phase transition" that I will introduce now.

Topological phase transitions can be seen through the signature of topological defects or excitations. The most famous example of such a transition is the Berezinski-Kosterlitz-Thouless (BKT) transition [Jos13; Ber71; KT73] which led to the Nobel prize shared in 2016 between J. M. Kosterlitz, D. J. Thouless and F. D. M. Haldane for their understanding about topological phase transitions and topological phases of matter.

In their theory, Kosterlitz and Thouless investigated the XY model, i.e. with the spins lying in the plane [KT73]. They showed that such kind of system "likes" to create vortices or antivortices (see Fig. 1.11(a)) of spins to minimize its free energy. Vortices and antivortices are topological defects, since it is impossible to deform each of them continuously to recover a state where all the spins point along the same direction. Topology is somehow the art of making loops (in a more scientific language, we speak about homology), and therefore, one can attribute to these defects a "topological number" $n \in \mathbb{Z}$ (also called winding number), characterizing how the spins are rotating. In the case of a vortex, $n = 1$, meaning that if one draws an oriented loop (for example oriented clockwise) encircling

the origin of the vortex, the spins on the loop will rotate clockwise [10]. In contrast for an antivortex, $n = -1$, meaning that if one draws the same loop, the spins rotate counter clockwise (see Fig. 1.11(a)). To minimize its free energy, the system prefers to generate free (i.e. decorrelated) vortices/antivortices above the critical temperature T_{BKT}, while it prefers to create bound vortex-antivortex pairs below T_{BKT}. This corresponds to the BKT transition. What is interesting to notice is that a vortex and an antivortex can annihilate each other, resulting in an homogeneous magnetization [HS06].

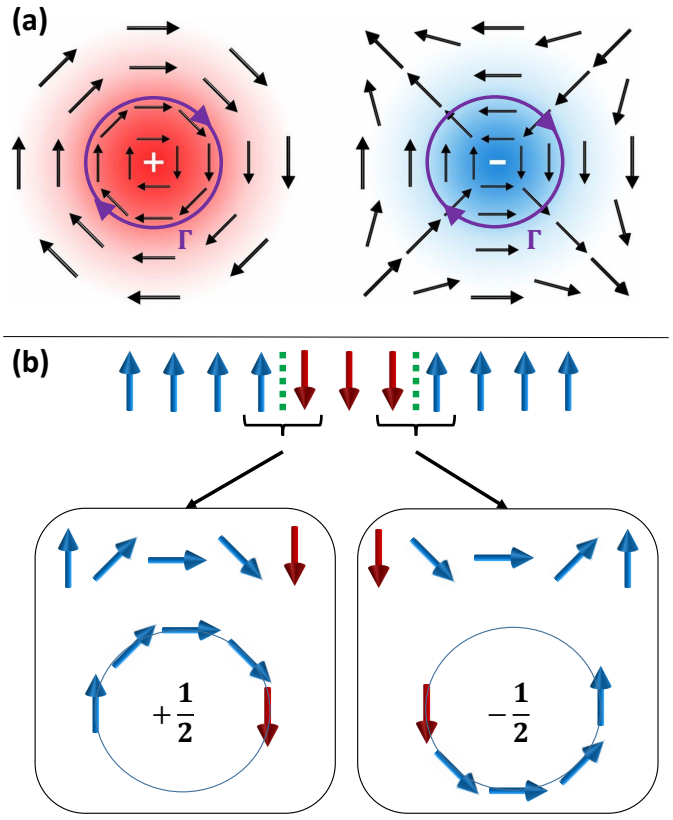

Figure 1.11: **Topological defects: vortices and spinons.** (a) Vortex (left) and antivortex (right) in an XY 2D FM system. These topological defects carry a topological index of ± 1. Figure extracted from [FN17]. (b) Pair of spinons in an Ising 1D FM system. These excitations are topological defects since each domain wall can be seen as the rotation of the magnetic moment in a semi-loop rotating clockwise or anticlockwise, thus carrying a topological index $+1/2$ and $-1/2$ respectively.

The spinons can also be described in terms of topological defects. Indeed these solitons, which can be seen as domain walls created in pairs, cannot be deformed individually in a continuous way to recover the ground state [11]. This can be understood with the help

[10] Formally, this writes $\oint_\Gamma ds \cdot \nabla\theta = 2\pi n$ where Γ is the loop encircling the origin of the vortex and θ the angle indicating the orientation of the spin.

[11] In contrast, in the classical limit, the excitations are spin-waves which are topologically "trivial". These excitations can be seen as the precession of the magnetic moment around their equilibrium position and it is easy to imagine bringing back continuously the excited state to the ground state ordering.

of Fig. 1.11(b). Let us consider an infinite chain. Imagine now that you want to erase one of the two defects, for example the spinon on the left, this would imply to flip all the blue spins on its left. The only way to bring back the FM order is, like in the case of vortex and antivortex, that the two spinons collide to annihilate with each other.

While the BKT transition is rather a condensation of topological objects, what I will present in Chap. 4 is a different topological quantum phase transition (driven by the quantum fluctuations) where the topological nature of the excitations changes.

Before presenting the state of the art of $BaCo_2V_2O_8$ in zero-field, let me now introduce some theoretical tools widely used for 1D quantum magnetism as it will be useful to understand the following.

1.5 Theoretical tools for studying spin-1/2 AF quantum chains

1.5.1 Fermionization

The aim of the fermionization procedure is to map any system, in our case an AF spin-1/2 chain, to a fermionic system. Jordan and Wigner have observed that the $|\uparrow\rangle$ and the $|\downarrow\rangle$ states of the spins can be thought as an occupied or empty fermion state [JW28].

The Jordan Wigner transformations write as follows:

$$\begin{aligned} S_j^+ &= c_j^\dagger e^{i\pi \sum_{i<j} c_i^\dagger c_i} \\ S_j^- &= c_j e^{i\pi \sum_{i<j} c_i^\dagger c_i} \\ S_j^z &= c_j^\dagger c_j - 1/2 \end{aligned}$$

where $c_j^\dagger$ and c_j are the creation and annihilation operators of a fermion at site j respectively [12]. The term $e^{i\pi \sum_{i<j} n_i}$, with $n_i = c_i^\dagger c_i$ the density operator, is called "string" operator and is introduced to preserve the commutation of spin operators $[S_i^\alpha, S_j^\beta] = 0$ with $\alpha, \beta = x, y, z$, as the fermionic operators anticommute $\left\{c_i^\dagger, c_j\right\} = \delta_{ij}$. In other words: spin operator = string operator $\times$ fermionic operator.

It is easy to introduce these transformations in the XXZ Hamiltonian of Eq. (1.11) and one obtains (up to a constant):

$$\mathscr{H}_{\mathrm{XXZ}} = J/2 \sum_j \left(c_j^\dagger c_{j+1} + c_j c_{j+1}^\dagger\right) + J\Delta \sum_j n_j n_{j+1} \tag{1.13}$$

To get a conventional fermionic Hamiltonian, it is convenient to make the canonical transformation $c_j \to (-1)^j c_j$, which consist in shifting the momentum of the fermions by

[12] As $c_i^\dagger c_i = \{0, 1\}$ (i.e. it describes an empty or occupied fermion state), the third equation gives indeed the two values of the spin $S^z = \pm 1/2$.

π [13]. The Hamiltonian described by Eq. (1.13) can be thus rewritten:

$$\begin{aligned}\mathscr{H}_{\mathrm{XXZ}} &= -J/2\sum_j \left(c_j^\dagger c_{j+1} + c_j c_{j+1}^\dagger\right) + J\Delta\sum_j n_j n_{j+1} \\ &= -t\sum_j \left(c_j^\dagger c_{j+1} + c_j c_{j+1}^\dagger\right) + U\sum_j n_j n_{j+1} \\ &= H_{\mathrm{free}} + H_{\mathrm{U}}\end{aligned} \tag{1.14}$$

where $t = J/2$ is the hopping matrix element and $U = J\Delta$ is the nearest neighbor interaction.

We then recover a model describing spinless fermions. The first term describes a free electron system while the second one describes the interactions between electrons [14].

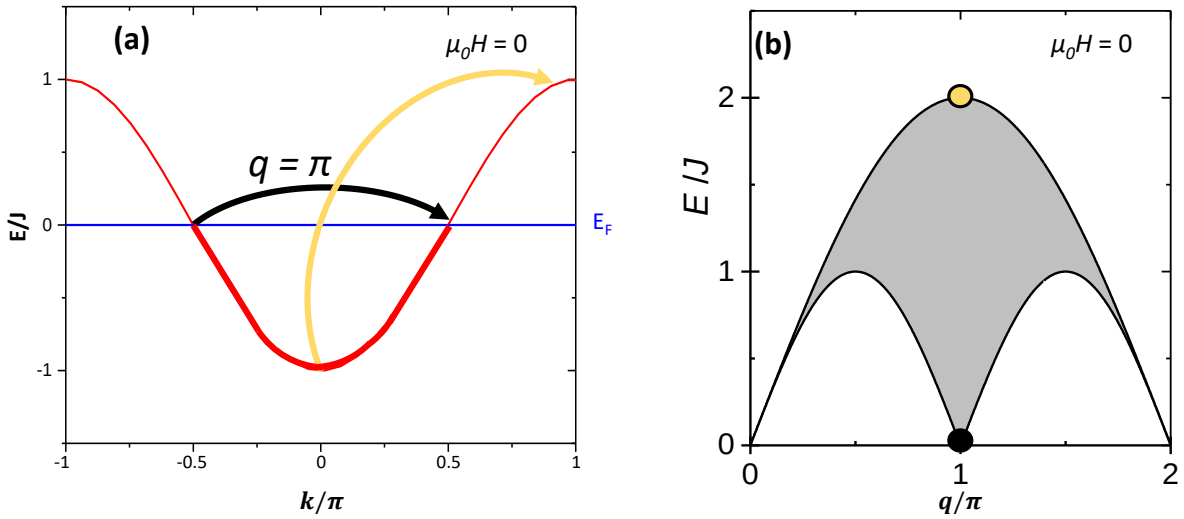

Figure 1.12: **Construction of the 2-spinons continuum by a fermionic representation.** (a) Particle-hole band obtained through Jordan-Wigner transformations applied on the XY Hamiltonian. Two specific particle-hole excitations, at zero-field in the Brillouin zone, are pointed out by black and yellow arrows: they correspond to zero-energy and maximum energy excitations, respectively. E_{F} denotes the Fermi level set to zero. The fermions are located below E_{F} (thick line) while the holes are located above (thin line). (b) 2-spinon continuum expected for an AF XY linear spin-1/2 chain at zero-field. This dispersion can be obtained from the particle-hole excitations at zero-field. Black and yellow points are the excitations relative to the black and yellows arrows in the left panel.

Mattis and Lieb were the first ones to point out that the XY model can be solved exactly by mapping it onto a tight binding Hamiltonian describing a half filled band of non-interacting fermions where one electron can hope to a hole [LSM61]. Indeed we have:

[13] In terms of spin language, this transformation consists in: $S_j^x \to (-1)^j S_j^x$, $S_j^y \to (-1)^j S_j^y$ and $S_j^z \to S_j^z$. These transformations respect the anticommutation rules of the spin operators. This changes $J_{xx} = J_{yy} = J \to -J$ and does not change $J_{zz} = J\Delta \to J\Delta$.

[14] The kinetic operator $S_j^+ S_{j+1}^-$ allows the spinons to move along the chain and can be seen as the $c_j^\dagger c_{j+1}$ operator allowing the electrons to hop from one site to the next one. In contrast the Ising term $J\Delta S_j^z S_{j+1}^z$ forces the spins to be antiferromagnetically coupled along the z direction and thus can be understood as an interaction term avoiding the hopping of electrons.

$$\mathscr{H}_{\rm XY} = -J/2 \sum_j \left(c_j^\dagger c_{j+1} + c_j c_{j+1}^\dagger \right) \tag{1.15}$$

In terms of the Fourier transform operators defined as: $c_j = \frac{1}{\sqrt{N}} \sum_k c_k e^{i\vec{k}\cdot\vec{r}_j}$ and $c_j^\dagger = \frac{1}{\sqrt{N}} \sum_k c_k^\dagger e^{-i\vec{k}\cdot\vec{r}_j}$ where N is the number of sites, $\vec{k}$ the momentum and $\vec{r_j}$ the position of the electron/hole, the Hamiltonian of Eq. (1.15) can be rewritten:

$$\begin{aligned} \mathscr{H}_{\rm XY} &= \sum_k \hbar\omega(k) c_k^\dagger c_k \\ \text{with} \quad & \hbar\omega(k) = -J \cos ka \end{aligned} \tag{1.16}$$

where a is the lattice spacing.

Interestingly, one can reconstruct from this representation the 2-spinon continuum of a linear spin-1/2 chain as shown in Fig. 1.12. Indeed Fig. 1.12(a) shows the half filled band obtained from the fermionization of a XY chain in zero-field and Fig. 1.12(b) shows the 2-spinon continuum for a XY chain [15] obtained by doing many different particle-hole excitations in the half-filled band (see the black and yellow arrows in Fig. 1.12(a)). The same excitation spectrum is obtained for $-1 < \Delta \leq 1$, but with renormalized energies due to the interaction between fermions as soon as $\Delta \neq 0$.

At first sight, this simple mapping allows us to fully understand quantum XXZ AF spin-1/2 chains. However, it can be shown that the spin-spin correlation functions turn to be very complicated, especially because the string operator is non-local. In addition fermions anticommute (Pauli principle) and are thus difficult to treat theoretically. One way to get rid of these problems is to change of representation and to approach the system by means of "bosonization".

I will briefly introduce it now as this is also widely used in 1D systems [GP04].

1.5.2 Bosonization

Generally, the nature of the bosons, in particular the fact that they commute, make them much easier to treat theoretically as one has to deal with density operators making the wave-functions of bosons much easier to write.

The basic idea of bosonization is that electron-hole excitations are naturally bosonic in nature. Here I would like to emphasize two facts: first, bosonization is only an effective theory, in the sense that it only describes low-energy properties of the system; second I do not pretend to be an expert of the bosonization technique. Thus I will just recall basic concepts behind it as it will help the readers to understand some of the theoretical descriptions of $BaCo_2V_2O_8$ in Chap. 4. For more detailed lectures, the reader can refer to [GP04; DS98; Mir03].

Let us consider the XXZ Hamiltonian expressed in terms of fermionic operators given by Eq. (1.14).

$$\begin{aligned} \mathscr{H}_{\rm XXZ} &= -J/2 \sum_j \left(c_j^\dagger c_{j+1} + c_j c_{j+1}^\dagger \right) + J\Delta \sum_j n_j n_{j+1} \\ &= \mathscr{H}_{\rm free} + \mathscr{H}_{\rm U} \end{aligned} \tag{1.17}$$

[15] The fermionization of the Heisenberg model (and more generally of the XXZ model with $0 < \Delta \leq 1$) leads to the same conclusion than the XY one though the fermions are now weakly interacting so that approximations have to be done.

where $\mathscr{H}_{\text{free}}$ is the Hamiltonian describing a free electron system and $\mathscr{H}_{\text{U}}$ the interactions.

Let us now make the assumption that the interaction term $\mathscr{H}_{\text{U}}$ is weak enough so that only the low-energy states are much affected [16]. It is therefore reasonable to linearize the spectrum (as the cosine function, coming from $\mathscr{H}_{free}$ and the linear one only differ at higher energy) as shown in Fig. 1.13.

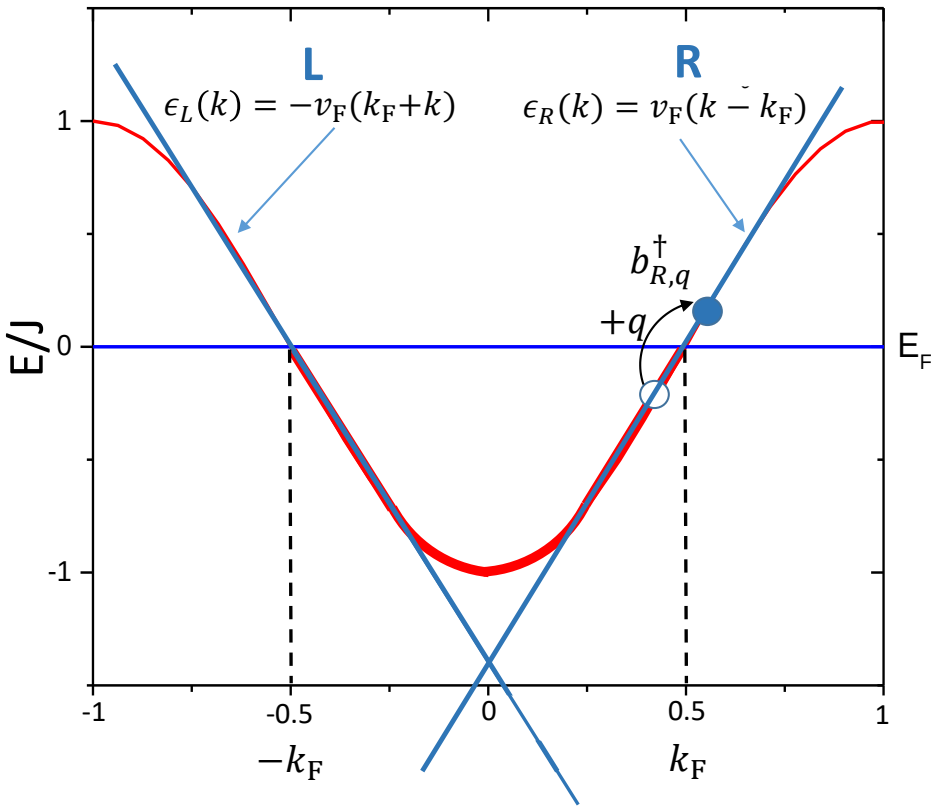

Figure 1.13: **Linearization of the half-filled band** given by the Jordan-Wigner transformation of the XY model. The left (L) and right (R) branches have the dispersion relation $\epsilon_{\text{L}} = -v_F(k_F + k)$ and $\epsilon_{\text{R}} = v_F(k - k_F)$. An example of the bosonic operator $b^\dagger_{\text{R,q}}$ acting on the right branch is shown. It creates a particle-hole excitation with a momentum $+q$.

Therefore there are two branches: the left branch (L) and right branch (R) having an energy $\epsilon_{\text{L}}(k) = -v_F(k_F + k)$ and $\epsilon_{\text{R}}(k) = v_f(k - k_F)$ respectively where k_F is the Fermi vector and $v_F = \frac{\partial \epsilon}{\partial k}\Big|_{k=k_F} = Ja\sin(k_F a)$ is the Fermi velocity. These branches can be extended to $-\infty$ and $+\infty$ and thus one can understand easily that we work now in the continuum limit [17]. We thus work now in field theory and we can then define "fermionic

[16] Indeed this can be understood easily through the second order perturbation theory where the second perturbation order writes: $\Delta E_0^{(2)} \simeq \sum_{n\neq 0} \frac{\langle 0|\mathscr{H}_{\text{U}}|n\rangle\langle n|\mathscr{H}_{\text{U}}|0\rangle}{E_0 - E_n}$ and $\Delta\,|0\rangle^{(2)} \simeq \sum_{n\neq 0} \frac{\langle 0|\mathscr{H}_{\text{U}}|n\rangle}{E_0 - E_n}\,|n\rangle$. Here $\mathscr{H}_{\text{U}}$ is weak enough so that the denominator suppresses the corrections of higher energy excitations.

[17] There is now an infinite number of state k in each branch. This is equivalent to $a \to 0$ such that $\sum_i \underset{a\to 0}{\longrightarrow} \int dx$.

field operators" $\psi(x)$ [18] by:

$$\begin{aligned}\psi(x) &= \frac{1}{\sqrt{L}}\sum_{k=-\infty}^{+\infty} e^{ikx}c_k \\ \psi^\dagger(x) &= \frac{1}{\sqrt{L}}\sum_{k=-\infty}^{+\infty} e^{-ikx}c_k^\dagger\end{aligned} \tag{1.18}$$

If we denote the momentum $q = k - k_F$, then the effective Hamiltonian $\mathscr{H}_0$ describing the two branches is:

$$\mathscr{H}_0 = v_F q \sum_q \left\{c^\dagger_{k_F+q}c_{k_F+q} - c^\dagger_{-k_F+q}c_{-k_F+q}\right\} \tag{1.19}$$

then, in terms of density operators:

$$\mathscr{H}_0 = -iv_F\left\{\psi^\dagger_{\mathrm{R}}\partial_x\psi_{\mathrm{R}} - \psi^\dagger_{\mathrm{L}}\partial_x\psi_{\mathrm{L}}\right\} \tag{1.20}$$

where $\psi_{\mathrm{R,L}} = \sum_q e^{iqx}c_{\pm k_F+q} = \sum_q e^{iqx}c_{\mathrm{R,L}}$ are the density operators of the right (R) and left (L) branch. This is the starting point of the bosonization technique that I will not develop further. One can notice that the Hamiltonian is still written in fermionic language. To solve this Hamiltonian, one can focus only on half of the Hamiltonian, for instance on the right branch. To go further and by taking a big shortcut, bosonic operators $b_{\mathrm{R,q}}$, $b^\dagger_{\mathrm{R,q}}$ and the bosonic field $\varphi_{\mathrm{R}}(x)$ are defined as:

$$b_{\mathrm{R,q}} = 1/\sqrt{n_q}\sum_{k=-\infty}^{+\infty} c^\dagger_{\mathrm{R,k-q}}c_{\mathrm{R,q}} \tag{1.21}$$

$$b^\dagger_{\mathrm{R,q}} = 1/\sqrt{n_q}\sum_{k=-\infty}^{+\infty} c^\dagger_{\mathrm{R,k+q}}c_{\mathrm{R,q}} \tag{1.22}$$

$$\varphi_{\mathrm{R}}(x) = -\sum_q \frac{1}{\sqrt{n_q}}e^{-iqx}b_{\mathrm{R,q}}e^{-\alpha q/2} \tag{1.23}$$

where $n_q = \frac{Lq}{2\pi}$ a relative number associated to q and α a cut off introduced to ensure that the higher energy modes do not produce divergence in the calculation of the correlation functions. Note that the bosonic operators $b_{\mathrm{R,q}}$ and $b^\dagger_{\mathrm{R,q}}$ create particle-hole excitations with a momentum $+q$ and $-q$ respectively (see an example in Fig. 1.13).

After some transformations, the important equation relating the fermionic field ψ_{R} and the bosonic field φ_{R} is obtained:

$$\psi_{\mathrm{R}}(x) = \frac{1}{2\pi\alpha}\kappa_{\mathrm{R}}e^{-i2\sqrt{\pi}\varphi_{\mathrm{R}}(x)} \tag{1.24}$$

where κ_{R} is called the "Klein" factor introduced to preserve the anticommutation of ψ_{R}.

Finally, the two dual bosonic fields $\phi(x)$ and $\theta(x)$ can be defined [19]:

$$\phi(x) = \varphi_{\mathrm{R}}(x) + \varphi_{\mathrm{L}}(x) \tag{1.25}$$

$$\theta(x) = -\varphi_{\mathrm{R}}(x) + \varphi_{\mathrm{L}}(x) \tag{1.26}$$

[18] These operators are the continuum limit analog of the annihilation creators c_j and satisfy the anti-commutation rule $\{\psi(x), \psi(y)\} = \delta(x-y)$.

[19] They are called dual since they do not commute. Indeed $[\phi(x), \theta(x')] = -\frac{i}{2}\mathrm{sign}(x-x')$ where the function $\mathrm{sign}(x) = +1$ for $x > 0$ and $\mathrm{sign}(x) = -1$ for $x < 0$.

With all these relations, one can rewrite the Hamiltonian $\mathscr{H}_0$ given by Eq. (1.20) in terms of the two dual bosonic field operators $\phi(x)$ and $\theta(x)$ [GP04; DS98]:

$$\mathscr{H}_0 = \frac{v_F}{2\pi}\int dx \left\{ \left(\frac{d\phi(x)}{dx}\right)^2 + \left(\frac{d\theta(x)}{dx}\right)^2 \right\} \tag{1.27}$$

By taking into account the interactions (weak enough so that they can be renormalized), the Hamiltonian becomes the one of the TLL theory:

$$\mathscr{H}_{\text{TLL}} = \frac{v_F}{2\pi}\int dx \left\{ \frac{1}{K}\left(\frac{d\phi(x)}{dx}\right)^2 + K\left(\frac{d\theta(x)}{dx}\right)^2 \right\} \tag{1.28}$$

where K is the Luttinger parameter which takes into account the interactions (which are thus renormalized). This Hamiltonian describes many 1D systems where the interactions are weak enough, for instance Heisenberg AF spin-1/2 chains. Actually, as we will see in Chap. 4, the bosonic fields $\phi(x)$ and $\theta(x)$ can be seen semi-classically as the polar and azimutal angles of the staggered magnetization vector for an AF spin-1/2 quantum spin-chain.

If the interactions are strong enough, i.e. for $\Delta > 1$, the Hamiltionian $\mathscr{H}_U$ cannot be treated at a first order of perturbation and thus cannot be renormalized. To get rid of this problem, it can be shown that a correction has to be included leading to another term in the Hamiltonian which then becomes:

$$\mathscr{H}_{\text{SG}} = \frac{v_F}{2\pi}\int dx \left\{ \frac{1}{K}\left(\frac{d\phi(x)}{dx}\right)^2 + K\left(\frac{d\theta(x)}{dx}\right)^2 \right\} - \frac{2\lambda}{(2\pi\alpha)^2}\int dx \cos 4\phi(x) \tag{1.29}$$

where λ is a constant reflecting the strong interactions in the system

This is the so called sine-Gordon (SG) Hamiltonian [GP04; Raj82] describing for instance Ising-like spin-1/2 chains. Qualitatively, in order to minimize the energy of the system the second term has to be minimized and hence $2\phi(x) = \pi n$ with $n \in \mathbb{Z}$, which means in other words that the spins point along a privileged axis, i.e. the Ising-axis. The sine-Gordon model is widely used in physics and describes soliton-like excitations. Indeed one of the excitations predicted by this Hamiltonian is a pair made of a soliton and an antisoliton, describing then the two spinons in the case of quantum spin-chains [Raj82]. We will see the solutions of this equation at the end of Chap. 4.

Let me now present the state of the art at zero-field of $BaCo_2V_2O_8$.

1.6 State of the art of $BaCo_2V_2O_8$, an Ising-like quasi-1D antiferromagnet

In this section, I will introduce the $BaCo_2V_2O_8$ compound which is a quasi-1D Ising-like antiferromagnet. This compound has raised a lot of interest because of its moderate anisotropy ($\varepsilon \simeq 0.5$) allowing strong quantum fluctuations leading to a very interesting physics as we will see in the next chapters. I will first present the crystallographic structure of $BaCo_2V_2O_8$ and its general magnetic properties. Then I will present the magnetic

structure and the dynamical properties of $BaCo_2V_2O_8$ at zero-field obtained from neutron scattering experiments.

1.6.1 Crystallographic structure

$BaCo_2V_2O_8$ crystallizes in the tetragonal space group $I4_1/acd$ (n° 142). This space group is centrosymmetric and the unit cell is body-centered. The lattice parameters at ambiant temperature are: $a = b = 12.444$ Å and $c = 8.415$ Å. Each unit cell contains 8 chemical formulas (Z = 8) [RH86]. Fig. 1.14 shows the crystallographic structure of $BaCo_2V_2O_8$.

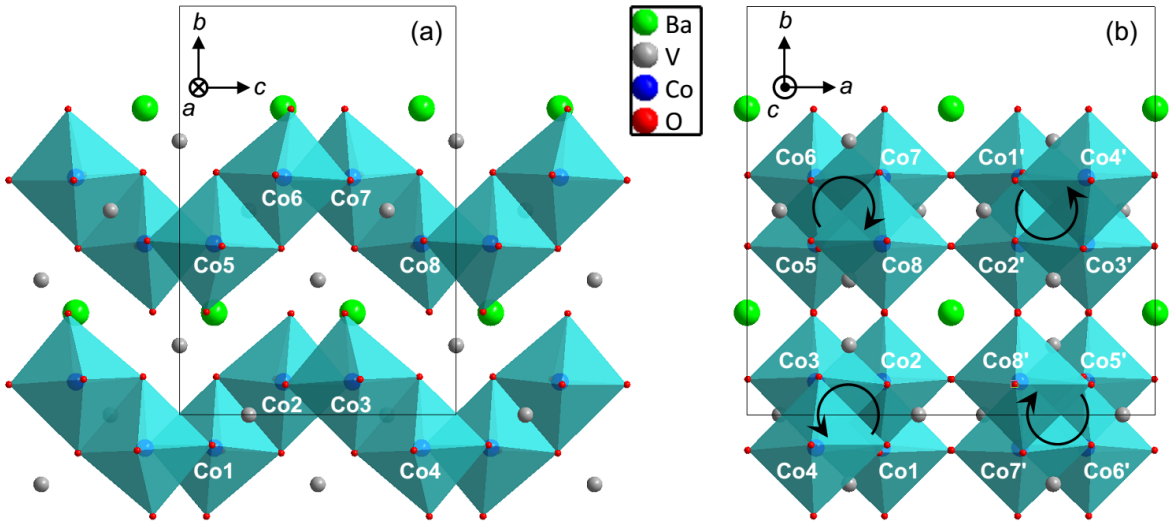

Figure 1.14: **Crystallographic structure of $BaCo_2V_2O_8$.** (a) Projection in the (b, c) plane. For more clarity, only two chains are represented here. (b) Projection in the (a, b) plane of the four chains contained in the unit cell. The clockwise and anticlockwise arrows indicates the sense of rotation of the screw chains when z increases. Figure taken from [Can+13]. Co_1, $Co_{1'}$, Co_5, $Co_{5'}$ are located at $z = 1/8$, Co_2, $Co_{2'}$, Co_6, $Co_{6'}$ at $z = 3/8$, Co_3, $Co_{3'}$, Co_7, $Co_{7'}$ at $z = 5/8$ and Co_4, $Co_{4'}$, Co_8, $Co_{8'}$ at $z = 7/8$. The $Co_{3'}$ atom is obtained from Co_1 $(x, y, z = 1/8)$ by the body-centering translation and is thus located at $(x + 1/2, y + 1/2, z = 5/8)$.

The magnetic ions Co^{2+} are contained in the octahedra formed by the neighboring atoms of oxygen. Each CoO_6 octahedron shares an edge with two neighboring octahedra forming screw chains along the c-axis. Each screw chain is separated from its neighboring chains by non-magnetic VO_4 (V^{5+}) tetrahedra and Ba^{2+} ions, thus giving to the magnetic system a strong one-dimensional character with interchain magnetic interactions much smaller than the intrachain one. One can notice in Fig. 1.14(b) that there are two types of screw chains:

- The 4_1-axis parallel to the c-axis and located at $(x = 1/4, y = 0)$ transforms the Co_1 atom at coordinate $z = 1/8$ into the Co_2 $(z = 3/8)$, then into the Co_3 $(z = 5/8)$ and finally into the Co_4 $(z = 7/8)$, thus forming a screw chain of CoO_6 octahedra rotating counter clockwise while z increases.

- The 4_3-axis parallel to the c-axis and located at $(x = 1/4, y = 1/2)$ transforms the Co_5 atom at coordinate $z = 1/8$ into the Co_6 ($z = 3/8$), then into the Co_7 ($z = 5/8$) and finally into the Co_8 ($z = 7/8$), thus forming a screw chain rotating clockwise while z increases.

The chains | $Co_{1'}$...$Co_{4'}$ | and | $Co_{5'}$...$Co_{8'}$ | are simply obtained by the body-centering of the unit cell, i.e. by applying the translation $(1/2, 1/2, 1/2)$. Therefore, the Co_1 atom produces the $Co_{3'}$, Co_5 produces $Co_{7'}$ and so forth. Finally, each unit cell contains 4 screw chains parallel to the c-axis and 16 Co^{2+} magnetic ions.

1.6.2 Effective spin-1/2 and Ising-like anisotropy

The magnetism in $BaCo_2V_2O_8$ is due to the Co^{2+} ions which have an orbital angular momentum $L = 3$ and a spin $S = 3/2$ as a free ion. The atom of Vanadium V^{5+} is non-magnetic. The crystal field theory of the magnetic ion Co^{2+} (d^7) was widely studied in the 50's and the 60's by Abragham and Pryce in 1951 [AP51], by Lines in 1963 [Lin63] and later by Goodenough in 1968 [Goo68]. In $BaCo_2V_2O_8$, because of the spin-orbit coupling and the compression of the CoO_6 octahedra along the c-axis [20], it can be shown that the crystal field ground state is given by a Kramers doublet. The gap ΔE between this Kramers doublet and the first excited state was found to be about 30 meV (thus about 350 K) [Can10]. As we will see later, the energy range of the magnetic excitations in $BaCo_2V_2O_8$ is much lower than this energy (typically below 10 meV) and therefore, we can consider that only the ground state Kramers doublet is populated in all this work. This latter can be considered as fictitious spin states $\pm 1/2$. Consequently, the real spin $S = 3/2$ can be replaced by anisotropic effective spin $S = 1/2$ and $BaCo_2V_2O_8$ at zero-field can be described by the XXZ Hamiltonian given by Eq. (1.11) with effective spins 1/2.

While this compound was first synthesized by R. Wichmann and H. Müller-Buschbaum [RH86], it tooks more than a decade to see a strong interest raising for $BaCo_2V_2O_8$ after the studies of Z. He et *al.* [He+05a; He+05b] and of S. Kimura et *al.* [Kim+06; Kim+07; Kim+08b; Kim+08a].

Fig. 1.15(a) shows the susceptibility as a function of the temperature measured on a $BaCo_2V_2O_8$ single-crystal by Z. He et *al.* [He+05b]. One can see that $BaCo_2V_2O_8$ exhibits a strong anisotropic behavior depending on the orientation of the applied magnetic field: the susceptibility curve observed when the field is applied along the c-axis, i.e. parallel to the chains, is almost twice larger than the one when the field is perpendicular. Thus the easy-axis of anisotropy is along c. When the magnetic field is applied along the c-axis, the susceptibility reaches a maximum at around $T \simeq 30$ K. This behavior is characteristic of 1D correlations in AF spin chain systems [Joh+00].

Fig. 1.15(b) shows the specific heat measurements as a function of the temperature in zero-field. One can see a sharp λ-like peak around $T = T_N \simeq 5.5$ K, pointing out a Néel ordering below this temperature. The fact that a long range order is possible [21] is due to the presence of weak interchain interactions (i.e. 3D couplings) in $BaCo_2V_2O_8$.

[20] This comes from the Jahn Teller effect which stipulates that any (non-linear) molecule presenting a degenerate ground state will undergo a geometrical distortion so that it lifts the degeneracy because the distortion lowers the overall energy [JT37]

[21] Let me recall that for a pure 1D spin-1/2 system, only a quasi long range order is possible.

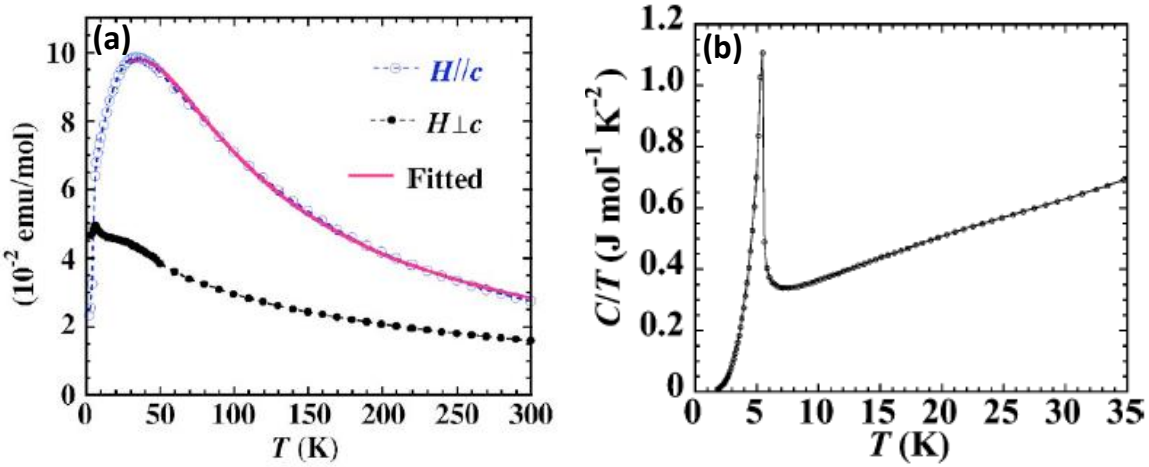

Figure 1.15: **Macroscopic characterization of the magnetic properties of $BaCo_2V_2O_8$.** (a) Susceptibility χ as a function of T for two different orientations of the magnetic field set to $\mu_0 H = 1$ T. (b) Temperature dependance of the specific heat at zero-field. Figures extracted from [He+05a; He+05b].

To summarize, $BaCo_2V_2O_8$ consists in screw-chains parallel to the c-axis. It shows an Ising-like anisotropy where the moments want to align antiferromagnetically along the c-axis. The system enters into a Néel phase below the critical temperature $T_N \simeq 5.5$ K because of the interactions between the chains. Let us now turn to the studies using neutron scattering which allowed to determine the magnetic structure and the dynamical properties of $BaCo_2V_2O_8$.

1.6.3 Magnetic structure at zero-field

The magnetic structure of $BaCo_2V_2O_8$ was first investigated by powder diffraction by Kawasaki et *al.* [Kaw+11]. E. Canévet et *al.* then determined the magnetic structure of $BaCo_2V_2O_8$ at zero-field by neutron diffraction on a single crystal [Can+13].

In their experiment, the propagation vector, which reflects the periodicity of the magnetic unit cell with respect to the crystallographic one, was found to be:

$$\vec{k} = (1, 0, 0) \tag{1.30}$$

This means that the hkl magnetic Bragg peaks are such that $h + k + l$ is odd (in contrast to the nuclear ones for which $h + k + l$ is even due to the body-centering of the cell). $\vec{k} = (1, 0, 0)$ or equivalently $\vec{k} = (0, 1, 0)$ rather than $\vec{k} = (0, 0, 1)$ comes from the fact that $a > c$ [Ros87].

Figs. 1.16(a-b) show the magnetic structure refined at zero-field projected both in the (a, b) and the (a, c) planes. One can see that the magnetic moments are antiferromagnetically coupled ($J > 0$) and aligned along the c-axis, confirming that the Ising-axis

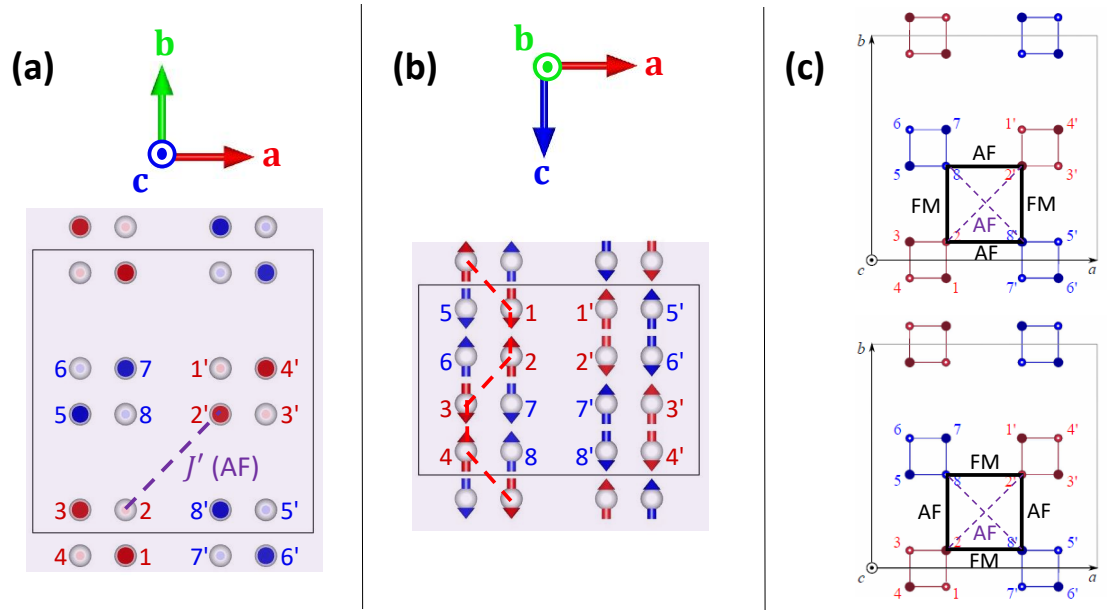

Figure 1.16: **Magnetic structure of $BaCo_2V_2O_8$ at zero-field.** The blue and red colors denote chains rotating clockwise and counter clockwise respectively. (a-b) Projections in the (a, b) and (a, c) plane respectively. The red dashed line on panel (b) shows the $|\ Co_1...Co_4\ |$ spin chain in the unit cell. (c) The two magnetic domains. The interaction in diagonal (dashed purple line) between two chains having the same chirality stabilizes the magnetic structure and implies frustration between chains having a different chirality. Here AF and FM denote the fact that the magnetic moments are antiparallel and parallel respectively (the parallel or antiparallel arrrangement for the pair Co_2-$Co_{8'}$ is the same as the one for Co_1-$Co_{7'}$ mentionned in the text). Figure extracted from [Can+13].

is along $\vec{c}$ as observed in macroscopic measurements (see Fig. 1.15(a)). The staggered magnetization has been obtained as $m_c = 2.167(3)\ \mu_B/Co^{2+}$ at $T = 1.8$ K [Can+13].

Actually, two magnetic domains had to be included in the magnetic structure refinement. These magnetic domains are related by the 4_1 screw axis symmetry element (lost when going from the paramagnetic to the ordered phase). These two domains were found to be equipopulated and are shown in Fig. 1.16(c). One can see that the magnetic order is characterized by some interchain frustration. For instance the pairs of Co_1-$Co_{7'}$ and Co_2-$Co_{8'}$ are symmetrically equivalent (through the 4_1 screw axis) but one is FM and the other one AF (reversed from one domain to the other) which shows that the corresponding magnetic interaction is frustrated. Actually, a small orthorhombic distorsion of the structure (leading to a a bit larger or smaller than b) stabilizes this magnetic order by removing partially some of the frustration. Finally the interchain interaction that seems to stabilize the 3D order is between two chains in diagonal, i.e. two chains having the same chirality (clockwise or counter clockwise) [Can+13; Kla+15]. This interaction is denoted J' (see Fig. 1.16 (a)).

To summarize, the magnetic order of $BaCo_2V_2O_8$ corresponds to an AF arrangement along the chain of the magnetic moments oriented along the c-axis. Moreover the interchain interaction stabilizing the structure is found to be the one in diagonal between two chains of the same nature.

1.6.4 Dynamical properties at zero-field

B. Grenier et *al.* investigated the spin-dynamics of $BaCo_2V_2O_8$ by means of inelastic neutron scattering [Gre+15a].

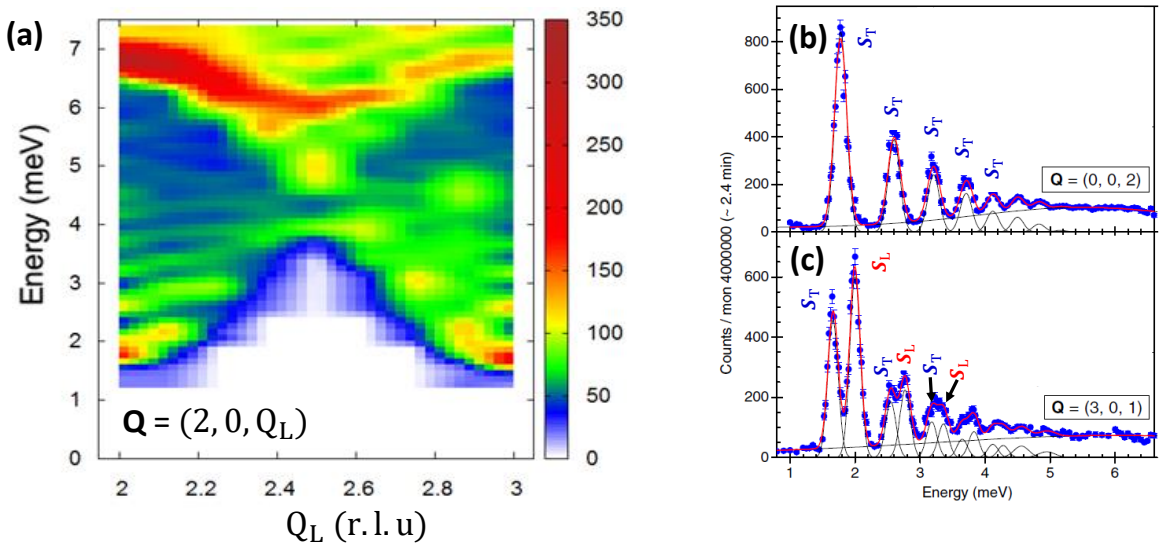

Figure 1.17: **Spin-dynamics of $BaCo_2V_2O_8$ at zero-field.** (a) Dispersion spectrum of $BaCo_2V_2O_8$ along Q_L (i.e. along the chain axis) at zero-field and $T = 1.6$ K. Q_L is expressed in reciprocal lattice units (r.l.u). (b-c) Energy scan at zero-field and $T = 1.6$ K on the two positions ZC of the scattering $\vec{Q} = (0, 0, 2)$ and $\vec{Q} = (3, 0, 1)$. The red solid curves are Gaussian fits. The transverse S_T and longitudinal S_L character of the modes are indicated. Figures extracted from [Gre+15a].

Fig. 1.17(a) shows the dispersion spectrum of $BaCo_2V_2O_8$ in the part of the Brillouin zone delimited by the zone center (ZC) position $\vec{Q} = (2, 0, 2)$ and the antiferromagnetic (AF) position $\vec{Q} = (2, 0, 3)$. One can see two main differences between the spectrum of $BaCo_2V_2O_8$ and the one of a Heisenberg spin 1/2 chain (for instance, see the dispersion of $KCuF_3$ in Fig. 1.7). First, there is an energy gap $\Delta \simeq 1.7$ meV. This comes mostly from the Ising-like anisotropy which forces the spins to point along the c-axis, thus making it more difficult for them to fluctuate (in contrast to the Heisenberg case). Secondly, there is a series of discretized excitations as one can see in Fig. 1.17(b-c) instead of a continuum. This comes from the sizable interchain interaction J' which confines the spinons. One can understand this effect through Fig. 1.18.

These discretized excitations are called "Zeeman ladders" and have been theoretically predicted by H. Shiba for the case of a strong Ising (i.e. $\varepsilon << 1$) quasi-1D spin 1/2 system where the interchain interaction is treated as a perturbation in mean field theory [Shi80]. One remarkable feature in $BaCo_2V_2O_8$ is that it shows two types of Zeeman ladders:

- Transverse (T) ones, i.e. fluctuations perpendicular to the ordered magnetic moment, i.e. in the $(\vec{a}, \vec{b})$ plane, denoted S_T.
- Longitudinal (L) ones, i.e. fluctuations parallel to the ordered magnetic moment, i.e. along the $\vec{c}$ direction, denoted S_L.

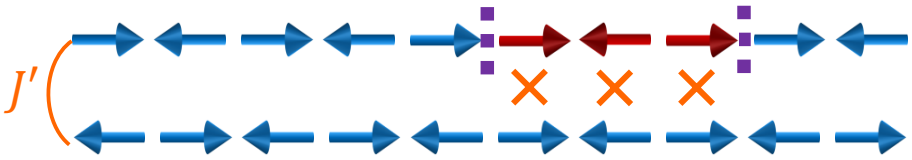

Figure 1.18: **Confinement of the spinons.** This effect is pictured in the Ising case for sake of clarity. Two spin-chains, with one pair of spinons in one of them, are coupled antiferromagnetically through J'. The presence of this interaction will cost an energy proportional to the distance between the two spinons preventing them from propagating along the chain (while in the pure 1D case, the spinons can propagate with no energy cost).

The latter have no classical analogue [22] and are a signature of quantum effects. It has been established theoretically that the intensity of the longitudinal mode in an Ising-like chain is proportional to ϵ^2 [IS80]. This is why they are clearly visible in $BaCo_2V_2O_8$ ($\varepsilon \simeq 0.5$) while it was impossible to observe them in the strong AF Ising-like compounds $CsCoCl_3$ and $CsCoBr_3$ ($\varepsilon \simeq 0.1$) [HY79].

The existence of such T and L modes in $BaCo_2V_2O_8$ can be proven through Fig. 1.17(b-c). Indeed one has to remember that a geometrical factor is involved in the magnetic scattering cross sections of the neutrons, since the neutrons only see the components of the magnetic moment perpendicular to the scattering vector $\vec{Q}$ both in the ordered phase and in the dynamics. In Fig. 1.17(b), the scattering vector is $\vec{Q} = (0, 0, 2)$ so that only the transverse fluctuations of the ordered moments S_{T} are probed and hence the series of peaks are transverse modes. In contrast, in Fig. 1.17(c), the scattering vector is set to $\vec{Q} = (3, 0, 1)$ so that both perpendicular S_{T} and parallel S_{L} fluctuations are probed. One can see that another series of peaks appears, hence evidencing the longitudinal character of these additional modes.

The transverse and longitudinal fluctuations correspond to an odd and even number of reversed spins, respectively. Thus the total magnetization of the transverse modes is $S^z = \pm 1$ while the one of the longitudinal modes is $S^z = 0$ [23]. Such excitations are shown in Fig. 1.19. In the following chapters, I will denote these zero-field energy modes $|j\ \mathrm{T}\rangle = |j, S^z = \pm 1\rangle$ and $|j\ \mathrm{L}\rangle = |j, S^z = 0\rangle$, the transverse (T) and longitudinal (L) modes respectively where j is the number of the T or L mode, starting from the lowest energy one of the considered series.

From the measured dispersion spectrum and using both the theory of Shiba [Shi80] and the one of Bougourzi [BKM98], the latter describing the continuum of excitation expected for an AF Ising-like spin-1/2 chain with any value of $\varepsilon < 1$ and without interchain interaction, B. Grenier et *al.* were able to extract the following parameters: $J = 4.8$ meV,

[22] The spin-waves are always transverse fluctuations as the precession of the spins implies a component transverse to the order moments.

[23] In a hand-waving way, it is somehow as if the transverse excitations were obtained by the application of the spin-flip operators (thus implying a difference of magnetization between the Néel state and the excited state $\Delta S^z = \pm 1$) related to the "transverse operator" S^x and S^y while the longitudinal excitations are obtained by application of the "longitudinal" operator S^z (conserving the magnetization and thus $\Delta S^z = 0$).

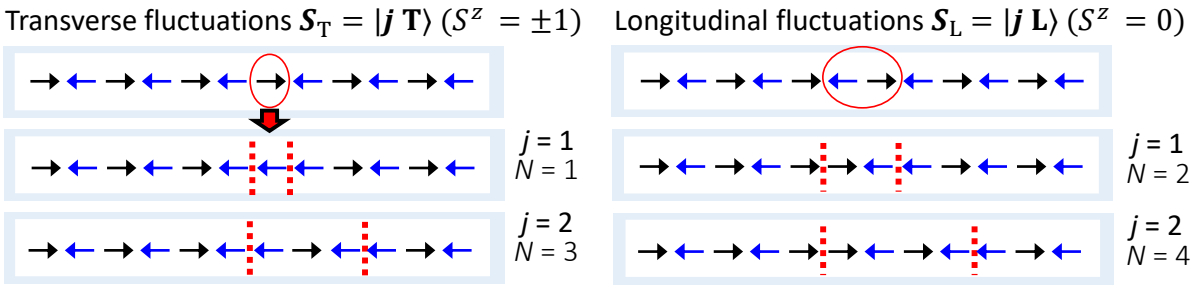

Figure 1.19: **Transverse $S_T = |j\ T\rangle$ and longitudinal $S_L = |j\ L\rangle$ 2-spinons excitations for $j = 1, 2$.** They correspond to an odd and even number N of reversed spins, thus carrying a total magnetization $S^z = \pm 1$ and $S^z = 0$ respectively.

$\varepsilon \simeq 0.56$ and $J' \simeq 0.2$ meV [Gre+15a], consistent with what was found in the previous studies [Kim+06; Kim+07]. We will see later that numerical calculations give a more accurate estimation of these parameters.

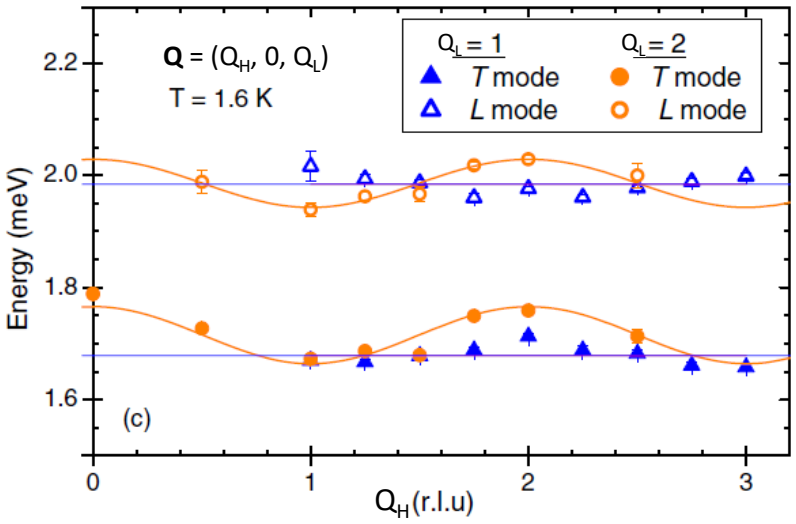

Figure 1.20: **Dispersion of the excitations along a^*** obtained from constant-Q energy scans at $T = 1.6$ K for $Q_L = 1$ and $Q_L = 2$ at zero-field. The orange solid line is a fit with the phenomenological law: $E = \sqrt{\Delta^2 + (E_m^2 - \Delta^2)\sin^2[(Q_H - 1)\pi/2]}$, where Δ is the gap and E_m is the maximum of the dispersion. Figure extracted from [Gre+15a].

B. Grenier et *al.* have also probed the dispersion perpendicular to the chain in order to determine the interchain interactions. Fig. 1.20 shows the dispersion along a^* of the first transverse T and longitudinal L excitations. The dispersion is very little Q_L dependent: flat for $Q_L = 1$ and with a dispersion amplitude of about 0.1 meV for $Q_L = 2$. The fact that the excitations are almost non-dispersive perpendicularly to the chains is probably

a signature of the frustration between neighboring chains in $BaCo_2V_2O_8$, which means that the effective interchain interaction responsible for the dispersion of the excitations is much reduced with respect to the strongest individual interchain interactions.

Finally let me emphasize that there is a folding of the dispersion in $BaCo_2V_2O_8$ due to the screw structure of the chain. This means that the AF point behaves like the ZC one and vice versa (one can see it on Fig. 1.17(a), where what is observed on the AF point $\vec{Q} = (2, 0, 3)$ is also observed on the ZC point $\vec{Q} = (2, 0, 2)$.

1.6.5 $BaCo_2V_2O_8$ samples

In this PhD, I have exclusively worked with single crystals of $BaCo_2V_2O_8$. The samples where previously synthesized by Pascal Lejay at the Néel Institute, Grenoble. They were grown by the floating zone technique in an image furnace [Lej+11], leading to large single crystals as shown in Fig. 1.21.

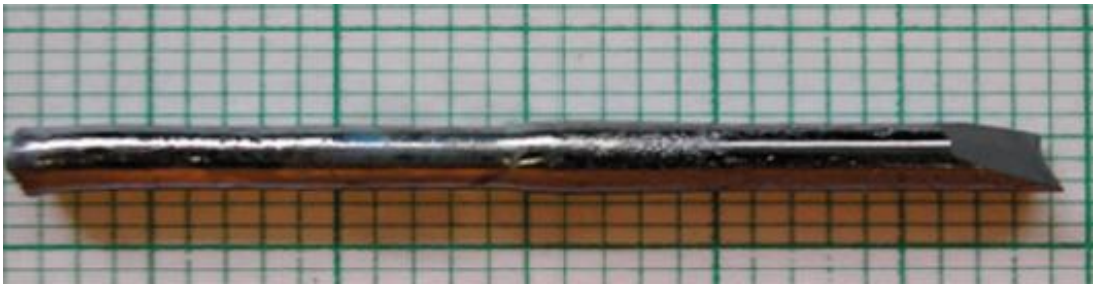

Figure 1.21: **Single crystal of $BaCo_2V_2O_8$** obtained by the floating zone method. The crystals grown by this technique have the typical dimension of about 3 mm diameter and 5 cm long. Figure extracted from [Lej+11].

The $Ba(Co_{1-x}Mg_x)_2V_2O_8$ samples (that I will present in Chap. (6)) were grown by the same method by Sandra Niesen [Nie+14] at Köln University for $x = 5\%$ and by P. Lejay for $x = 2\%$.

Chapter 2

Experimental techniques

Sommaire

2.1 Summury

2.1.1 Abstract

The aim of this chapter is to introduce the different experimental techniques used during this thesis. The first part explain in details the neutron scattering techniques by introducing the different key concepts such as the nuclear and magnetic scattering cross sections. Secondly are exposed the cases of the elastic and inelastic neutron scattering experiments. Finally the different instruments used during this PhD are briefly described. The second part of this chapter deals with the specific heat measurements under high pressure. First is presented the preparation of a diamand anvil cells, device allowing to reach pressure up to 10 GPa. Then the AC-calorimetry principle is explained in details. This qualitative technique allowed us to extract the different values of the critical temparatures and critical fields for different values of pressure and magnetic field.

2.1.2 Résumé en français

Le deuxième chapitre est dédié aux différentes techniques expérimentales utilisées au cours de cette thèse. La première partie expose en détail les techniques de diffusion des neutrons, en introduisant les différents concepts clés tels que les sections efficaces de diffusion nucléaire et magnétique des neutrons. Ensuite est exposé le cas de la diffusion élastique des neutrons, i.e. à transfert d'énergie nul. Ce cas correspond à la diffraction des neutrons qui permet en pratique de déterminer la structure nucléaire et magnétique d'un échantillon. La diffusion inélastique des neutrons, qui correspond à un transfert d'énergie non-nul est alors décrite. Cette technique permet de sonder les excitations de la matière tels que les spinons dans le cas de $BaCo_2V_2O_8$. Enfin, les différents instruments utilisés au cours de cette thèse comme les diffractomètres pour monocristaux et les spectromètres trois axes sont exposés brièvement.

La deuxième partie de ce chapitre est axée sur les mesures de chaleur spécifique sous haute pression. En premier est exposé le montage d'une cellule à enclumes diamant, dispositif permettant d'atteindre des pressions de l'ordre de 10 GPa. Ensuite est expliquée la technique de calorimétrie-AC qui permet de mesurer la chaleur spécifique de l'échantillon. Cette technique qualitative nous a permis d'extraire les différentes valeurs des températures critiques et des champs critiques pour différentes valeurs de la pression et du champ magnétique.

2.2 Neutron scattering

Different kinds of experiments have been done during my thesis such as specific heat measurements under pressure and neutron scattering. As the latter has been the most widely used technique, I will first introduce it.

Neutron scattering refers to the scattering of free neutrons by matter. It is a powerful technique used to investigate materials and has many applications in a lot of fields such as condensed matter, soft matter, chemistry or biology. Neutrons are powerful as they allow to probe microscopic informations in materials. Neutron scattering is also one of the most powerful technique to investigate magnetic materials and is often a crucial step after the first macroscopic characterizations. Moreover neutron diffraction (elastic scattering) and inelastic neutron scattering can both be performed, allowing to determine many informations such as nuclear and magnetic structures or the dynamics (i.e. the excitations) of the systems.

In the present chapter, I will first introduce some generalities about the neutron such as its properties, its scattering cross sections and how we can manipulate a neutron beam. Secondly I will discuss about neutron diffraction by first explaining the nuclear and magnetic scattering, then diffraction by a cristal and finally I will describe the diffractometers that I have used. The third and last part will be about the inelastic neutron scattering where I will present the magnetic dynamical structure factor and then show examples of three-axis spectrometers which were mainly used in my PhD.

2.2.1 Why using neutrons?

The neutron is a particle discovered by J. Chadwick in 1931 and was used for the first time for a neutron diffraction experiment fifteen years latter [Shu95]. In terms of particle physics, the neutron is a baryon consisting of three fermions called quarks: 1 quark up with a charge $+2/3$ and 2 quarks down with a charge $-1/3$. This results in a particle with a spin $S = 1/2$ and a charge $C = 0$. The properties of the neutron make it an excellent tool to investigate the static and the dynamic properties of nuclear and magnetic systems.

- The neutron is a neutral particle (hence its name...) and then is not sensitive to the electron cloud of the atoms contrary to X-rays. Therefore it can deeply penetrate the matter. The neutrons interact with the atomic nucleus via strong interaction.

- The neutron carries a spin $S = 1/2$ and hence, is sensitive to magnetic fields. That is why neutron is a favored microscopic probe for magnetic systems with which it interacts via dipolar interaction.

- The energies and the wavelengths accessible in neutron scattering experiments are well adapted to study condensed matter. Neutrons used for scattering experiments have a wavelength of the order of the Å which is comparable to the inter-atomic distances [1]. They generally have an energy smaller than 100 meV while X-rays produced in synchrotrons have an energy of the order of the keV. Therefore neutrons are much more suited to probe low-energy dynamics such as magnetic excitations or phonons.

[1] The X-rays has also a wavelength of the same magnitude. Hence both techniques are well suited for diffraction

- Finally, while X-rays are sensitive to the atomic number Z and hence to the size of the atoms, neutrons are sensitive to isotopes and to light elements such as hydrogen, oxygen and so forth.

As any particle, the wave-particle duality stands for the neutrons. Then we can assign them a wavelength λ and a wave-vector $\vec{k}$ and write the following equation for the energy E of the neutrons:

$$E = \frac{p^2}{2m_n} = \frac{h^2}{2m_n\lambda^2} = \frac{\hbar^2 k^2}{2m_n} \text{ where } \vec{p} = \hbar\vec{k} \text{ and } \lambda = \frac{2\pi}{k} \tag{2.1}$$

with $\vec{p}$ the momentum of the neutron, $m_n = 1.675.10^{-27}$ kg the neutron mass, and $\hbar = h/2\pi$ with h the Planck constant.

2.2.2 Cross sections and interaction potentials

A neutron scattering experiment provides an indirect way to probe microscopic details of matter. It simply consists in measuring and analysing the initial and final state of the neutrons after interacting with the sample. The sample is subjected to a neutron beam with initial wave-vector $\vec{k_i}$, initial spin-state σ_i and initial energy $E_i = \frac{\hbar^2 k_i^2}{2m_n}$. The neutrons are then scattered by the sample and they acquire a final state with a wave-vector k_f, a final spin state σ_f and a final energy $E_f = \frac{\hbar^2 k_f^2}{2m_n}$. During this scattering process, the system (neutron + sample) is changing from an initial state $< k_i, \sigma_i, \alpha_i >$ to a final state $< k_f, \sigma_f, \alpha_f >$ with α_i and α_f, the initial and final states of the sample, associated to an initial and a final energy E_{α_i} and E_{α_f} respectively. During this scattering process, the total energy is conserved: $E_i + E_{\alpha_i} = E_f + E_{\alpha_f}$. The scattering vector $\vec{Q}$, corresponding to the momentum transfer, and the energy transfer $\hbar\omega$ of the neutron are then defined as follows:

$$\begin{cases} \vec{Q} = \vec{k_i} - \vec{k_f} \\ \hbar\omega = E_i - E_f = E_{\alpha_f} - E_{\alpha_i} \end{cases} \tag{2.2}$$

The fundamental quantity measured during a neutron scattering experiment is the partial differential cross section which has the dimension of a surface per energy and per solid angle. This quantity represents the number of scattered neutrons per second in the solid angle $d\Omega$ around $\vec{k_f}$ and with a final energy between E_f and $E_f + dE_f$. By using the Fermi's golden rule which describes the probability for the system (neutron + sample) to go from an initial state $(\vec{k_i}, \sigma_i, \alpha_i)$ to a final state $(\vec{k_f}, \sigma_f, \alpha_f)$ and the Born approximation which reflects the fact that the neutron only see one atom, the partial differential cross section can be written:

$$\boxed{\left(\frac{d^2\sigma}{d\Omega dE_f}\right)_{i\to f} = \frac{k_f}{k_i}\left(\frac{m_n}{2\pi\hbar^2}\right)^2 \sum_{\sigma_i,\alpha_i} p_{\sigma_i} p_{\alpha_i} \sum_{\sigma_f,\alpha_f} |\left\langle k_f\sigma_f\alpha_f\right| \hat{V}(\vec{r}) \left|k_i\sigma_i\alpha_i\right\rangle|^2 \delta(\hbar\omega - E_i - E_f)} \tag{2.3}$$

where:

- p_{σ_i} and p_{α_i} are the probabilities of having the neutrons in an initial spin state σ_i and the sample in an initial state α_i respectively.
- $\hat{V}(\vec{r})$ is the interaction potential between the neutron and the sample.

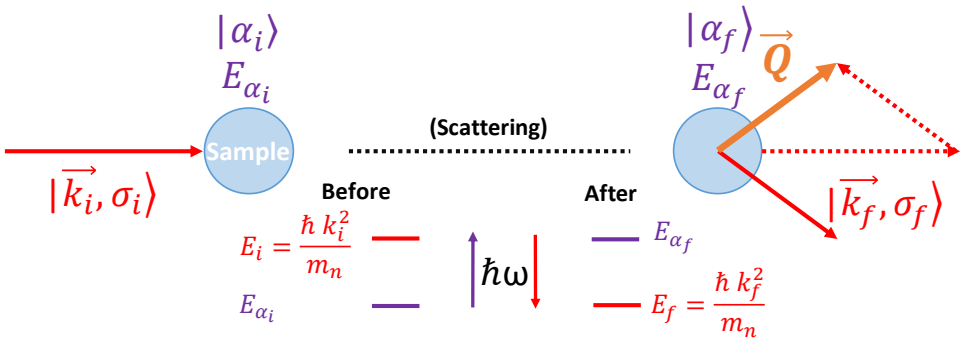

Figure 2.1: **Scattering process and definition of the parameters.** $\vec{Q} = \vec{k_i} - \vec{k_f}$ is the scattering vector. In the present picture, the neutron with an initial energy $E_i > E_f$ (thus $\hbar\omega > 0$) gives an energy $\hbar\omega$ to the sample when it is scattered. Its energy decreases down to E_f while the energy of the sample increases to E_{α_f}. As all the experiments of my PhD were performed at low temperature, only the ground state is populated and this picture is the correct one in our case. Nevertheless, an energy transfer from the sample to the neutron is also possible at higher temperature (then $\hbar\omega < 0$).

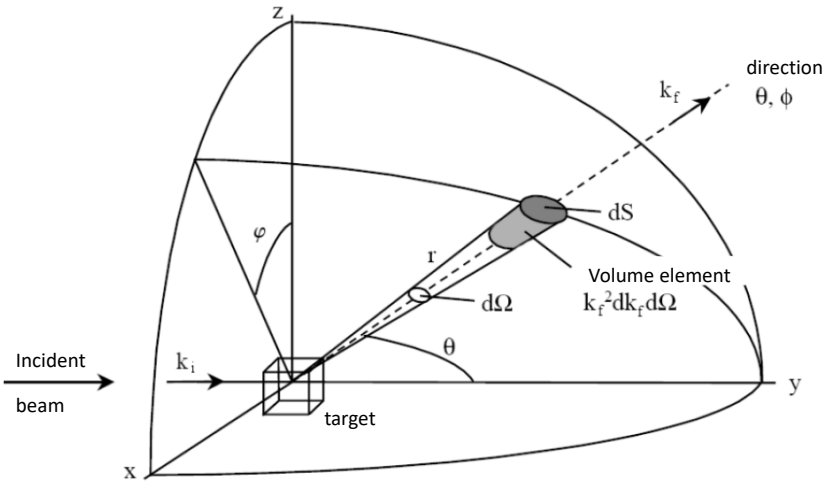

Figure 2.2: **Sketch of a scattering process by a "target".** k_i and k_f denote the initial (incident) and the final (scattered) wave-vector respectively. The scattered beam is indicated by the angles ϕ and θ. Figure taken from [Son16; Gre11].

- $\delta(\hbar\omega - E_i - E_f)$ is the Dirac function reflecting the energy conservation.

The differential partial cross section depends on the type of the interaction potential which can be of two kinds:

- The nuclear interaction which describes the interaction between the neutron and the nucleus of an atom of the sample.

- The magnetic interaction describing the interaction between the spin of the neutron and the magnetic moment of an atom of the sample.

2.2.2.1 Nuclear interaction

The nuclear interaction between the neutron and the nucleus of an atom occurs because of the strong interaction. As the characteristic length of this interaction is much smaller than the inter-atomic distances and than the wavelength of the neutron, the potential takes the form of a Fermi pseudo-potential as follows:

$$\hat{V_N}(\vec{r}) = \frac{2\pi\hbar^2}{m_n} b\ \delta(\vec{r} - \vec{R}) \tag{2.4}$$

where $\vec{R}$ is the position of the nucleus of the atom, $\vec{r}$ the position of the neutron, and b the scattering length which depends in the number of protons and neutrons of the atom. Hence this length is different for each atom, but also for each isotope. Its value is randomly depending on the atoms (or isotopes) and that is why neutrons provide different information than X-rays (see Fig. 2.3). Moreover b is independent of $\vec{Q}$ while the scattering length of X-rays acquires a form factor $f(\vec{Q})$ which comes from the Fourier transform of the electronic environment of the atoms and is thus proportional to the number of electrons.

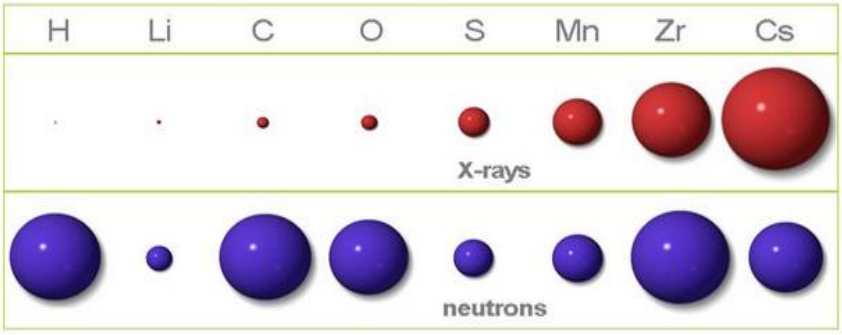

Figure 2.3: **Difference between neutrons and X-rays cross sections.** The cross section of the X-rays is increasing with the size of the atom, i.e. its number of electrons and thus its atomic number Z: $\sigma_{\mathrm{X_{rays}}} \propto Z^2$. For the neutrons, we have $\sigma_{\mathrm{neutrons}} \propto b^2$ with b the scattering length which varies randomly from one atom to another. In particular, neutrons are very sensitive to hydrogen while X-rays are not.

In any condensed matter system (gas, liquid, or solid), the total interaction potential writes as the sum over each site (denoted by j in the following). Therefore, by integrating the energy of the neutron and by making the statistic average on the initial and final states, the nuclear partial differential cross section takes the following form:

$$\left(\frac{d^2\sigma}{d\Omega dE_f}\right)_{nuc}(\vec{Q},\omega) = \frac{k_f}{k_i}\frac{1}{2\pi\hbar}\sum_{j,j'}\int_{-\infty}^{+\infty}\left\langle b_j b_{j'}^* e^{-i\vec{Q}\cdot\vec{R_{j'}}(0)}\cdot e^{i\vec{Q}\cdot\vec{R_j}(t)}\right\rangle e^{-i\omega t}dt \tag{2.5}$$

where $\langle ... \rangle$ denotes the statistical average.

Let us focus on the scattering length b_j. This quantity is real when the scattering process occurs without absorption and its amplitude characterizes the strength of the interaction between the neutron and the target. It depends on the chemical specy, the considered isotope and the spin state of the nucleus. We have:

$$\overline{b_j b_{j'}} = \overline{b}^2 + \left(\overline{b^2} - \overline{b}^2\right) \delta_{j,j'} \tag{2.6}$$

where $\overline{b}$ stands for the average scattering length and $\left(\overline{b^2} - \overline{b}^2\right)$ is the standard deviation of $\overline{b}$. Hence the nuclear partial differential cross section can be split in two independent terms:

$$\left(\frac{d^2\sigma}{d\Omega dE_f}\right)_{nuc}(\vec{Q},\omega) = \left(\frac{d^2\sigma}{d\Omega dE_f}\right)_{nuc}^{coh}(\vec{Q},\omega) + \left(\frac{d^2\sigma}{d\Omega dE_f}\right)_{nuc}^{inc}(\vec{Q},\omega) \tag{2.7}$$

The first term describes the interference phenomena between nuclei from different sites having the same average scattering length $\overline{b}$ (coherent scattering). By noting N_{at} the number of scattering nuclei we have:

$$\left(\frac{d^2\sigma}{d\Omega dE_f}\right)_{nuc}^{coh}(\vec{Q},\omega) = \frac{k_f}{k_i} N_{at} \overline{b}^2 S_{coh}\left(\vec{Q},\omega\right) \tag{2.8}$$

$$\text{with} \quad S_{coh}\left(\vec{Q},\omega\right) = \frac{1}{N_{at}} \frac{1}{2\pi\hbar} \int_{-\infty}^{+\infty} e^{-i\omega t} \sum_{j,j'} \left\langle e^{-i\vec{Q}\cdot\vec{R}_j(0)} \cdot e^{i\vec{Q}\cdot\vec{R}_{j'}(t)} \right\rangle dt \tag{2.9}$$

where $S_{coh}\left(\vec{Q},\omega\right)$ is the scattering function corresponding to the double Fourier transform in space and time of the pair correlation function $\left\langle \rho_{j'}(\vec{r},t) \cdot \rho_j(\vec{0},0) \right\rangle$ of the nuclear density. It describes the probability to find a nucleus j' at time t and position $\vec{r}$ when we have a nucleus j at time 0 and position $\vec{0}$. Thus, in the case of a crystal (which has a translational symmetry), this coherent term reflects the periodicity of the lattice for both the structure and the excitations and it gives a structured signal in $\vec{Q}$ and ω.

The second term describes the interaction of the nucleus with itself (incoherent scattering). We have:

$$\left(\frac{d^2\sigma}{d\Omega dE_f}\right)_{nuc}^{inc}(\vec{Q},\vec{\omega}) = \frac{k_f}{k_i} \frac{1}{2\pi\hbar} N_{at} \left(\overline{b^2} - \overline{b}^2\right) S_{inc}\left(\vec{Q},\omega\right) \tag{2.10}$$

$$\text{with} \quad S_{inc}\left(\vec{Q},\omega\right) = \frac{1}{N_{at}} \frac{1}{2\pi\hbar} \int_{-\infty}^{+\infty} e^{-i\omega t} \sum_{j,j'} \left\langle e^{-i\vec{Q}\cdot\vec{R}_j(0)} \cdot e^{i\vec{Q}\cdot\vec{R}_j(t)} \right\rangle dt \tag{2.11}$$

where $S_{inc}\left(\vec{Q},\omega\right)$ is the double Fourier transform in space and time of the autocorrelation function $\left\langle \rho_j(\vec{r},t) \cdot \rho_j(\vec{0},0) \right\rangle$. This term describes the time correlations of a given atom with itself and hence, gives a structured signal in time only. Moreover it implies deviations from the average scattering length $\overline{b}$ and thus leads to no interference.

The cross section can be written in a more compact way:

$$\left(\frac{d^2\sigma}{d\Omega dE_f}\right)_{nuc}(\vec{Q},\vec{\omega}) = \frac{k_f}{k_i} \frac{1}{2\pi\hbar} \int_{-\infty}^{+\infty} \left\langle N^\dagger\left(\vec{Q},0\right) N\left(\vec{Q},t\right) \right\rangle e^{-i\omega t} dt \tag{2.12}$$

or, in a reduced notation:

$$\left(\frac{d^2\sigma}{d\Omega dE_f}\right)_{nuc}(\vec{Q},\vec{\omega}) = \left\langle N^\dagger\left(\vec{Q},0\right) N\left(\vec{Q},t\right) \right\rangle_\omega \tag{2.13}$$

with $N(\vec{Q},t) = \sum_j b_j e^{i\vec{Q}\cdot R_j(t)}$ the nuclear structure factor. The † notation describes the Hermitian transpose (in this case, simply the complex conjugate).

2.2.2.2 Nuclear spin interaction

The neutrons can also interact with the nuclear spin of the nucleus. This is the reason why the scattering length b varies from one isotope to the another. This interaction can in principle be neglected, except at really low temperature or in presence of a large magnetic field where a nuclear spin order can occur. In this study, this aspect will be ignored.

2.2.2.3 Magnetic interaction

The magnetic interaction is due to the dipolar interaction between the magnetic moment of the neutron and the one of the unpaired electrons of an atom. The neutron has an intrinsic magnetic moment defined by $\hat{\mu_n} = \gamma\mu_B\hat{\sigma}$ where γ is the gyromagnetic factor, μ_B is the Bohr magneton and $\hat{\sigma}$ is the spin operator. The interaction potential takes the following form:

$$\hat{V_m}(\vec{r}) = -\hat{\mu_n}\cdot\vec{H}(\vec{r}) \tag{2.14}$$

where $\vec{H}(\vec{r}) = \frac{\mu_0}{4\pi}\left(\vec{\nabla}\times\left(\frac{\vec{\mu_e}\times\vec{r}}{r^3}\right) - \frac{2\mu_B}{\hbar}\frac{\vec{p_e}\times\vec{r}}{r^3}\right)$ is the sum of the magnetic fields produced on the neutron by the unpaired electrons with a spin and an orbital contribution. $\vec{r}$ gives the positions of the neutron, $\vec{\mu_e} = -g\mu_B\vec{\sigma_e}$ with $g = 2$ and $\vec{p_e}$ are the spin and orbital magnetic moments of the electron, respectively. We can demonstrate [Lov84] that the contribution of the magnetic part to the partial differential cross section given by Eq. (2.3) takes the following form:

$$\left(\frac{d^2\sigma}{d\Omega dE_f}\right)_{mag}\left(\vec{Q},\omega\right) = \frac{k_f}{k_i}\frac{p^2}{2\pi\hbar}S\left(\vec{Q},\omega\right) = \frac{k_f}{k_i}\frac{p^2}{2\pi\hbar}\sum_{\alpha,\beta}\left(\delta_{\alpha\beta} - \frac{Q_\alpha Q_\beta}{Q^2}\right)S^{\alpha\beta}\left(\vec{Q},\omega\right)$$
$$\text{with}\quad S^{\alpha,\beta}\left(\vec{Q},\omega\right) = \int_{-\infty}^{+\infty} e^{-i\omega t}\left\langle\left(M_j^\alpha\right)^*(0)M_{j'}^\beta(t)f_j(\vec{Q})f'_j(\vec{Q})e^{i\vec{Q}\cdot\left(\vec{R'_j}(t)-\vec{R_j}(0)\right)}\right\rangle dt \tag{2.15}$$

where:

- $p = \gamma\frac{e^2}{2m_e} = 0.2696\ 10^{-12}$ cm/μ_B is the equivalent scattering length for a magnetic moment of 1 μ_B at $\vec{Q} = \vec{0}$. e and m_e are the charge and the mass of the electron respectively.
- the tensor $\left(\delta_{\alpha,\beta} - \frac{Q_\alpha Q_\beta}{Q^2}\right)$ is the orientation factor which comes from the dipolar nature of the interaction. This means that only the magnetic components perpendicular to $\vec{Q}$ are probed. We will see later that this term is very useful in inelastic neutron scattering, especially to know the direction (polarization) of the fluctuations with respect to the ordered moments. One can understand this term through Fig. 2.4.
- M_j^α is the component of the magnetic moment along the α direction carried by the atom j.
- $S\left(\vec{Q},\omega\right)$ is the scattering function corresponding to the double Fourier transform in space and time of the magnetization density $\left\langle\vec{M}_\perp^{j'}(\vec{r},t)\cdot\vec{M}_\perp^{j}(\vec{0},0)\right\rangle$ where $M_\perp^j$ is the component of the magnetization carried by the atom j perpendicular to the scattering vector $\vec{Q}$.

- $f_j(\vec{Q})$ is the magnetic form factor of atom j, corresponding to the Fourier transform of the electronic density of the unpaired electrons (in the case of X-rays, it is the Fourier transform of electronic density). This quantity accounts for the spatial extension of the unpaired electrons which cannot be seen as punctual (contrary to the case of the nucleus). As a result $f_j(\vec{Q})$ decreases with increasing Q (while the scattering length b_j is constant for the nuclear interaction as this interaction is seen as punctual).

The scattering function $S\left(\vec{Q},\omega\right)$ is related to the imaginary part of the dynamic susceptibility $\chi(\vec{Q},\omega)$ through the fluctuation-dissipation theorem:

$$S\left(\vec{Q},\omega\right) = \frac{1}{\pi}\frac{1}{1-exp\left(-\frac{\hbar\omega}{k_BT}\right)}\,\chi\left(\vec{Q},\omega\right) \tag{2.16}$$

The dynamical susceptibility is defined as the linear response of the system to a local magnetic field varying in ω and $\vec{Q}$.

$$M\left(\vec{Q},\omega\right) = \chi\left(\vec{Q},\omega\right) H\left(\vec{Q},\omega\right) \tag{2.17}$$

It is as if the neutron was creating a microscopic field varying in frequency and in wave-vector in the sample and was measuring the answer of the system to this field.

The equation (2.15) can be written in a more compact way:

$$\left(\frac{d^2\sigma}{d\Omega dE_f}\right)_{mag}\left(\vec{Q},\omega\right) = \frac{k_f}{k_i}\frac{p^2}{2\pi\hbar}\int_{-\infty}^{+\infty} e^{-i\omega t}\left\langle \vec{M}_\perp^\dagger(\vec{Q},0)\cdot\vec{M}_\perp(\vec{Q},t)\right\rangle dt \tag{2.18}$$

$$\left(\frac{d^2\sigma}{d\Omega dE_f}\right)_{mag}\left(\vec{Q},\omega\right) = \left\langle \vec{M}_\perp^\dagger(\vec{Q},0)\cdot\vec{M}_\perp(\vec{Q},t)\right\rangle_\omega \tag{2.19}$$

with $\vec{M}_\perp\left(\vec{Q},t\right)$ the magnetic interaction vector describing the projection of the magnetic moment $\vec{M}(\vec{Q},t)$ in the plane perpendicular to the scattering vector $\vec{Q}$.

Finally, by occulting the part of the nuclear spin contribution, the total scattering cross section writes as the sum of the nuclear and magnetic contributions:

$$\left(\frac{d^2\sigma}{d\Omega dE_f}\right)\left(\vec{Q},\omega\right) = \left\langle N^\dagger(\vec{Q},0)N(\vec{Q},t)\right\rangle_\omega + \left\langle \vec{M}_\perp^\dagger(\vec{Q},0)\cdot\vec{M}_\perp(\vec{Q},t)\right\rangle_\omega \tag{2.20}$$

Those two interactions can give many information depending on the type of experiment:

- Elastic scattering (diffraction): in this case, $|\vec{k_i}| = |\vec{k_f}|$ and hence there is no energy transfer to the sample. This method allows to determine the nuclear and magnetic structures of the sample.
- Inelastic scattering: in this case, $|\vec{k_i}| \neq |\vec{k_f}|$ and hence an energy transfer occurs. This kind of experiment allows to probe the dynamics of the system and hence the "strength" of the interactions, for examples between atoms (phonons) or between the magnetic moments of the atoms (magnons or more generally magnetic excitations).

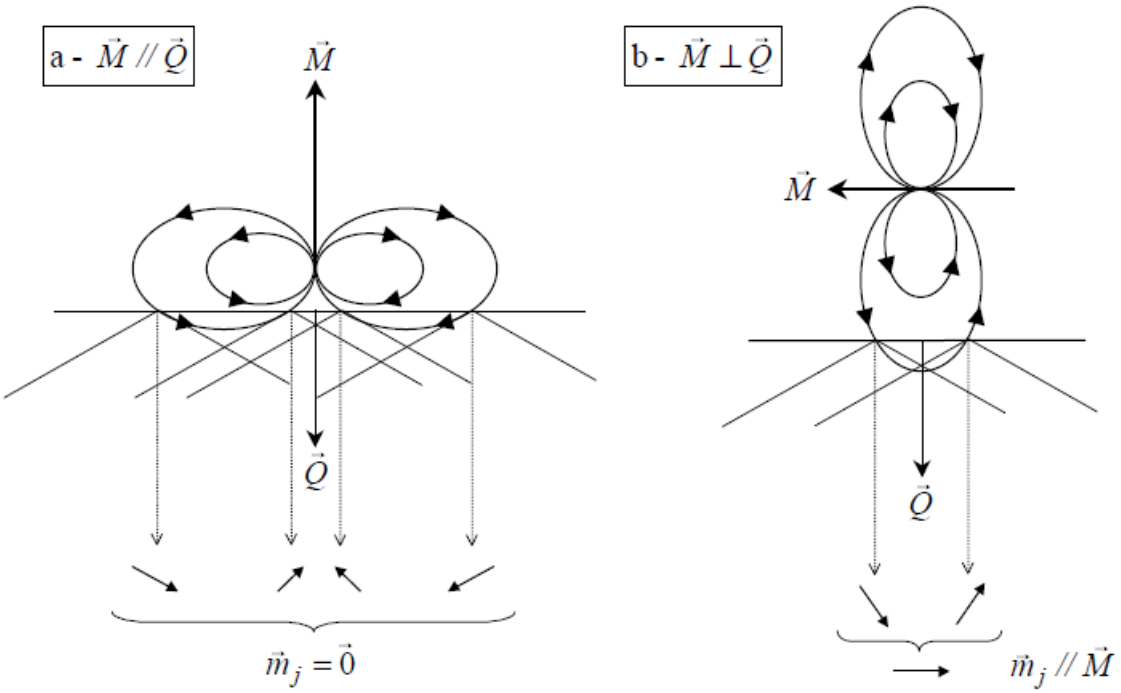

Figure 2.4: **Geometrical factor of the magnetic cross section.** Sketch of the effect of the relative direction between the magnetization $\vec{M}$ and the scattering vector $\vec{Q}$ on the scattering by a dipolar interaction. Here the magnetic moment $\vec{M}$ in the sample can be assimiled to a dipolar magnetic field from the unpaired electrons. When $\vec{M} \parallel \vec{Q}$, the planes perpendicular to $\vec{Q}$ intercept the magnetic field lines in 4 points in such a way that, because of symmetry, the total field cancels. This is not the case when $\vec{M} \perp \vec{Q}$ as the planes intercept the magnetic field lines in 2 points leading, by symmetry, to a non-zero total magnetization. Figure extracted from [Gre11].

While both techniques are different as I will discuss later, they are both complementary. I like to take the example of a car where you need to know its structure (diffraction) and then know how the motor works (dynamics). Let us now turn to the case of the elastic coherent neutron scattering for a (periodic) crystal.

2.2.3 Elastic coherent neutron scattering

As explained above, in the case of elastic neutron scattering, we have $|\vec{k_i}| = |\vec{k_f}|$ and thus $E_i - E_f = E_{\alpha_f} - E_{\alpha_i} = \hbar\omega = 0$. In this case, we have:

$$\left(\frac{d^2\sigma}{d\Omega dE_f}\right)\left(\vec{Q}, \omega = 0\right) = \left\langle N^\dagger(\vec{Q}, 0) N(\vec{Q}, t)\right\rangle_{\omega=0} + \left\langle \vec{M}_\perp^\dagger(\vec{Q}, 0) \vec{M}_\perp(\vec{Q}, t)\right\rangle_{\omega=0} \tag{2.21}$$

2.2.3.1 Nuclear coherent scattering

In a crystal, we can decompose the position of an atom l in a unit cell m as follows:

$$\vec{R}_{m,l}(t) = \vec{R}_m + \vec{r}_l + \vec{u}_{m,l}(t) \tag{2.22}$$

where $\vec{R}_m$ gives the position of the unit cell in the crystal, r_l is the position of the atom in this unit cell and $\vec{u}_{m,l}$ is the deviation of the atom from its equilibrium position (due to thermal fluctuations or to collective motions). The nuclear interaction in the crystal writes:

$$V_N(\vec{r}) = \frac{2\pi\hbar^2}{m}\delta\left(\vec{r} - \vec{R}_{m,l}\right) \tag{2.23}$$

where $\vec{r}$ is the position of the neutron.

Let us rewrite the elastic coherent part of the scattering cross section given in eq. (2.5) by integrating on the energies:

$$\left(\frac{d\sigma}{d\Omega}\right)_{nuc}^{coh}\left(\vec{Q}\right) = \int_{-\infty}^{+\infty}\left(\frac{d^2\sigma}{d\Omega dE_f}\right)_{nuc}^{coh}\left(\vec{Q},\omega\right)d\omega \tag{2.24}$$

$$= \int_{-\infty}^{+\infty}\int_{-\infty}^{+\infty} e^{-i\omega t}\delta(\omega)\sum_{m,m',l,l'}\left\langle \overline{b}_l\overline{b}_{l'}e^{-i\vec{Q}\cdot\vec{R}_{m,l}(0)}\cdot e^{i\vec{Q}\cdot\vec{R}_{m',l'}(t)}\right\rangle dtd\omega \tag{2.25}$$

$$\left(\frac{d\sigma}{d\Omega}\right)_{nuc}^{coh}\left(\vec{Q}\right) = \sum_{m,m'} e^{i\vec{Q}\cdot(\vec{R}_{m'}-\vec{R}_m)}\sum_{l,l'}\overline{b}_l\overline{b}_{l'}e^{i\vec{Q}\cdot(\vec{r}_{l'}-\vec{r}_l)}\left\langle e^{-i\vec{Q}\cdot\left(\vec{u}_{m,l}(0)-\vec{u}_{m',l'}(t)\right)}\right\rangle \tag{2.26}$$

We have $\sum_{m,m'} e^{i\vec{Q}\cdot(\vec{R}_{m'}-\vec{R}_m)} = \frac{(2\pi)^3}{V}N_{cell}\sum_{\vec{H}}\delta\left(\vec{Q}-\vec{H}\right)$ with $\vec{H}$ a vector of the reciprocal lattice, N_{cell} the number of cells in the crystal and $\frac{(2\pi)^3}{V}$ the volume of a reciprocal unit cell. By developing the factor $e^{-i\vec{Q}\cdot\left(\vec{u}_{m,l}(0)-\vec{u}_{m',l'}(t)\right)}$ to the first order, we get the final form of the nuclear differential elastic cross section:

$$\boxed{\begin{array}{c}\left(\frac{d\sigma}{d\Omega}\right)_{nuc}^{coh}\left(\vec{Q}\right) = \frac{(2\pi)^3}{V}N_{cell}\sum_{\vec{H}}\left|F_N\left(\vec{Q}\right)\right|^2\delta\left(\vec{Q}-\vec{H}\right) \\ \text{with} \quad F_N\left(\vec{Q}\right) = \sum_l \overline{b}_l e^{i\vec{Q}\cdot\vec{r}_l}e^{-W_l}\end{array}} \tag{2.27}$$

where:

- W_l is the Debye-Waller factor of atom l defined as $W_l = \langle u\rangle^2 Q^2/2$ with $\langle u\rangle$ the thermal average displacement of atom l. This term comes from the first order approximation of the displacement $\vec{u}_{m,l}$ and describes the reduction of the coherence of the scattered waves (and thus of the signal) by the thermal fluctuations.
- the term $\delta(\vec{Q}-\vec{H})$ comes from the Bragg condition for a reflection. It means that a scattering occurs only if the scattering vector $\vec{Q}$ coincides with a vector of the reciprocal lattice $\vec{H}$.
- $F_N\left(\vec{Q}\right)$ is the nuclear structure factor and contains all the information about the content of the unit cell, i.e. the nature of the atoms and their coordinates $\vec{r}_l$.

Therefore, the position of the Bragg peaks will give information about the unit cell, i.e. the lattice parameters a, b, c, $\widehat{(b,c)} = \alpha$, $\widehat{(a,c)} = \beta$ and $\widehat{(a,b)} = \gamma$ while the intensities of the peaks will inform about the nature and coordinates of the atoms.

This result obtained in the case of the nuclear scattering can be extended to the case of magnetic scattering as we will see now.

2.2.3.2 Magnetic coherent scattering

We now consider only the magnetic atoms of the crystal at position $R_{m,l}$ and carrying a magnetic moment $\vec{M}_{m,l}$. This magnetic distribution which is periodic in space can be Fourier expended and then gives:

$$\vec{M}_{m,l} = \sum_{\vec{k}} \vec{\mathcal{M}}_l^{\vec{k}} e^{-i\vec{k}\cdot\vec{R}_m} \tag{2.28}$$

where $\vec{\mathcal{M}}_l^{\vec{k}}$ are the Fourier components of the distribution associated to the propagation vector $\vec{k}$. This propagation vector is characterizing the periodicity of the magnetic lattice with respect to the nuclear one. One can show, by integrating on the energy the equation (2.15) and by using the above formula, that the coherent magnetic differential cross section takes the following form:

$$\left(\frac{d\sigma}{d\Omega}\right)_{mag}^{coh}\left(\vec{Q}\right) = \int_{-\infty}^{+\infty}\left(\frac{d^2\sigma}{d\Omega dE_f}\right)_{mag}^{coh}\left(\vec{Q},\omega\right)d\omega \tag{2.29}$$

$$\boxed{\begin{array}{c}\left(\frac{d\sigma}{d\Omega}\right)_{mag}^{coh}\left(\vec{Q}\right) = \frac{(2\pi)^3}{V}N_{cell}\sum_{\vec{H}}\sum_{\vec{k}}\left|\vec{F}_{M_\perp}\left(\vec{Q}\right)\right|^2\delta\left(\vec{Q}-(\vec{H}+\vec{k})\right)\\ \text{with}\quad \vec{F}_{M_\perp}\left(\vec{Q}\right) = p\sum_l f_l(\vec{Q})\vec{\mathcal{M}}_{\perp,l}^{\vec{k}}e^{i\vec{Q}\cdot\vec{r}_l}e^{-W_l}\end{array}} \tag{2.30}$$

where:

- the term $\delta\left(\vec{Q}-(\vec{H}+\vec{k})\right)$ means that the magnetic peaks appear when $\vec{Q}$ coincides with the sum of a vector from the reciprocal lattice $\vec{H}$ and the propagation vector $\vec{k}$ of the magnetic structure. This latter vector reflects the periodicity L of the magnetic structure ($k \propto 1/L$) and the direction in which it propagates. For example, in the case of a ferromagnet (FM), the periodicity of the magnetic lattice is the same as the nuclear one and thus $\vec{k}_{FM} = \vec{0}$. For an antiferromagnet (AF) containing one magnetic atom per unit cell with antiparallel moments along the c-axis, the periodicity of the magnetic lattice is twice that of the nuclear one in the real space so that $\vec{k}_{AF} = (0,0,1/2)$. As we will see later, this propagation vector can be trickier as we can have for instance an incommensurate order or a multi-k magnetic structure.

- $\vec{F}_{M_\perp}\left(\vec{Q}\right)$ is the projection in the plane perpendicular to $\vec{Q}$ of the magnetic structure factor which contains the information on the magnetic ordering in the unit cell (amplitude and orientation of the magnetic moments).

- $f_l(\vec{Q})$ is the magnetic form factor defined in section 2.2.2.3.

Let us examine the case of $BaCo_2V_2O_8$. Because of the body-centering of the unit cell (translation $(1/2, 1/2, 1/2)$ in the real space, the magnetic structure factor $\vec{F}_M(\vec{Q})$ writes:

$$\vec{F}_M(\vec{Q}) = pf(\vec{Q}) \sum_{j=1}^{N/2} \left[\vec{\mathcal{M}}_{1,j}^{\vec{k}} + \vec{\mathcal{M}}_{2,j}^{\vec{k}} e^{i\pi(h+k+l)} \right] e^{2i\pi(hx_j+ky_j+lz_j)} \tag{2.31}$$

with $f(\vec{Q})$ the magnetic form factor of the Co^{2+} ions, N the number of Co atoms in a unit cell ($N = 16$), $\vec{\mathcal{M}}_{1,j}^{\vec{k}}$ the Fourier component of the magnetic moment carried by the Co atom at (x_j, y_j, z_j) position and $\vec{\mathcal{M}}_{2,j}^{\vec{k}}$ the one carried by the Co atom at $(x_j + 1/2, y_j + 1/2, z_j + 1/2)$, $\vec{Q} = h\vec{a}^* + k\vec{b}^* + l\vec{c}^*$ is the scattering vector. Here the Debye-Waller factors are not taken into account for more clarity. Now let us consider the two cases:

- $\vec{\mathcal{M}}_{1,j}^{\vec{k}} = -\vec{\mathcal{M}}_{2,j}^{\vec{k}} \Rightarrow \vec{F}_M(\vec{Q}) \neq \vec{0}$ if $h + k + l = 2n + 1$ with n an integer
- $\vec{\mathcal{M}}_{1,j}^{\vec{k}} = \vec{\mathcal{M}}_{2,j}^{\vec{k}}, \Rightarrow \vec{F}_M(\vec{Q}) \neq \vec{0}$ if $h + k + l = 2n$

Besides, the body-centering of the structure imposes $F_N(\vec{Q}) \neq 0$ if $h + k + l = 2n$, in other words, the lattice vectors $\vec{H}$ are such that $h + k + l = 2n$. Thus, the propagation vector $\vec{k} = (1, 0, 0)$ or equivalently $\vec{k} = (0, 1, 0)$ found experimentally in $BaCo_2V_2O_8$ at $H = 0$ (see section 1.6.3) means that magnetic peaks are observed at $\vec{H} + \vec{k} = (h+1, k, l)$ with $h + k + l = 2n$, or, in other words, at $\vec{Q} = (h, k, l)$ with $h + k + l = 2n$. This means that the magnetic coupling between the two Cobalt atoms corresponding by the body-centering translation $(1/2, 1/2, 1/2)$ is AF.

2.2.4 Inelastic coherent neutron scattering

In this case $|\vec{k_i}| \neq |\vec{k_f}|$ and thus the scattering cross section has the general form:

$$\left(\frac{d^2\sigma}{d\Omega dE_f} \right) \left(\vec{Q}, \omega \right) = \left\langle N^\dagger(\vec{Q}, 0) N(\vec{Q}, t) \right\rangle_\omega + \left\langle \vec{M}_\perp^\dagger(\vec{Q}, 0) \vec{M}_\perp(\vec{Q}, t) \right\rangle_\omega \tag{2.32}$$

2.2.4.1 Nuclear contribution: Phonons

The phonons are the quasi-particles due to the coherent and collective vibrations of the atoms. They can be seen classically as the collective motions of the atoms inside the lattice. In a crystal, if we consider p atoms per unit cell denoted by the index l and since each atom has 3 degrees of freedom (one in each direction x, y and z), then we have $3p$ branches labeled by the index α. We have then: 3 acoustic branches + $(3p - 3)$ optical branches. If we develop equation (2.26) to higher orders, then we obtain the following formula for the creation or the annihilation of one phonon by the neutron (lattice excitations):

$$\left(\frac{d^2\sigma}{d\Omega dE_f} \right)_{\pm phon}^{coh} \left(\vec{Q}, \omega \right) = \frac{k_f}{k_i} N \frac{(2\pi)^3}{V} \sum_{\alpha, \vec{H}} \delta \left(\vec{Q} - \left(\vec{H} \pm \vec{q} \right) \right) \left| F_\alpha(\vec{Q}) \right|^2 \left\langle n_{B\pm}(\omega_{\vec{q}}^\alpha) \right\rangle \delta \left(\omega \mp \omega_{\vec{q}}^\alpha \right)$$

$$\text{with} \quad F_\alpha \left(\vec{Q} \right) = \sum_l \bar{b}_l e^{-W_l} e^{+i\vec{Q}\cdot\vec{r}_l} \left(\frac{\hbar}{2m_l \omega_{\vec{q}}^\alpha} \right)^{\frac{1}{2}} \left(\vec{e}_{\vec{q},l,\alpha} \cdot \vec{Q} \right) \tag{2.33}$$

where:

- $\delta\left(\vec{Q} - \left(\vec{H} \pm \vec{q}\right)\right)$ means that $\vec{Q} = \vec{H} \mp \vec{q}$ with $\vec{H}$ a vector of the reciprocal lattice and $\vec{q}$ a vector inside the Brillouin zone.

- $\delta\left(\omega - \omega_{\vec{q}}^{\alpha}\right)$ and $\delta\left(\omega + \omega_{\vec{q}}^{\alpha}\right)$ are corresponding to the energy condition for the creation and annihilation of a photon, respectively.

- $\langle n_B \pm \rangle$ the Bose-Einstein factor giving the number of bosons (here the phonons). For a creation and an annihilation process we have respectively:

$$\left\langle n_{B+}(\omega_{\vec{q}}^{\alpha})\right\rangle = \left\langle n_B(\omega_{\vec{q}}^{\alpha}) + 1\right\rangle = \frac{1}{1 - exp\left(-\frac{\hbar\omega_{\vec{q}}^{\alpha}}{k_B T}\right)}$$

$$\left\langle n_{B-}(\omega_{\vec{q}}^{\alpha})\right\rangle = \left\langle n_B(\omega_{\vec{q}}^{\alpha})\right\rangle = \frac{1}{exp\left(+\frac{\hbar\omega_{\vec{q}}^{\alpha}}{k_B T}\right) - 1}$$

  This shows that when $T \to 0$, only creation processes are possible (indeed $\left\langle n_{B-}(\omega_{\vec{q}}^{\alpha})\right\rangle \to 0$ and $\left\langle n_{B+}(\omega_{\vec{q}}^{\alpha})\right\rangle \to 1$) as the system is in its fundamental state so it can only receive energy (from the neutron) and reciprocally the neutron cannot take energy from the system. However for $T \to +\infty$ both processes are equally allowed (indeed $\left\langle n_{B-}(\omega_{\vec{q}}^{\alpha})\right\rangle \to +\infty$ and $\left\langle n_{B+}(\omega_{\vec{q}}^{\alpha})\right\rangle \to +\infty$) which means that the system creates and annihilates phonons in an equally distributed way. Those conditions are well known as the principle of detailed balance.

- $F_{\alpha}\left(\vec{Q}\right)$ is the dynamical structure factor of the lattice, m_l is the mass of the atom l. $\vec{e}_{\vec{q},l,\alpha}$ is the polarization of the mode which is thus longitudinal if $\vec{e}_{\vec{q},l,\alpha} \parallel \vec{Q}$ and transverse if $\vec{e}_{\vec{q},l,\alpha} \perp \vec{Q}$ and $\omega_{\vec{q}}^{\alpha}$ is the frequency (energy) of the considered mode.

One can see that this expression involves the square of $\left(\vec{e}_{\vec{q},l,\alpha} \cdot \vec{Q}\right)$ and thus Q^2. This shows first that when we are probing phonons, we generally work at a high value of $||\vec{Q}|| = ||\vec{H} \pm \vec{q}||$, second that the signal is maximum for $\vec{Q} \parallel \vec{e}_{\vec{q},l,\alpha}$ and thus we can play with the orientation of $\vec{Q}$ to probe the transverse or longitudinal character of the modes. Finally, one can also observe that the above formula is inversely proportional to the energy $\omega_{\vec{q}}^{\alpha}$ so it means that the low-energy branches (the acoustic ones) give the maximum of intensity. Indeed a low-frequency mode has a huge amplitude of vibration (one can convince himself with the equipartition energy theorem).

2.2.4.2 Magnetic contribution: Magnons

The magnons are the quasi-particles created by coherent excitations of the electronic spins of the system. As explained in Chap. (1), the magnons are quantized boson modes of the spin lattice and can be viewed classically through the spin-waves. For an unpolarized beam and considering one magnetic ion per unit cell with only spin-magnetism, one can show that the creation and the annihilation of one magnon by a neutron is given by the following formula:

$$\left(\frac{d^2\sigma}{d\Omega dE_f}\right)^{coh}_{\pm magn}\left(\vec{Q},\omega\right) = \frac{k_f}{k_i}\frac{(2\pi)^3}{V}\frac{S}{2}\left(1+\frac{Q_\parallel^2}{Q^2}\right)(\gamma r_0)^2\left(\frac{1}{2}gf(\vec{Q})\right)^2(\vec{Q})e^{-2W} \sum_{\vec{H}}\sum_{\alpha}\left\langle n_{B\pm}(\omega^\alpha_{\vec{q}})\right\rangle \delta\left(\omega \mp \omega^\alpha_{\vec{q}}\right)\delta\left(\vec{Q}-(\vec{H}\pm\vec{q})\right) \tag{2.34}$$

with:

- S the value of the spin
- $f(\vec{Q})$ the magnetic form factor that is decreasing with Q, which means that contrary to the case of phonons, probing magnons requires to work at a small scattering vector amplitude Q.
- $n_{B\pm}$ means that the magnons (like the phonons) follow the Bose-Einstein statistics.
- $1+\frac{Q_\parallel^2}{Q^2}$, with $Q_\parallel$ the projection of $\vec{Q}$ on the direction of the ordered moment, is the geometrical term describing the fact that the neutron is only sensitive to the fluctuations of the moments perpendicular to the scattering vector $\vec{Q}$.

At this stage, we have described the cross sections for an unpolarized beam of neutrons. Let us now turn to the case where the neutrons are polarized.

2.2.5 Polarized neutrons

The use of unpolarized neutrons a useful technique to investigate both the statics and the dynamics of spin systems. However, in some cases, the magnetic structure can be complex and the excitations can be complicated such as a superposition of magnetic and nuclear modes or excitations with different polarizations, i.e. different directions of fluctuation. It is in those particular cases that the use of polarized neutrons becomes interesting.

A neutron scattering experiment using polarized neutrons starts with an incident beam of neutrons polarized with a polarization $\vec{P}_i$ in the spin state $|\uparrow\rangle$ or $|\downarrow\rangle$. The neutrons are then scattered by the sample which will produce a flipping (spin-flip process) or not (non spin-flip process) of the initial polarization into a final polarization $\vec{P}_f$. I will first briefly present the Blume-Maleyev equations derived for polarized neutrons and then only focus on the particular case of the analysis of the uniaxial polarization which was used during this PhD. For more informations about polarized neutrons for inelastic neutron scattering, I invite the reader to read [Reg07].

The so called Blume-Maleyev equations were established independently by Blume and Maleyev during the 60s [Mal61], [Blu63]. The first Blume-Maleyev equation is giving the general expression of the cross section in function of the incident polarization $\vec{P}_i$ and has the following form:

$$\left(\frac{d^2\sigma}{d\Omega dE_f}\right)\left(\vec{Q},\omega\right) = \left\langle N^\dagger(\vec{Q},0)N(\vec{Q},t)\right\rangle_\omega + \left\langle \vec{M}_\perp^\dagger(\vec{Q},0)\vec{M}_\perp(\vec{Q},t)\right\rangle_\omega + \vec{P}_i\cdot\left\langle N^\dagger(\vec{Q},0)\vec{M}_\perp(\vec{Q},t) + N(\vec{Q},t)\vec{M}_\perp^\dagger(\vec{Q},0)\right\rangle_\omega + i\vec{P}_i\cdot\left\langle \vec{M}_\perp^\dagger(\vec{Q},0)\times\vec{M}_\perp(\vec{Q},t)\right\rangle_\omega$$

where:

- the first term is the usual nuclear contribution σ_N and the second term is the standard symmetric magnetic contribution σ_M. Those two terms have already been explained above.
- the third term R is a nuclear/ magnetic interference term nuclear/magnetic R which involves products between the nuclear and magnetic structure factors.
- the fourth term M_{chiral} is an antisymmetric (chiral) magnetic which can be non zero for some materials showing a magnetic order characterized by a chiral vector such as helicoidal magnetic structures.

The second equation gives the scattered polarization $\vec{P}_f$ as a function of the incident polarization $\vec{P}_i$ and of the different cross sections:

$$\begin{aligned}\vec{P}_f\left(\frac{d^2\sigma}{d\Omega dE_f}\right)\left(\vec{Q},\omega\right) =& \vec{P}_i\left\langle N^\dagger(\vec{Q},0)N(\vec{Q},t)\right\rangle_\omega - \vec{P}_i\left\langle \vec{M}_\perp^\dagger(\vec{Q},0)\vec{M}_\perp(\vec{Q},t)\right\rangle_\omega \\ &+ \left\langle N^\dagger(\vec{Q},0)\vec{M}_\perp(\vec{Q},t) + N(\vec{Q},t)\vec{M}_\perp^\dagger(\vec{Q},0)\right\rangle_\omega \\ &+ i\left\langle\left(\vec{P}_i\times\vec{M}_\perp^\dagger(\vec{Q},0)\right)\cdot N(\vec{Q},t)\right\rangle_\omega - i\left\langle N(\vec{Q},0)\cdot\left(\vec{P}_i\times\vec{M}_\perp(\vec{Q},t)\right)\right\rangle_\omega \\ &+ \left\langle \vec{M}_\perp^\dagger(\vec{Q},0)\cdot\left(\vec{P}_i\cdot\vec{M}_\perp(\vec{Q},t)\right)\right\rangle_\omega + \left\langle\left(\vec{P}_i\cdot\vec{M}_\perp^\dagger(\vec{Q},0)\right)\cdot\vec{M}_\perp(\vec{Q},t)\right\rangle_\omega \\ &- i\left\langle \vec{M}_\perp^\dagger(\vec{Q},0)\times\vec{M}_\perp(\vec{Q},t)\right\rangle_\omega\end{aligned}$$

In a neutron scattering experiment using polarized neutrons, three directions of the polarization $\vec{P}$ (standing for $\vec{P}_i$ and $\vec{P}_f$) are usually defined which are described by a referential linked to the scattering vector $\vec{Q}$:

- $\vec{P} \parallel \vec{X}$: the direction of the polarization is along $\vec{Q}$.
- $\vec{P} \parallel \vec{Y}$: the direction of the polarization is perpendicular to $\vec{Q}$ and in the scattering plane .
- $\vec{P} \parallel \vec{Z}$: the direction of the polarization is perpendicular to the scattering plane.

Different orientations of the incident and final polarization are possible in this referential. This leads to the matrix of polarization P [2]:

$$P = \begin{pmatrix} P_{xx} & P_{yx} & P_{zx} \\ P_{xy} & P_{yy} & P_{zy} \\ P_{xz} & P_{yz} & P_{zz} \end{pmatrix}$$

[2] An element $P_{\alpha\beta}$ of P can be understood as the polarization of the outgoing beam along β when the ingoing beam was polarized along α.

Let us now turn to a method called "uniaxial (or longitudinal) polarization analysis". This method was first proposed by Moon et *al.* [MRK69] in 1969. They have shown that we earn a lot of information by analysing the polarization of the scattered neutrons thanks to an analyser placed behind the sample. In this type of experiment the incident and the final polarization have the same direction according to the referential defined above and thus only the quantities P_{xx}, P_{yy} and P_{zz} are accessible (to probe the other terms, one should use a spherical polarimetry experiment). In such an experiment, one can initially polarize the neutron with a + or − spin state (where + and − denote the $|\uparrow\rangle$ and the $|\downarrow\rangle$ polarized spin states of the neutron respectively) and analyze the + or − spin states also. Let us denote the various differential cross sections as follows:

$$\begin{array}{ll} \left(\frac{d^2\sigma}{d\Omega dE_f}\right)^{+-}(\vec{Q},\omega) = \sigma^{+-} & \left(\frac{d^2\sigma}{d\Omega dE_f}\right)^{-+}(\vec{Q},\omega) = \sigma^{-+} \\ \left(\frac{d^2\sigma}{d\Omega dE_f}\right)^{++}(\vec{Q},\omega) = \sigma^{++} & \left(\frac{d^2\sigma}{d\Omega dE_f}\right)^{--}(\vec{Q},\omega) = \sigma^{--} \end{array}$$

where σ^{+-} and σ^{-+} correspond to the for spin-flip processes and σ^{--} and σ^{++} to the non-spin flip processes.

These terms can be related to the σ_N, σ_M, M_{chiral} and R terms defined above by the following relations:

$$\begin{aligned} \sigma_{xx}^{++} &= \sigma_{xx}^{--} = \sigma_N \\ \sigma_{xx}^{+-} &= \sigma_M^y + \sigma_M^z + P_i M_{chiral} \\ \sigma_{xx}^{-+} &= \sigma_M^y + \sigma_M^z - P_i M_{chiral} \\ \sigma_{yy}^{++} &= \sigma_N + \sigma_M^y + P_i R_y \\ \sigma_{yy}^{--} &= \sigma_N + \sigma_M^y - P_i R_y \\ \sigma_{yy}^{+-} &= \sigma_{yy}^{-+} = \sigma_M^z \\ \sigma_{zz}^{++} &= \sigma_N + \sigma_M^z + P_i R_z \\ \sigma_{zz}^{--} &= \sigma_N + \sigma_M^z - P_i R_z \\ \sigma_{zz}^{+-} &= \sigma_{zz}^{-+} = \sigma_M^y \end{aligned} \tag{2.35}$$

Therefore, by doing an experiment of longitudinal polarization analysis and by measuring the intensities $I_{xx}^{\pm\pm}$, $I_{yy}^{\pm\pm}$, $I_{zz}^{\pm\pm}$, $I_{xx}^{\mp\pm}$, $I_{yy}^{\mp\pm}$ and $I_{zz}^{\mp\pm}$, one can extract the nuclear part σ_N, the magnetic part σ_M, the chiral part M_{chiral} and the interference R between the nuclear and magnetic contributions of the cross sections. Moreover one can extract the direction of those different contributions depending on the polarization axis X, Y or Z. Thus, as we will see later, one can extract the direction of the fluctuations during an inelastic polarized neutron scattering experiment.

2.2.6 Experimental setup: neutron beam, monochromatization and polarization

To be able to do neutron scattering experiments we need ... neutrons! Two types of neutron sources exist: the spallation sources and the nuclear reactors. The former is using a particle accelerator (synchrotron) to produce neutrons by the collision of an incident particle (such as a proton, a neutron or an electromagnetic wave having a high energy) and a heavy nucleus. Those kinds of sources can be pulsed and the neutrons are then emitted by pulses at a frequency of a few tens of Hz. They have raised a lot of interest in the past few years as the waste treatment is highly facilitated. Let us cite SINQ at PSI in

Switzerland, ISIS in United Kindgom or the ESS (European Spalliation Source) project which will operate in Sweden.

Nuclear reactors produce neutrons via the fission of enriched uranium nucleus ${}^{235}_{92}U$. This kind of production is self-powered by the chain reaction of induced fission by a neutron:

$$ {}^{235}_{92}U + {}^{1}_{0}n \rightarrow {}^{236}_{92}U \rightarrow X + Y + k\ {}^{1}_{0}n \tag{2.36} $$

with X and Y the fission products and k the number of emitted neutrons by the fission process, in average 2.5.

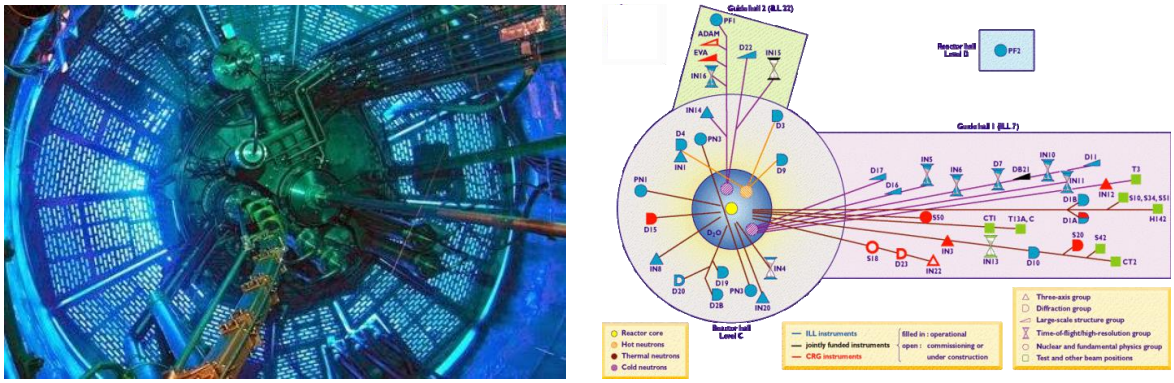

Figure 2.5: **Picture of the high-flux reactor Institut Laue-Langevin (ILL).** Left: view of the pool where the core of the reactor is contained. Right: Distribution of the different kinds of neutrons to the instruments.

Examples of reactors are the LLB-Orphï¿½e in Saclay and the ILL-reactor in Grenoble. While nuclear reactors use uranium bars which are, in addition to being expensive, radioactive, spalliation source becomes emancipated of it. The advantage of using uranium bars is to get a continuous beam, generally much more stable than the pulsed beam.

In the core reactor, the neutrons have an energy of about a few MeV. To keep the chain reaction going, they have to lose a lot of energy down to a few tens of meV. It turns out that this energy range is ideal for neutron scattering experiments in condensed matter. This is achieved with moderators which are light nuclei such as deuterium [3], heated berylium or graphite. The lighter the nucleus, the more efficient the inelastic process is and then, the more the energy is lowered. Those moderators determine the type of neutrons that will be use for the experiment ("cold", "thermal", or "hot" as explained below). After some collisions with those moderators, the neutrons are in a thermal equilibrium with their environment (the moderator having an average thermal energy of $k_B T$). They then follow a Maxwell-Boltzmann distribution (see Fig. 2.6).

$$ \Phi(v) \propto v^3 exp\left[-\left(\frac{v}{v_0}\right)^2\right] = v^3 exp\left[-\left(\frac{E}{E_0}\right)\right] \tag{2.37} $$

where v_0 is the average value of the velocity of the neutrons, $\Phi(v)dv$ is the neutron flux with a velocity between v and $v + dv$, E the kinetic energy of the neutrons defined by $E = \frac{m_n v^2}{2}$ and E_0 the average kinetic energy.

[3] Heavy water at ambiant temperature or cold liquid deuterium.

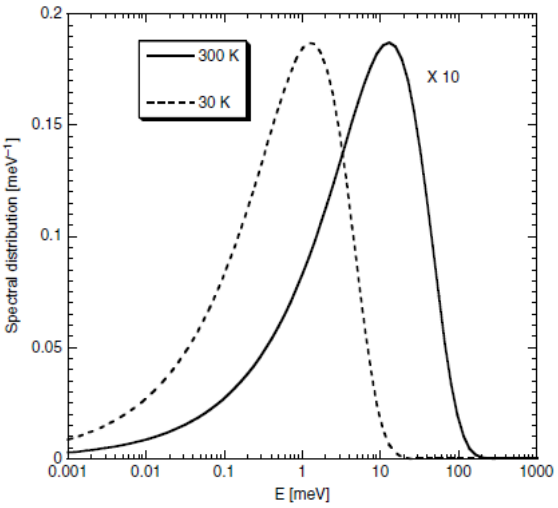

Figure 2.6: **Examples of Maxwell-Boltzmann energy distribution** for moderators of 300 K and 30 K. Figure extracted from [LRS09].

The neutrons provided by the source are classified by their energy.

- under 10 meV (i.e. $\lambda > 2.9$ Å), the neutrons are called "cold neutrons". The neutrons are previously moderated using e.g. liquid water D_2 at 20 K at ILL. In this thesis I have mainly used three-axis-spectrometers using cold neutrons such as IN12 (ILL), ThALES (ILL) or TASP (PSI).

- between 10 meV and 100 meV ($2.9 > \lambda > 0.9$ Å), the neutrons are called "thermal neutrons". They are previously moderated using D_2O at about 300 K. I have worked on different kinds of instruments using thermal neutrons: the two diffractometers 6T2 (LLB) and D23 (ILL) and the three-axis-spectrometer IN22 (ILL).

- from 100 meV to 500 meV ($0.9 > \lambda > 0.4$ Å), the neutrons are called "hot neutrons". These neutrons are obtained using e.g. a moderator of graphite heated at 2000 K at ILL. As the energy range of interest for $BaCo_2V_2O_8$ is well below, no spectrometer using hot neutrons has been used during this thesis.

These different kinds of neutrons (cold, thermal and hot) are extracted around the core or in different guides (see Fig. 2.5) as an unpolarized neutron beam with an energy distribution that still has to be monochromotized and eventually polarized.

2.2.6.1 Monochromatization

The selection of the energy from the polychromatic neutron beam is achieved with monochromators. There are different kinds of monochromators. Here I will focus on three of them which were used during this PhD and which are highly used in the neutron community: the first one is using a Bragg reflection while the others are selecting the neutron velocity.

- The former one consists in co-aligned **single crystals** which can be made of graphite, copper, germanium or silicon depending on the energy-range. Those monochromators select one incident wavelength (and hence one energy) via a Bragg reflection:

$$\lambda = 2d_m \sin\theta_m \tag{2.38}$$

where d_m is the d-spacing and $2\theta_m$ the Bragg angle. By rotating the monochromator, θ_m rotates and hence, one is able to select the desired wavelength. Let us cite two typical monochromators: the pyrolithic graphite PG (002) with $d_m = 3.35$ Å, mainly used with cold and thermal neutrons, which selects a wavelength range between 1.5 Å ($\approx$ 36 meV) and 6 Å ($\approx$ 2 meV) and the copper (111) or copper (220), mainly used with thermal neutrons, which select a wavelength range between 0.8 Å ($\approx$ 128 meV) and 1.5 Å ($\approx$ 36 meV) (see Fig. 2.7(a-b))

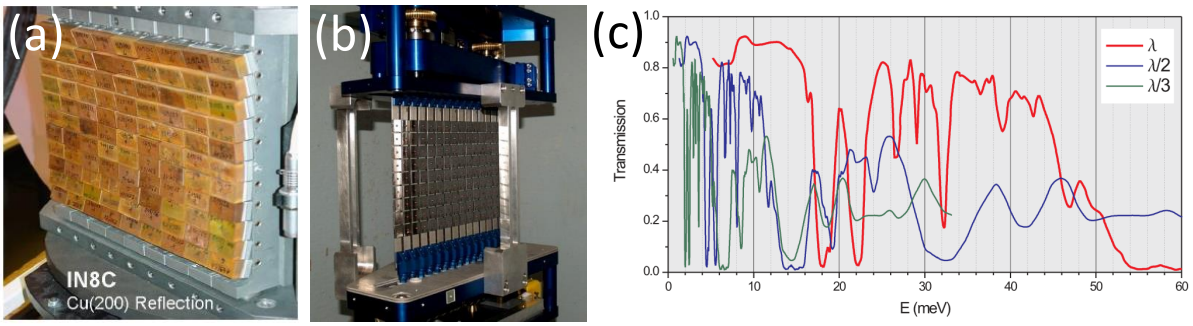

Figure 2.7: **Examples of monochromator:** (a) of copper and (b) of silicon. (c) Graphic showing the transmission of the fundamental wavelength λ and its two first harmonics $\lambda/2$ and $\lambda/3$ by a Pyrolitic Graphite (PG) filter. For $E = 13.5$ meV ($\approx$ 2.46Å), the two harmonics are suppressed. Figure extracted from [ETH].

Therefore we obtain a continuous beam with a wavelength λ (hence an energy $E = h^2/2m_n\lambda^2$) but also all the harmonics $\lambda/2, \lambda/3...\lambda/n$ which come from the virtual planes (the Bragg law can be read as $\lambda = 2\frac{d}{n}sin\theta$ and then one can see that there are virtual planes distanced by d/n). To avoid those harmonics, filters, mainly made of berylium (for cold neutrons) or graphite (for thermal neutrons) are used (see Fig. 2.7(c)).

- The second device consists in at least two perforated disks, made of a highly absorbing material, called "**choppers**" which are rotating with a certain frequency around their axis that does not coincide with the neutron beam. The first disk chops the beam and then only a few neutrons go through the hole of the disk. We then have a pulsed beam still polychromatic. The second disk will only let travel neutrons with the good speed and hence the good energy leading to a monochromatic pulsed beam. To avoid the harmonics $\lambda/2...\lambda/n$, more choppers are used. This technics is mainly used for Time Of Flight (TOF) diffractometers or spectrometers.

- The last device is called "**mechanical velocity selector**". It consists in a helicoidal device made of a highly absorbing material. This device is rotating at a given speed around its rotation axis which does not coincide with the neutron beam and then

stops (absorbs) the neutrons which do not have the good velocity. Therefore it only selects a unique velocity v and thus a unique wavelength (indeed $\lambda = h/mv$). This device has the advantage of keeping the beam continuous (while the choppers produce pulsed beam).

At this step, we have a monochromatic beam but still unpolarized.

2.2.6.2 Polarization of the neutron beam

To polarize the incident neutron beam, one can use:

- a **Heusler Cu_2MnAl crystal**: It is a single-domain ferromagnetic crystal obtained by the application of a vertical uniform magnetic field $\vec{B}$. In this crystal, for the 1 1 1 reflection $F_{M_\perp} = -F_N$. We can show that for a scattering vector perpendicular to $\vec{B}$, i.e. perpendicular to the direction of the magnetic structure factor, that the intensity $I^\pm$ of the $|\uparrow\rangle$ and $|\downarrow\rangle$ incident neutron beam polarizations writes as: $I^\pm \propto |F_N \pm F_{M_\perp}|^2$. One of the most used polarizer satisfying this condition is the Heusler crystal Cu_2MnAl for the 1 1 1 Bragg reflection [WC09]. The direction of polarization of the emerging beam is thus given by the direction of the magnetic field.
- **super-mirrors** called *benders*: they consist in magnetic multi-layers for which the reflectivity index depends on the spin-state of the neutrons. The application of a magnetic field can increase the scattering contrast (i.e. the number of spins $|\uparrow\rangle$ or $|\downarrow\rangle$ which are filtered).
- **^{3}He polarizer**: The absorption cross section of the polarized ^{3}He (the nuclear spin of ^{3}He is polarized prior to the experiment and the device is placed in a magnetic field) is null if the spin of the neutron and the one of ^{3}He are in the same direction and large if the polarizations are in opposite directions. Then one of the two polarizations is absorbed.

This polarization is sustained by guide fields (adiabatic process) up to the sample and after to avoid the depolarization of the beam (for example by magnetic noise). These polarized neutrons are scattered by the sample and their polarization is analyzed afterwards by an analyzer, often also made of Heusler single crystals. We can also manipulate the polarization of the spins by putting flippers before and after the sample. These flippers will flip the spin of the neutrons via a non-adiabatic process.

2.2.7 Description of the instruments

Many instruments have been used in this PhD. The diffractometers D23, D1B, and Orient express and the three-axis spectrometers IN12, IN22 and ThALES at ILL (Grenoble, France), the diffractometer 6T2 at in LLB (CEA-Saclay, France), the three axis spectrometer TASP at PSI (Villigen, Switzerland) and the diffractometer HFM/EXED at HZB (Berlin, Germany).

2.2.7.1 Diffractometers

The diffractometers are used to probe nuclear and magnetic structures of a sample. The wavelength λ of the incident beam is selected by a monochromator. Then, some of the neutrons will be absorbed by the sample or will be transmitted and then will be absorbed

by a "beamstop". The other neutrons are scattered by the sample in an elastic or an inelastic way. The scattered beam is intercepted by a detector, often constituted of ^{3}He, absorbing the neutrons and then creating a charged particle. This particle creates an electric current which is measured. In the case of diffraction, the background, the elastic and the inelastic signal (much weaker than the elastic one) are measured. The diffraction signal actually results from the integration in energy of the signal between $-k_BT$ and E_i . In the case of a powder, $I\left(\left|\left|\vec{Q}\right|\right|\right)$ is measured while $I(\vec{Q})$ is measured for a single crystal. Thus different diffractometers exist adapted to the nature of the sample. I will now explain briefly what we do in practice to determine magnetic structures.

Determination of the propagation vector: The positions of the magnetic Bragg reflections, usually identified first by a powder neutron diffraction experiment, allow to find the propagation vector $\vec{k}$ from the Bragg's law. For complex propagation vectors, programs can be used with the 2θ positions of the magnetic Bragg peaks and the cristallographic characteristics of the sample as input. In case the propagation vector is zero, the magnetic Bragg peaks are at the same position than the nuclear ones and they are identified by the difference between the low temperature diffractogram and the one recorded at a temperature above the magnetic ordering transition temperature.

If only single crytals are available, the search for the propagation vector is more tedious and consists in scanning the reciprocal space to find the magnetic signal.

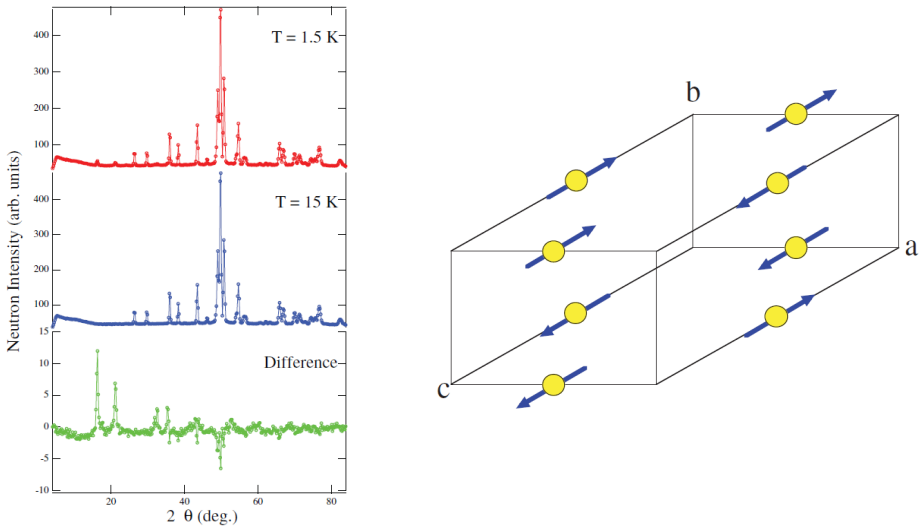

Figure 2.8: **Example of the determination of a magnetic structure.** Left: Powder diffraction patterns recorded below and above the transition temperature in the compound $Cr[C(CN)_3]_2$ and difference. Right: Schematic representation of the magnetic structure of Cr[C(CN)3]2 at 2K. For sake of clarity, only the Cr atoms of the unit cell have been represented. Figures extracted from [MRM00]

Determination of the amplitude and direction of the magnetic moments: The magnetic structure determination can be attempted either from a powder diffractogram through a Rietveld analysis or from single-crystal measurements. In this case, a collect

of the integrated intensities of a large set of magnetic Bragg peaks is done. From a least square refinement procedure, this is compared to calculated intensities of magnetic structures with varying amplitude and orientation fo the unit cell magnetic moments. This converges usually towards the magnetic structure. It can be done using softwares like Fullprof [Rod93].

The magnetic intensity of one Bragg reflection measured in such an experiment is given by:

$$I(\vec{Q}) \propto \mathcal{M}_{\perp}^2 f^2(\vec{Q}) < \sin^2\alpha > \left\{ \sum_{\vec{H}} \left(\delta(\vec{H} - \vec{Q} - \vec{k}) + \delta(\vec{H} - \vec{Q} + \vec{k}) \right) \right\}^2 \tag{2.39}$$

where α is the angle between the magnetic structure factor and the scattering vector $\vec{Q}$ (for $\alpha = 0$, the intensity is null and is consistent with the fact that neutrons only probe the component of the magnetization perpendicular to $\vec{Q}$). Through this, one is able to understand that the measurement of many magnetic Bragg peaks allows to determine the orientation of the magnetic moments. An example of the determination of a magnetic structure is given in Fig. 2.8.

Let us now turn to the different diffractometers that I have used.

D1B (ILL): This 2-axis powder diffractometer is a CRG-CNRS instrument. The wavelength $\lambda = 2.52$ Å of the incident beam is selected thanks to a Pyrolitic Graphite (PG) monochromator. The neutrons are then scattered by the sample and detected by a "banana" multi-detector 1D-PSD (Position Sensitive Detectors) of ^{3}He: 400 cells covering an angular opening of 80ï¿½ which can be moved to measure in a window $2° < 2\theta < 130°$. A sketch and a picture of this instrument are shown in Fig. 2.9.

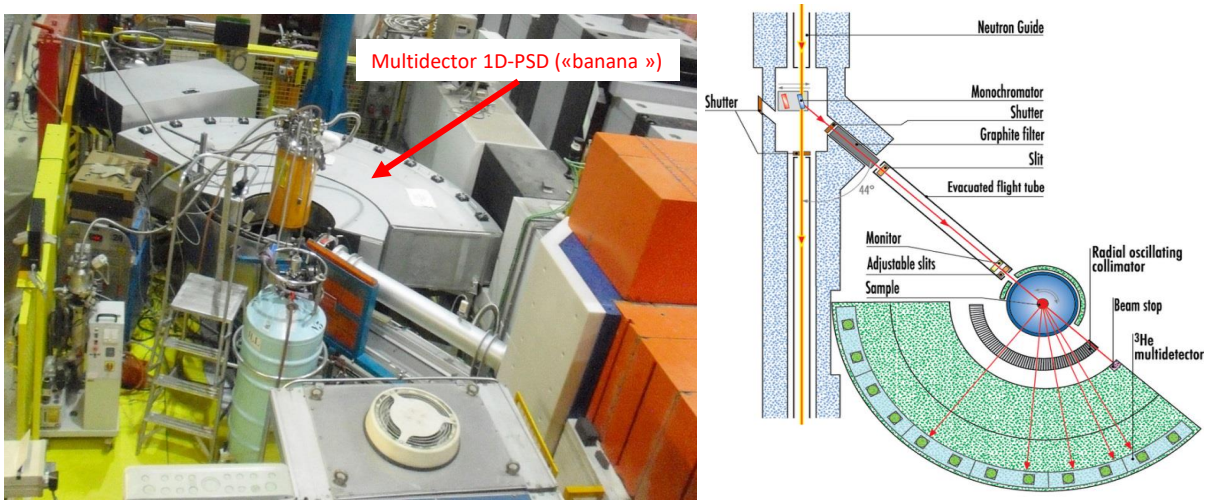

Figure 2.9: **D1B diffractometer at ILL.** Left: Picture of the instrument (one can see the multi-detector covering a large angular region). Right: Sketch of the instrument.

D23 (ILL): This is a CRG-CEA instrument devoted to the diffraction study of single crystals. This 2-axis diffractometer with a lifting-detector uses thermal neutrons in the incident wavelength range 1 Å $< \lambda <$ 3 Å. The first rotation "axis" coincide with the vertical axis of the monochromator made of PG or Cu. The second "axis" is characterized by the angle ω describing the rotation of the sample around the vertical axis perpendicular to the scattering plane. The detector can rotate around the sample by an angle γ (with an amplitude of $\pm 130°$) in the horizontal plane and an angle ν (with an amplitude of $\pm 30°$) in above and below the scattering plane (see Fig. 2.10). The position of the detector is seen at the angle 2θ between the incident and final wavevectors $\vec{k_i}$ and $\vec{k_f}$ (in the case of a scattering process in the horizontal plane, $\gamma = 2\theta$, otherwise $\cos\theta = \cos\gamma\cos\nu$ generally). Different sample environments can be used such as cryomagnets up to 15 T, pressure cell up to 30 kbar or a cryostat equiped with a dilution fridge. This instrument is characterized by a good flux and a good signal over noise ratio. A sketch and a picture of this instrument are shown in Fig. 2.10. Polarized neutrons are also available but were not used during my PhD.

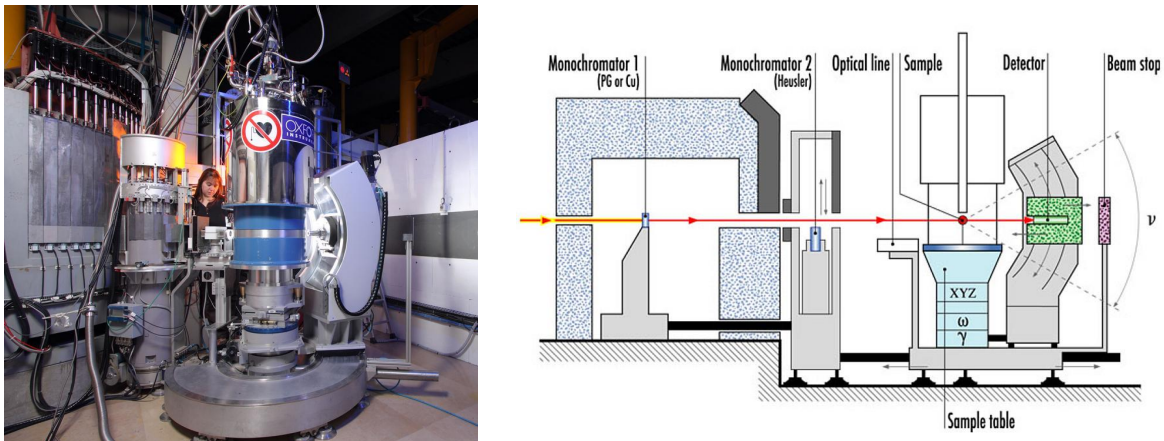

Figure 2.10: **2-axis diffractometer D23 at ILL.** Left: picture of the diffractometer with a 12 T vertical cryomagnet. Right: Sketch of the instrument with the different angles: ω for the rotation of the sample and (γ, ν) for the lifting-detector position. Figure extracted from [D23].

Orient express (ILL): This instrument has been mainly used to orient the single crystals prior to the experiments. This is a Laue-diffractometer which uses a polychromatic beam of thermal neutrons beam with a wavelength range 0.8 Å $< \lambda <$ 3.2 Å. It uses a CCD (Charge Coupled Device) camera with a high resolution. This allows to get the Laue pattern of a whole crystal in a very short time and thus to see a sizable part of the reciprocal space in only one picture. By putting the beam parallel to a symmetry axis or a plane of symmetry, one can see the symmetries on the snapshots. By indexing these pictures, one can rapidly obtain the orientation of the sample which is generally placed on a goniometer so one is able to orient the crystal along one specific direction.

HFM/EXED (HZB): This instrument is the combination of a "High Magnetic Field" (HFM) obtained from is an hybrid magnetic coil reaching fields up to 26 T and EXtreme Environment Diffractometer (EXED) (see Fig. 2.11). This is the strongest continuous magnetic field available for neutron scattering experiments in the world so far. EXED is a time of flight (TOF) instrument using neutrons in the wavelength range of 0.7 Å $< \lambda <$ 15 Å. In this type of experiment the detectors are fixed (here four 2D-PSD). The quantity which is varying is no longer θ like in the case of the 2-axis diffractometers but rather λ (Bragg law $Q = 2\sin(\theta)/\lambda$).

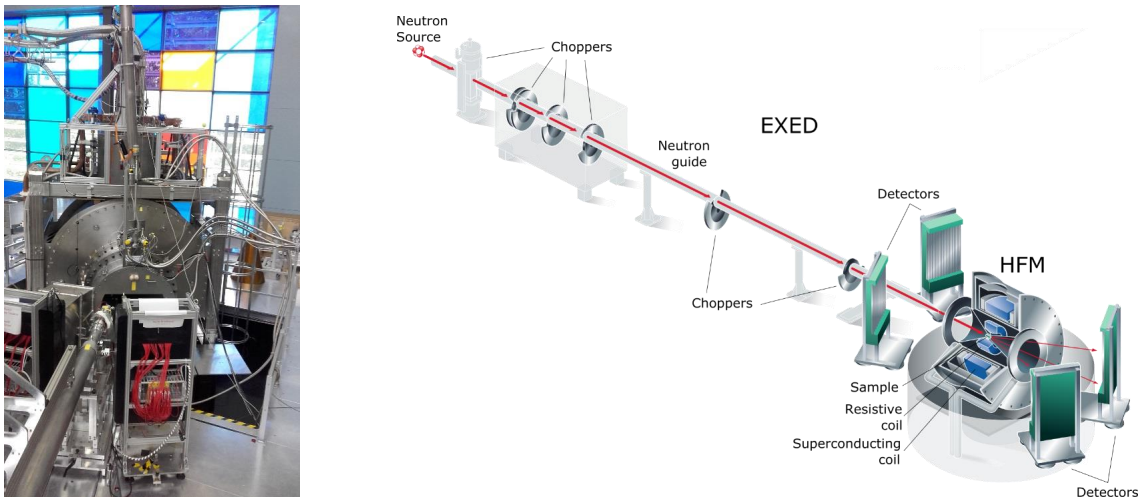

Figure 2.11: **HFM/EXED at HZB**. Left: picture of the hybrid magnetic coil HFM. Right: Sketch of the instrument with the TOF diffractometer EXED and the magnetic coil HFM. Figure extracted from [HFM].

2.2.7.2 3-axis spectrometers

The 3-axis spectrometer (TAS) is a 2-axis diffractometer to which has been added a crystal similar to the ones used for the monochromators which allows to analyse the final energy of the neutrons and thus to determine the energy transfer $\hbar\omega$ between the neutrons and the sample. It is placed between the sample and the detector and by rotation, this analyser is positioned in Bragg condition for the desired final wave vector k_f. It is the third "axis" of the spectrometer.

$$k_f = \frac{2\pi}{2d_a \sin\theta_a} \tag{2.40}$$

Therefore 3-axis spectrometers allow to measure in the $\left(\vec{Q}, \omega\right)$ space the excitations in condensed matter and to probe their dispersion, their magnetic-field dependence and so forth. A sketch which summarizes the triple axis spectrometer is shown in Fig. 2.13.

Principle of an inelastic neutron scattering measurements: During an inelastic scattering experiment, two kinds of measurements are usually done (see Fig. 2.12). The former consists in fixing the energy and scanning the scattering vector $\vec{Q}$ ("Q-scan" at constant energy). The second method consists in fixing the scattering vector $\vec{Q}$ and

varying the energy ("E-scan" at constant scattering vector). A series of such scans allow to determine step by step the dispersion spectrum of the excitations (see Fig. 2.12).

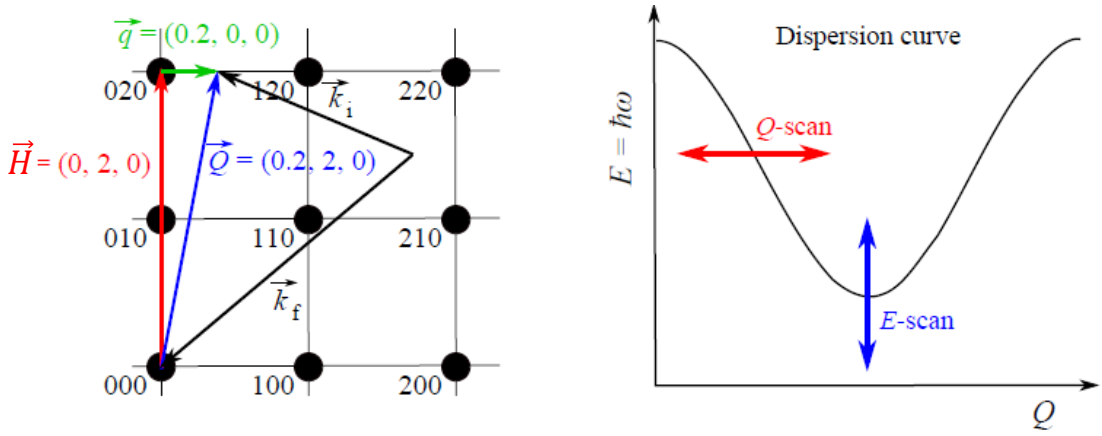

Figure 2.12: **Principe of an inelastic neutron scattering experiment.** Left: $k_i \neq k_f$ with $\vec{Q}$ in the horizontal plane (a^*, b^*). $\vec{H}$ is a vector of the reciprocal lattice, $\vec{q}$ is a wave-vector of the Brillouin zone. Right: The two kinds of measurements leading to the dispersion curve $E = f(Q)$: Q-scan at constant energy (in red) and E-scan at constant scattering vector $\vec{Q}$ (in blue). Figures extracted from [Can10]

These experiments are usually longer than diffraction experiments as the intensity of the signal is much weaker and based on the E-scans and Q-scans consisting in measuring point by point with an adapted interval dE and dQ. The E-scans are well adapted when the slope of the dispersion is weak while Q-scans are more adapted in the opposite case.

ThALES (ILL): This 3-axis spectrometer has been built in collobaration between ILL and The Charles University of Prague. It is located next to the core reactor whereas all the other mentionned ILL instruments are in the guide hall, and thus has a high flux of neutrons. It uses cold neutrons and allows to study low-energy excitations in a range of about 0.2 meV to 10 meV.

IN12 (ILL): This 3-axis spectrometer is a CRG-CEA-Jülich instrument using cold neutrons and allowing to study low-energy excitations in a range of about 0.2 meV to 10 meV and with polarized neutrons.

IN22 (ILL): This 3-axis spectrometer is a CRG-CEA instrument using thermal neutrons and devoted to the study of excitations in the energy range 5 meV to 100 meV.

The spectrometers described above allow to use large sample environments such as low-temperature cryostat/dilution fridge, vertical magnet up to 15 T, pressure cell up to 1 GPa, horizontal magnetic field up to 6.8 T or polarized neutrons (spherical and longitudinal polarimetry).

TASP (PSI): This 3-axis spectrometer is located in the neutron guide of SINQ spallation source and is a collaborating instrument between the Laboratory of Neutron Scattering (LNS) of PSI and the Laboratory of Quantum Magnetism (LQM) of the Ecole

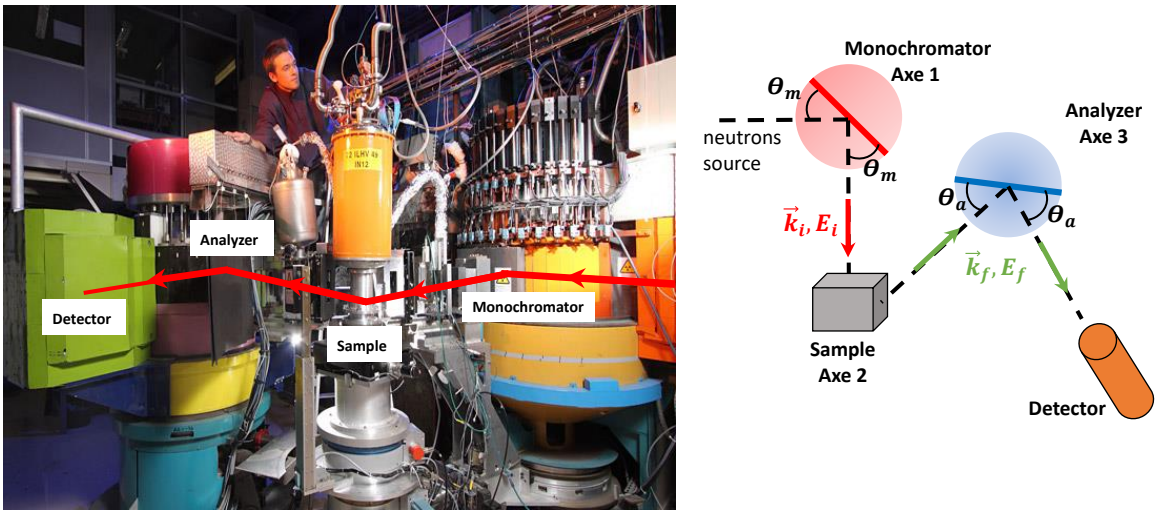

Figure 2.13: **Three-axis-spectrometer.** Left: Picture of the 3-axis spectrometer **IN12 at ILL**. Figure extracted from [IN1]. Right: Sketch of the principle of a triple-axis spectrometer from a top view.

Polytechnique de Lausanne (EPFL). It uses cold neutrons and was used because of the 6.8 T horizontal cryomagnet available there.

2.3 Specific heat measurements under high pressure

To probe the (H, P, T) phase diagram of $BaCo_2V_2O_8$, specific heat measurements using diamond anvil cells (DACs) have been performed. In the next paragraph, I will first present the characteristic of a DAC: its main constituents, the preparation of such a pressure cell. Then I will briefly explain the principle of specific heat measurements and present the experiment that we have performed.

2.3.1 Preparation of diamond anvil cells

While other pressure cells such as piston cylinder or indenter are in general more used than DACs because they allow a bigger working volume, and thus a much easier sample preparation, they are limited to lower pressures. Depending on its size, a DAC achieve pressures up to 300 GPa. One advantage to use DAC is that diamonds are transparent and thus, measuring the pressure *in-situ* is possible. To do that we use the ruby fluorescence technique that allows to measure the pressure in-situ as I will explain later.

Fig. 2.14 shows the main components and a scheme of a DAC. To measure the ac-calorimetry of our sample, we used a 0.7 mm culet. These small dimensions allow to go to a high pressure value.

The principle of a DAC is simple: one diamond anvil is fixed at the bottom while the other one is glued on the mobile piston. A gasket with a hole is placed between them for sealing the sample, the pressure indicator (ruby) and the pressure medium are placed

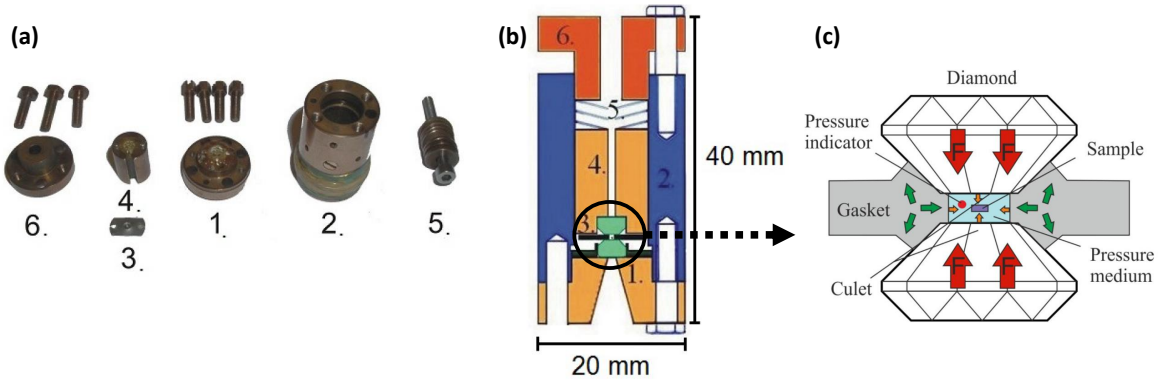

Figure 2.14: **Diamond anvil cell.** (a) Picture of the main components of the diamond anvil cell: 1) fixed bottom diamond cell, 2) body of the cell, 3) gasket (in stainless steel), 4) mobile upper diamond cell fixed on the piston, 5) Belleville spring washers, 6) top closing elements with screws. (b) scheme with all the assembled elements. Typical dimensions are also given. Figure extracted from [Fer12]. (c) Zoom on the DAC: the pressure indicator is the ruby and the pressure medium is argon (Ar) in our case. Figure extracted from [Wae12].

inside this hole which constitutes the chamber. The piston is well guided through the pressure cell and the Belleville spring washers are put to minimize the pressure changes due to thermal cycling. Therefore, by locking the top with the screws, one can apply a force on it which will be transmitted to the diamonds and thus, the volume of the chamber will contract and then its internal pressure will increase. The pressure medium will then transmit in a hydrostatical way (thus the applied pressure is isotropic) the pressure on the sample.

While the design of such a DAC seems simple, loading the DAC for electrical and calorimetry measurements turns out to be very complicated by the necessity to include wires inside the chamber. Indeed it implies a lot of possible failures, for instance the breaking of the wires at the border of the hand-drilled hole by the diamonds because of a possible leakage. Moreover the gasket has to be covered by an insulating layer to avoid short-circuits and this step is a crucial stage as we will see later. Failures during the loading of the pressure transmitting medium inside the chamber may also happen. Furthermore, changing the pressure at room-temperature can also damage the wires because of the successive cooling-heating cycles.

Let me explain now the main steps for the preparation of such a DAC:

Gasket Initially the gasket consists in a stainless layer of $\sim 500\,\mu m$. First we have to preform it by putting it between the two diamond anvils and by applying a force of ~ 7000 N in order to reduce its thickness down to $\sim 100\,\mu m$. Then an imprint of the diamond anvils is left at the center of the gasket. A hole of $\sim 350\,\mu m$ is drilled by hand at the center of this imprint and is chamfered afterwards at both sides to avoid breaking the wires. At this stage, the gasket has the good shape but is still metallic. It needs to be insulated to avoid short-circuits. To do that, one can recover the gasket by an insulating layer made of a mixture between an epoxy (white Stycast 12%) saturated with alumina

powder to improve its mechanical strength. This is the crucial and somehow the most difficult part of this preparation. Indeed if the mixture is not enough saturated or is too thick, then the mixture can be deformed or can slide inside the chamber because it is too fluid and thus it covers the sample and breaks the wires as soon as the pressure is increased.

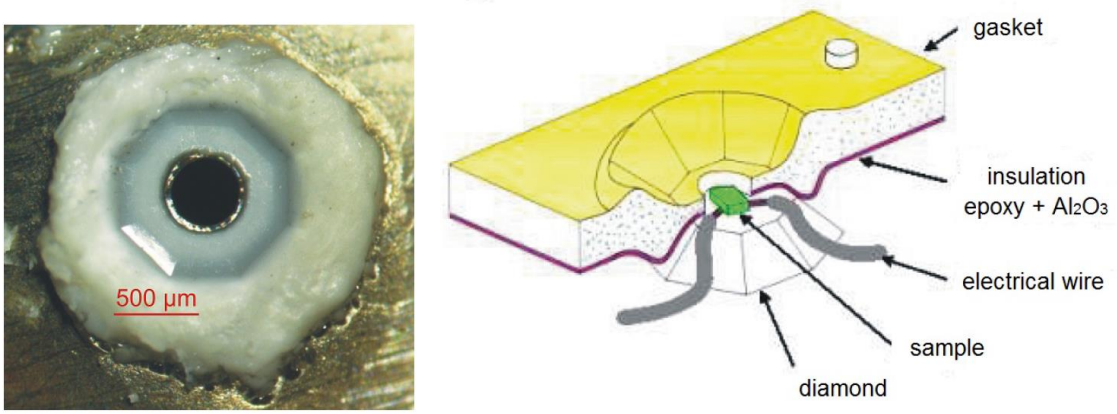

Figure 2.15: **Elaboration of the gasket.** Left: gasket with the insulating mixture. One can see the hole at the center of the gasket and the imprint of the diamond anvils. Right: Scheme of the setup of a DAC cell with the gasket, the wires, the sample and the anvils. Figure extracted from [Fer12].

If it is too thin or too saturated, the insulating layer can easily crack and thus there are great chances of having short-circuits. When the gasket is recovered with the insulating mixture, the next step is to put it between the two anvils and to apply a force of about 1000 N and then put it in the furnace for 1 hour at 70° C, so that the mixture polymerizes. Therefore the hole where the wires should pass through is recovered by this insulating layer which is now flat and has taken the imprint of the anvils. Then the hole is drilled again and its contour is insulated with epoxy (see Fig. 2.15). To be sure that the mixture is well polymerized, we often put again the gasket in the oven for 24 h.

Now that the gasket is done, one has to prepare the wires. In our case we have done AC-calorimetry measurements requiring a thermocouple.

Sample Because of the small size of the chamber, the size of the sample must be very small, typically a square of about 150 x 150 μm^2 with a thickness of about 50 µm (see Fig. 2.16). Its extremely small size makes the sample really difficult to manipulate.

Thermocouple One of the wires of the thermocouple is made of Au of 12 µm diameter whereas the other one is made of Au(0.07% Fe) of 25 µm diameter. The latter is flattened to avoid short-circuits. These two wires are then welded perpendicularly to each other. While this stage is simple, the most complicated part was to glue the sample at the center of the thermocouple. Indeed while one can directly weld it when it is metallic, the fact that $BaCo_2V_2O_8$ is insulating makes things much more difficult. Indeed one needs to glue this small sample on the thermocouple which has also a micrometric size (see

Fig. 2.16) without destroying the pre-made thermocouple (the glue tends to cover the whole thermocouple by capillarity).

When the thermocouple is done, all the components of the DAC cell have to pieced together by putting the thermocouple at the center of an anvil cell and by checking that it is also well centred with respect to the hole of the gasket. To be able to measure the pressure inside the cell, some ruby chips are deposed which will serve as pressure sensors. Now, the next step is to add the pressure medium inside the chamber. This is what is called the "loading" step.

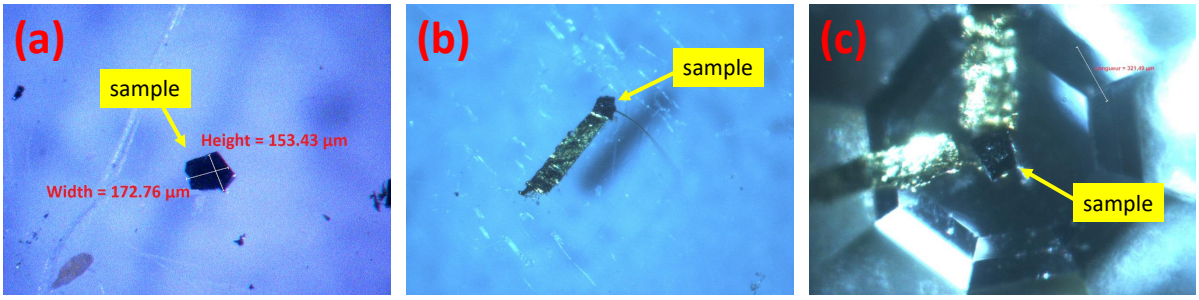

Figure 2.16: **Sample and thermocouple**. (a): $BaCo_2V_2O_8$ sample cut using a scalpel blade with a size of 150 × 170 µm^2 and a thickness of about 50 µm. (b): Au:Au(0.07% Fe) thermocouple with the sample of $BaCo_2V_2O_8$ glued on it. (c): thermocouple and sample placed at the center of the bottom diamond anvil. Two layers of Au and Au(0.07% Fe) are glued on the diamond faces and make the electrical connection between the thermocouple and the thermometer.

Pressure medium and loading For those DACs, argon has been chosen as pressure medium due to its high hydrostaticity up to 10 GPa. Helium could be also a good candidate because of its highest hydrostaticity but its strong compressibility at low temperatures makes it less comfortable to work with. This argon is then liquefied thanks to liquid nitrogen and then the DAC is submerged in the bath of liquid argon for 30 min. Finally, we close the top of the cell with the nut screws and we apply a force of $\sim$ 3000 N. One should ask if the argon is still liquid at really low temperature and at high pressure. The answer is no but the argon has the advantage to be a kind of "soft-solid". As a noble gaz, its interatomic forces are so weak that this makes argon still malleable and isotropic even in those extreme conditions.

Pressure measurement *in-situ* thanks to ruby fluorescence The ruby fluorescence is a well-known technique, very often used in DACs to measure the pressure *in-situ* [A F+72]. The principle is simple: the wavelength of the ruby sharpest line (called R-line) is pressure and temperature dependent above 35 K, and only pressure dependent below. The ruby grains are excited by an Argon laser via an optical fiber which goes through the whole cryostat. A second fiber transmits the outcoming signal to a monochromator and a spectrometer. Therefore, the wavelength value measured (i.e. the position of the R-line peak) gives the value of the pressure inside the cell (see Fig.2.17). Moreover the width of

the peak gives indications on the homogeneity of the pressure inside the chamber. Indeed if the hydrostaticity is not isotropic, then the different rubies will have slightly different R-lines and thus the average peak will be broader.

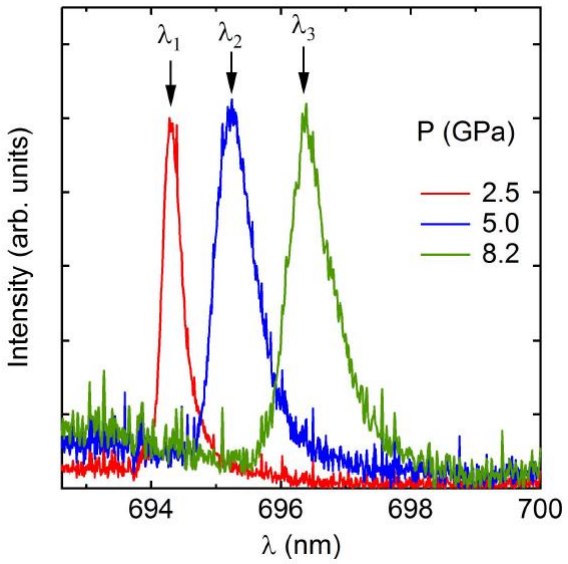

Figure 2.17: **Ruby fluorescence**. Measured ruby spectra at 4 K for different values of the pressure. One can see that the R-line peak shifts to higher values of λ with increasing the pressure.

Now that the DAC is ready, let me describe the principle of specific heat measurements.

2.3.2 Specific heat measurements

The specific heat C is the amount of heat (energy) per unit mass required to raise the temperature by 1 Kelvin. In the experiment done at CEA-Grenoble with the help of Daniel Braithwaite from the IMAPEC (Instrumentation, Matï¿½riaux Avancï¿½s, Physique des Electrons Corrï¿½lï¿½s) laboratory, specific heat has been measured by ac-calorimetry to probe the phase diagram of $BaCo_2V_2O_8$ under magnetic field and pressure. Indeed, it is well known that phase transitions are characterized by an anomaly (*i.e.* a discontinuity) in the thermodynamics quantities as a function of an external parameter. Thus by probing the heat capacity, one is able to extract the critical temperature as a function of pressure and magnetic field.

2.3.2.1 AC-calorimetry

The main problem of measuring the heat capacity is the thermal coupling between the sample and its environment (*i.e.* the gasket, the thermocouple Au:Au(0.07% Fe), the argon, and the body of the cell) as it is pressure and temperature dependent. To avoid this problem, one can probe the heat capacity by doing AC-calorimetry measurements.

This technique is well adapted for small samples where the time to achieve a steady state, *i.e.* the thermal equilibrium, is rather small. In the simple model proposed by Sullivan *et al.* [SS68], the sample is coupled to its environment via a thermal constant coupling κ. To heat the sample, an alternating power $P = P_0(1 + \cos(\omega t))$ is supplied (see Fig.4.18). Then, the alternative part of the temperature T_{AC} is given by the following formula [SS68],

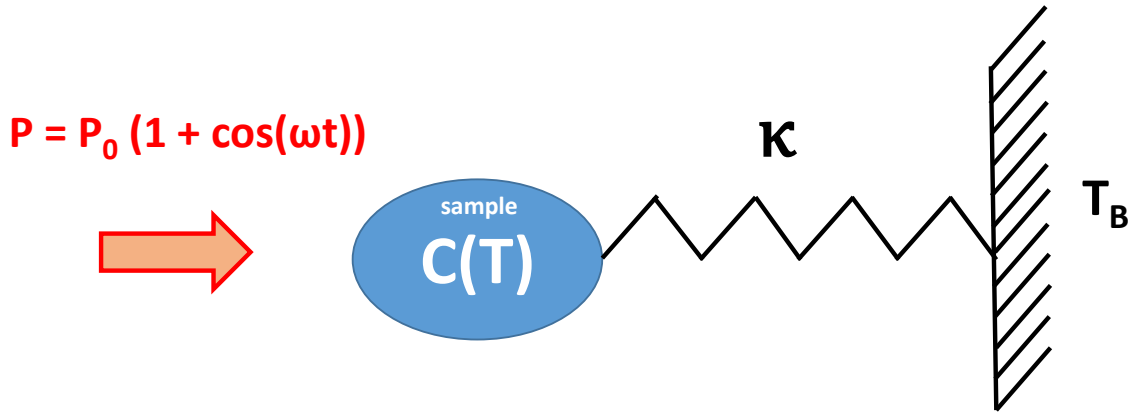

Figure 2.18: **Principle of AC-calorimetry**. The sample is coupled to a thermal bath at the temperature T_B via the thermal coupling κ and is heated by an alternating power $P = P_0(1 + \cos(\omega t))$.

[Wil03]:

$$T_{\mathrm{AC}} = \frac{P_0}{\omega C}\left(1 + \frac{1}{\omega^2\tau^2}\right)^{-\frac{1}{2}} \tag{2.41}$$

where P_0 is the average value of the supplied power, and $\tau = C/\kappa$ is the characteristic time for the sample temperature to relax to that of its environment.

If we choose ω high enough such that $\omega^2\tau^2 \gg 1$, then we get the following formula:

$$\boxed{T_{\mathrm{AC}} = \frac{P_0}{C\omega} \propto \frac{1}{C}} \tag{2.42}$$

and now, one can see that the sample is decoupled from the thermal bath. The temperature T_{AC} only depends on the frequency and is inversely proportional to the specific heat. Indeed by choosing a frequency much higher than $1/\tau$, the temperature of the sample does not have the time to relax through the thermal bath (on the contrary if $\omega << 1/\tau$, then the sample has time to relax through its environment). However the frequency has to be chosen not too high, so that the sample has the time to achieve the thermal equilibrium.

In practice a lock-in amplifier measures the oscillating voltage of the Au:Au(0.07% Fe) thermocouple V_{AC} (at the same frequency ω) which is directly proportional to T_{AC}, $V_{\mathrm{AC}} = S_{th}T_{\mathrm{AC}}$ with S_{th} the sensitivity of the thermocouple, previously known and calibrated. The lock-in is also measuring the phase-shift of the voltage with respect to the heating frequency. This measured signal is amplified by a factor of 10^5. To generate an alternating power, we use an argon laser ($\lambda = 476.5$ nm), with a maximum power of 50 mW, coupled to a chopper with an adjustable frequency.

While this method has the advantage to decouple the sample from its environment, it only leads to semi-quantitative measurements as the average power supply P_0 is not known. Actually there is an unknown part of heat which goes to the sample environment. Nevertheless the anomaly is still present in the measurements and one is able to extract temperature transitions.

Chapter 3

Numerical technique: a code to probe quasi-one dimensional systems

Sommaire

3.1 Summary

3.1.1 Abstract

The third chapter is devoted to the explanation of my own numerical code based on exact diagonalization of Hilbert spaces. This program allowed me to calculate the dynamical structure factor of a single quantum spin chain. The numerical calculations have then been compared to the experimental results obtained for $BaCo_2V_2O_8$. Despite the fact that there is only a qualitative agreement because of the strong limitations of the calculations (huge truncation of the Hilbert space), we will see in the next chapters that those ones have been particularly useful for the understing of $BaCo_2V_2O_8$ under magnetic field.

3.1.2 Résumé en français

Le troisième chapitre est consacré à l'explication de mon code numérique basé sur des diagonalisations exactes d'espaces de Hilbert. Ce programme m'a permis de calculer le facteur de structure dynamique d'une chaîne de spins. Les calculs numériques ont ainsi pu être comparés aux résultats expérimentaux obtenus pour $BaCo_2V_2O_8$. Malgré une concordance seulement qualitative due au fait d'une sérieuse limitation des calculs (troncation très brutale de l'espace de Hilbert), nous verrons dans les chapitres suivants que ceux-ci se sont montrés très utiles quant à la compréhension de $BaCo_2V_2O_8$ sous champ magnétique.

3.2 Introduction

One-dimensional (1D) systems are a subject of great interest as many theories in the 1D case are integrable ([Bet31],[Hal83b],[Hal83a]). For twenty years, numerical calculations are in constant evolution and are able to simulate strongly correlated systems and in particular more and more precisely 1D one, then leading to an enormous gain of knowledge in the understanding of those ones. A lot of experiments have been carried out on the Ising-like quasi-one dimensional system $BaCo_2V_2O_8$. To compare with our data and to understand deeper the behavior of the excitations, I have written a numerical program using exact diagonalization that computes the dynamical structure factor $S(\vec{Q},\omega)$ of the excitations of a quasi-1D Ising-like compound with spin S = 1/2 using the Mathematica software. All the calculations are made on a simple chain coupled to other chains in a mean field way. First we will see how the numerical calculations catch the main physics of quasi-one dimensional systems at zero-field. Then I will discuss the limitations of this model. Here, I want to emphasize the fact that all the calculations were done on my own computer which highly limits the numerical calculations capabilities compared to calculations done on a cluster.

3.3 Theoretical model for the simulation

3.3.1 Parameters

n: Number of sites
ns: Number of states in the Hilbert space
$npairs$: Number of pairs of spinons
$ntruncated$: Number of sites that remains after the truncation
ε: Anisotropy parameter ($\varepsilon < 1$ in the Ising-like case)
J_{inter}: Constant coupling of interchain interaction
J: Constant coupling of intrachain interaction
H: applied magnetic field
τ: Energy resolution
μ_B: Bohr magneton in meV/T
$g_{\alpha\alpha}$: Diagonal component of the Landé tensor for the α-direction
$g_{\alpha\beta}$: Off diagonal component of the Landé tensor coupling the α and β directions

3.3.2 Building of the base of the so called "spinons"

When doing quantum calculations, it is important to well define the basis of spinons and to make the good approximations. I have built the basis in two parts.

3.3.2.1 Complete basis

I consider a spin chain of n atoms.
Magnetic excitations in the 1D case are quasi-particles called spinons. They are created in pairs by neutrons (with the selection rule $\Delta S_z = \pm 1$), carry a spin 1/2 and can be seen as domain walls between 180° Néel states in the Ising case. A pair of spinons creates two defaults by mean of the intrachain coupling (Fig.3.1). It is on this argument that I have created the basis of spinons. First, I have calculated all the possible positions for these

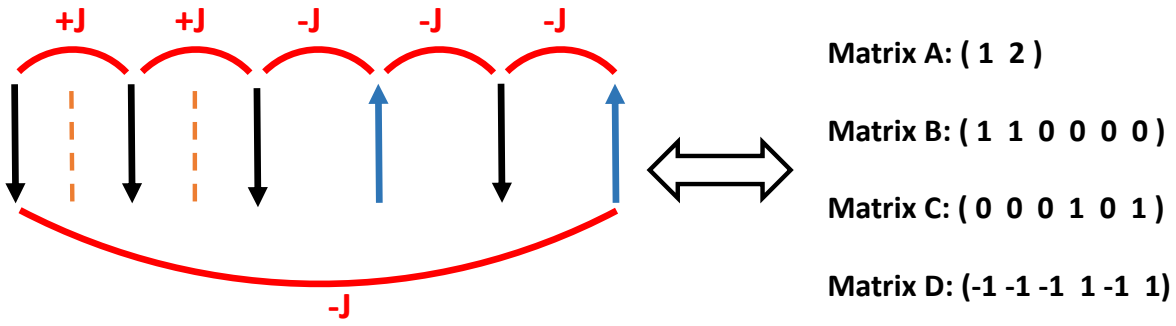

Figure 3.1: **Building of the spinons basis.** Schematic picture of spinons in the Ising-limit for an AF spin chain. One spin-flip in the chain creates two domains walls (the two orange dashed lines) and costs an energy proportional to the intrachain coupling J (red lines). Hence, the creation of two spinons can be seen as two defaults in terms of intrachain coupling J. On this sketch, the periodic boundary condition is shown. The equivalence of this state with the A, B, C and D matrices is indicated (see text).

defaults with the Mathematica function "Subsets" which allows to define all subsets with an even number of defaults in a system containing exactly n elements. An example (the matrix A) is given below for $n = 6$ and for 2 defaults (which means that we only consider excitations with two spinons) but we can calculate the whole basis with more defaults (k-spinons, $k \in [2, 4.., n]$) and with a larger number of sites n. The A matrix represents the location of the bond-defaults. For instance, the first line $\begin{pmatrix} 1 & 2 \end{pmatrix}$ in the A matrix specifies that the bonds between the spin on sites 1 and 2 (first term) and on sites 2 and 3 (second term) are not satisfied.

The matrix A leads to the matrix B which is the basis expressed in terms of "bonds" between each spin: if the value is 1 at the i^{th} position, it means that there is a default, hence that the spins at the position i and $i + 1$ are parallel (in our case we study an AF compound), otherwise if the value is 0, it means that the spins are antiparallel. For example the first state of the B-matrix (1 1 0 0 0 0) is equivalent to the spin chain (- - - + - +) where "+" means S = +1/2, whereas "-" means S = −1/2 (or equivalently (+ + + - + -) but I have chosen the former convention for the C matrix that I explain below). In the whole program, there is a periodic boundary condition (thus the last 0 in the state (1 1 0 0 0 0) means that the last spin $i = 6$ is antiparallel to the first spin. Then, I construct a basis (represented by the matrix C) in terms of spin S = 1/2 and not of bonds.

$$A = \begin{pmatrix} 1 & 2 \\ 1 & 3 \\ 1 & 4 \\ 1 & 5 \\ 1 & 6 \\ 2 & 3 \\ 2 & 4 \\ 2 & 5 \\ 2 & 6 \\ 3 & 4 \\ 3 & 5 \\ 3 & 6 \\ 4 & 5 \\ 4 & 6 \\ 5 & 6 \end{pmatrix} \Rightarrow B = \begin{pmatrix} 1 & 1 & 0 & 0 & 0 & 0 \\ 1 & 0 & 1 & 0 & 0 & 0 \\ 1 & 0 & 0 & 1 & 0 & 0 \\ 1 & 0 & 0 & 0 & 1 & 0 \\ 1 & 0 & 0 & 0 & 0 & 1 \\ 0 & 1 & 1 & 0 & 0 & 0 \\ 0 & 1 & 0 & 1 & 0 & 0 \\ 0 & 1 & 0 & 0 & 1 & 0 \\ 0 & 1 & 0 & 0 & 0 & 1 \\ 0 & 0 & 1 & 1 & 0 & 0 \\ 0 & 0 & 1 & 0 & 1 & 0 \\ 0 & 0 & 1 & 0 & 0 & 1 \\ 0 & 0 & 0 & 1 & 1 & 0 \\ 0 & 0 & 0 & 1 & 0 & 1 \\ 0 & 0 & 0 & 0 & 1 & 1 \end{pmatrix} \Rightarrow C = \begin{pmatrix} 0 & 0 & 0 & 1 & 0 & 1 \\ 0 & 0 & 1 & 1 & 0 & 1 \\ 0 & 0 & 1 & 0 & 0 & 1 \\ 0 & 0 & 1 & 0 & 1 & 1 \\ 0 & 0 & 1 & 0 & 1 & 0 \\ 0 & 1 & 1 & 1 & 0 & 1 \\ 0 & 1 & 1 & 0 & 0 & 1 \\ 0 & 1 & 1 & 0 & 1 & 1 \\ 0 & 1 & 1 & 0 & 1 & 0 \\ 0 & 1 & 0 & 0 & 0 & 1 \\ 0 & 1 & 0 & 0 & 1 & 1 \\ 0 & 1 & 0 & 0 & 1 & 0 \\ 0 & 1 & 0 & 1 & 1 & 1 \\ 0 & 1 & 0 & 1 & 1 & 0 \\ 0 & 1 & 0 & 1 & 0 & 0 \end{pmatrix}$$

$$D = \begin{pmatrix} -1 & 1 & -1 & 1 & -1 & 1 \\ 1 & -1 & 1 & -1 & 1 & -1 \\ -1 & -1 & -1 & 1 & -1 & 1 \\ -1 & -1 & 1 & 1 & -1 & 1 \\ -1 & -1 & 1 & -1 & -1 & 1 \\ -1 & -1 & 1 & -1 & 1 & 1 \\ -1 & -1 & 1 & -1 & 1 & -1 \\ -1 & 1 & 1 & 1 & -1 & 1 \\ -1 & 1 & 1 & -1 & -1 & 1 \\ -1 & 1 & 1 & -1 & 1 & 1 \\ -1 & 1 & 1 & -1 & 1 & -1 \\ -1 & 1 & -1 & -1 & -1 & 1 \\ -1 & 1 & -1 & -1 & 1 & 1 \\ -1 & 1 & -1 & -1 & 1 & -1 \\ -1 & 1 & -1 & 1 & 1 & 1 \\ -1 & 1 & -1 & 1 & 1 & -1 \\ -1 & 1 & -1 & 1 & -1 & -1 \\ 1 & 1 & 1 & -1 & 1 & -1 \\ 1 & 1 & -1 & -1 & 1 & -1 \\ 1 & 1 & -1 & 1 & 1 & -1 \\ 1 & 1 & -1 & 1 & -1 & -1 \\ 1 & 1 & -1 & 1 & -1 & 1 \\ 1 & -1 & -1 & -1 & 1 & -1 \\ 1 & -1 & -1 & 1 & 1 & -1 \\ 1 & -1 & -1 & 1 & -1 & -1 \\ 1 & -1 & -1 & 1 & -1 & 1 \\ 1 & -1 & 1 & 1 & 1 & -1 \\ 1 & -1 & 1 & 1 & -1 & -1 \\ 1 & -1 & 1 & 1 & -1 & 1 \\ 1 & -1 & 1 & -1 & -1 & -1 \\ 1 & -1 & 1 & -1 & -1 & 1 \\ 1 & -1 & 1 & -1 & 1 & 1 \end{pmatrix}$$

At this step, '0' stands for '-' state and '1' stands for '+' state. Now we have a basis in

terms of spins. Indeed in the B matrix, the first state (1 1 0 0 0 0) is now (0 0 0 1 0 1) in the C matrix, which means that the first, the second and the third spin are parallel with $S = -1/2$. What is missed is only the Néel state. Moreover one can see that we have the half of the complete basis (the states where all the spins are reversed are missing, i.e. the time reversal symmetry). If we add those states and change the '0' by '-1', then we obtain the complete basis (matrix D) where '-1' stands for '-' state and '1' stands for '+' state respectively.

3.3.2.2 Truncated basis

Keeping the entire basis with a large number of sites n and k spinons ($k \in [2, 4.., n]$) is not possible as it makes heavy calculations. Indeed the size of the Hamiltonian is growing up exponentially with the number of states ns. To solve this problem I decided to truncate the basis trying to make the good approximations.
The first truncation is somehow an "intrachain filter" where we only keep the easiest states to create (i.e. the most probable, and thus carrying the major part of the spectral weight), i.e. with the smallest number of spinons as possible, for example the two possible Néel states and those made of the 2-spinons basis. For instance, in all the calculations that I have performed, the biggest Hilbert space that I considered was the 2-spinons $\oplus$ 4-spinons basis.

What can be done also is to reduce the size of the basis by applying an "interchain filter". To label the states, I have created a function which gives the number of reversed spins between the two spinons, and the corresponding nature of the excitation: transverse "T" (resp. longitudinal "L") if the number of spins is odd (resp. even). The coupling between two chains is antiferromagnetic. The function is simple: it simply counts the number of interchain defaults between the considered state and a reference Néel state chosen to be (- + - + - +). The truncation procedure consists then in limiting the number of spins between the 2-spinons.

This truncation and this labelling are relevant only on the 2-spinons subspace of the entire Hilbert space which I used in most of my calculations. Indeed these states are the lowest energy modes for a 1D spin chain and hence they can be believed as the most relevant ones. This procedure allows to take a larger number of sites n. Nevertheless, I will discuss the validity of this truncation later.

For example, the interchain truncation to 4 interchain defects in the $n = 6$ chain applied on the complete basis (D matrix) above gives:

$$\begin{pmatrix} -1 & -1 & 1 & -1 & 1 & -1 \\ -1 & 1 & 1 & -1 & 1 & -1 \\ -1 & 1 & -1 & -1 & 1 & -1 \\ -1 & 1 & -1 & 1 & 1 & -1 \\ -1 & -1 & 1 & 1 & -1 & 1 \\ -1 & -1 & 1 & -1 & -1 & 1 \\ -1 & -1 & 1 & -1 & 1 & 1 \\ -1 & 1 & 1 & -1 & -1 & 1 \\ -1 & 1 & 1 & -1 & 1 & 1 \\ -1 & 1 & -1 & -1 & 1 & 1 \\ 1 & -1 & 1 & -1 & 1 & -1 \\ 1 & -1 & -1 & 1 & -1 & 1 \\ 1 & -1 & 1 & 1 & -1 & 1 \\ 1 & -1 & 1 & -1 & -1 & 1 \\ 1 & -1 & 1 & -1 & 1 & 1 \\ 1 & 1 & 1 & -1 & 1 & -1 \\ 1 & 1 & -1 & -1 & 1 & -1 \\ 1 & 1 & -1 & 1 & 1 & -1 \\ 1 & 1 & -1 & 1 & -1 & -1 \\ 1 & -1 & -1 & -1 & 1 & -1 \\ 1 & -1 & -1 & 1 & 1 & -1 \\ 1 & -1 & -1 & 1 & -1 & -1 \\ 1 & -1 & 1 & 1 & 1 & -1 \\ 1 & -1 & 1 & 1 & -1 & -1 \\ 1 & -1 & 1 & -1 & -1 & -1 \end{pmatrix} \Leftrightarrow \begin{pmatrix} 1 & T \\ 2 & L \\ 3 & T \\ 4 & L \\ 4 & L \\ 3 & T \\ 2 & L \\ 4 & L \\ 3 & T \\ 4 & L \\ 0 & Neel \\ 4 & L \\ 3 & T \\ 2 & L \\ 1 & T \\ 1 & T \\ 2 & L \\ 3 & T \\ 4 & L \\ 1 & T \\ 2 & L \\ 3 & T \\ 1 & T \\ 2 & L \\ 1 & T \end{pmatrix}$$

In the present case, I have truncated all the states above the 4-L states (which means that the 5-T and 6-L modes are not taken into account). Here, the states order of this matrix is different than the one in D because of the truncation. Note that the 6-L mode is equivalent to the reference Néel state (- + - + - +). One can see this mode like a state where all the spins have been flipped. It is the highest energy mode in terms of interchain coupling. One can notice that this state does not have intrachain defaults and thus the energy of the intrachain coupling, which is much higher than the interchain one is lower for this state than for the 2-spinons state. However this contradiction is removed for the case of an infinite chain (even for a long enough chain) as its interchain energy is becoming infinite (for the ∞-L mode). Then we are able to truncate our complete basis.

3.3.3 Hamiltonian of the system

3.3.3.1 General Hamiltonian of the system

The considered Hamiltonian for our quasi-1D Ising-like antiferromagnet system under an applied magnetic field writes as follows:

$$\mathscr{H} = \sum_{\nu}\sum_{j} J[S^z_{j,\nu}S^z_{j+1,\nu} + \varepsilon(S^x_{j,\nu}S^x_{j+1,\nu} + S^y_{j,\nu}S^y_{j+1,\nu})] \tag{3.1}$$

$$+ \sum_{\nu,\nu'}\sum_{j} J_{inter}S^z_{j,\nu}S^z_{j,\nu'} + \sum_{\nu}\sum_{j} \mu_B \vec{S}_{j,\nu}\widetilde{g_j}\vec{H} \tag{3.2}$$

$$\mathscr{H} = \mathscr{H}_{XXZ} + \mathscr{H}_{interchain} + \mathscr{H}_{field} \tag{3.3}$$

where ν and j denote the index of the chain and of the site respectively, $\widetilde{g_j}$ is the Landé tensor (which depends on the site j in the laboratory frame), ε is the anisotropy parameter, H is the applied field, J is the intrachain coupling (taken > 0) and J_{inter} is the interchain coupling. The first part of the Hamiltonian is the well known XXZ model, the second one describes the interaction between the ν^{th} chain and its neighbouring chains ν' and the third part describes the effect of the magnetic field.

What I would like to calculate is the Hamiltonian of one chain coupled to neighbouring ones. To treat the interachain interaction, I used the mean-field theory as a first order approximation.
We have $S^z_{j,\nu} =< S^z_{j,\nu} > +\delta S^z_{j,\nu}$ with $< S^z_{j,\nu} >= m_{j,\nu}$ the average magnetization on site j of the ν^{th} chain and $\delta S^z_{j,\nu} = S^z_{j,\nu} - < S^z_{j,\nu} >$ the fluctuations of the spin. Thus:

$$S^z_{j,\nu}S^z_{j,\nu'} = [< S^z_{j,\nu} > +\delta S^z_{j,\nu}][< S^z_{j,\nu'} > +\delta S^z_{j,\nu'}] \tag{3.4}$$

$$=< S^z_{j,\nu} >< S^z_{j,\nu'} > +\delta S^z_{j,\nu} < S^z_{j,\nu'} > +\delta S^z_{j,\nu'} < S^z_{j,\nu} > +\delta S^z_{j,\nu}\delta S^z_{j,\nu'} \tag{3.5}$$

The last term is of second order and can thus be neglected. Keeping in mind that $\delta S^z_{j,\nu} = S^z_{j,\nu} - < S^z_{j,\nu} >$, the Hamiltonian describing the interchain interaction can be rewritten (up to a constant) as follows:

$$\mathscr{H}_{interchain} = \sum_{\nu,\nu'}\sum_{j} J_{inter}(S^z_{j,\nu} < S^z_{j,\nu'} > +S^z_{j,\nu'} < S^z_{j,\nu} >) \tag{3.6}$$

$$= 2\sum_{\nu,\nu'}\sum_{j} J_{inter} S^z_{j,\nu} < S^z_{j,\nu'} > \tag{3.7}$$

In this model, I consider only one chain (let us say the chain ν) antiferromagnetically coupled to another one in the Néel state (the chain ν'). Then considering an antiferromagnetic interaction between the two chains we get $< S^z_{j,\nu} >= - < S^z_{j,\nu'} >$. As we have only one chain coupled to an effective field (describing the interchain coupling), we do not need the ν-index. Finally the Hamiltonian of the interchain interaction can be written as:

$$\mathscr{H}_{interchain} = -2\sum_{j} J_{inter} S^z_j < S^z_j > \tag{3.8}$$

Using the following formulas:

$$\left\{ \begin{array}{l} S^+ = S^x + iS^y \\ S^- = S^x - iS^y \end{array} \right. \Rightarrow \left\{ \begin{array}{l} S^x = \frac{S^+ + S^-}{2} \\ S^y = \frac{S^+ - S^-}{2i} \end{array} \right.$$

the entire Hamiltonian for one chain is written as:

$$\mathscr{H} = \sum_j \underbrace{J[S^z_j S^z_{j+1} + \frac{\varepsilon}{2}(S^+_j S^-_{j+1} + S^-_j S^+_{j+1})]}_{1} \underbrace{- 2J_{inter} < S^z_j > S^z_j}_{2} + \underbrace{\mu_B \vec{S}_j \widetilde{g_j} \vec{H}}_{3} \tag{3.9}$$

To summarize, there are three terms in this Hamiltonian:
1: XXZ Hamiltonian: intrachain interactions.
2: molecular field Hamiltonian due to the interchain coupling between the considered excited chain (containing two spinons) and a neighboring chain (taken as a Néel state at the beginning of the calculations). $< S^z_j >$ represents the average magnetization of the j^{th} site of the neighbouring chain.

3: Hamiltonian due to the applied magnetic field.

As $BaCo_2V_2O_8$ has an Ising-like anisotropy ($\varepsilon \simeq 0.5$), we can distinguish two configurations for the magnetic field: longitudinal (resp. transverse) when the applied magnetic field is applied along (resp. perpendicular to) the direction of the ordered moments in zero-field (hence the chain-axis in the case of $BaCo_2V_2O_8$). I will present the study of $BaCo_2V_2O_8$ for these two orientations of the field in Chap. 4 and Chap. 5.

Longitudinal magnetic field: In this case $\vec{H} = H\vec{e_z}$ with $\vec{e_z}$ a unitary vector along the z-direction. The Hamiltonian describing the effect of the magnetic field takes the following form:

$$\mathscr{H}_{field} = \sum_j \mu_B g_{zz} H S_j^z \tag{3.10}$$

Transverse magnetic field: Now, the magnetic field is applied in the plane perpendicular to the ordered moments. This case is much more subtle for $BaCo_2V_2O_8$. According to Kimura et *al.* [Kim+13], additional staggered effective fields emerge from the anisotropic $\widetilde{g}$ tensor which is not diagonal. This non-diagonality is due to the tilt of the local easy-axis of anisotropy with respect to the c-axis ($\theta \simeq 5°$) and the fact that this tilt rotates around the c-axis by an angle of $\pi/2$ from one Co atom to the next one along the chain [Kim+13]. The Hamiltonian due to the magnetic field is now:

$$\mathscr{H}_{field} = \mu_B H \sum_j \left(g_{yy} \frac{S_j^+ + S_j^-}{2} + g_{yz} S_j^z \cos\left[\phi + \frac{\pi(j-1)}{2}\right] + g_{yx} \sin[2\phi + \pi(j-1)] \frac{S_j^+ - S_j^-}{2i} \right) \tag{3.11}$$

where ϕ is an angle describing the direction of the magnetic field: $\phi = 0°$ in the XY plane (resp. $\phi = 45°$) for the field along $x + y$ (resp. y). g_{yy} is the diagonal component of the Landé tensor along y, g_{zy} and g_{xy} are the off-diagonal components of the Landé tensor coupling the z and x directions to the y one. In our case we have studied $BaCo_2V_2O_8$ for $\vec{H} = H\vec{e_y}$ with $\vec{e_y}$ a unitary vector along the y-axis. Taking the same parameters as Kimura et *al.* [Kim+13], we have: $\phi = 45°$, $g_{yy} = 2.75$, $g_{xy} = 0.4 g_{yy} \simeq 1.1$ and $g_{zy} = 0.1\sqrt{2} g_{yy} \simeq 0.39$.

In my calculations, I consider this Hamiltonian for different orientations and values of the magnetic field. For each field value, I calculate the eigenstates and eigenvalues of the Hamiltonian. The normalized eigenvectors are: $|\Psi\rangle = \sum_{i=1}^{ns} a_i |\Phi_i\rangle$ where $|\Phi_i\rangle$ are the vectors forming the basis of the Hilbert space.

3.3.3.2 Self-consistent calculations

In order to be more precise, I calculated in a self consistent way the effective magnetization for each site of the neighbouring chain.

At a given magnetic field h, we calculate the Hamiltonian and diagonalize it. Then we write the ground state as a linear combination of the vectors forming the basis of the

Hilbert space $|GS^{(m)}\rangle = |0^{(m)}\rangle = \sum_{i=1}^{ns} a_i^{(m)} |\Phi_i\rangle$ where m is the number of iterations, i.e. the number of times that we recalculate the ground state at a given field h (the states $|\Phi_i\rangle$ are not m dependent, only the coefficients of the linear combination a_i depend on the number of iterations). What we need to calculate is the average of the magnetization on each site $< S_j^z >^{(m)}$ of the ground state $|0)^{(m)}\rangle$ at a step m. We have:

$$< S_j^z >^{(m)} = \langle 0^{(m)}| S_j^z |0^{(m)}\rangle \tag{3.12}$$

$$= \sum_{i,i'=1}^{ns} (a_i^{(m)})^* a_{i'}^{(m)} \langle \Phi_i| S_j^z |\Phi_{i'}\rangle \tag{3.13}$$

$$\tag{3.14}$$

where '*' denotes the complex conjugate. As the quantization axis is z, then S_j^z is diagonal, so that:

$$< S_j^z >^{(m)} = \sum_{i,i'=1}^{ns} (a_i^{(m)})^* a_{i'}^{(m)} S_j(\Phi_{i'}) \langle \Phi_i|\Phi_{i'}\rangle \tag{3.15}$$

$$= \sum_{i,i'=1}^{ns} (a_i^{(m)})^* a_{i'}^{(m)} S_j(\Phi_{i'}) \delta_{i,i'} \tag{3.16}$$

$$= \sum_{i=1}^{ns} |a_i^{(m)}|^2 S_j(\Phi_i) \tag{3.17}$$

where $\delta_{i,i'}$ is the Kronecker symbol defined as $\delta_{i,i'} = 1$ if $i = i'$ and 0 otherwise.

To be sure that the difference between two iterations $\delta^{(m)} = < S_j^z >^{(m+1)} - < S_j^z >^{(m)}$ has fairly converged towards a null value (indeed one expects $\lim_{m\to+\infty} \delta^{(m)} = 0$), I implemented the following condition: while $\delta^{(m)} > 10^{-4}$, then it continues to iterate, which means that the initial reference Néel state for the interchain interaction is now replaced by the calculated ground state $|0^{(m)}\rangle$ at step (m). Then we re-diagonalize the Hamiltonian and get the ground state $|0^{(m+1)}\rangle$ at step $(m+1)$, which is compared to the previous one, and so forth.

3.3.4 Calculation of the dynamical structure factor $\mathbf{S}(\vec{Q},\omega)$

We now focus on the dynamical structure factor $\mathrm{S}(\vec{Q},\omega)$ which is the double Fourier transform in time and space of the spin-spin correlation function, one at position $\vec{0}$ and time 0 and the other one at position $\vec{r}$ and time t. As the neutrons are only sensitive to the magnetic components perpendicular to the scattering vector $\vec{Q}$, we can write the dynamical structure factor as follows:

$$S(\vec{Q},\omega) = \iint e^{i(\omega t - \vec{Q}\cdot\vec{r})} < \vec{S}_{\perp\vec{Q}}(\vec{0},0) \cdot \vec{S}_{\perp\vec{Q}}(\vec{r},t) > \, dt\, d\vec{r} \tag{3.18}$$

with $\vec{S}_{\perp\vec{Q}} = \vec{S} - (\vec{S}\cdot\vec{Q})\vec{Q}/Q^2$ the component of the spin perpendicular to the scattering vector $\vec{Q}$. Let us write $\vec{r} = \vec{R_{j'}} - \vec{R_j}$ (here we go from a continuous space to a discrete one), and make a change in space origin by a translation of $\vec{R_j}$. Then we can rewrite equation (3.18) as:

$$S(\vec{Q},\omega) = \int e^{i\omega t} (\sum_{j,j'} < \vec{S}_{\perp\vec{Q}}(\vec{R_j},0) \cdot \vec{S}_{\perp\vec{Q}}(\vec{R_{j'}},t) > e^{-i\vec{Q}\cdot(\vec{R_{j'}}-\vec{R_j})}) dt \tag{3.19}$$

By using the Heisenberg representation we get: $\vec{S}_{\perp\vec{Q}}(\vec{R_\alpha},t) = e^{-\frac{i}{\hbar}Ht}\vec{S}_{\perp\vec{Q}}(\vec{R_\alpha},0)e^{\frac{i}{\hbar}Ht}$ where $\alpha = j, j'$. The average of an operator A is given by:

$$< A > = Tr(A\rho) \tag{3.20}$$
$$= \sum_k p_k \langle k| A |k\rangle \tag{3.21}$$
$$= \sum_k \frac{e^{-\beta H}}{Tr(e^{-\beta H})} \langle k| A |k\rangle \tag{3.22}$$
$$= \sum_k \frac{e^{-\beta H}}{Z} \langle k| A |k\rangle \tag{3.23}$$

where ρ is the density matrix, $|k\rangle$ are the eigenvectors of the system, $\beta = \frac{1}{k_B T}$, p_k is the Boltzmann weight of state $|k\rangle$ and $Z = Tr(e^{-\beta H})$, the partition function of the system. Let us rewrite the scattering function with these two ingredients:

$$S(\vec{Q},\omega) = \int e^{i\omega t} \sum_{j,j'}\sum_k p_k \langle k| \vec{S}_{\perp\vec{Q}}(\vec{R_j},0)e^{-\frac{i}{\hbar}Ht}\vec{S}_{\perp\vec{Q}}(\vec{R'_j},0)e^{\frac{i}{\hbar}Ht} |k\rangle e^{-i\vec{Q}\cdot(\vec{R'_j}-\vec{R_j})}dt \tag{3.24}$$

We now introduce the identity operator defined as $\mathbb{1} = \sum_m |m\rangle \langle m|$ and inject it in Eq. (3.24). We obtain:

$$S(\vec{Q},\omega) = \int e^{i\omega t} \sum_{j,j'}\sum_{k,m} p_k \langle k| \vec{S}_{\perp\vec{Q}}(\vec{R_j},0)e^{-\frac{i}{\hbar}Ht} |m\rangle \langle m| \vec{S}_{\perp\vec{Q}}(\vec{R_{j'}},0)e^{\frac{i}{\hbar}Ht} |k\rangle e^{-i\vec{Q}\cdot(\vec{R_{j'}}-\vec{R_j})}dt \tag{3.25}$$

which leads to:

$$S(\vec{Q},\omega) = \int e^{i(\frac{E_k-E_m}{\hbar}+\omega)t} \sum_{j,j'}\sum_{k,m} p_k \langle k| \vec{S}_{\perp\vec{Q}}(\vec{R_j},0) |m\rangle \langle m| \vec{S}_{\perp\vec{Q}}(\vec{R_{j'}},0) |k\rangle e^{-i\vec{Q}\cdot(\vec{R_{j'}}-\vec{R_j})}dt \tag{3.26}$$
$$= \sum_{k,m} p_k \sum_{j,j'} \langle k| \vec{S}_{\perp\vec{Q}}(\vec{R_j},0) |m\rangle \langle m| \vec{S}_{\perp\vec{Q}}(\vec{R_{j'}},0) |k\rangle e^{-i\vec{Q}\cdot(\vec{R_{j'}}-\vec{R_j})} \int e^{i(\frac{E_k-E_m}{\hbar}+\omega)t}dt \tag{3.27}$$
$$= \sum_{k,m} p_k \sum_{j,j'} \langle k| \vec{S}_{\perp\vec{Q}}(\vec{R_j},0) |m\rangle \langle m| \vec{S}_{\perp\vec{Q}}(\vec{R_{j'}},0) |k\rangle e^{-i\vec{Q}\cdot(\vec{R_{j'}}-\vec{R_j})}\delta(E_k - E_m + \hbar\omega) \tag{3.28}$$
$$= \sum_{k,m} p_k (\sum_j \langle k| \vec{S}_{\perp\vec{Q}}(\vec{R_j},0) |m\rangle e^{i\vec{Q}\cdot\vec{R_j}})(\sum_{j'} \langle m| \vec{S}_{\perp\vec{Q}}(\vec{R_{j'}},0) |k\rangle e^{-i\vec{Q}\cdot\vec{R_{j'}}})\delta(E_k - E_m + \hbar\omega) \tag{3.29}$$
$$= \sum_{k,m} p_k (\sum_j \langle m| \vec{S}_{\perp\vec{Q}}(\vec{R_j},0) |k\rangle e^{-i\vec{Q}\cdot\vec{R_j}})^\dagger (\sum_j \langle m| \vec{S}_{\perp\vec{Q}}(\vec{R_j},0) |k\rangle e^{-i\vec{Q}\cdot\vec{R_j}})\delta(E_k - E_m + \hbar\omega) \tag{3.30}$$
$$= \sum_{k,m} p_k |\sum_j \langle m| \vec{S}_{\perp\vec{Q}}(\vec{R_j}) |k\rangle e^{-i\vec{Q}\cdot\vec{R_j}}|^2\delta(E_k - E_m + \hbar\omega) \tag{3.31}$$

where † denotes the Hermitian conjugate. To simplify the numerical calculations, we assume that we are at $T = 0$ K. Then only the ground state is populated ($p_0 = 1$, with

$|GS\rangle = |0\rangle$). It means that in an intrinsic way, only the excitations from the ground state to the excited states have a non-zero spectral weight. Therefore, we have the dynamical structure factor $S(\vec{Q},\omega)$ given by:

$$S(\vec{Q},\omega) = \sum_m \left| \sum_j \langle m| \vec{S}_{\perp\vec{Q}}(\vec{R}_j) |0\rangle e^{-i\vec{Q}.\vec{R}_j} \right|^2 \delta(E_0 - E_m + \hbar\omega) \tag{3.32}$$

$$= \sum_m A_m \delta(E_0 - E_m + \hbar\omega) \tag{3.33}$$

where $A_m = \left| \sum_j \langle m| \vec{S}_{\perp\vec{Q}}(\vec{R}_j) |0\rangle e^{i\vec{Q}.\vec{R}_j} \right|^2$ is the probability amplitude of the transition from the ground state to the m^{th} mode of the system, driven by the operator $S_{\perp\vec{Q}}$. The Dirac distribution $\delta(E_0 - E_m + \hbar\omega)$ represents the conservation of energy. To be able to see peaks on the calculated plot, I have replaced the Dirac distribution by a Gaussian peaks with a full width at half maximum σ fixed at 0.2 meV (which is about the energy resolution that we had during the different inelastic neutron experiments) for all calculations. Then the dynamical structure factor takes the definitive form:

$$S(\vec{Q},\omega) = \sum_m A_m \exp\left\{ -4\ln 2 \left[\frac{\hbar\omega - (E_m - E_0)}{\sigma} \right]^2 \right\} \tag{3.34}$$

It is important to understand that the dynamical structure factor built here is the one corresponding to a simple linear spin chain and not to $BaCo_2V_2O_8$. A step further would be to take into account the magnetic structure factor of $BaCo_2V_2O_8$ which is more complex due to the screw nature of the chains. Because I consider a simple chain, the propagation vector in the present program is $\vec{k}^{AF}_{calc} = (0,0,\frac{1}{2})$ instead of having the experimental propagation vector $\vec{k}^{AF}_{exp} = (0,0,1)$, or rigorously speaking, $\vec{k}^{AF}_{exp} = (1,0,0)$ since $a > c$ in $BaCo_2V_2O_8$.

3.4 Calculations at zero-field: validity of the model and its limitations

At this stage I have built an entire code to catch the spin-dynamics of one dimensional systems. The first question now is: is this model valid? And what about its limitations? In order to answer these questions, I have performed test calculations at zero-field and compare the numerical simulations to the experimental results obtained in $BaCo_2V_2O_8$ [Gre+15a].

3.4.1 Confinement of spinons

In the ordered phase, the propagation of the spinons upsets the neighbouring chains and thus costs a potential energy $V(n_{reversed})$ which grows linearly with the number of reversed spins $n_{reversed}$ between two spinons. Therefore this potential confines the spinon pairs. This was already investigated by Shiba and the excitations are known as the Zeemann ladders [Shi80]. Because of this linear potential, the Schrödinger equation admits solutions of the form [Col+10]:

$$E_j^{\mathrm{T,L}} = 2E_0^{\mathrm{T,L}} + z_j\alpha \tag{3.35}$$

with $2E_0^{\mathrm{T,L}}$ the mass of the transverse (T) and longitudinal (L) modes, $\alpha \simeq (J\varepsilon J_{inter}^2)^{1/3}$ and z_j the negative zeros of the Airy function ($Ai(-z_j) = 0$). We propose here to see first if our calculations in the case of a basis restricted to two spinons reproduce this type of law for the excited states. For all the simulation below, I will use the following parameters: $J = 5$ meV, $J_{inter} = 0.3$ meV, $\varepsilon = 0.5$. These parameters are close to the ones found experimentally in $BaCo_2V_2O_8$ ([Kim+07; Kim+13; Kim+08b; Gre+15a]).

Fig. 3.2(a) shows both the calculated transverse (T) dynamical structure factor S_{xx} and the longitudinal (L) one S_{zz} as a function of the energy at the AF position $\vec{Q} = (1, 0, 0.5)$, to be compared to the measured spectrum at $\vec{Q} = (2, 0, 1)$ in the experiment. One can notice that there are two series of discrete T and L excitations and that the longitudinal ones cost more in energy than the transverse ones. The difference in energy $E_j^L - E_j^T \simeq 0.25$ meV is consistent with what has been seen in $BaCo_2V_2O_8$ (see Fig.3.2 and Fig. 3.3). This additional cost has already been understood and simply comes from the interchain interaction [Gre+15a]. However, if we compare with the experimental data (see Fig. 3.2(b)), one can see that the energy scale of the calculated modes is much higher than the experimental ones. Indeed the energy of the first T mode is about 5.8 meV while the experimental one is about 1.8 meV. In addition, the intensity of the L modes is much lower (by about a factor 5) than the T ones while it is almost the same in the experiment. This comes from the restriction of the Hilbert space to the 2-spinons basis as explained later.

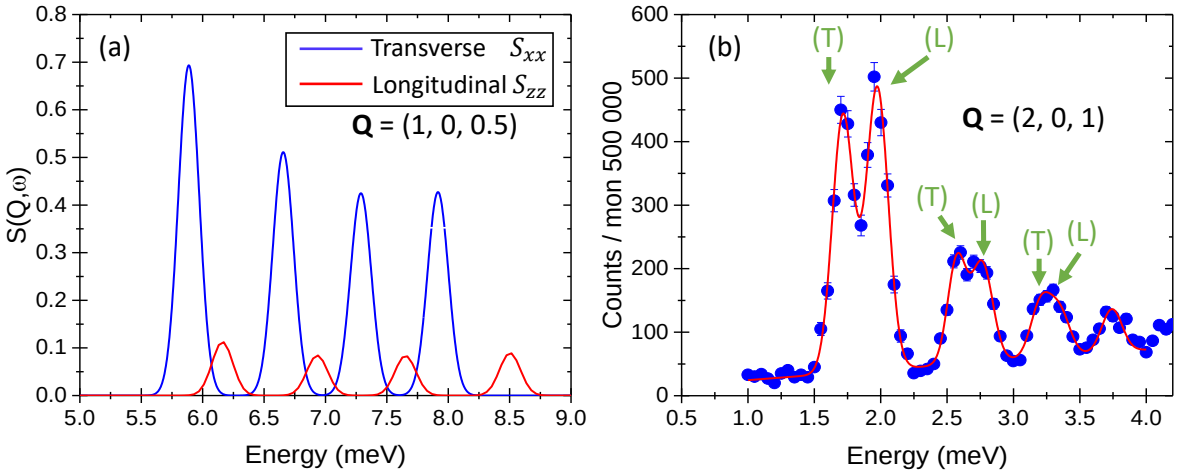

Figure 3.2: **Calculated vs experimental energy-scan.** (a) Calculated transverse and longitudinal dynamical structure factors S_{xx} and S_{zz} (blue and red lines respectively). The calculations were done with $n = 30$. $S(\vec{Q}, \omega)$ is calculated on an AF point $\vec{Q} = (1, 0, 0.5)$ which is not parallel to the c-axis and thus to the ordered moment, so that we are able to see both the L and T excitations (this $\vec{Q}$ vector is chosen to keep the same angle in the (a, c) plane than $\vec{Q} = (2, 0, 1)$ in the experiment). (b) Q-constant energy scan measured by inelastic neutron scattering obtained at $T = 1.5$ K and $H = 0$ at the AF point $\vec{Q} = (2, 0, 1)$ for $BaCo_2V_2O_8$. The red solid line corresponds to a fit with a series of Gaussian functions. The symbols (T) and (L) point out the transverse or longitudinal nature of the excitation. Only the first four excitations for each type of mode (T and L) are plotted.

In Fig. 3.3 are plotted the energies of the calculated T (blue points) and L (red points) excitations as a function of the negative zeros of the Airy function z_j. The data were fitted linearly and show an excellent agreement with the predicted law of Eq. (3.35). The calculated and experimental fits give (almost) the same slope (the difference of the intercepts has already been discussed above). The following coefficients of the slope are found from the fit (solid lines) of the T and L excitations: $\alpha(\mathrm{T}) \simeq 0.57$ meV and $\alpha(\mathrm{L}) \simeq 0.60$ meV in good agreement with the theoretical coefficient $\alpha(th) = (J\varepsilon J_{inter}^2)^{1/3} \simeq 0.60$ meV. Finally $\alpha(\mathrm{T}) \simeq \alpha(\mathrm{L})$ which is consistent with the fact that this coefficient does not depend on the nature of the excitations.

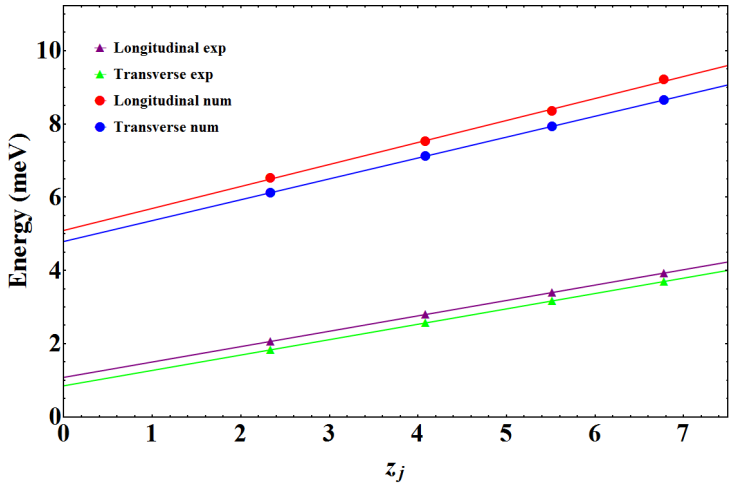

Figure 3.3: **Confinement of spinons, linear potential and Airy function.** Calculated energies for transverse (blue circles) and longitudinal (red circles) modes as a function of the negative zeros of the Airy function z_j. The experimental T and L energies are also plotted (green and purple triangles respectively). Blue and red (resp. green and purple) solid lines represent the linear fits of the calculated (resp. experimental) excitations energy vs z_j.

These results seem quite promising in spite of the discrepancies already mentioned between the calculations and the experiment: weaker spectral weight for the longitudinal excitations and a global shift in energy.

3.4.2 Mass $2E_0^{\mathrm{T,L}}$ and coefficient α as a function of the interchain interaction and of the anisotropy parameter ε

In this section, we study the dependence of the mass $2E_0^{\mathrm{T,L}}$ and of the coefficient α as a function of J_{inter} and of the anisotropy parameter ε.

In Fig. 3.4(a), one can see that for the ε-dependence of the calculated $\alpha(\mathrm{T})$ and $\alpha(\mathrm{L})$ coefficients is in a really good agreement with the theoretical values calculated as $\alpha(th) = (J\varepsilon J_{inter}^2)^{1/3}$ up to $\varepsilon = 0.5$ and start to deviate above this value. This enhances one of the limitations of this model based on strong Ising anisotropy. For the J_{inter}-dependence of the same coefficients (see Fig. 3.4(b)), the calculated ones match well the theoretical ones only for an interchain coupling between 0.3 meV and 0.6 meV while they deviate for lower and higher values of J_{inter}. One possible reason for the deviation of higher values could be that this model is only valid for a weak interchain coupling, as it is

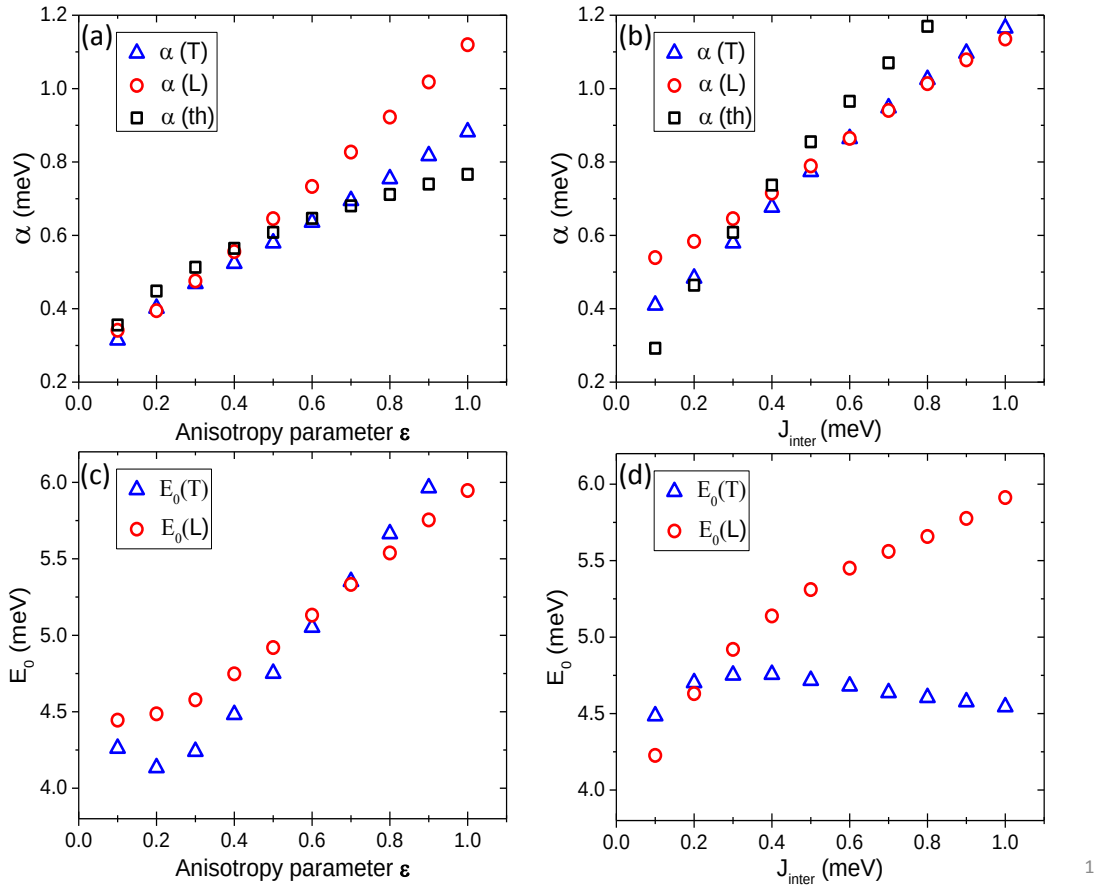

Figure 3.4: **Dependence of the coefficient α and of the mass $E_0^{\mathrm{T,L}}$** as a function of J_{inter} for $\varepsilon = 0.5$ (right panels) and of the anisotropy parameter ε for $J_{inter} = 0.3$ meV (left panels). The calculations were made with $n = 30$ spins. The blue open triangle symbols correspond to the T modes, the red open circles to the L ones and the black open squares to the theoretical ones using Eq. (3.35).

treated in the approximation of the mean-field theory. Concerning the low values of J_{inter}, the deviation may come from the fact that in the weak interchain regime, the system is close to a pure 1D system and hence the 2-spinons basis (which is more relevant in the presence of interchain interactions as the latter confines them) is not enough to describe the system correctly.

Concerning the mass E_0 of the T and L excitations, at low ε (strong Ising limit), the two masses do not match. By increasing the anisotropy parameter, they are both increasing and cross each other at $\varepsilon = 0.7$. Then the mass of the T mode becomes larger than the L one contrary to the low ϵ limit (see Fig. 3.4(c)). Concerning the J_{inter}-dependence of the masses, by increasing the interchain interaction the energy of the T excitations is decreasing while that of the L ones is increasing, thus the energy difference between the two is increasing also (Fig. 3.4(d)). Those results should be taken cautiously as we have two approximations here: First the model of Zeeman Ladders works only in the limit of weak interchain interaction and of a strong Ising anisotropy as it is treated in

a mean-field approximation. Second, the basis is limited to 2-spinons states.

3.4.3 Excitation spectrum of $BaCo_2V_2O_8$ at zero-field

Figs. 3.5(a-c) show the calculated excitation spectra of $BaCo_2V_2O_8$.

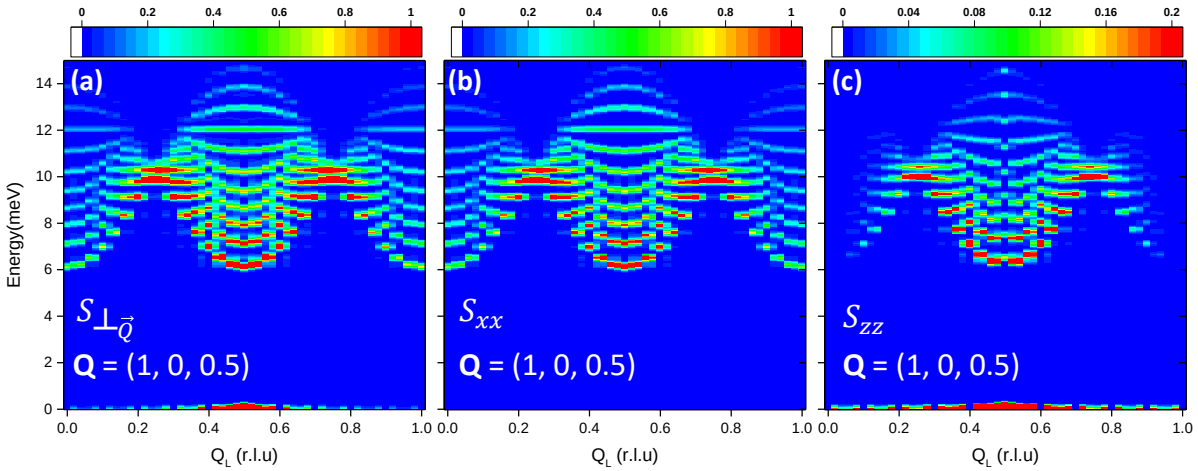

Figure 3.5: **Calculated excitation spectra** $S_{\perp_{\vec{Q}}}$, S_{xx} and S_{zz} (panels (a-c) respectively) at zero-field and around the AF point $\vec{Q} = (1, 0, \frac{1}{2})$ with $n = 30$. The step in energy (resp. Q_L) is 0.08 meV (resp. 0.02 r.l.u). The colorscale of the S_{zz} spectrum is enlarged by a factor 5 since L modes have a lower spectral weight as discussed above.

One can see directly that the whole spectrum shows a series of discrete modes consistent with the presence of Zeemann ladders. The spectra of $\vec{S}_{\perp_{\vec{Q}}}$ and S_{xx} are very similar because of the much lower intensities of the longitudinal modes (about a factor 5). We can clearly see that the minimum in energy is obtained at the AF point $\vec{Q} = (1, 0, \frac{1}{2})$. In each series of modes (T and L), the spectral weight is maximum at this point for the two lowest energy T and L excitations and then it slightly decreases when the energy increases. This is consistent with what has been seen experimentally in $BaCo_2V_2O_8$ (see Fig.3.2 (b)) [Gre+15a]. We clearly see the large amplitude of the gap $\Delta \simeq 6$ meV already discussed above.

3.4.4 Limitations of the calculations

One can see that the calculations reproduce qualitatively the main behaviors of our system. However, the numerical results never give the good values of energy and that the details of the excitations do not match exactly with the experiment. This is mainly due to two reasons:
-the first one is the finite chain size that we consider.
-the second is the truncated Hilbert space which is necessary to be able to do the calculations.
Indeed, the whole problem when doing numerical calculations on quantum physics is the size of the Hilbert space which grows as 2^n with n the number of spins. It is possible to

take the entire Hilbert space but as the size of the Hilbert space grows as 2^n, the calculations becomes really heavy for $n > 12$ (for instance for $n = 16$, the number of states in the entire Hilbert space is $2^{16} = 65536$).

Actually, the previous calculations were done with the "2-spinons" subspace of the entire Hilbert space with $n = 30$. For this number of sites, the size of the entire Hilbert space is given by $2^{30} \simeq 10^9$ while the size of the 2-spinons subspace is given by $2 \times C_{30}^2 +$ the two Néel states $= 872$. The entire Hilbert space was highly truncated and this allowed calculations. The two-spinons states are the most entangled states with the fundamental state $|0\rangle$ and have also the lowest energies. That is why, we recover the main physics (Zeeman ladders, spectrum). But the brutal truncation of the other $2k$-spinons with $k \in [2, 3, .., \frac{n}{2}]$ leads to a loss of information and of agreement with the experimental results.

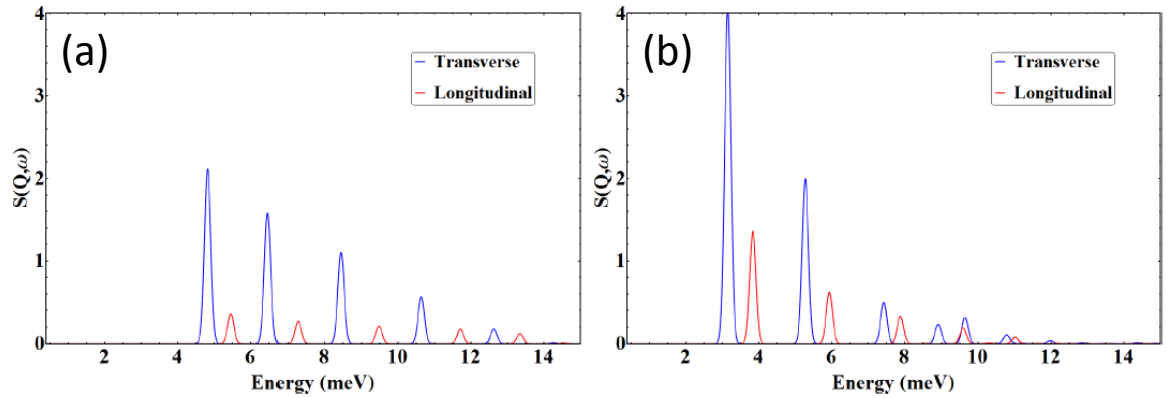

Figure 3.6: **Limitation of the calculations and size of the Hilbert space.** Calculated $S(\vec{Q}, \omega)$ on an AF point $\vec{Q} = (1, 0, \frac{1}{2})$. The Hilbert space corresponds to the: (a) 2-spinons subspace, (b) 2-spinons $\oplus$ 4-spinons subspace. To make possible the calculations with the 4-spinons states, the number of spins is taken as $n = 16$ for both subspaces.

Fig. 3.6 shows the comparison between calculations results for a 2-spinons subspace and for a 2-spinons$\oplus$4-spinons subspace. One can see that for the 2-spinons$\oplus$4-spinons states, the energies of the peaks are shifted to lower energies (the gap is much smaller) and that the intensities of the longitudinal modes S_{zz} are much bigger. While the gap is $\simeq 4.75$ meV for the 2-spinons states, the gap of the 2-spinons$\oplus$4-spinons states $\simeq 3$ meV which is closer to the experimental gap $\simeq 1.8$ meV. This shows that not taking the higher energy states into account is at the origin of the discrepancies already mentioned and thus to a loss of quantitative information.

In conclusion, exact diagonalization calculations is a valuable tool but are rapidly unachievable because of the exponential expansion of the Hilbert space and then the truncation of the basis becomes necessary. This is how and where the DMRG (Density Matrix Renormalization Group) emerges and why this technique is so powerful.

Keeping in mind the limitations of the calculations, I assume that we will never reach quantitative information. Nevertheless, we can reproduce some qualitative properties and acquire an understanding of the physics at play, as I will show in Chap. (4), Chap. (5) and Chap. (6).

A last important remark that I should mention is that the term of "exact diagonalization" is perhaps not correct in the case of my calculations as I strongly truncate the Hilbert space since the beginning. However my numerical code allows to perform an exact diagonalization and I will continue to use this formulation all along this manuscript.

3.4.5 Some words about DMRG and surrounding techniques

Here I would like to describe briefly my little understanding of the DMRG technics. For more details, the readers can refer to [Fei13; Sch05; Sch11].

The DMRG technique is a numerical technique which allows to truncate in a "good way" the Hilbert space. The DMRG method is variational (even if it based on diagonalization) in the sense that the aim is to approximate the wave functions of the system in a truncated Hilbert space and hence to minimize the loss of information.

But which states have to be kept? and which ones do we have to discard? Naively, one can think that keeping only the lowest energy modes should be enough to probe the whole physics of a quantum system. However it is not so simple. It has been shown by S. White [Whi92], and then in many other studies that the good way to truncate a quantum system (especially in the 1-D case because of the strong fluctuations) is to keep only the states which are highly entangled with the ground state.

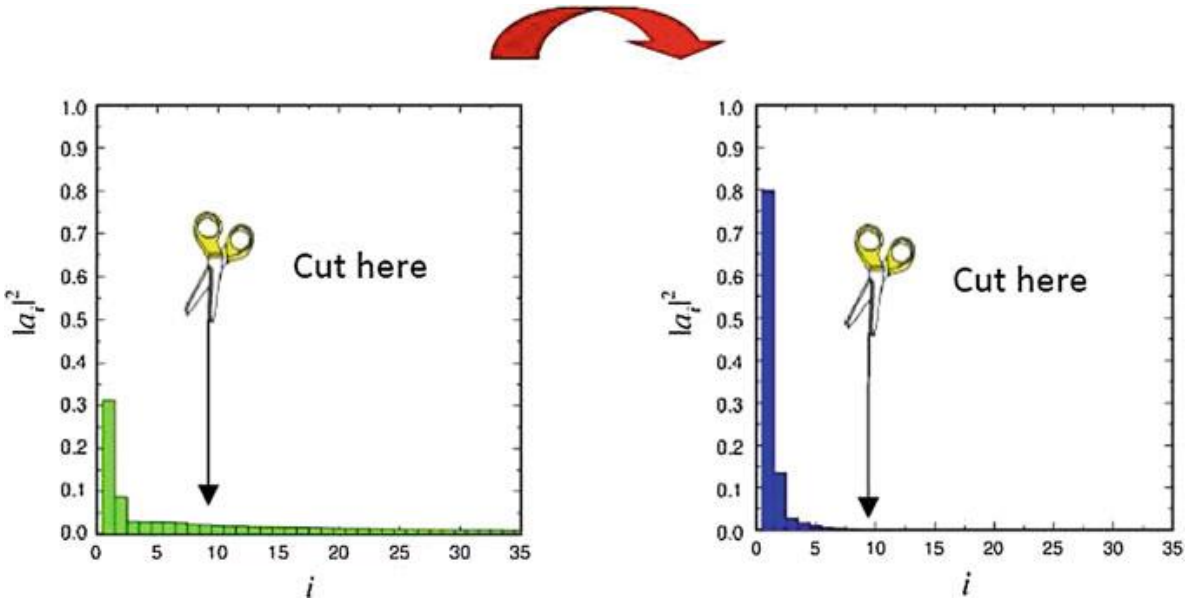

Figure 3.7: **Truncation of the basis.** Left: basis where the spectral weight $|a_i|^2$ are non null for each state. The truncation is then not appropriate is this case. The red arrow points out a rotation of the Hilbert space. Right: After the rotation, all the spectral weight $|a_i|^2$ is contained in the first few states and the truncation becomes possible. Figure extracted from [Fei13]

To picture this, suppose that you want to diagonalize a Heisenberg chain with a ground state of the form $|\psi\rangle = \sum_i a_i |\phi_i\rangle$. If we plot the different weights $|a_i|^2$, we may find the

distribution in the left picture of Fig. 3.7 where the majority of the spectral weight is contained in a few states (for example in our case, such states would be the Néel state or the 2-spinons excitations which are easier to create and thus more "probable") while the rest of the spectral weight is spread over the tail. One would like to truncate the basis by only keeping the first few states containing the majority of the spectral weight. However the states which are truncated with a smaller spectral weight are responsible of the interesting physics, i.e. the fluctuations, and thus cannot be neglected by this "brutal" truncation. Here I would like to emphasize that this is exactly what I am doing in my numerical calculations when, for example, I limit the Hilbert space to the 2-spinons basis. So, how to get rid of this problem? This is a basis dependent problem, which means that if someone finds a representation of the basis such as the one depicted in the right picture of Fig. 3.7, then the "brutal" truncation done previously becomes valid in this case. In this example, the number of states is reduced from 35 to 10 while keeping all the information. This is the main idea of DMRG calculations where a Schmidt decomposition using "density matrices" is used to rotate the Hilbert space, i.e. to find the good representation of the basis. One can understand this rotation with a simple mechanical problem. Suppose that you have a speed vector $\vec{v}$ expressed in the $(\vec{e}_x, \vec{e}_y)$ basis with the form: $\vec{v} = v_x\vec{e}_x + v_y\vec{e}_y$. In this case, two vectors are needed to describe $\vec{v}$. Suppose now that we rotate the basis such as $\vec{v} = v\vec{u}$ with $\vec{u}$ a unitary vector and $v = \sqrt{v_x^2 + v_y^2}$. Now, one single vector is needed to describe $\vec{v}$ and all the information is preserved.

The DMRG is in constant evolution as it has been shown recently that it has inspired the MPS (Matrix Product States) and Tensor Networks Method which are widely used in many-body problems. For example the iTEBD (infinite Time-Evolving Block Decimation) method [Vid07; PVM12] has been in the present project used by the theoretical team involved in this work, namely Shintaro Takayoshi and Thierry Giamarchi from the university of Geneva.

Chapter 4

$BaCo_2V_2O_8$ under a transverse magnetic field

Sommaire

4.1 Summary

4.1.1 Abstract

This chapter is devoted to the study of the Ising-like antiferromagnet $BaCo_2V_2O_8$ under a transverse magnetic field (i.e. perpendicular to the easy-axis of magnetization and thus to the c-axis). I will explain first the context and the motivations of this study and what has already been done before. The second part will treat the static properties of $BaCo_2V_2O_8$ under a transverse field. Then I will present how the spin-dynamics is affected by this configuration of the magnetic field. Finally, I will conclude by discussing and giving an interpretation of the results with the help of numerical calculations and field theory.

4.1.2 Résumé en français

Le quatrième chapitre est dédié à l'étude de $BaCo_2V_2O_8$ sous champ magnétique transverse, i.e. perpendiculaire à l'axe Ising. Dans $BaCo_2V_2O_8$, l'axe Ising est légèrement incliné par rapport à l'axe c. Cette inclinaison tourne d'un quart de tour lorsque l'on passe d'un site à l'autre le long de la chaîne. Il en résulte un tenseur de Landé non-diagonal, ce qui signifie que lorsqu'un champ magnétique uniforme est appliqué, par exemple selon l'axe b, un champ magnétique alterné proportionnel au champ uniforme est induit selon l'axe a. Nous avons montré au travers de notre étude que ce champ alterné rentre en compétition avec l'anisotropie du système, induisant alors une transition de phase quantique à $\mu_0 H_c \simeq 10$ T, transition qui apparaît bien en dessous de la valeur du champ à saturation ($\simeq 40$ T). En effet notre étude des propriétés statiques par diffraction des neutrons à montré que les moments magnétiques au dessus de la transition de phase sont antiferromagnétiquement alignés selon l'axe a, i.e. selon le champ local alterné. Nous avons ensuite étudié les propriétés dynamiques de $BaCo_2V_2O_8$ sous champ magnétique au moyen de la diffusion inélastique des neutrons (polarisés ou non).

Nous avons observé que le mode de plus basse énergie à champ nul se scinde en deux branches lorsque le champ augmente: une des branches augmente en énergie lorsque le champ augmente tandis que l'autre diminue en énergie pour atteindre un minimum à la transition de phase. Il est à noter que les deux branches ont une dépendance non-linéaire en champ magnétique, ce qui nous indique que le champ transverse produit un mélange des fonctions d'ondes du système. Nous avons ensuite suivi la dépendance en champ magnétique des excitations. Nous avons pu observer que l'excitation de plus basse énergie, polarisée selon a et b à champ nul (i.e. correspondant à des fluctuations transverses au moment magnétique aligné selon c), devient progressivement polarisée selon c, pour n'être plus que selon c au dessus de la transition. Ceci est cohérent avec des fluctuations de spins qui restent transverses en accompagnant la rotation des spins de c à a.

Pour aller plus loin dans notre analyse, nous avons eu recours à des calculs numériques, d'une part des diagonalisations exactes en utilisant mon propre code et d'autre part des calculs iTEBD (infinite Time Evolving Block Decimation) effectués par Shintaro Takayoshi et Thierry Giamarchi (Univ. Genève). Les deux techniques ont ainsi pu confirmer les résultats expérimentaux, en particulier la polarisation des modes sous champ magnétique et le fait que le champ alterné est l'élément clé à l'origine de la transition. Les calculs iTEBD reproduisent extrêmement bien les résultats expérimentaux de manière quantitative. Ainsi, l'Hamiltonien du système a pu être confirmé et les paramètres de celui-ci extraits.

Shintaro Takayoshi et Thierry Giamarchi ont alors pu établir une théorie des champs, nous permettant de comprendre de façon qualitative la nature des excitations. La théorie des champs associée à $BaCo_2V_2O_8$ sous champ magnétique transverse correspond au modèle dit de "Double sine-Gordon", qui a permis de révéler la nature topologique des excitations de part et d'autre de la transition. Nous avons ainsi pu montrer que les excitations à bas champ correspondent à deux spinons (déconfinés si l'on omet l'interaction interchaîne), tandis que les excitations au dessus de la transition correspondent à deux paires de spinons liés (chacune des paires pouvant se propager librement le long de la chaîne). Notre travail a mis en évidence la première réalisation expérimentale du modèle de "Double sine-Gordon".

4.2 Context and motivations

The one dimensional Ising model in a transverse magnetic field is an archetypal example of quantum phase transition that was early solved theoretically [Pfe70; Sac11]. It was only recently studied experimentally in the Ising-like ferromagnet $CoNb_2O_6$ where an order-disorder phase transition has been observed from a ferromagnetic phase at zero-field to a paramagnetic phase above the critical field [Col+10]. The excitations found in the paramagnetic phase have also been investigated and have been found to be "spin-flip" excitations [Cab+14]. Some studies with a transverse magnetic field applied on Ising-like antiferromagnets such as $CsCoCl_3$ and $CsCoBr_3$ were also done but the strong anisotropy ($\varepsilon \simeq 0.1$) and the strong intrachain interactions in those systems yield the critical field up to 75 T [HY79; Nag+82] [Ama+90; Kim+05], unreachable by means of neutron scattering experiments.

Thus, at first sight, because of its weak anisotropy (and thus a lower energy gap) and of an intrachain interaction weaker than in the case of $CsCoCl_3$ and $CsCoBr_3$, $BaCo_2V_2O_8$ was the first potential candidate to observe such a quantum phase transition in an antiferromagnet with the help of microscopic probes such as neutrons. This was the initial motivation for this study but, as we will see later, our work evidenced a totally different kind of quantum phase transition.

Indeed what we have found in $BaCo_2V_2O_8$ is an exotic transition which comes from the competition between the Ising-like anisotropy and a staggered field induced by the uniform field applied perpendicularly to the Ising-axis [Fau+18]. The effect of a staggered field has been investigated in Heisenberg chains [Ken+05; Koh+01; OA97] and it has been shown that such systems, as anisotropic spin-chains, can be mapped onto the celebrated sine-Gordon model which plays a central role in quantum field theory [Raj82]. In our case, $BaCo_2V_2O_8$ presents these two ingredients and we have shown that this system under a transverse magnetic field can be mapped onto the so called "double" sine-Gordon model [GS88; LGN02], describing a topological quantum phase transition driven by the competition between two dual topological excitations.

4.3 State of the art and Hamiltonian of the system

4.3.1 $H-T$ phase diagram of $BaCo_2V_2O_8$ in a transverse magnetic field

Macroscopic measurements such as thermal expansion, magnetostriction, thermal conductivity and magnetization were performed and have led to the $H-T$ magnetic phase diagram of $BaCo_2V_2O_8$ for different orientations of a uniform transverse field [Nie+13; Oku+15; Kim+06; Zha+12] (see Fig. 4.1).

Fig. 4.1(a) shows the magnetic phase diagram of $BaCo_2V_2O_8$ with the uniform magnetic field applied along the [100] direction, thus along the a-axis. One can see that the critical temperature decreases by increasing the field and becomes null at the critical field $\mu_0 H_c \simeq 10$ T. The Néel order present in the zero field phase is then suppressed at the quantum phase transition where the system enters into a new phase which was unknown before our study.

Fig. 4.1(b) shows the magnetic phase diagram of $BaCo_2V_2O_8$ with the uniform magnetic field applied along the [110] direction. One can observe that the critical temperature

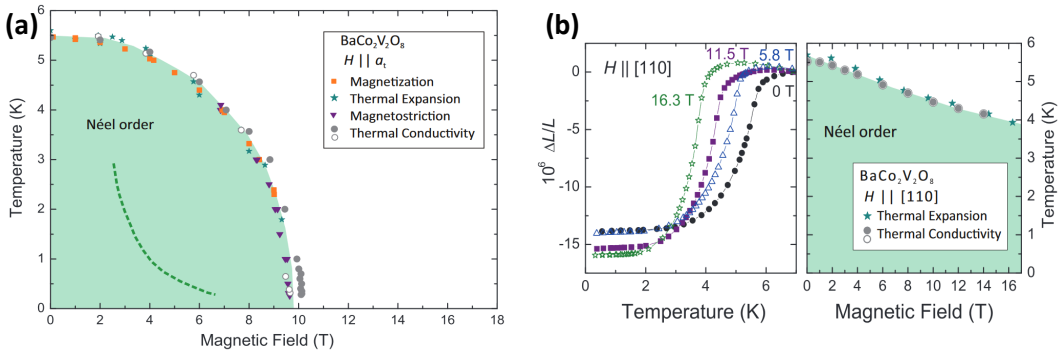

Figure 4.1: $H-T$ **phase diagrams of $BaCo_2V_2O_8$ under a magnetic transverse field obtained by various macroscopic measurements.** (a) Phase diagram for $\vec{H} \parallel \vec{a}$ (or equivalently, $\vec{H} \parallel \vec{b}$). (b) Left: Thermal expansion measured for different values of the magnetic field with $\vec{H} \parallel \vec{a}+\vec{b}$. Right: Phase diagram for $\vec{H} \parallel \vec{a}+\vec{b}$. Those figures were taken from [Nie+13]

is decreasing smoothly while increasing the field.

Kimura et *al*. have shown by high field magnetization measurements [Kim+06] that there are two critical fields for this orientation of the applied field. The first one is observed around $\mu_0 H_{c_1}^{exp} \simeq 30$ T. This is consistent with the theoretical critical field $\mu_0 H_{c_1}^{th} = \frac{\sqrt{J(J/2+1)}}{g_{xx}\mu_B} \simeq 30$ T assumed to correspond to an order-disorder transition [HOA01]. The second one is found at $\mu_0 H_s^{exp} \simeq 40$ T [Kim+06] and is consistent with the theoretical value $\mu_0 H_s^{th} = \frac{J}{2\varepsilon g_{aa}\mu_B} \simeq 40$ T expected for the saturation field of an anisotropic spin-1/2 chain under a transverse field [DKO02].

From those measurements, it is clear that the (a, b) plane is not isotropic, as the orientation of the applied uniform transverse field leads to different magnetic phase diagrams whether it is applied along [100] or along [110]. These considerations raise some interrogations: what is the key ingredient which drives the quantum phase transition occurring at a rather low field in the case of the field parallel to the [100] direction? And what about the nature of the phase transition? Our study, based on neutron scattering experiments and theoretical calculations, is answering these questions.

4.3.2 Induced effective staggered field by a uniform field

By analysing magnetization measurements, Kimura et *al*. developped a model to describe these anisotropic behaviors in the (a, b) plane [Kim+13]. This model is based on the peculiar screw structure of $BaCo_2V_2O_8$ (see Fig. 4.2(a)). Indeed, the magnetization local easy-axes of the Co^{2+} ions are actually tilted away from the chain c-axis by $\simeq 5°$ and rotate by $\simeq 90°$ when moving along the 4-fold c-axis (see Fig. 4.2(b)). This leads to a non-diagonal Landé tensor $\widetilde{g}$ (thus fully anisotropic). It means, in other terms, that now, if a uniform magnetic field is applied along a given direction, it will induce effective fields along other directions, whose nature and orientation depends on the direction of the

applied field. In their paper, Kimura et *al.* proposed the following Hamiltonian [Kim+13]:

$$\mathscr{H} = \mathscr{H}_{XXZ} + \mathscr{H}_{field} \tag{4.1}$$

$$\mathscr{H} = \sum_j J\left[S_j^Z S_{j+1}^Z + \varepsilon(S_j^X S_{j+1}^X + S_j^y S_{j+1}^Y)\right] - \sum_j \mu_B \vec{S_Y}\,\widetilde{g_j}\vec{H} \tag{4.2}$$

where the first term is the Hamiltonian of an anisotropic spin-1/2 chain and the second one corresponds to the Zeeman Hamiltonian describing the interaction between the spins of the system and the applied field. Here the interchain interaction is not taken into account.

By considering the 5° tilt of the easy-axis of magnetization with respect to the 4-fold c-axis and by developing the Zeeman term, they showed that the Hamiltonian takes the form:

$$\begin{aligned}\mathscr{H} = &\sum_j J\left[S_j^Z S_{j+1}^Z + \varepsilon(S_j^X S_{j+1}^X + S_j^Y S_{j+1}^Y)\right] \\ &- \mu_B H \sum_j \left(g_{XX} S_j^X + g_{XZ} S_j^Z \cos\left[\phi_1 + \frac{\pi(j-1)}{2}\right] + g_{XY} S_j^Y \sin[2\phi_1 + \pi(j-1)]\right)\end{aligned} \tag{4.3}$$

where $g_{\alpha\alpha}$ and $g_{\alpha\beta}$ $(\alpha, \beta = X, Y, Z)$ correspond to the diagonal and off diagonal components of the Landé factor $\widetilde{g}$ respectively. Here $\vec{X} \parallel \vec{H}$, $\vec{Z} \parallel \vec{c}$ and $\vec{Y} \perp (\vec{X}, \vec{Z})$. ϕ_1 is an angle defining the direction of the uniform magnetic field in the (a, b) plane: $\phi_1 = 0$ when $H \parallel [110]$ and $\phi_1 = \pi/4$ when $H \parallel [100]$ (equivalently [010]).

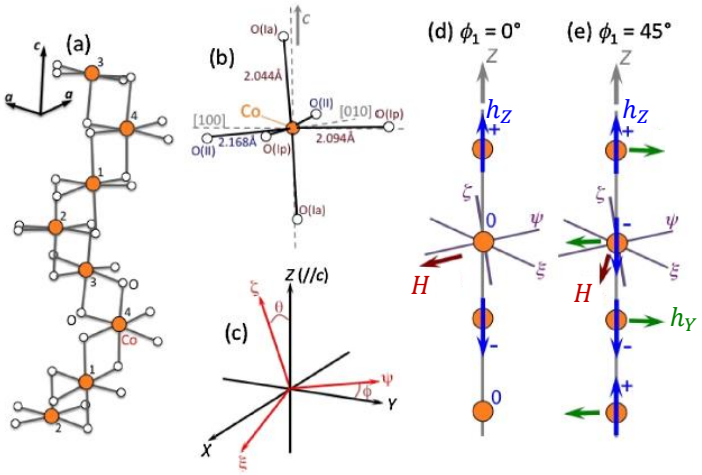

Figure 4.2: **Cristallographic peculiarities of $BaCo_2V_2O_8$ and effective fields induced by a uniform transverse field.** (a) View of the Co-O chain. (b) CoO_6 octahedron. The small 5° tilt of the easy-axis of magnetization with respect to the c-axis can be seen through this picture. (c) $\xi\psi\zeta$ local coordinate system related to the XYZ one used to obtain the Hamiltonian of Eq. (4.3). (d-e) Effective fields induced by the applied (uniform) field: (d) $\vec{h}_Z$ in the case of $\vec{H} \parallel [110]$ ($\phi_1 = 0°$), (e) $\vec{h}_Y$ and $\vec{h}_Z$ in the case $\vec{H} \parallel [100]$ ($\phi_1 = 45°$). Those figures were taken from [Kim+13].

Let us have a look at the Zeeman term of the Hamiltonian for these two particular cases:

$$\mathscr{H}_{field}(\phi_1 = 0) = -\mu_B H \sum_j \left(g_{XX} S_j^X - g_{XZ} S_j^Z \sin\left[\frac{\pi j}{2}\right] \right) \tag{4.4}$$

$$\mathscr{H}_{field}(\phi_1 = \frac{\pi}{4}) = -\mu_B H \sum_j \left(g_{XX} S_j^X + g_{XZ} S_j^Z \cos\left[\frac{\pi j}{2} - \frac{\pi}{4}\right] + g_{XY} S_j^Y (-1)^j \right) \tag{4.5}$$

These two Hamiltonians were used to fit the magnetization measurements for the two orientations of the field and have shown a really good agreement with the experiment [Kim+13]. One can see that applying a uniform field perpendicularly to the c-axis induces an effective field along the c-direction in both cases. However, the nature of this effective field is different depending on the value of ϕ_1. When the uniform field is applied along the [110] direction ([100] direction), the effective field along the Z-axis consists in an "up-zero-down-zero" ("up-down-down-up") configuration (see Figs. 4.2(d),(e)). The most surprising effect arises for the case $\phi_1 = \pi/4$, i.e. $\vec{H} \parallel [100]$ or equivalently $\vec{H} \parallel [010]$. In this case, applying a uniform magnetic field along the b-direction induces an effective staggered field, i.e. an alternate local field, along the a-direction.

4.3.3 Hamiltonian of the system

From now, I will denote $X = b$, $Y = a$ and $Z = c$.

Let us now construct the full Hamiltonian of $BaCo_2V_2O_8$ under a uniform transverse field applied along the b-axis. The interchain interaction is present in the Hamiltonian which accounts for the spinon-confinement (while this term is not relevant for macroscopic measurements, it will be useful for the numerical calculations of the spin-dynamics in $BaCo_2V_2O_8$ as we will see later). Thus, the Hamiltonian takes the following form [1]:

$$\mathscr{H} = \underbrace{\sum_j J[S_j^c S_{j+1}^c + \frac{\varepsilon}{2}(S_j^+ S_{j+1}^- + S_j^- S_{j+1}^+)]}_{1} - \underbrace{\sum_j J' < S_j^c > S_j^c}_{2} - \underbrace{\mu_B H g_{bb} \sum_j S_j^b}_{3}$$
$$- \underbrace{\mu_B H g_{ba} \sum_j S_j^a (-1)^j}_{4} - \underbrace{\mu_B H g_{bc} \sum_j \cos\left[\frac{\pi j}{2} - \frac{\pi}{4}\right] S_j^c}_{5}$$

with:

1 : XXZ Hamiltonian.

2 : interchain interaction treated in mean field theory.

3 : Zeeman Hamiltonian of the uniform field $\vec{H}$ along the b-axis.

4 : Zeeman Hamiltonian of the induced effective staggered field $\vec{h}_a$ along the a-axis.

5 : Zeeman Hamiltonian of the induced effective field "up-down-down-up" $\vec{h}_c$ along the c-axis.

(4.6)

[1] The Hamiltonian for this system under a field applied along the $\vec{a} + \vec{b}$ direction (i.e. the [110] direction) would be: $\mathscr{H} = \sum_j J[S_j^c S_{j+1}^c + \frac{\varepsilon}{2}(S_j^+ S_{j+1}^- + S_j^- S_{j+1}^+)] - \sum_j J' < S_j^c > S_j^c - \mu_B H g_{bb} \sum_j S_j^b + \mu_B H g_{bc} \sum_j \sin\left[\frac{\pi j}{2}\right] S_j^c$. In this case, no field is induced along a.

In their paper, Kimura et *al*. have proposed the following parameters [Kim+13]: $g_{bb} = 2.75$, $g_{ba}/g_{bb} = 0.4$ and $g_{bc}/g_{bb} = 0.14$ for $\phi_1 = \pi/4$. In our study, g_{bb} was chosen slightly smaller, equal to 2.35, while the parameters of Kimura were used for g_{ba}/g_{bb} and g_{bc}/g_{bb}. This choice of parameters was done in order to reproduce the measured critical field occurring at $\mu_0 H_c \simeq 10$ T (while the one found in the study of Kimura was a bit lower and thus led to a larger Landé value g_{bb}). One important thing that one has to keep in mind is that the staggered field along $\vec{a}$ is directly proportional to the uniform field applied along the b-axis.

To summarize, the application of a uniform magnetic field along the b-axis induces a staggered field along the a-axis and an effective field with an "up-down-down-up" configuration along the c-axis. While the latter is not relevant in our study as we will see in the following, the former is the key ingredient which drives the quantum phase transition occuring at $\mu_0 H_c \simeq 10$ T. To better understand this transition, we have performed both neutron diffraction and inelastic neutron scattering experiments to probe the ground-state and the excitations evolution when increasing the applied transverse field.

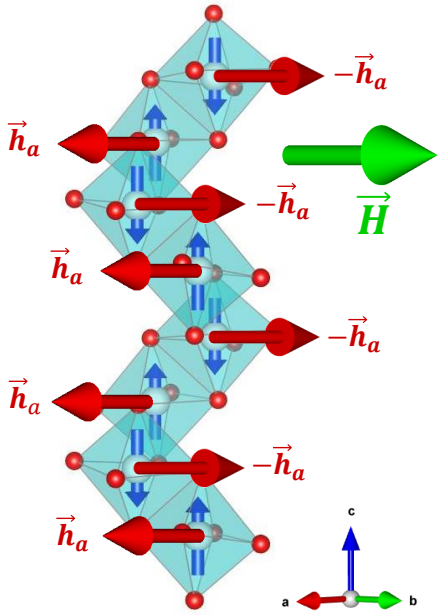

Figure 4.3: **Sketch of the effective staggered field induced by a transverse uniform field in $BaCo_2V_2O_8$.** Effective staggered field $\vec{h}_a$ (red arrows) along the a-axis induced by a uniform magnetic field $\vec{H}$ applied along the b-axis. The effective fields along the c-axis are not shown as they are not relevant in our study.

4.4 Diffraction study: probing the high-field phase

4.4.1 Experimental details

The magnetic structure of $BaCo_2V_2O_8$ under a transverse magnetic field was probed by using the CEA-CRG D23 single-crystal two-axis diffractometer at ILL [D23]. The sample was previously aligned with the b-axis vertical on the Laue diffractometer OrientExpress at

ILL and was installed on D23 in a 12 T vertical field cryomagnet. A maximum transverse magnetic field of 12 T ($\vec{H} \parallel \vec{b}$) could be reached with a base temperature of 1.5 K. An incident wavelength of 1.28 Å was used, from a copper monochromator, thus allowing us to measure $h0l$ and $h1l$ Bragg peaks with a maximum value of 17 for h and 11 for l.

4.4.2 Evolution of the magnetic structure

4.4.2.1 Magnetic Bragg peaks above the phase transition

The first step in this experiment was to probe magnetic Bragg peaks in the high field phase. As I will explain in more details a bit later, if we make the hypothesis that the magnetic moments are aligned antiferromagnetically along the staggered field induced along $\vec{a}$ above the phase transition, the propagation vector is then theoretically predicted to be $\vec{k'} = (0, 0, 0)$ with the condition $h + k + l$ even, therefore different from the one in the Néel phase $\vec{k} = (1, 0, 0)$. Indeed because $BaCo_2V_2O_8$ is body-centered, two chains in diagonal correspond to each other through the translation $(1/2, 1/2, 1/2)$. The staggered field originates from the tilt between the c-axis and the local easy-axis of magnetization and thus is associated to the symmetry of the nuclear structure. In other words, it means that the staggered field $\vec{h}_a$ for the atom of Co in position (x, y, z) must be the same than for the one in position $(x + 1/2, y + 1/2, z + 1/2)$ and thus these two Co atoms must have parallel magnetic moments. This means that the magnetic Bragg peaks above $\mu_0 H_c$ must appear on nuclear Bragg reflections (with the condition $h + k + l$ even). Because these reflections are magnetic, they should also appear on forbidden nuclear Bragg reflections [2] as some of the symmetries leading to the extinction of the nuclear Bragg peaks are not preserved for the magnetic structure [3].

Because the intensity of the magnetic Bragg peaks in the high field phase is actually much lower than the one of the nuclear ones, we have searched such magnetic reflections above $\mu_0 H_c$ by doing ω-scans on forbidden positions for different values of the magnetic field. Fig. 4.4 shows examples of such rocking curves for two magnetic reflections $\bar{2}\,1\,0$ and $3\,0\,3$ associated to the known magnetic structure in the zero-field phase and to the assumed magnetic structure in the high field phase above the transition respectively. One can see on Fig. 4.4(a) that the intensity of the magnetic Bragg peak associated to the zero-field structure is decreasing from $\mu_0 H = 0$ to 6 T and becomes null above the phase transition occurring at $\mu_0 H_c = 10$ T. On the other hand, the intensity of the magnetic Bragg peak $3\,0\,3$ is almost null at zero-field (thus consistent with the fact that this corresponds to a forbidden nuclear reflection) and increases progressively with increasing the field, already before the phase transition, to reach a maximum at $\mu_0 H = 12$ T.

Let me explain in more details this change of the propagation vector. If the magnetic moments are antiferromagnetically aligned along the staggered field induced along $\vec{a}$, thus the interchain interaction between two chains in diagonal is FM instead of AF. As $BaCo_2V_2O_8$ is body centered, we have the following formula for the magnetic structure factor per unit cell $\vec{F}_M(\vec{Q})$:

$$\vec{F}_M(\vec{Q}) = pf(\vec{Q}) \sum_{j=1}^{N/2} \left[\vec{\mathcal{M}}_{1,j}^{\vec{k}} + \vec{\mathcal{M}}_{2,j}^{\vec{k}} e^{i\pi(h+k+l)} \right] e^{2i\pi(hx_j + ky_j + lz_j)} \tag{4.7}$$

[2] i.e. nuclear reflections allowed by the I centering of the lattice but forbidden either by a glide plane of the space group or by the screw axis 4_1

[3] In other word, the magnetic space group is a subgroup of the nuclear one and has thus less symmetries

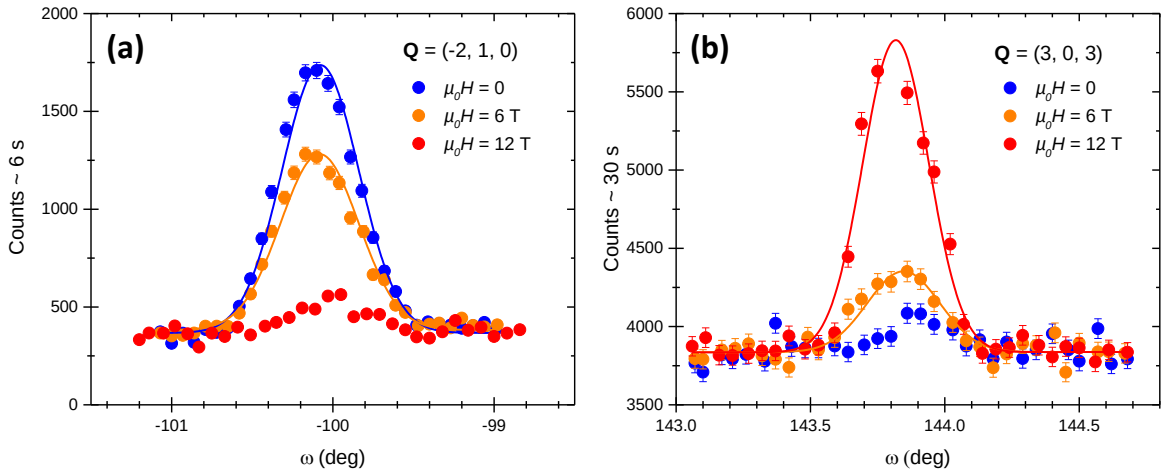

Figure 4.4: **Field evolution of magnetic reflections.** Rocking curves of: (a) the magnetic reflection $\bar{2}\,1\,0$ relative to the zero-field phase for the three magnetic field $\mu_0 H =$ 0, 6 T and 12 T. (b) the magnetic reflection $3\,0\,3$ associated to the high field phase for the same three magnetic field values. Solid lines are Gaussian fits.

with $f(\vec{Q})$ the magnetic form factor of the Co^{2+} ions, N the number of Co atoms in a unit cell ($N = 16$), $\vec{\mathcal{M}}^{\vec{k}}_{1,j}$ the Fourier component of the magnetic moment carried by the Co atom at the (x_j, y_j, z_j) position and $\vec{\mathcal{M}}^{\vec{k}}_{2,j}$ the one carried by the Co atom at $(x_j + 1/2, y_j + 1/2, z_j + 1/2)$. Here the Debye-Waller factors are not taken into account for more clarity. Now let us consider the two cases:

- $\vec{\mathcal{M}}^{\vec{k}}_{1,j} = -\vec{\mathcal{M}}^{\vec{k}}_{2,j} \Rightarrow \vec{F}_M(\vec{Q}) \neq \vec{0}$ if $h + k + l = 2n + 1$ with n an integer
- $\vec{\mathcal{M}}^{\vec{k}}_{1,j} = \vec{\mathcal{M}}^{\vec{k}}_{2,j} \Rightarrow \vec{F}_M(\vec{Q}) \neq \vec{0}$ if $h + k + l = 2n$

Thus if the magnetic coupling between the two Cobalt atoms corresponding by the body-centering translation $(1/2, 1/2, 1/2)$ is AF (first case) it leads to the propagation vector $\vec{k} = (1, 0, 0)$ or equivalently $\vec{k} = (0, 1, 0)$ [4] which corresponds to the one in the zero-field phase. If now the magnetic coupling is ferromagnetic (second case), it leads to a propagation vector $\vec{k}' = (0, 0, 0)$.

Now let us turn to the refinement of the magnetic structure in the high field phase.

4.4.2.2 Refined magnetic structures

At $\mu_0 H = 0$, 288 nuclear reflections, allowed in the $I4_1/acd$ space group of $BaCo_2V_2O_8$, reducing to 149 independent ones, were collected at $T = 1.5$ K by performing rocking curves (see exemples in Fig. 4.4). From the measured integrated intensities, the nuclear structure was then refined using the Fullprof software [Rod93] in order to determine the necessary information for the magnetic structure refinement (i.e. the scale factor, the coordinates and Debye-Waller factor of Co, the extinction parameters, and the $\lambda/2$ ratio).

[4] This labeling of the propagation vector (instead of $\vec{k} = (0, 0, 1)$) comes from the fact that $a > c$ [Ros87].

The calculated intensities I_{calc} plotted in Fig. 4.5(a) as a function of the observed ones I_{obs} emphasize the quality of the fit. 103 magnetic reflections, associated to the $\vec{k} = (1, 0, 0)$ propagation vector and reducing to 48 independent ones, were then collected. Let us remind that they correspond to reflections $h\,k\,l$ with $h + k + l = 2n + 1$, that is, to Bragg positions for which the nuclear intensity is always null because of the body-centering of the crystallographic structure. The same magnetic structure as in Canévet *et al.* [Can+13] was found, with a staggered moment $m_c = 2.184(8)\ \mu_B/Co^{2+}$ (see Fig. 4.5(b) for the plot of I_{calc} vs I_{obs}). As mentioned above, $\vec{k} = (1, 0, 0)$ implies an AF coupling in the diagonal $a \pm b$ direction, that is between two chains of the same nature (both described by a 4_1 screw axis, plotted in red in Fig. 4.6, or by a 4_3 screw axis, plotted in blue). Consequently, the magnetic structure presents an AF coupling along $\vec{a}$ and a FM one along $\vec{b}$ (see top left panel of Fig. 4.6) while it is the reverse in the second magnetic domain, i.e. an AF coupling along $\vec{b}$ and a FM one along $\vec{a}$ (see Fig. 1.16).

The same nuclear reflections were then collected at $\mu_0 H = 12\ \text{T} > \mu_0 H_c$, yielding the same crystallographic structure as in zero-field with comparable agreement factors. 48 magnetic reflections, with a new propagation vector $\vec{k}' = (0, 0, 0)$, were then collected, reducing to 30 independent ones. This set of measured reflections corresponds to pure magnetic reflections associated to the AF component of the magnetic moments [5]. Nevertheless, some of them were not strictly null at zero-field because of the presence of a sizable $\lambda/2$ and/or mostly because of small defects in the crystal. As a result, they had to be collected in both phases and the difference between the $\mu_0 H = 12$ T collect and the $\mu_0 H = 0$ one was then used for the magnetic refinement. For this reason and because of the small magnetic signal, a counting rate of 30 seconds per point was used. The magnetic structure refinement was then performed, yielding the anticipated magnetic structure with a staggered magnetic moment $m_a = 0.91(2)\ \mu_B/Co^{2+}$ (see Figs 4.5(e,f) for the I_{calc} vs I_{obs} plots of the nuclear and magnetic refinements at 12 T). As said before the propagation vector of the high field magnetic structure, $\vec{k}' = (0, 0, 0)$ implies a FM coupling in the diagonal $a \pm b$ direction (see top right panel of Fig. 4.6). Consequently, an AF coupling both along $\vec{a}$ and along $\vec{b}$ now occurs, thus lifting some frustration and yielding a single magnetic domain (see right pannels of Fig. 4.6). It is worth noting that, in principle, the effective field along $\vec{c}$ also induces a magnetic component along c. As we will see later, the numerical calculations yield a component of 0.04 μ_B at $\mu_0 H = 12$ T and thus this value is too small to be refined. This effective field has consequently no relevant role in the phase transition (it has been also confirmed by numerical calculations).

Finally, the magnetic structure at intermediate field $\mu_0 H = 6\,\text{T} = 0.6\,\mu_0 H_c$ consists in a superposition of the $\vec{k} = (1, 0, 0)$ and $\vec{k}' = (0, 0, 0)$ phases, as shown by the rocking curves at 6 T in Figs. 4.4(a-b) and further evidenced by the field dependencies plotted in Fig. 4.7 in the next section. The same magnetic reflections as for $\mu_0 H = 0$ and $\mu_0 H = 12$ T were collected, with respective counting rates of 6 and 30 seconds. Here again, the difference with the zero-field phase was used for the second set of reflections. The results of the magnetic refinement is shown for both contributions (see Figs 4.5(c,d)). The following values of the staggered components were found: $m_c = 1.916(7)\ \mu_B/Co^{2+}$ for the zero-field contribution and $m_a = 0.44(2)\ \mu_B/Co^{2+}$ for the high field one. The very small value of the latter component, in addition to the data treatment that had to be applied (difference

[5] There is also a FM component rising on the allowed nuclear reflections.

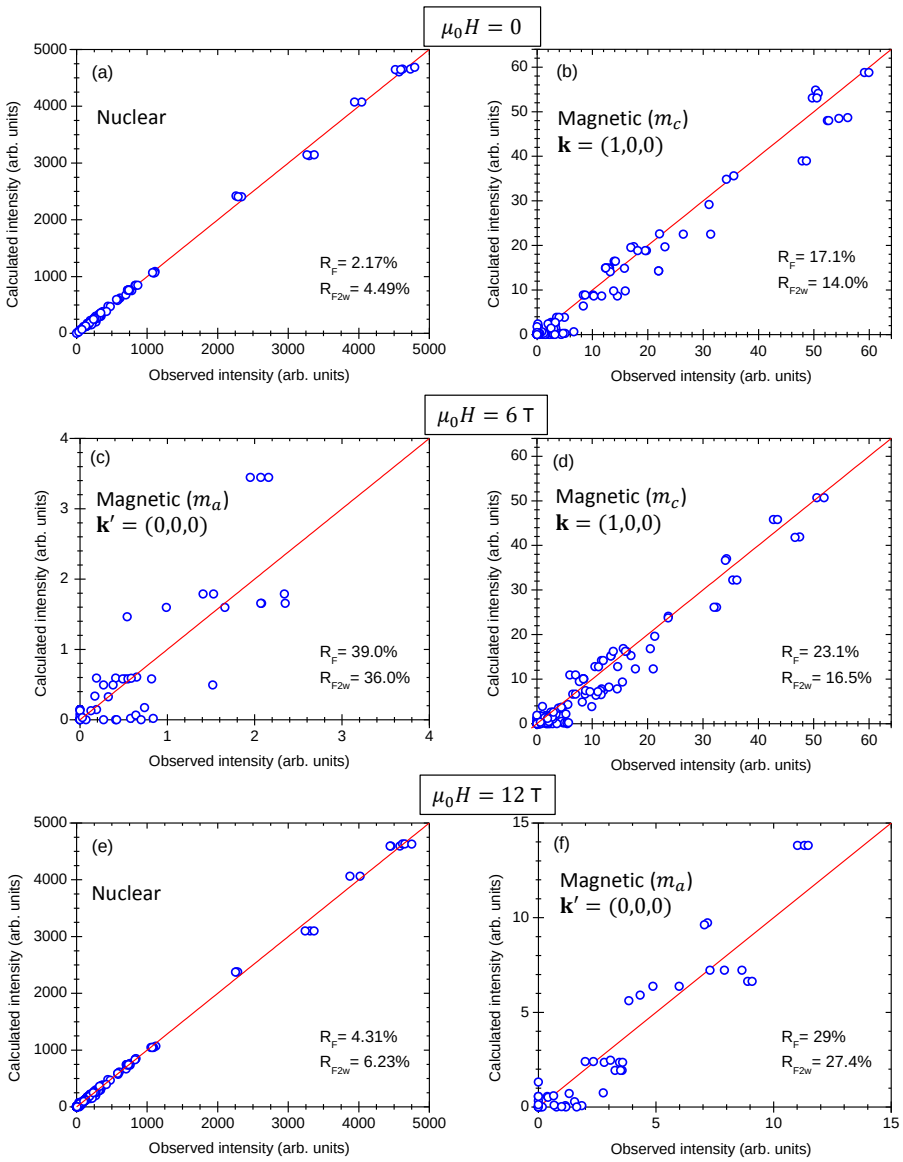

Figure 4.5: **Single-crystal diffraction data at 1.5 K, presented as calculated versus observed reflections intensities:** (a) Nuclear structure refinement in zero field. (b) Magnetic structure refinement in zero field with the moments oriented along $\vec{c}$ $[\vec{k} = (1,0,0)]$. (c) and (d) Magnetic structure refinement at 6 T for the component of the moments along $\vec{a}$ $[\vec{k}' = (0,0,0)]$ and along $\vec{c}$ $[\vec{k} = (1,0,0)]$, respectively. (e) Nuclear structure refinement at 12 T. (f) Magnetic structure refinement at 12 T with the magnetic moments oriented along $\vec{a}$ $[\vec{k}' = (0,0,0)]$. The agreement factors are reported on the figures.

with the zero-field data) explains the poorness of the fit. The non collinearity of the 6 T structure comes from the fact that it is a double $\vec{k}$ magnetic structure. It can be simply understood by comparing the exchange couplings along $\vec{a}$ and $\vec{b}$ in the zero field structure (one is AF the other one is FM) to those in the high field phase (both are AF): As a result, half of the spins rotate clockwise and the other half anti-clockwise (see middle panels of Fig. 4.6). In the former, the interchain magnetic arrangement is due

to the interchain interactions, while in the latter it is constrained by the staggered field [SO04]. This subtle modification points out the role of the staggered field, which forces a magnetic structure that competes with the interchain interactions. Indeed, this evolution of the staggered moment orientation from the Ising c-axis to the a-axis originates from an energetic compromise, between on the one hand the intrachain AF exchange interaction, and on the other hand the Zeeman energy gain due to the effective transverse fields, that overcomes the anisotropy and the interchain energy [SO04; Fau+18].

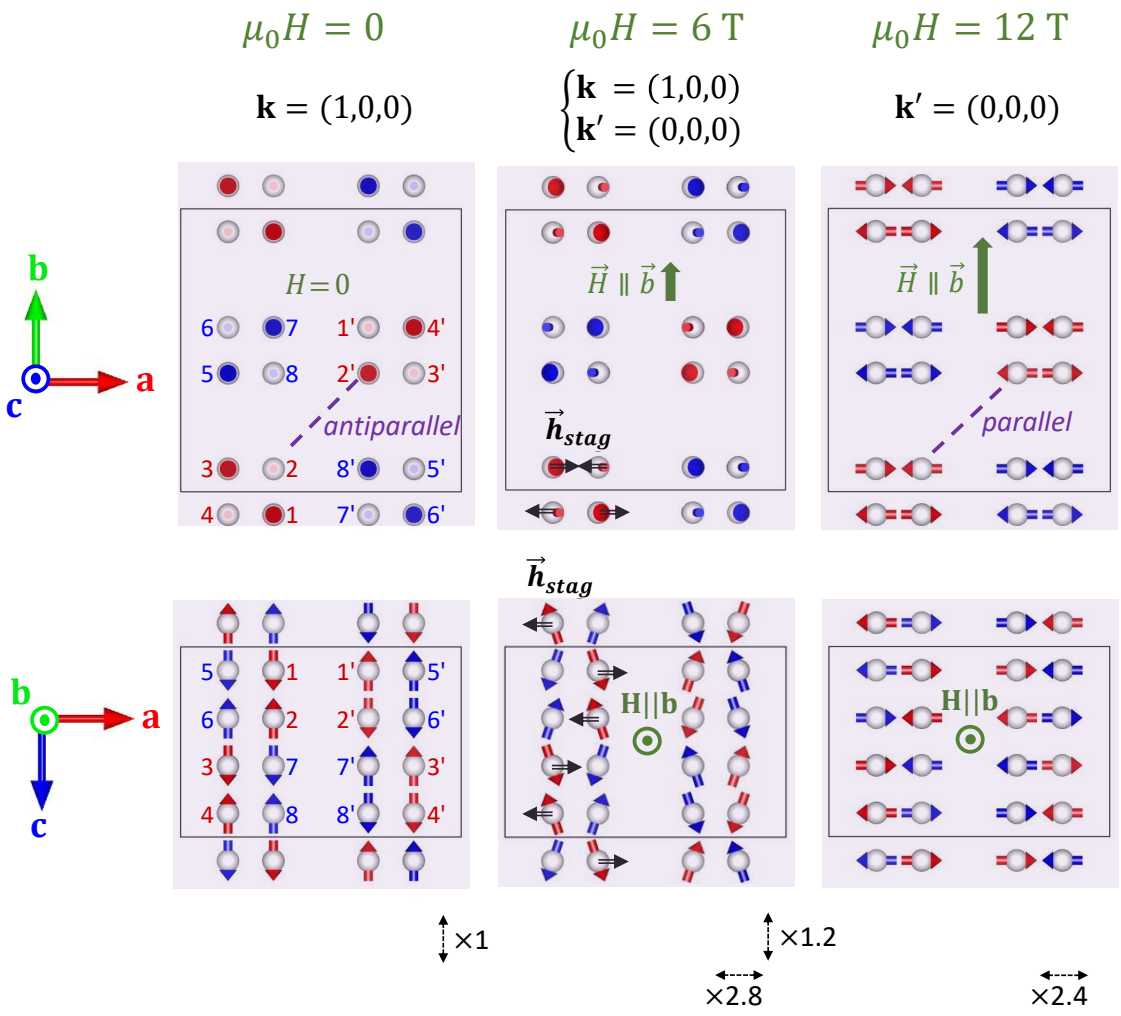

Figure 4.6: **Evolution of the magnetic structure under a uniform transverse field.** Magnetic structures of $BaCo_2V_2O_8$ for $\vec{H} \parallel \vec{b}$ shown in the (a, b) plane (top) and in the (a, c) plane (bottom) at 0, 6, and 12 T, obtained from the structure refinement described in the main text. The two kinds of chains are plotted in red and blue, respectively, and the Co atoms are numbered in the zero-field panels, like in Ref. [Can+13]. For a better visualization, the amplitude of the magnetic moments was multiplied along the a and c axes by the values indicated below the figures. The staggered field $\vec{h}_{\text{stag}}$ is represented with black arrows, only in the panels corresponding to the 6 T magnetic structure for one chain.

To summarize, with increasing H, the magnetic moments remain staggered but progressively rotate in the $(\vec{a},\vec{c})$ plane, from the Ising $c-$axis to the $a-$axis. Because the two magnetic structures at zero-field and above the phase transition at $\mu_0 H_c = 10$ T have not the same propagation vector ($\vec{k} = (1,0,0)$ and $\vec{k}' = (0,0,0)$ respectively), we were able to follow independently the magnetic field dependence of the staggered magnetizations m_a and m_c.

4.4.3 Field dependence of the staggered magnetizations

m_c and m_a have been then probed while increasing the field by counting at the top of the two magnetic reflections $\bar{2}\,0\,1$ and $3\,0\,3$, relative to both structures. Indeed, the observed intensities $\mathrm{I}(H)_{\bar{2}01}$ and $\mathrm{I}(H)_{303}$ are directly proportional to $|m_c|^2$ and $|m_a|^2$ respectively. By knowing the refined value of $|m_c|$ at zero-field and the one of $|m_a|$ at $\mu_0 H \simeq 12$ T, and by applying the following formula $m_c(H) = m_c(0)\sqrt{\frac{I(H)_{\bar{2}01}}{I(0)_{\bar{2}01}}}$ and $m_a(H) = m_a(12\text{ T})\sqrt{\frac{\mathrm{I(H)}_{303}}{\mathrm{I(12\ T)}_{303}}}$, we were able to extract the field dependence of the staggered magnetizations $m_c(H)$ and $m_a(H)$ of the ordered magnetic moments as shown in Fig. 4.7.

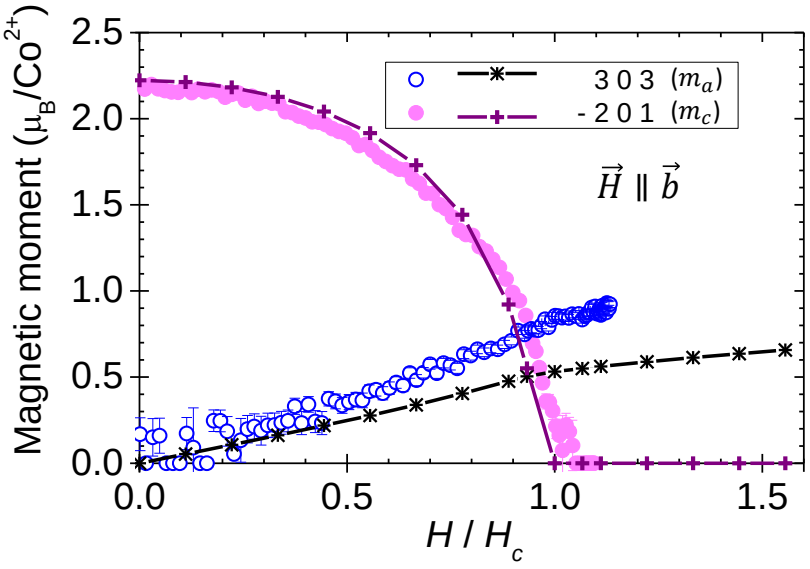

Figure 4.7: **Field dependence of the staggered magnetic moments** of the two competing magnetic phases determined at 1.5 K from the square root of the intensity of the $\bar{2}\,1\,0$ and $3\,0\,3$ pure magnetic reflections for the low and high field phases respectively (pink and blue circles). These experimental staggered moments m_c and m_a are compared to the ones calculated by numerical iTEBD calculations described in subsection 4.6.2 (purple and black crosses connected by solid lines).

From this figure, one can see that m_c decreases with increasing the field and vanishes at the transition. Moreover it shows a conventional behavior for an order parameter which is the staggered magnetization in our case. On the other hand, m_a increases as soon as $H \geq 0$.

Finally one can see that the iTEBD calculations that I will detail later reproduce quite well the observed data. However a global scaling factor seems to exist for the staggered magnetization m_a that will be explained later (see paragraph 4.6.2.2).

4.4.4 Nature of the high-field phase

The peculiar nature of the high field phase at $\mu_0 H = 12$ T is further illustrated in Fig. 4.8(a). It shows the measured temperature dependence of the staggered order parameter (m_a) compared to the uniform ferromagnetic component ($M_\parallel$) induced along $\vec{b}$ by the external uniform field. These measurements were performed at $\mu_0 H = 12$ T by following, while increasing the temperature, the neutron counts on top of the magnetic Bragg peaks 1 0 1 and $\bar{1}\,1\,\bar{2}$, which are proportional to $|m_a|^2$ and $|M_\parallel|^2$ respectively.

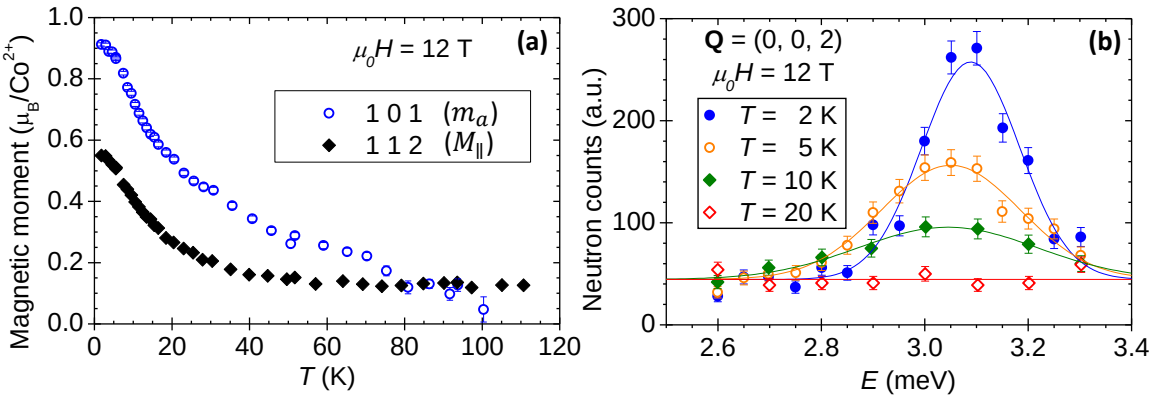

Figure 4.8: **Nature of the high field phase.** (a) Temperature dependence at $\mu_0 H = 12$ T of the AF (m_a) and FM ($M_\parallel$) components of the high field phase, obtained from the square root of the intensity of the 1 0 1 and 1 1 2 reflections, respectively. (b) Temperature dependence of the lowest energy magnetic excitation at a zone center position and at $\mu_0 H = 12$ T, measured on the IN12 three-axis spectrometer. The solid lines are Gaussian fits.

In contrast with the usual abrupt drop of the order parameter expected when the temperature becomes larger than the interactions between the magnetic moments (see for instance Fig. 6 of reference [Can+13]), m_a decreases smoothly up to high temperature. m_a is thus induced by the staggered magnetic field $\vec{h_a}$ as $M_\parallel$ is induced by the uniform magnetic field $\vec{H}$. The intrachain interaction J is still effective in the high field phase, and gives rise to well-defined excitations as shown in Fig. 4.8(b). Note that these excitations disappear between 10 and 20 K when the intrachain interactions are no more effective, and thus at a much lower temperature than the staggered magnetization.

To conclude on this diffraction study, while, in addition to the AF intrachain interaction present in the complete field range, the interchain interaction stabilizes the magnetic structure at zero-field, the staggered field along the a-axis induced by the external uniform magnetic field along $\vec{b}$ stabilizes the high field magnetic order. Well defined excitations are still observed below 10 K at $\mu_0 H = 12$ T but they are actually quite unconventional as described in the next section.

4.5 Spin-dynamics under a transverse magnetic field

The diffraction study helped us to understand the evolution of the ground state under a transverse magnetic field. A way to understand deeper the nature of this quantum phase transition is to study the evolution of the spin-dynamics, i.e. the excitations of the system under the application of such a field. In this section, I will present our study of the magnetic excitations in $BaCo_2V_2O_8$ under a transverse magnetic field by means of inelastic neutron scattering. I will expose our investigation of the field dependence of the excitations both in the Néel phase up to $\mu_0 H_c = 10$ T and above up to $\mu_0 H = 12$ T for different values of the scattering vector $\vec{Q}$. Then I will present the dispersion spectrum parallel to the chain axis in the high-field phase as well as the magnetic field dependence of the dispersion perpendicular to the chain axis between zero-field and $\mu_0 H = 12$ T. I will present in parallel our inelastic neutron scattering experiment using polarized neutrons, and more precisely longitudinal polarimetry analysis (LPA), used to get informations about the polarization of the magnetic excitations (i.e. the directions along which the spin fluctuates).

4.5.1 Experimental details

The unpolarized inelastic neutron scattering (INS) experiment was performed on the cold-neutron ThALES triple-axis spectrometer at Institut Laue Langevin (ILL), using a vertical cryomagnet, allowing to apply magnetic fields up to 12 T. Prior to the INS experiment, the $BaCo_2V_2O_8$ crystal was first aligned with the b-axis vertical using the triple-axis spectrometer IN3 at ILL. Once the sample glued, the alignment was checked to be better than 1° on the neutron Laue diffractometer OrientExpress at ILL. The magnetic field was applied on ThALES perpendicularly to the (a^*, c^*) scattering plane. A series of energy scans at constant scattering vector $\vec{Q}$ and different magnetic fields was measured in the Néel phase and in the phase above the transition. All the data were measured at a fixed final wave vector of 1.3 $Å^{-1}$ and at the temperature of 1.8 K. The resolution in energy was around 0.15 meV.

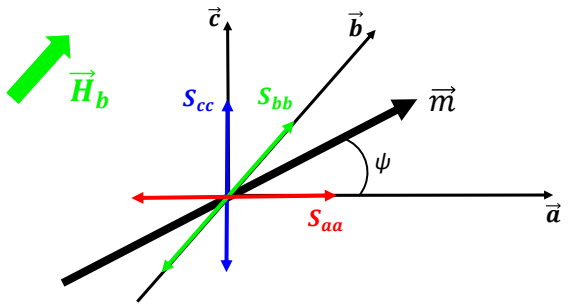

Figure 4.9: **Notations for the fluctuations of the ordered moment.** S_{aa}, S_{bb} and S_{cc} define the fluctuations of the ordered moment $\vec{m}$ along the a, b and c directions respectively, and the angle ψ, the angle between $\vec{m}$ and $\vec{a}$ in the (a, c) plane.

An experiment with longitudinal polarization analysis (LPA) in a vertical magnetic field parallel to the b-axis has also been carried out on the cold neutron IN12 triple-axis

spectrometer. At zero-field, all the moments are along the c-axis, thus parallel (longitudinal $S_{\parallel}$) and perpendicular (transverse $S_{\perp}$) fluctuations to the ordered moment correspond to fluctuations along the c-axis (namely S_{cc}) and along the a and b-axes (namely S_{aa} and S_{bb}), respectively. As we have seen in the previous section, the ordered moments rotate from the c-axis to the a-axis while increasing the field. Thus, it is more convenient to use the notations S_{aa}, S_{bb} and S_{cc} instead of $S_{\parallel}$ and $S_{\perp}$ which is no longer meaningful as $S_{\parallel}$ and $S_{\perp}$ keep rotating in the (a, c) plane and in two different ways for the spins of the two different chains. The S_{aa}, S_{bb} and S_{cc} fluctuations can be probed using LPA as explained below.

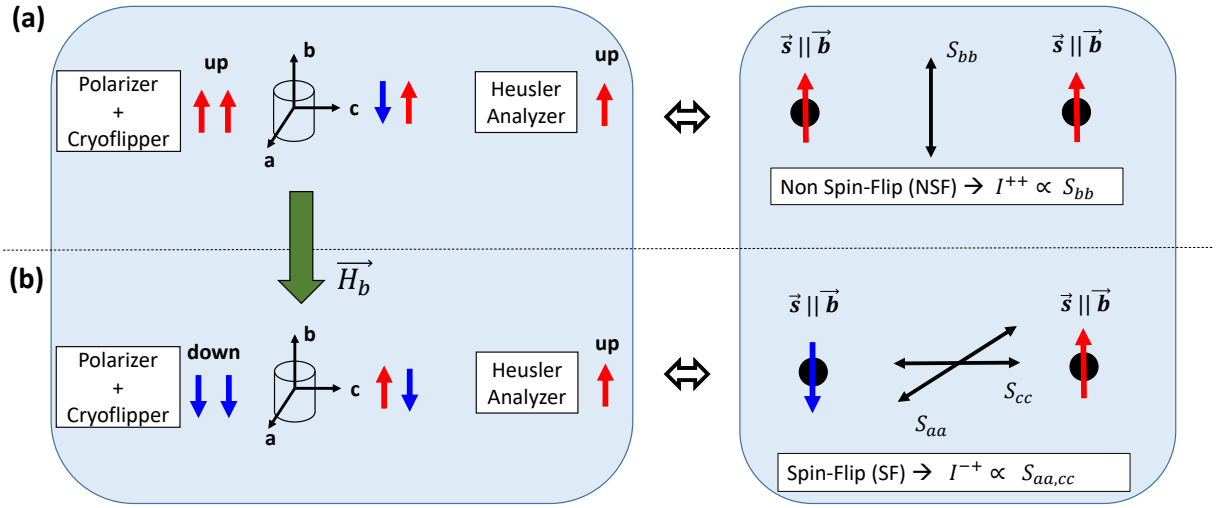

Figure 4.10: **Longitudinal polarization analysis (LPA) on IN12** (a) Non-spin flip channel: The neutrons carrying a spin $\vec{s}$ are polarized along $\vec{b}$ with an up configuration before being scattered by the sample. The fluctuations of the ordered moment along the b-axis, namely S_{bb} do not flip the spin of the neutrons and thus lead to a non spin-flip (NSF) process. The scattered intensities are then analyzed and only the neutrons with an up configuration are scattered by the analyzer. Thus the intensity in the NSF channel I^{++} is proportional to the S_{bb} fluctuations. (b) Spin-flip channel: The neutrons are now still polarized along the b-axis but with a down polarization thanks to the cryoflipper. The fluctuations of the ordered moment perpendicular to the b-axis, namely S_{aa} and S_{cc} flip the spin of the neutrons and thus lead to a spin-flip (SF) process. Thus the intensity in the SF channel I^{-+} is proportional to a combination of S_{aa} and S_{cc} fluctuations, namely $S_{aa,cc}$.

The set-up of the LPA experiment carried out on IN12 (see Fig. 4.10) is the following: the neutron beam is polarized vertically by a cavity transmission polarizer and its initial wavevector is selected by a graphite PG(002) monochromator both located in a vertical magnetic field. The cryoflipper allows to choose either an up $s = 1/2$ or a down $s = -1/2$ configuration for the neutron spins. The vertical magnetic field at the sample position then keeps the spin $\vec{s}$ of the incident neutrons parallel or antiparallel to the b-axis. The scattered intensity is then analyzed using a Heusler analyzer which only scatters the up polarization and thus separates the spin-flip (SF) and non-spin-flip (NSF) contributions, corresponding respectively to processes where the neutron spin has flipped or not. These scattering

processes give information respectively about the spin fluctuations perpendicular to the field direction b, namely $S_{aa,cc}$ (without discriminating between the a and c directions) and parallel to it, namely S_{bb}.

From the equations given in Eq. (2.35), and neglecting the chiral term, we have the following inelastic scattering cross sections for the NSF and SF process:

$$\sigma^{NSF} = \sigma^{++} = \sigma^{--} \propto S_{bb} \tag{4.8}$$

$$\sigma^{SF} = \sigma^{-+} = \sigma^{+-} \propto S_{aa,cc} \propto \cos\theta^2 S_{aa} + \sin\theta^2 S_{cc} \tag{4.9}$$

where $\theta = \widehat{(\vec{Q}, \vec{c})}$. Indeed, when $\vec{Q} \parallel \vec{c}$, and thus $\theta = 0$, only the S_{aa} fluctuations are probed in the SF process because of the geometrical factor of the magnetic cross section. On the other hand, when $\vec{Q} \perp \vec{c}$, and thus $\theta = 90°$, the neutrons only see the S_{cc} fluctuations.

Let us now have a look at the results, and first, the magnetic-field dependence of the excitations.

4.5.2 Magnetic-field dependence of the excitations

4.5.2.1 Unpolarized neutrons on ThALES

To probe the evolution of the excitations under a transverse magnetic field in $BaCo_2V_2O_8$, we have performed energy scans for different values of the magnetic field (with a step of 1 T) and for several scattering vectors $\vec{Q}$: two zone-centers (ZC) $\vec{Q} = (3, 0, 1)$ and $\vec{Q} = (0, 0, 2)$ and one antiferromagnetic point (AF) $\vec{Q} = (2, 0, 1)$ (see examples of scans for $\mu_0 H = 3$ T and 12 T in Figs. 4.11(d-i)). From those energy scans we were able to plot the intensity color maps in Fig. 4.11 (a-c) showing the measured magnetic field evolution of the lowest zero-field energy excitations ($|1\ \mathrm{T}\rangle = |1, S_z = \pm 1\rangle$, $|1\ \mathrm{L}\rangle = |1, S_z = 0\rangle$, $|2\ \mathrm{T}\rangle = |2, S_z = \pm 1\rangle$ and $|2\ \mathrm{L}\rangle = |2, S_z = 0\rangle$) of the Zeeman ladders, as a function of the transverse field $\vec{H} \parallel \vec{b}$. At zero-field, all the moments are aligned along the c-axis and thus the $|j\ T\rangle$ and $|j\ \mathrm{L}\rangle$ modes, which are the j^{th} transverse and longitudinal excitations, correspond to the fluctuations $S_{aa} = S_{bb}$ and S_{cc} respectively. One can see that by increasing H, the zero-field $|1\ \mathrm{T}\rangle = |1, S_z = \pm 1\rangle$ mode, which is a transverse excitation with respect to the zero-field magnetic structure, splits into two branches (see Figs 4.11(a-c)). The energy dependence of these two branches is not linear. The upper branch exhibits an upward variation up to $\mu_0 H = 12$ T while the lower branch decreases down to $\mu_0 H = 10$ T $= \mu_0 H_c$. At this field, this branch reaches its minimum energy before increasing again, as seen e.g. at the AF position $\vec{Q} = (2, 0, 1)$. The softening of the lower branch at $\mu_0 H_c$ thus marks the quantum phase transition, as already observed by Electron Spin Resonance (ESR) [Oku+15] and by a recent neutron scattering experiment done in parallel to our study [Mat+17]. Note that a small energy gap of about 0.2 meV which is due to the interchain coupling is still present at the AF position [TFG18] (see Fig. 4.11(a)) and is larger for the ZC points (see Fig. 4.11(b-c)) [6]. The width of these two modes remains resolution-limited, indicating that they must still be considered as long lived quasiparticles.

I now consider the next excitation, the $|1\ \mathrm{L}\rangle = |1, S_z = 0\rangle$ mode which is longitudinal at zero-field. The energy of this mode is not constant with the field but increases with increasing field up to about 3 T. At this field, an anti-crossing with the lowest branch

[6] iTEBD calculations were done without interchain interaction and led to the closure of the gap.

issued from the zero-field $|2\ \mathrm{T}\rangle = |2, S_z = \pm 1\rangle$ mode occurs (see dashed white lines in Fig. 4.11(a)). As H increases above $\mu_0 H = 3$ T, the lowest of the two hybridized branches broadens while its energy decreases, to finally disappear completely at the critical field.

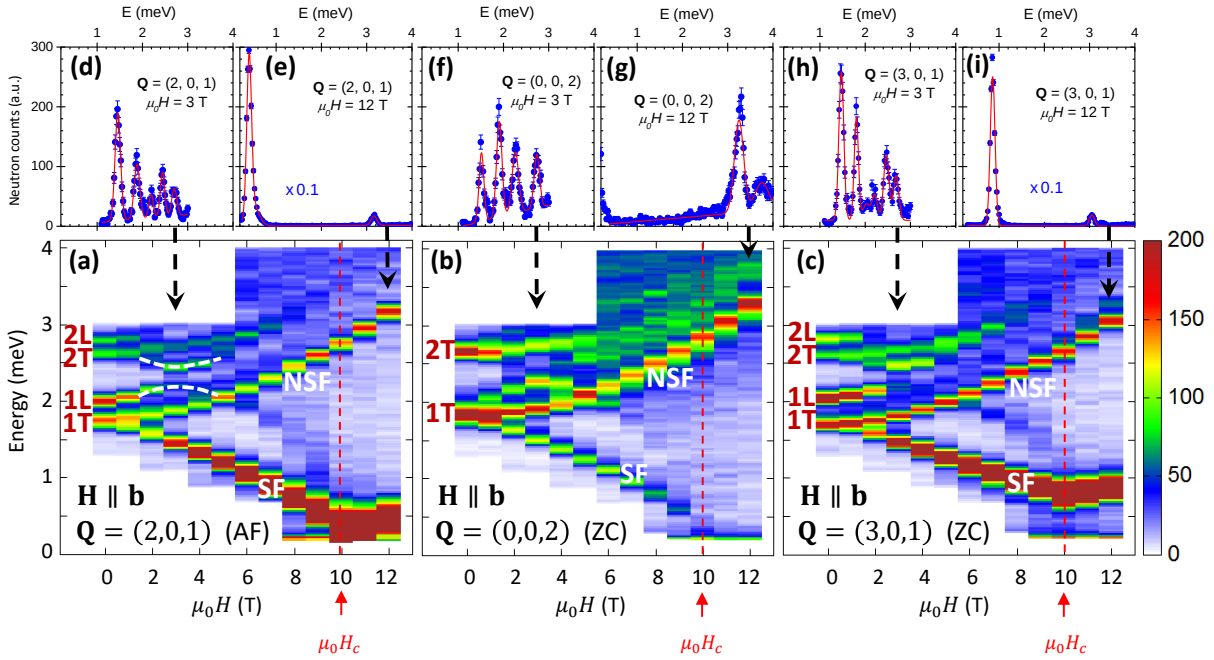

Figure 4.11: **Magnetic excitations in a transverse magnetic field.** (a-c) Experimental intensity color maps showing the field dependence of the magnetic excitations in $BaCo_2V_2O_8$ for a transverse field. Three positions were investigated: AF $\vec{Q} = (2, 0, 1)$ and two ZC $\vec{Q} = (0, 0, 2)$ and $\vec{Q} = (3, 0, 1)$. The polarization at zero field (T or L) of the modes is indicated on the maps. Note that the color scale was truncated to about 10 to 15 times less than the maximum number of counts at high field for $\vec{Q} = (2, 0, 1)$ and $(3, 0, 1)$, for the weak modes to be visible. This gives the false impression that the lowest branch broadens as the field increases. The SF and NSF nature of the modes determined on IN12 using polarized neutrons is indicated. These three maps were obtained from energy scans performed on the ThALES triple-axis spectrometer at $T = 1.5$ K and every 1 T in the Néel phase ($0 \leq \mu_0 H \leq \mu_0 H_c \simeq 10$ T) and in the quantum phase above H_c (critical field at the red dashed line). (d-i) For each of these three scattering vectors, examples of such scans at $\mu_0 H = 3$ T and 12 T are shown above the corresponding map (blue points correspond to experimental data and red lines to fit by Gaussian functions).

This field-dependence of the excitations is very different from the case of an external longitudinal field (parallel to the Ising axis) for which the $|j\ \mathrm{T}\rangle = |j, S_z = \pm 1\rangle$ and $|j\ \mathrm{L}\rangle = |j, S_z = 0\rangle$ excitations remain decoupled. In this, the field produces a Zeeman splitting of the transverse excitations (linear field dependence) and has no effect on the longitudinal ones whose energy thus remains constant. This is indeed what is observed by ESR [Kim+07] and inelastic neutron scattering in $BaCo_2V_2O_8$ as we will see in the next chapter. The transverse field, on the other hand, allows the spinons to hop by one site and the $S_z = \pm 1$ and $S_z = 0$ sectors are no more independent. As a result, the field creates

a quantum overlap between the zero-field $|j\ \mathrm{T}\rangle = |j, S_z = \pm 1\rangle$ and $|j\ \mathrm{L}\rangle = |j, S_z = 0\rangle$ excitations. This hybridization process produces non-linearities to second order in H. Another way to say this is: as the magnetic field is applied perpendicularly to the axis of quantization, it leads to a mixing of the wavefunctions and thus to a non-linearity of the energy modes. In the present case, there are two kinds of transverse fields, the uniform one along $\vec{b}$ and the staggered one along $\vec{a}$. As we will see, the latter plays a crucial role since it produces the rapid decrease of the lower branch towards the critical field compared to almost no field dependence in its absence.

Another interesting feature is the field dependence of the intensity of the two branches arising from the splitting of the $|1\ \mathrm{T}\rangle$ mode. Indeed the lowest energy branch displays a drastically different spectral weight evolution for the equivalent ZC $(0, 0, 2)$ and $(3, 0, 1)$ positions (see Figs 4.11(b, c)). In the latter case, it gets more intense as the critical field is approached, while in the former case, it progressively vanishes. On the other hand, the upper branch has an intensity which remains almost constant with increasing the field (see Fig. 4.11(a, b, c)). To understand this behavior, we have studied the polarization of the modes.

4.5.2.2 Polarization of the excitations on IN12

To probe the polarization of the fluctuations, we have used LPA on IN12 as described in Fig. 4.10. As explained above, this allows us to discriminate the S_{bb} fluctuations (NSF channel) from the $S_{aa,cc}$ ones (SF channel). Let us recall that in addition, a geometrical term enters the scattering cross section, reflecting the fact that only spin fluctuations perpendicular to the scattering vector $\vec{Q}$ contribute to the intensity. This argument helps us to discriminate the a component from the c one in the SF channel. Indeed, as in the zero-field case, the inelastic unpolarized neutron cross section in the case of $\vec{Q} = (0, 0, 2)$ is only proportional to a combination of S_{aa} and S_{bb} while it implies the three components S_{aa}, S_{bb} and S_{cc} for the case of $\vec{Q} = (3, 0, 1)$. Let us summarize these two conditions, i.e. the longitudinal polarization analysis plus the geometrical factor in terms of scattering cross section for a better understanding:

- For $\vec{Q} = (0, 0, 2)$:
  - $\sigma^{SF} \propto S_{aa}$
  - $\sigma^{NSF} \propto S_{bb}$
- For $\vec{Q} = (3, 0, 1)$
  - $\sigma^{SF} \propto S_{aa,cc} \propto \cos^2\theta_{(3,0,1)} S_{aa} + \sin^2\theta_{(3,0,1)} S_{cc} \simeq 0.2 S_{aa} + 0.8 S_{cc}$
  - $\sigma^{NSF} \propto S_{bb}$

where $\theta_{(3,0,1)} \simeq 63.8°$, the angle between $\vec{Q} = (3, 0, 1)$ and the c-axis.

Fig. 4.12 shows energy-scans for both SF and NSF channels for different values of the magnetic field and for the two scattering vectors $\vec{Q}$ mentioned above. Let us focus first on the splitting of the $|1\ \mathrm{T}\rangle$ zero-field excitation spotted in Fig. 4.12(c). At $\mu_0 H = 1.5$ T the splitting of this mode is already observable (branch in blue at $E \simeq 1.65$ meV and branch in red at $E \simeq 1.80$ meV in Fig. 4.12(c),(f)). While increasing the field, the NSF excitation, corresponding to S_{bb} fluctuations (in red) increases in energy (see Fig. 4.12(b-c),(e-f)) and thus this peak corresponds to the upper branch of the splitting. At $\mu_0 H = 9$ T, its

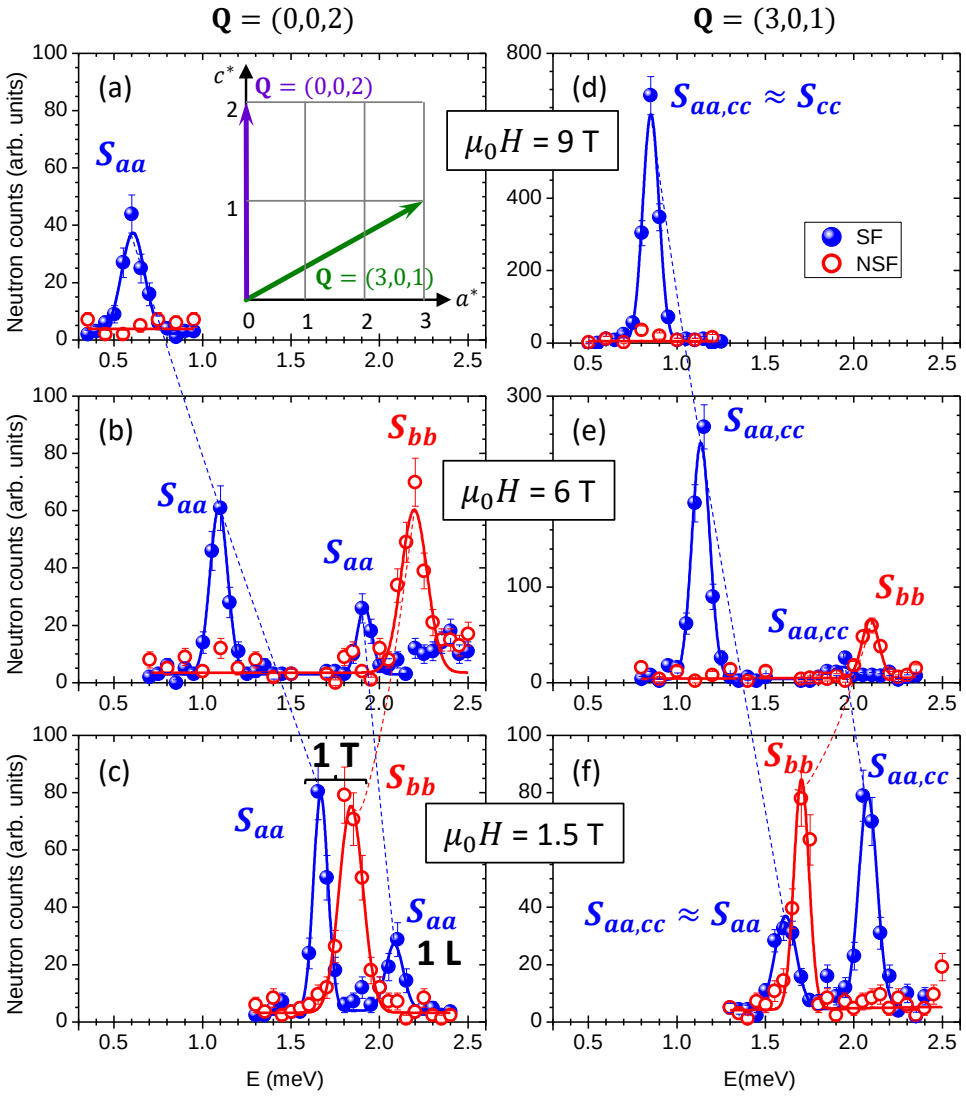

Figure 4.12: **Polarization of the excitations using LPA on IN12.** Energy scans measured in $BaCo_2V_2O_8$ at T = 1.5 K on IN12 using polarized neutrons (open and closed symbols) fitted to Gaussian functions (solid lines), for (a-c) $\vec{Q}$ = (0, 0, 2) and (d-f) $\vec{Q}$ = (3, 0, 1), in the non spin-flip (NSF) and spin-flip (SF) channels. These data were obtained for three different values of an applied transverse magnetic field $\vec{H} \parallel \vec{b}$: $\mu_0 H$ = 1.5 T (lower panels), $\mu_0 H$ = 6 T (central panels), $\mu_0 H$ = 9 T (upper panels). The dashed lines help to visualize the evolution of the three modes with the magnetic field, and in particular the variation in the intensity of the lowest energy mode decreasing with the field for $\vec{Q}$ = (0, 0, 2) and increasing for $\vec{Q}$ = (3, 0, 1). Note that an enlarged vertical scale (neutron counts) was used for panels (d) and (e), as compared to the four other panels.

energy is even higher ($E \simeq 2.5$ meV) and was not measured. On the other hand, the SF low-energy mode (in blue), corresponding to S_{aa} or $S_{aa,cc}$ depending on $\vec{Q}$, is decreasing in energy and thus corresponds to the lowest branch in Fig. 4.11(a-c). For $\vec{Q}$ = (0, 0, 2), the intensity of this excitation decreases with increasing the field while it increases

for $\vec{Q} = (3, 0, 1)$. This proves that the lowest energy branch, corresponding to pure S_{aa} fluctuations at zero-field, becomes progressively polarized along the c-axis with increasing this field, and is then purely S_{cc} above the phase transition.

Concerning the evolution of the zero-field $|1\ \mathrm{L}\rangle$ excitation (which is purely S_{cc} at $\mu_0 H = 0$), one can see from Fig. 4.12(e-f) that its intensity for $\vec{Q} = (3, 0, 1)$ has been drastically suppressed and its width broadened while increasing the field. Above $\mu_0 H = 6$ T and with increasing the field, this excitation becomes broader and vanishes around the phase transition in both $\vec{Q}$ and thus does not appear on Fig. 4.12(a-b). This is consistent with what has been observed in Fig. 4.11.

To summarize, the upper energy branch issued from the splitting of the zero-field $|1\ \mathrm{T}\rangle$ excitation corresponds to S_{bb} fluctuations, while the lowest energy branch corresponds to pure S_{aa} fluctuations at zero field and becomes progressively more and more polarized along the c-axis while increasing the field to be purely S_{cc} above the critical field. This is consistent with the rotation of the ordered moment from the c-axis to the a-axis and with the fact that magnetic systems usually prefer to fluctuate perpendicularly to both the magnetic field and the direction of the ordered moments. In other words, the lowest energy branch consists in fluctuations always perpendicular both to the magnetic field applied along $\vec{b}$ and to the ordered moment rotating from $\vec{c}$ to $\vec{a}$, while the upper one consists in fluctuations along $\vec{b}$, hence parallel to the direction of the applied field. This branch is thus increasing in energy as it is more and more difficult to fluctuate along the field direction when increasing the field.

A convenient way to interpret the data is to consider longitudinal (L) and transverse (T) fluctuations with respect to the direction of the ordered moment $\vec{m}$ for a given field $\vec{H}$. Since the direction of $\vec{m}$ (in addition to its amplitude) changes with the field, a rotating frame $(\hat{\vec{\ell}}, \hat{\vec{b}}, \hat{\vec{t}})$ is introduced (see Fig. 4.13a). $\hat{\vec{\ell}}$ is the (rotating) quantization axis, $\hat{\vec{t}}$ and $\hat{\vec{b}}$ are two orthogonal vectors such that $\hat{\vec{t}} = \hat{\vec{\ell}} \times \hat{\vec{b}}$ with $\hat{\vec{b}}$ being the direction of the applied magnetic field. These unit vectors are defined as:

$$\begin{aligned} \hat{\vec{\ell}} &= \frac{\vec{m}}{m} = \cos\psi\ \frac{\vec{a}^*}{a^*} + \sin\psi\ \frac{\vec{c}^*}{c^*} \\ \hat{\vec{t}} &= -\sin\psi\ \frac{\vec{a}^*}{a^*} + \cos\psi\ \frac{\vec{c}^*}{c^*} \\ \hat{\vec{b}} &= \frac{\vec{b}^*}{b^*} \end{aligned}$$

where ψ is the $\widehat{(\vec{a}^*, \vec{m})}$ angle. Using this frame, the partial differential cross section reads:

$$\frac{d^2\sigma}{d\Omega dE} \propto \sum_{x,y=t,b,\ell} \left\langle S_x \left(\delta_{xy} - \frac{Q_x Q_y}{Q^2} \right) S_y \right\rangle \tag{4.10}$$

For a $\vec{Q}$ vector making an angle φ with $\vec{a}^*$ in the $(\vec{a}^*, \vec{c}^*)$ scattering plane, we have $Q_t = Q\sin(\varphi - \psi), Q_b = 0, Q_\ell = Q\cos(\varphi - \psi)$, hence:

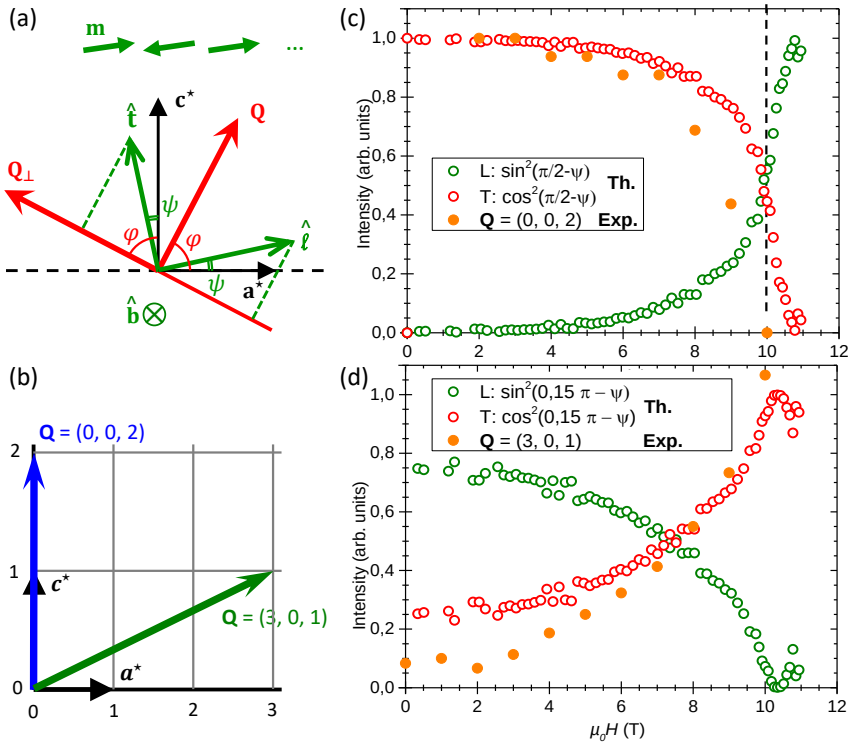

Figure 4.13: **Analysis of the polarization.** (a) Rotating local frame $(\vec{\ell}, \vec{b}, \vec{t})$. The $\vec{\ell}$ (resp. $\vec{t}$) unitary vector is parallel (resp. perpendicular) to the ordered magnetic moment. The directions of the scattering vector $\vec{Q}$ and of $\vec{\ell}$ with respect to $\vec{a}^\star$ are identified by the φ and ψ angles, respectively. (b) Location in the reciprocal lattice of the two ZC positions investigated here. (c, d) Normalized intensity of the lowest energy branch as a function of the transverse field for $\vec{Q} = (0,\ 0,\ 2)$ and $\vec{Q} = (3,\ 0,\ 1)$ ZC positions respectively, as measured (orange points), and calculated for hypothetical longitudinal (green circles) and transverse (red circles) fluctuations. This clearly evidences the transverse nature of this excitation mode.

$$\frac{d^2\sigma}{d\Omega dE} \propto \left[1 - \sin^2(\varphi - \psi)\right]\langle S_t S_t\rangle + \langle S_b S_b\rangle + \left[1 - \cos^2(\varphi - \psi)\right]\langle S_\ell S_\ell\rangle \tag{4.11}$$

$$- 2\cos(\varphi - \psi)\sin(\varphi - \psi)\langle S_t S_\ell\rangle$$

$$\propto \underbrace{\cos^2(\varphi - \psi)\langle S_t S_t\rangle}_{\text{transverse fluctuations}} + \langle S_b S_b\rangle + \underbrace{\sin^2(\varphi - \psi)\langle S_\ell S_\ell\rangle}_{\text{longitudinal fluctuations}} - 2\cos(\varphi - \psi)\sin(\varphi - \psi)\langle S_t S_\ell\rangle \tag{4.12}$$

Here I will only focus on the polarization of the lowest branch, i.e. the $S_{aa,cc}$ fluctuations and thus S_{bb} is neglected. The neutron cross section for longitudinal and transverse fluctuations (which means fluctuations along $\vec{\ell}$ and $\vec{t}$ respectively) acquires a geometrical factor $\sin^2(\varphi - \psi)$ and $\cos^2(\varphi - \psi)$ respectively. Note that the cross term $\langle S_t S_\ell\rangle$ is usually small and is thus neglected. A stringent comparison between the measured field dependence of the spectral weight for $\vec{Q} = (0, 0, 2)$ and $(3, 0, 1)$ (see Figs 4.11(b-c)) and

the calculation using the above geometrical factors is shown in Figs 4.13(c-d). While the magnetic moments rotate from the c-axis ($\psi = \pi/2$) at zero-field to the a-axis ($\psi = 0$) at $H \geq H_c$, the lowest energy branch originating from the split $|1\ \mathrm{T}\rangle$ mode indeed follows the transverse geometrical factor with in particular $\varphi = \pi/2$ for $\vec{Q} = (0, 0, 2)$ and $\varphi \approx 26.2° \simeq 0.15\pi$ for $\vec{Q} = (3, 0, 1)$.

The field dependence of ψ has been extracted through the experimental field dependence of the staggered magnetizations m_a and m_c (see Fig. 4.7) through the following formula:

$$\begin{cases} m_a = m\cos\psi \\ m_c = m\sin\psi \end{cases} \Rightarrow \psi = \arccos\frac{m_a^2}{\sqrt{m_a^2 + m_c^2}} \tag{4.13}$$

This analysis further confirms (on a quantitative point of view) that the lowest energy branch corresponds to purely transverse fluctuations.

As we have understood the evolution of the excitations under a transverse magnetic field, let us now study their dispersion along the chain direction in the phase above the transition where all the moments are now antiferromagnetically ordered along the a-axis.

4.5.3 Dispersion along Q_L in the high field phase

The dispersion of the excitations along the chain axis has been obtained on ThALES by doing energy-scans (not shown here) in the Brillouin Zone (BZ) with a 0.1 r.l.u step.

Figs. 4.14 (a-b) show the dispersion spectrum along c^* measured at $T = 1.8$ K and $\mu_0 H = 12$ T around $(Q_H, 0, Q_L)$ for $Q_H = 2$ and $Q_H = 0$ respectively (for the latter, I recall that only the S_{aa} and S_{bb} fluctuations are probed). The polarization of the low energy modes have been also investigated using LPA on IN12.

Well defined excitations can be observed at low energy ($E \leq 3.5$ meV), rather different from those in the Néel phase at zero-field. However, at higher energy (typically $E > 4$ meV), the excitations are broader and weaker in intensity. Part of this broadening comes from the fact that many branches cross each other in this dispersion spectrum and that the neutrons cannot resolve those crossings. This can be reproduced through the numerical calculations that I will present later. Here, I will only focus on the low energy branches.

One can see that the gap Δ is minimum at $\vec{Q} = (2, 0, 1)$ with a value of $\Delta \simeq 0.2$ meV (see Fig. 4.11(e)) while it is larger at $\vec{Q} = (2, 0, 2)$ with a value of $\Delta \simeq 1$ meV (see Fig. 4.14(a)). This is due to the folding of the dispersion in $BaCo_2V_2O_8$ due to the screw structure of the chain. This means that the AF point behaves like the ZC one and vice versa (one can see it from the dispersion spectrum at zero-field in [Gre+15a]). This difference of the energy gap Δ can be explained through the dispersion perpendicular to the chain as I will explain in the next section.

Let us compare the two spectra for $Q_H = 2$ and $Q_H = 0$ (see Fig. 4.14 (a-b)) and first focus on the lowest energy excitation, i.e. the one with an energy of about 1 meV (pointed out by the white dotted line in Fig. 4.14(a)) at $\vec{Q} = (2, 0, 2)$ corresponding to $\vec{Q} = (0, 0, 2)$ (i.e. positions with $h + k + l$ even). In the former case, this excitation

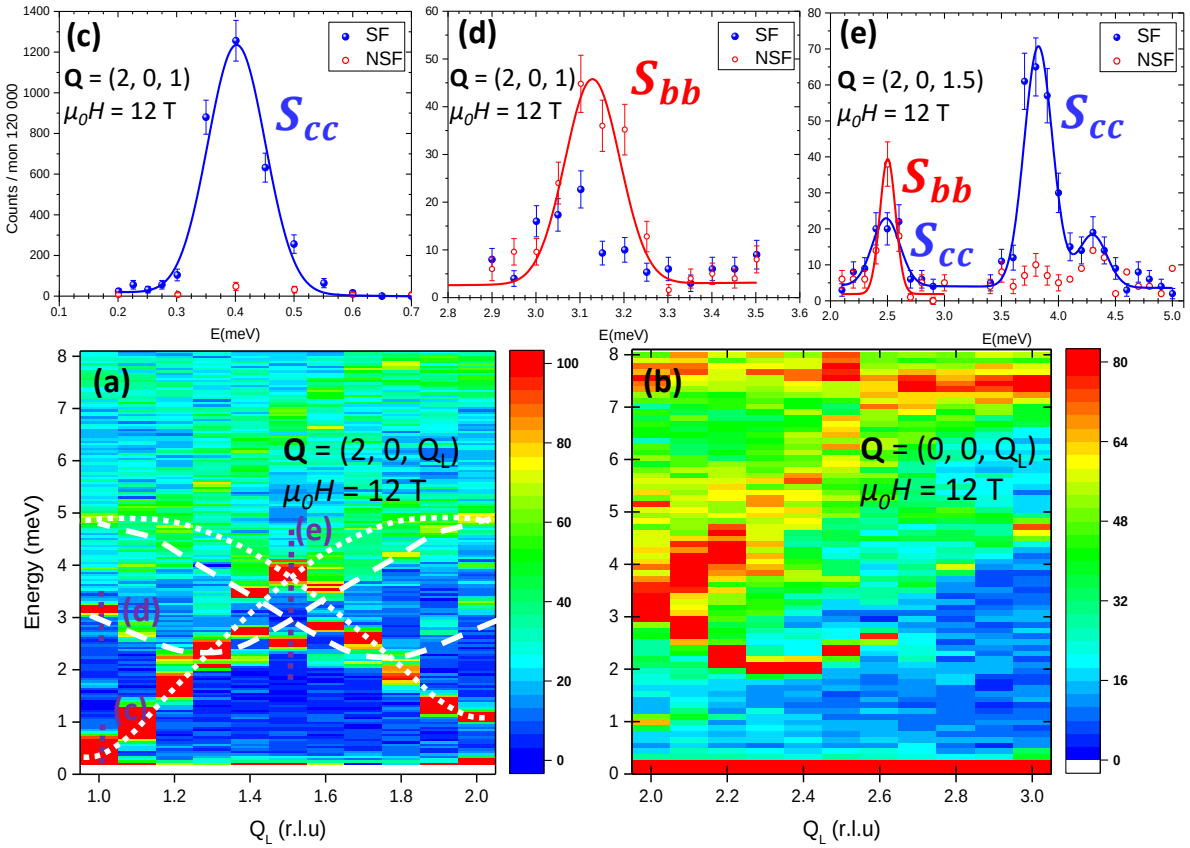

Figure 4.14: **Dispersion spectrum along** Q_L measured on ThALES for: (a) $Q_H = 2$ and (b) $Q_H = 0$ at $\mu_0 H = 12$ T. The dashed and dotted white lines in (a) point out modes that will be discussed when presenting the iTEBD calculations. (c-e) Energy scans measured in $BaCo_2V_2O_8$ at $T = 1.5$ K and $\mu_0 H = 12$ T on IN12 using LPA. They were fitted to Gaussian functions (red and blue solid lines for the NSF and SF channels respectively) for $\vec{Q} = (2, 0, 1)$ (c-d) and $\vec{Q} = (2, 0, 1.5)$ (e). These scans, shown on panel (a) with the dotted white lines, allowed to determine the polarization of the excitations.

has a very strong intensity for any value of Q_L while for $Q_H = 2$, the excitation has a very weak intensity which disappears rapidly with increasing Q_L (the excitation has completely disappeared for $Q_L = 2.2$). This strongly evidences the fact that the lowest energy mode at $\vec{Q} = (2, 0, 1)$ is mainly S_{cc}. This is consistent with what is observed with the polarization analysis as shown in the constant-Q energy scan in Fig. 4.14(c).

The second excitation pointed out by the white dashed line in Fig. 4.14(a) at higher energy (around $E \simeq 3$ meV) at $\vec{Q} = (2, 0, 1)$ corresponds to S_{bb} fluctuations as observed in the LPA analysis (see Fig. 4.14(d)).

In Fig. 4.14, an anticrossing seems to occur around $Q_L = 1.5$ and $E = 3$ meV. This is evidenced by the polarized analysis where the mode found around 2.5 meV and at $\vec{Q} = (2, 0, 1.5)$ corresponds to a superposition of S_{bb} and S_{cc} fluctuations as shown in Fig 4.14(e).

While complicated at first sight, this dispersion spectrum will become clearer when I will present the iTEBD calculations in section 4.6.2.2.

Let us now turn to these dispersions to get an insight on the evolution of the interchain interaction as a function of the applied field.

4.5.4 Dispersion along Q_H at various magnetic fields

The interchain dispersions were measured on IN12 at zero-field and on ThALES at $T = 1.8$ K and $\mu_0 H = 12$ T from constant-Q_H energy scans for $Q_L = 1$ and 2.

At zero field, the interchain couplings are believed to be complex, the observed magnetic structure being eventually stabilized by a dominant AF exchange interaction in the diagonal direction [Gre+15a; Kla+15; Gre+15b]. In a previous analysis of the excitations in zero field [Gre+15a], a combination of an analytical formula given by Bougourzi *et al.* [BKM98] and a formula proposed by Coldea *et al.* [Col+10] was adapted to account for the energy of the discrete modes. The former is describing the exact two-spinons dynamical structure factor of a XXZ chain (for any ε) without interchain interaction while the latter describes the spinon confinement in a linear potential for the case of a strongly Ising spin chain ($\varepsilon << 1$). This analysis yielded a molecular field resulting from the interchain coupling of ≈0.2 meV. This value is larger than the one estimated from the amplitude of dispersion along a^*, which was found to slightly depend on Q_L [Gre+15a]: flat for $Q_L = 1$ and with a small dispersion amplitude of about 0.1 meV for $Q_L = 2$ (see Fig. 1.20). Note that a huge theoretical progress has been done by S. Rutkevitch recently [Rut18], since he has found an analytical solution of the confinement (with J') of the spinons for an arbitrary XXZ spin-chain (for any ε). The fact that the excitations are almost non-dispersive perpendicularly to the chains is probably a signature of the frustration between neighboring chains in $BaCo_2V_2O_8$.

Figs. 4.15 (b-c) show the dispersion of the lowest mode measured in the high field phase at $T = 1.8$ K and $\mu_0 H = 12$ T, for $Q_L = 1$ and $Q_L = 2$. The amplitude of dispersion for both Q_L values is much stronger than in zero-field: $\Delta E(Q_L = 1) \simeq 0.45$ meV and $\Delta E(Q_L = 2) \simeq 0.67$ meV. From similar dispersions recorded at different magnetic fields, we were able to extract the field dependence of the amplitude of dispersion ΔE at $Q_L = 1$ and $Q_L = 2$, as shown in Fig. 4.16. The dispersion under field is stronger for $Q_L = 2$ than for $Q_L = 1$, as in zero-field. Both curves have the same behavior: ΔE increases with increasing field up to H_c and slightly decreases above. For both Q_L, the amplitude of dispersion has increased by ≈0.55 meV between $\mu_0 H = 0$ and $\mu_0 H = 12$ T. Let me emphasize that through Fig. 4.16, one is able to understand the difference of the gap Δ at different Q_L observed in the dispersion spectrum along the chain and in the magnetic field dependence of the excitations. For example at $\mu_0 H = 10\ T$, $\Delta \simeq 0.2$ meV for $\vec{Q} = (2, 0, 1)$ and $\Delta \simeq 0.75$ meV for $\vec{Q} = (3, 0, 1)$ leading to a difference of about 0.55 meV (see Figs. 4.11 (a),(c)).

Having in mind that the amplitude of dispersion is proportional to the average interchain coupling J', this increase can be understood by a removal of the frustration in the high field magnetic structure. This is consistent with what was found in the diffraction results. Indeed, while at zero field the frustrated interactions are between two nearest neighbor chains, the one in the high field phase is between two chains in diagonal. One can understand this with the help of Fig. 4.6: the nature of the diagonal interaction along $\vec{a} \pm \vec{b}$ has changed to a ferromagnetic interaction and all the first neighbors interactions

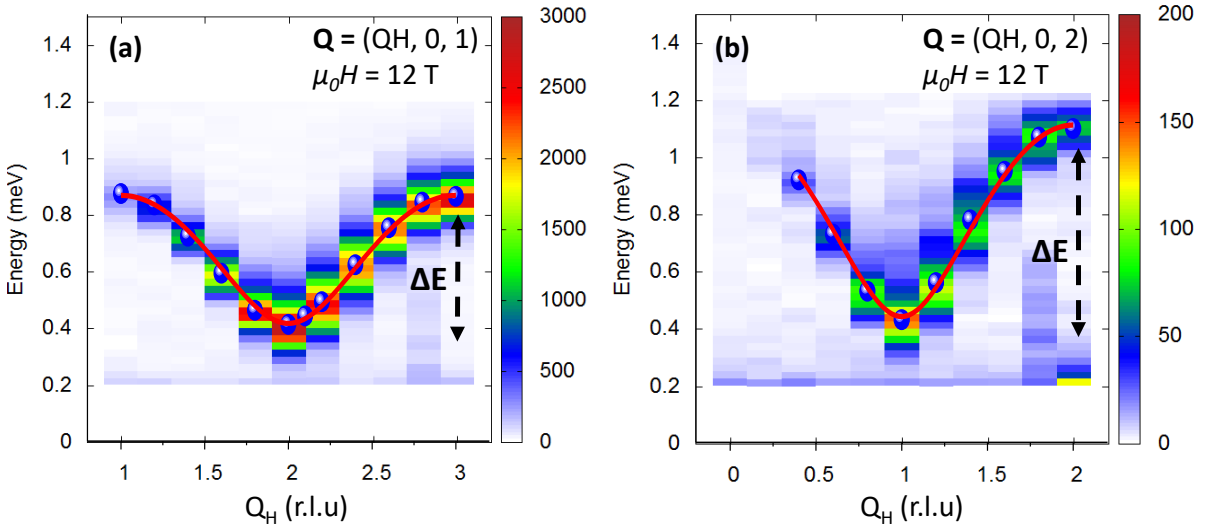

Figure 4.15: **Dispersion spectra of the excitations along** a^* obtained from constant-Q energy scans at $T = 1.8$ K for $Q_L = 1$ (a) and $Q_L = 2$ (b) at $\mu_0 H = 12$ T. The dispersions at zero field and at $\mu_0 H = 12$ T were fitted with the phenomenological law: $E = \sqrt{\Delta^2 + (E_m^2 - \Delta^2)\sin^2[\frac{h\pi}{2}]}$, where $h = Q_H$ or $Q_H - 1$ depending on the type of Bragg position, Δ is the gap and E_m is the maximum of the dispersion. This yields the following amplitudes of dispersion at 12 T: $\Delta E(Q_L = 1) \simeq 0.45$ meV and $\Delta E(Q_L = 2) \simeq 0.67$ meV.

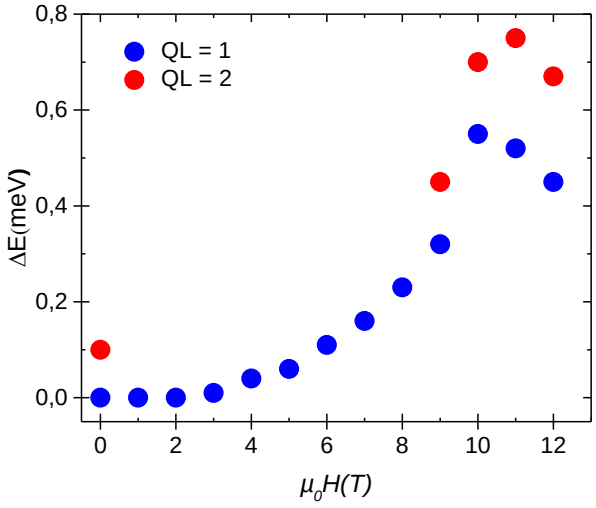

Figure 4.16: **Magnetic field dependence of the amplitude of dispersion** ΔE for $Q_L = 1$ and $Q_L = 2$, extracted from interchain dispersion curves measured along a^* at different values of the magnetic field (see an example in Fig. 4.15(b-c) for $\mu_0 H = 12$ T). The error bars are smaller than the symbol size.

along $\vec{a}$ and $\vec{b}$ are now AF and then no longer frustrated. This is due to the fact that the high field phase is stabilized by the staggered field and not by J'. The new magnetic arrangement changes the frustration of the interchain interactions and therefore their measured dispersion along a^*.

Above the phase transition, the amplitude of dispersion decreases. A possible explanation could arise from the fact that the amplitude of dispersion is directly proportional to the effective J' but also to the AF component of the ordered moments. Therefore, the decrease of this component at the expense of the FM component might qualitatively explain this effect. A further step would be to better understand the complex set of interchain interactions for instance with the help of spin wave calculations.

4.6 Numerical calculations

In this section I will try to give an interpretation of our measurements, first by showing my numerical calculations using my own program described in Chap. 3 and second by means of iTEBD calculations.

4.6.1 A first attempt to interpret our measurements by exact diagonalization

As discussed above in paragraph 4.3.2, under a transverse field applied along the b-axis, the Hamiltonian of $BaCo_2V_2O_8$ takes the following form:

$$\mathscr{H} = \mathscr{H}_{\text{XXZ}} + \mathscr{H}_{\text{interchain}} + \mathscr{H}_{\text{field}}$$

$$\text{with} \quad \mathscr{H}_{field} = -\mu_B H \sum_j \left\{ g_{bb} \frac{(S_j^+ + S_j^-)}{2} + g_{bc} S_j^c \cos\left[\frac{\pi}{4} + \frac{\pi(j-1)}{2}\right] + g_{ba}(-1)^j \frac{(S_j^+ - S_j^-)}{2i} \right\}$$

Starting from this Hamiltonian, under a strong value of a magnetic transverse field, more than one spin will be flipped along the chain. Therefore the 2-spinons basis is not enough to describe the system as multi-spinons states become relevant now. To be able to do calculations and to catch up the physics of this system, I used the 2-spinons $\oplus$ 4-spinons $\oplus$ 6-spinons basis for the calculation of the groundstate and the 2-spinons $\oplus$ 4-spinons basis only for the calculations of the magnetic excitations (as these ones are much heavier to calculate). Consequently, the number of sites had to be considerably reduced ($n = 14$ instead of $n = 30$ at zero-field). The parameters used in the calculations are those of Kimura et *al.* [Kim+13]: $g_{bb} = 2.75$, $g_{ba} = 0.4\ g_{bb} \simeq 1.1$, $g_{bc} = 0.1\sqrt{2}\ g_{bb} \simeq 0.39$. Let us discuss first about the evolution of the ground state under the transverse magnetic field. Then we will see the magnetic field dependence of both the energy and the spectral weight of the excitations.

4.6.1.1 Calculations of the groundstate: magnetic field dependence of the magnetizations

Fig. 4.17 shows the magnetic field dependence of the calculated staggered magnetizations m_a, m_c and of the uniform magnetization $M_\parallel$. These magnetizations have been calculated from the field dependence of the groundstate $|GS(H)\rangle$ as $m_a = \langle GS(H)|S^a|GS(H)\rangle$, $M_\parallel = \langle GS(H)|S^b|GS(H)\rangle$ and $m_c = \langle GS(H)|S^c|GS(H)\rangle$.

One can see that in addition to reproduce qualitatively the neutron data of Fig. 4.7, these calculations are able to reproduce quantitatively quite well (in contrast with the spin-dynamics) the experimental field dependence of the staggered magnetic moments. Indeed the calculations for m_c reproduces very well what is observed experimentally. However, as for the iTEBD calculations, there is a global scaling factor between the numerical calculations and the experiment for m_a.

Nevertheless the critical field of $\mu_0 H_c \simeq 10$ T is well reproduced. Indeed one can see that m_c decreases with increasing the field and (almost) vanishes at $\mu_0 H_c = 10$ T. The remaining of a small value of m_c above H_c is due to the effective field induced along $\vec{c}$ which is taken into account in the model. On the other hand m_a and $M_{\parallel}$ increase linearly with H in such a way that $m_a > M_{\parallel}$ and one can observe a break in the slope of m_a at $\mu_0 H_c$. This is consistent with the experimental observations.

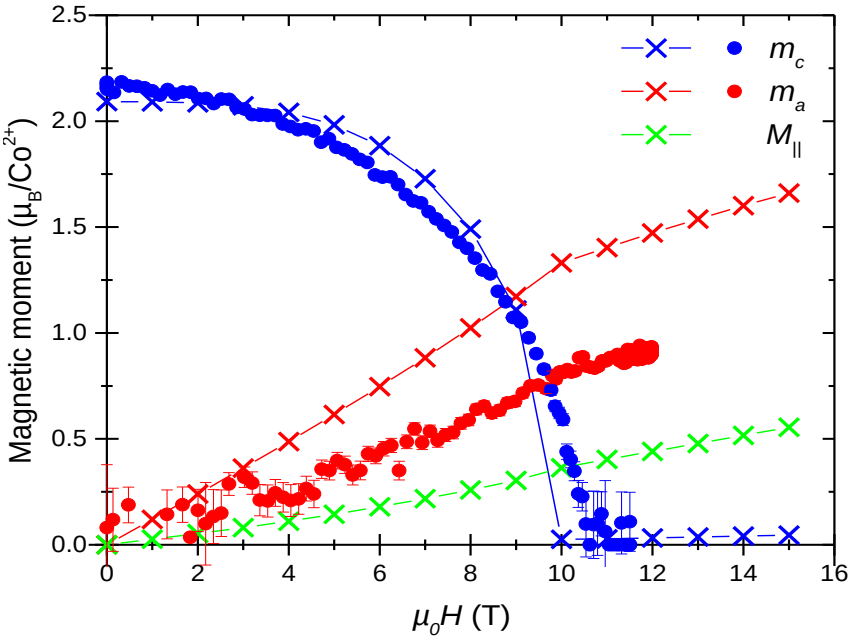

Figure 4.17: **Calculated field dependence of m_a, m_c and $M_{\parallel}$ using exact diagonalization**. The experimental staggered moments m_c and m_a (blue and red circles respectively) have to be compared with the calculated ones (blue and red crosses connected by solid lines). The calculated uniform magnetization $M_{\parallel}$ induced along $\vec{b}$ by the uniform field is also plotted (green crosses connected by solid lines). The Hilbert space consists in a 2-spinons $\oplus$ 4-spinons $\oplus$ 6-spinons basis. The calculations were made with $n = 14$ spins.

Thus, the calculations of the field dependence of the groundstate using exact diagonalization match well qualitatively with what was found experimentally. These calculations validate the Hamiltonian of the system. Let us now turn to the spin-dynamics of the system.

4.6.1.2 Magnetic field dependence of the energies

Fig. 4.18 shows the magnetic field dependence of the calculated lowest energy excitations with the two configurations of the magnetic field discussed in paragraph 4.3.2, i.e. $\vec{H} \parallel \vec{b}$ (with a staggered field along $\vec{a}$) and $\vec{H} \parallel \vec{a} + \vec{b}$ (without any staggered field along $\vec{a}$).

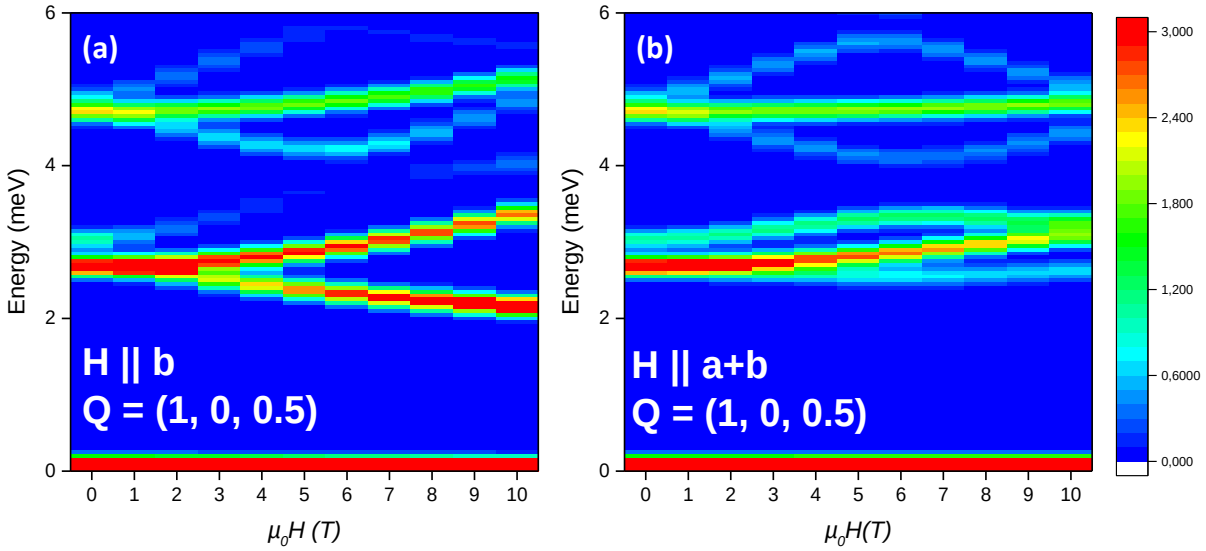

Figure 4.18: **Calculated field dependence of the excitations using exact diagonalization.** Intensity map $S_{\perp\vec{Q}}$ with $\vec{H} \parallel \vec{b}$ (a), i.e. with a staggered field along $\vec{a}$, and with $\vec{H} \parallel \vec{a}+\vec{b}$ (b). $S(Q,\omega)$ is calculated on an antiferromagnetic point (AF) $Q = (1, 0, 0.5)$ (I recall that my calculation are made for linear spin-chain). The step in energy (resp. H) is taken as 0.05 meV (resp. 1 T). The colorscale is in arbitrary units. Since the basis is large (the 2-spinons $\oplus$ 4-spinons basis), the calculations were made with $n = 14$ spins only.

First, we can see that the non-linear field dependence of the excitations is reproduced for both orientations of the field. This is well understood by the fact that the field is applied perpendicularly to the quantization axis (the c-axis here) and then a mixing of the wave-functions occurs. Indeed the uniform field flips spins through the operator S_j^+ (as well as the effective staggered field along $\vec{a}$) and thus mixes the two zero-field sectors $|j\ \mathrm{T}\rangle$ and $|j\ \mathrm{L}\rangle$. If we denote a magnetic excitation $|\Psi\rangle = a_\mathrm{T}\,|\phi_\mathrm{T}\rangle + a_\mathrm{L}\,|\phi_\mathrm{L}\rangle$ where $|\phi_\mathrm{T}\rangle$ and $|\phi_\mathrm{L}\rangle$ are a linear combination of the zero-field states $|j\ \mathrm{T}\rangle$ and $|j\ \mathrm{L}\rangle$ respectively, we can also see this effect in the present simulation by plotting the field dependence of the weights $|a_\mathrm{T}|^2$ and $|a_\mathrm{L}|^2$ (see Fig. 4.19).

Between the two orientations of the field, one can see a main difference. The energy of the lowest mode decreases with increasing field in one case ($\vec{H} \parallel \vec{b}$ in Fig. 4.18(a)) while it is almost constant in the other case ($\vec{H} \parallel \vec{a} + \vec{b}$ in Fig. 4.18(b)). This confirms that the non-diagonal components of the Landé tensor $\widetilde{g}$, and especially g_{ba} (the calculations without g_{bc} give the same behaviour) are responsible for the lowering of the lowest energy mode and therefore for the phase transition which occurs at $\mu_0 H \simeq 10$ T as seen in the experiments. In the present calculations we do not reproduce the phase transition (i.e. the closure of the energy gap) at this value of the field and the calculated energy of the

lowest excitation decreases much slower with the field than observed experimentally (see Fig. 4.11). This comes again from the truncation of the basis since the larger the magnetic field, the more the multi-spinons with a high number of flipped spins become relevant. In addition to this lowest energy mode, one can see that the numerical calculations show a qualitative agreement with what has been observed experimentally (see Fig. 4.18 to be compared to Fig. 4.11). Indeed, the splitting is well reproduced with one branch increasing and one decreasing in energy when the field increases, as well as the anticrossing (occuring at $\mu_0 H = 6$ T here instead of 3 T) between the $|1\ \mathrm{L}\rangle$ and $|2\ \mathrm{T}\rangle$ modes.

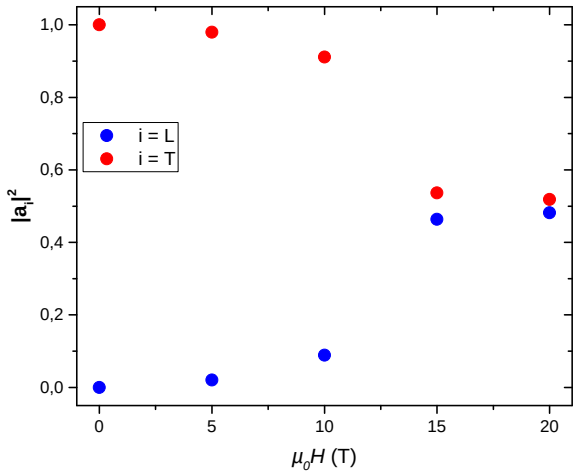

Figure 4.19: **Mixing of the wavefunctions by the magnetic field $\vec{H} \parallel \vec{b}$.** Calculated field dependence of the a_T and a_L coefficients of the $|1\ \mathrm{T}\rangle$ zero-field excitation. Here the calculations were made with $n = 8$ sites and the 2-spinons basis only for more convenience.

What is powerful with numerical techniques is that we can calculate directly the polarization of the modes. This is what I am going to discuss now.

4.6.1.3 Polarization of the magnetic excitations

Fig. 4.20 shows the polarization of the excitations, i.e. the direction of the fluctuations for both configurations of the field $\vec{H} \parallel \vec{b}$ and $\vec{H} \parallel \vec{a} + \vec{b}$. One can see on Fig. 4.20(a) and Fig. 4.20(c) that for $\vec{H} \parallel \vec{b}$, the spectral weight of the lowest energy excitation is purely S_{aa} at zero field and becomes progressively more and more S_{cc} with increasing the field in agreement with the experimental findings.

This is consistent with what has been already said, namely the fact that the g_{ba} non-diagonal component of the Landé tensor $\widetilde{g}$ induces a staggered magnetization along the a-axis proportional to the magnetic field $\mu_0 H$ and that this term competes with the Ising c-axis. Therefore, while S_{aa} (resp. S_{cc}) were the transverse (resp. longitudinal) fluctuations at $\mu_0 H = 0$ where all the spins are ordered along the c-axis, they become progressively longitudinal (resp. transverse) when the ordered moments are rotating in the (a, c) plane towards the a-axis.

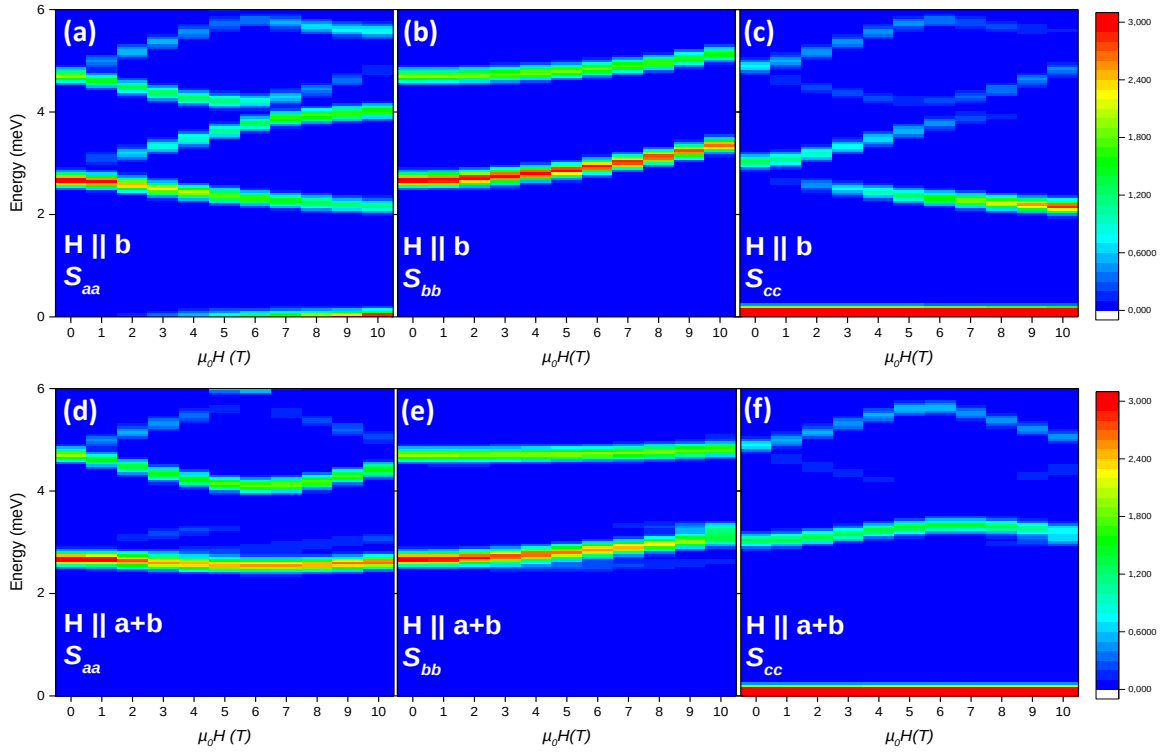

Figure 4.20: **Polarization of the excitations using exact diagonalization.** (a-c) Field evolution of the polarization of the excitations under a transverse magnetic field applied along the b-axis, i.e. with a staggered field. (d-f) same calculations but with an applied field along $\vec{a}+\vec{b}$, i.e. without a staggered field. The step in energy (resp. $\mu_0 H$) is taken as 0.05 meV (resp. 1 T) in both cases. The colorscale is in arbitrary units. As the basis is large (2-spinons $\oplus$ 4-spinons), the calculations were made with $n = 14$ spins only.

Another interesting remark is that in both cases, the S_{bb} branch arising from the splitting of the lowest mode is the one increasing in energy with increasing the magnetic field (see Fig. 4.20(b)). This shows again that the numerical results agree with the experimental findings.

4.6.1.4 Conclusion and discussion

To conclude on this part, the calculations are consistent with what has been seen in the experiment and consolidate our understanding of the behavior of $BaCo_2V_2O_8$ under a transverse field applied along the b-axis. The mismatch between the experimental values and the calculated ones comes again from the truncation of the Hilbert space. Nevertheless, one can see that we capture a lot of physics and that the calculations agree qualitatively very well with what was found experimentally. Above all it helps us to understand the key role played by the staggered field induced by the uniform one. Indeed these calculations show the necessity to include the staggered field $\vec{h}_a$ in the Hamiltonian to explain the experimental findings (whereas $\vec{h}_c$ is found to be not relevant). Thus the exact diagonalization calculations somehow confirm the Hamiltonian proposed in Eq. (4.6). All these preliminary conclusions were well confirmed by iTEBD calculations, a very powerful

technique as we will see now.

4.6.2 iTEBD calculations

During my PhD, we have collaborated with Shintaro Takayoshi and Thierry Giamarchi from the Theory of Quantum Matter Group at the University of Geneva. They have performed infinite Time Evolve Block Decimation (iTEBD) calculations on this system (as explained in section. 3.4.5) and also used a quantum field theory approach to better understand the low-energy properties of this system. This collaboration was really fruitful as it was a permanent back and forth discussion between experimentalists and theoreticians. In this section, I will expose the results of their calculations, first the calculations at zero-field which allowed to extract the parameters of the $BaCo_2V_2O_8$ system, and then I will present the iTEBD calculations in a transverse field.

4.6.2.1 Calculations at zero-field: fitting of the parameters

Contrary to my calculations, S. Takayoshi and T. Giamarchi took into account the full 4-fold screw symmetry of the $BaCo_2V_2O_8$ chain. As in my own program, they considered the contribution of interchain interaction J' by a mean field approximation, which gives rise to an effective staggered magnetic field h^{eff} along the $\vec{c}$ direction in the Hamiltonian (at $H = 0$):

$$\mathscr{H} = J\sum_n [\varepsilon(S^a_n S^a_{n+1} + S^b_n S^b_{n+1}) + S^c_n S^c_{n+1}] - g_{cc}\mu_B h^{\text{eff}} \sum_n (-1)^n S^c_n \tag{4.14}$$

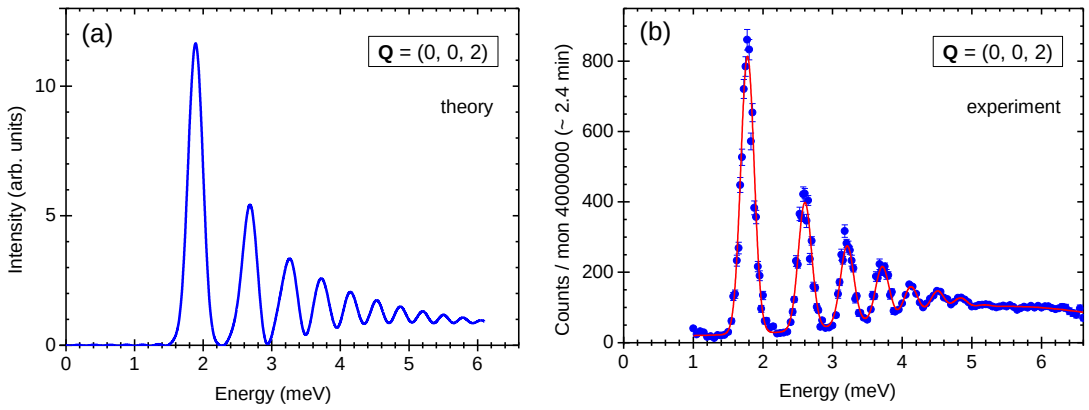

Figure 4.21: **Calculated energy scan vs experimental one.** (a) Intensity of scattered neutrons for $\vec{Q} = (0, 0, 2)$ at zero magnetic field calculated by iTEBD with $J = 5.8$ meV, $\varepsilon = 0.53$, and $g_{cc}\mu_B h^{\text{eff}} = 0.061$ meV. (b) Experimental results taken from Ref. [Gre+15a] for comparison (solid symbols). The red line is a fit to the data.

The parameters J, ε and h^{eff} were determined in such a way that the cross section for the scattering vector $\vec{Q} = (0, 0, 2)$ is reproduced. The differential neutron scattering cross section is given by (see Eq. (2.15)):

$$\frac{d^2\sigma}{d\Omega dE} \propto \frac{k_f}{k_i} \sum_{\alpha,\beta=x,y,z} \left(\delta_{\alpha\beta} - \frac{Q_\alpha Q_\beta}{|\vec{Q}|^2}\right) |f(\vec{Q})|^2 \int dt \sum_{\vec{r}} e^{i(\omega t - \vec{Q}\cdot\vec{r})} \langle S^\alpha(\vec{r}, t) S^\beta(\vec{0}, 0)\rangle, \tag{4.15}$$

where $f(\vec{Q})$ is the magnetic form factor and $\vec{k}_i$, $\vec{k}_f$ are the initial and final wave vectors, respectively ($\vec{Q} = \vec{k}_i - \vec{k}_f$). The space-time correlation functions $\langle S^\alpha(\vec{r},t)S^\beta(\vec{0},0)\rangle$ (with $\alpha,\beta = a,b,c$) are calculated using iTEBD [Vid07] with the infinite boundary condition [PVM12]. In the calculations, the time is taken to be $0 \leq t \leq 80J^{-1}$ with the discretization $dt = 0.05J^{-1}$. The truncation dimension (i.e., dimension of matrix product states) is $\chi = 60$. For the Fourier transform in Eq. (4.15), the summation is taken over the actual positions $\vec{r}$ of Co atoms. The scattering cross section for $\vec{Q} = (0,0,2)$ at zero magnetic field calculated by iTEBD with the parameters $J = 5.8$ meV, $\varepsilon = 0.53$, and $g_{cc}\mu_B h^{\text{eff}} = 0.061$ meV is shown in Fig. 4.21(a). It reproduces very well the experimental data [Gre+15a] reported in Fig. 4.21(b) and these parameters were used for all subsequent calculations. In mean field theory, $g_{cc}\mu_B h^{\text{eff}} = J'|\langle S_j^c\rangle|$, which yields $J' = 0.17$ meV and $|\langle S_j^c\rangle| = 0.366$ in agreement with the experiment.

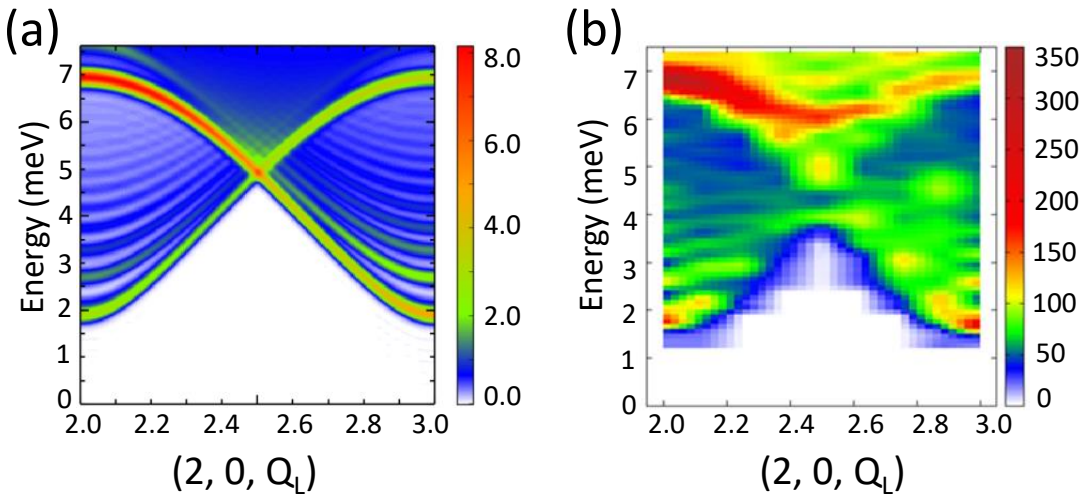

Figure 4.22: **Dispersion spectrum along Q_L at zero-field obtained by iTEBD calculations versus the experimental one.** (a) Numerically calculated magnetic excitations of $BaCo_2V_2O_8$ in zero field, which show the Zeeman ladders. The parameters of the calculations determined from a comparison with the zero-field measured excitations [Gre+15a; Gre+15b] are $J = 5.8$ meV, $\varepsilon = 0.53$, and $J' = 0.17$ meV. Both ε and J' are in excellent agreement with Ref. [Gre+15a] while J is about 20% larger. Note that the new parameters, with respect to those determined in [Gre+15a; Gre+15b], are more reliable since iTEBD calculations take both the inter-chain interaction and an arbitrary anisotropy into account, while it was not the case in Ref. [Gre+15a]. The color scale is in arbitrary units. (b) Dispersion spectrum obtained in Ref. [Gre+15a] for comparison to the calculated one.

The calculated full dispersion spectrum for $\vec{Q} = (2,0,Q_L)$ ($2 \leq Q_L \leq 3$) in Fig. 4.22(a) also agrees very well with the experiment (see Fig. 4.22(b)) except for the anticrossing observed around 4-5 meV at $\vec{Q} = (2,0,2.5)$. The nature of this anticrossing has been investigated by the theoreticians and has been proposed to be a consequence of a tetramerization in the chain. Indeed, because of the peculiar screw structure of $BaCo_2V_2O_8$, an hypothesis could be that the intrachain interaction changes slightly from two consecutive pairs of Cobalt atoms to the next ones. Fig. 4.23 shows a sketch of this tetramerization

and the spectrum calculated by iTEBD calculations taking into account this effect. One can see that the anticrossing is now reproduced. Nevertheless, this effect has not been considered in all subsequent calculations.

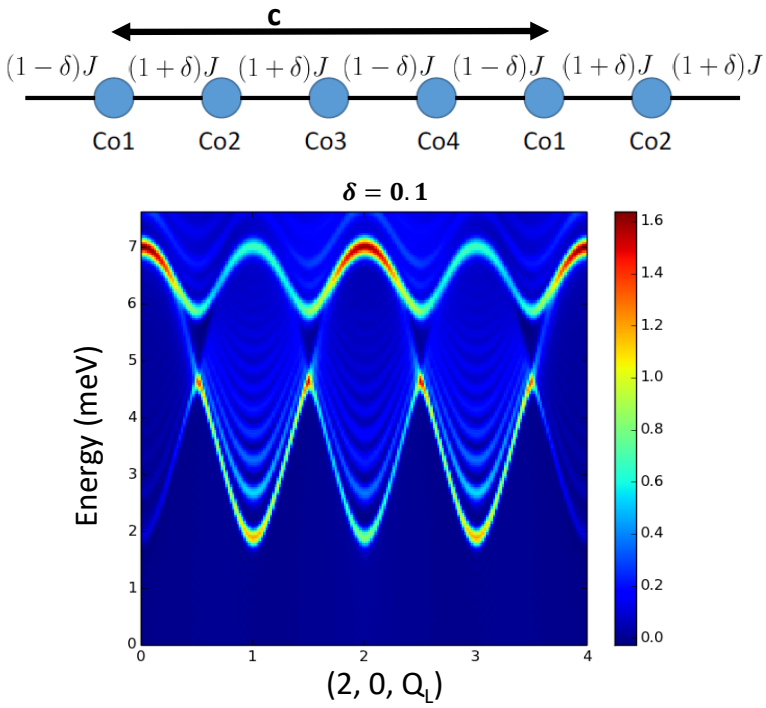

Figure 4.23: **Tetramerization scenario in $BaCo_2V_2O_8$.** Above: sketch of the tetramerization along the chain. The intrachain interaction is slighty different between two adjacent pairs of Co atoms and the next two ones. It can take two values $J(1-\delta)$ and $J(1+\delta)$, where δ is the tetramerization parameter. Below: Spectrum calculated with iTEBD calculations with the same parameters as in Fig. 4.23 and the additional tetramerization effect with $\delta = 0.1$.

The parameters J, J', ε determined from the zero-field calculations were used for all the calculations under magnetic field that I will present now.

4.6.2.2 Calculations in a transverse magnetic field along the b-axis

Evolution of the ground state: The numerical results are shown in Fig. 4.7 by the purple and black crosses connected by solid lines. One can see that the iTEBD calculations describe quite well the field dependence of the staggered magnetization along the chains m_c. For the component perpendicular to the chains, i.e. m_a, the overall trend of the data is correctly given by the numerics but a global scaling factor seems to exist with the experimental data.

The reason for this discrepancy could be due to factors such as: i) effect of temperature; ii) bigger sensitivity of this quantity on small uncertainties in the parameters, iii) treatment of the interchain interaction in the mean field theory. The latter gives a deviation from the true value of m_a and for this problem to be solved, we need a treatment beyond the mean field theory, which is a challenging problem. As we will see later, the set

of parameters used in the numerics was a compromise between having the good critical field and a good matching with the excitation spectrum data. Indeed, the large number of parameters in the Hamiltonian allows to take another set of parameters which could match better with the diffraction data, but it would be at the expense of the spin-dynamics data.

Field dependence of the excitations: Figs. 4.24 (a-c) show the field dependence of the excitations calculated by iTEBD for the three scattering vectors $\vec{Q} = (2,0,1)$, $\vec{Q} = (0,0,2)$ and $\vec{Q} = (3,0,1)$. The Hamiltonian is the one of Eq. (4.6), i.e. with a staggered field:

$$\mathscr{H} = J\sum_j [\varepsilon(S_j^a S_{n+1}^a + S_j^b S_{j+1}^b) + S_j^c S_{j+1}^c] - g_{cc}\mu_B h^{\text{eff}} \sum_j (-1)^n S_j^c - \mu_B H \sum_j \left\{ g_{bb} S_j^b + g_{bc} S_j^c \cos\left[\frac{\pi}{2} + \frac{\pi(j-1)}{2}\right] + g_{ba} S_j^a (-1)^j \right\} \quad (4.16)$$

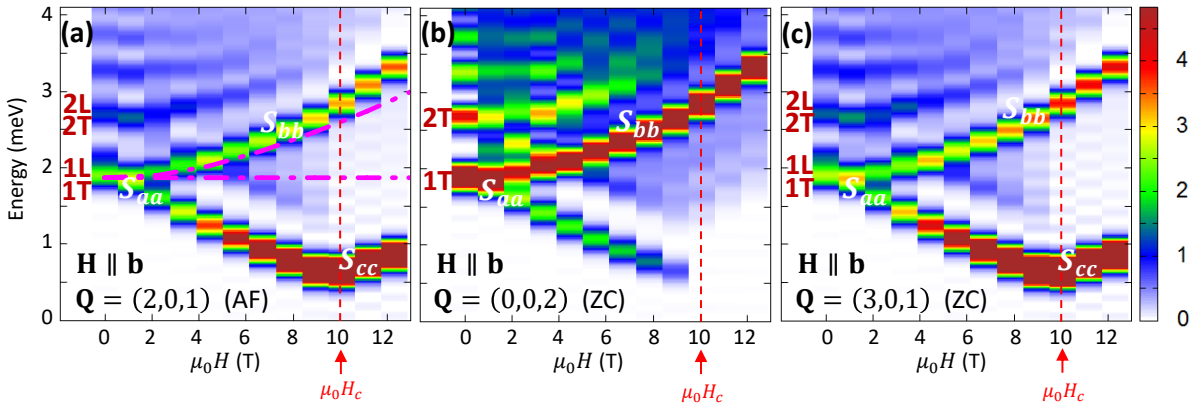

Figure 4.24: **Field dependence of the excitations obtained by iTEBD calculations.** Theoretical intensity color maps to be compared to the experimental ones in Fig. 4.11 (a-c), obtained from iTEBD calculations of the $S(\vec{Q},\omega)$ neutron scattering functions. The color scale was truncated and both the critical field and the polarization (T or L) of the modes in zero-field are pointed out. In addition, the polarization (labeled S_{aa}, S_{bb}, and S_{cc} for the $\vec{a}$, $\vec{b}$, and $\vec{c}$ directions, respectively) of the split branches arising from the $|1\ \mathrm{T}\rangle$ mode is indicated at $\mu_0 H > 0$. The pink dashed lines in panel (a) correspond to the field dependence these two branches would display in the absence of the staggered field along $\vec{a}$ (i.e. for the uniform magnetic field applied along $\vec{a}+\vec{b}$).

Here, as already explained in paragraph 4.3.3, the parameter $g_{bb} = 2.35$ is chosen slightly smaller than the value of Kimura *et* al. [Kim+13] in order to reproduce the critical field of the transition (see Fig. 4.7). The other parameters are $g_{ba}/g_{bb} = 0.4$ and $g_{bc}/g_{cc} = 0.14$ according to Ref [Kim+13]. Since h^{eff} is introduced from the mean field approximation of the interchain interactions, h^{eff} is determined from the self-consistency equation $h^{\text{eff}}(H)/h^{\text{eff}}(0) = m_c(H)/m_c(0)$, where m_c is the staggered magnetization of the Néel order along the c-axis. Scattering cross sections calculated using Eq. (4.15) under a magnetic field are shown in Fig. 4.24. The chosen set of parameters for the $\tilde{g}$ Landé tensor is the best compromise to reproduce the staggered ordered moments along $\vec{c}$ and $\vec{a}$,

the zero-field excitation spectrum, the value of the critical field and the field-dependence of the magnetic excitations.

While my calculations using exact diagonalization only show a qualitative agreement with the experiment, the results for the excitation spectrum using iTEBD calculations (see Figs. 4.24(a-c)) show a quantitative agreement with the experimental data (see Figs. 4.11(a-c)) accounting for the main modes observed experimentally. In addition, the numerics further validate the polarization of the modes and in particular the transverse nature of the lowest energy one. The rapid energy lowering of the lowest branch when the field is applied along $\vec{b}$ is confirmed numerically to be a consequence of the additional effective staggered field along $\vec{a}$ due to non diagonal components of the $\widetilde{g}$-tensor. Indeed (as the results of my program) the calculations without this term yield an absence of field dependence for the lowest energy branch in the investigated field range (see pink lines in Fig. 4.24(a)).

Dispersion along Q_L in the high field phase: The dispersion along the chain-axis, i.e. along Q_L, has also been calculated by iTEBD calculations. Fig. 4.25(a) shows the calculated dispersion spectrum at $\mu_0 H = 12$ T for $\vec{Q} = (2, 0, Q_L)$.

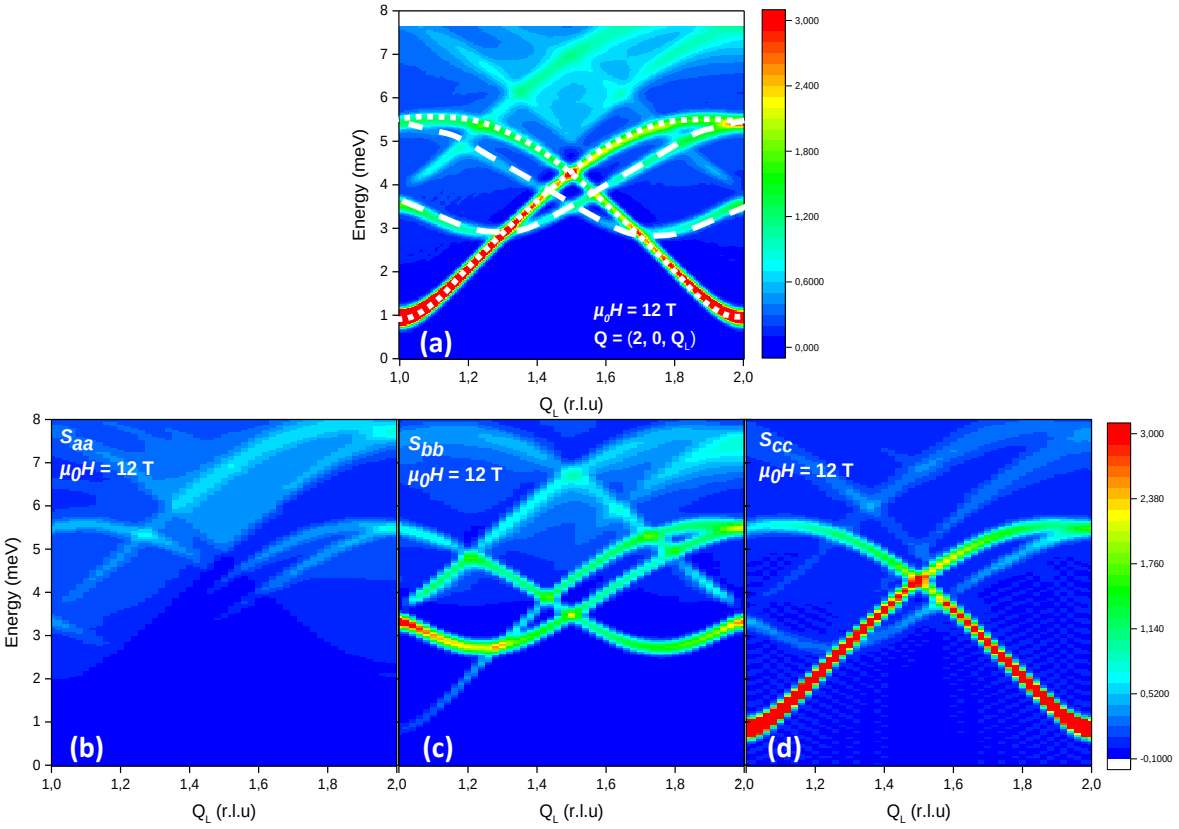

Figure 4.25: **Dispersion spectrum in the high field phase obtained by iTEBD calculations.** (a) Dispersion spectrum calculated along Q_L at $\mu_0 H = 12$ T and for $\vec{Q} = (2, 0, Q_L)$ to be compared to the experimental spectrum in Fig. 4.14(a). The dashed and dotted white lines point out the two different low energy modes respectively. (b-d) Contribution of the S_{aa}, S_{bb} and S_{cc} fluctuations to the above dispersion spectrum.

This calculated intensity map shows a very good agreement with the experimental one except for the anticrossing which appears around $Q_L = 1.5$ in the experiment (see Fig. 4.14(a)). This anticrossing may come from the tetramerization of the chain as suggested in zero-field. There are also many branch-crossings which occur in this spectrum. This may explain the broadening of the peaks seen in the experiment, as it is difficult to resolve two peaks close to each other.

Figs 4.25(b-d) show the polarization of the modes along the a, b and c axes of the calculated dispersion spectrum. These calculations agree with the experimental findings using polarized neutrons. Indeed excitation pointed out by dotted lines corresponds mainly to S_{cc} fluctuations while the other one pointed out by dashed lines corresponds mainly to S_{bb} fluctuations. A last interesting remark is that the S_{aa} fluctuations (longitudinal in the high field phase) have an intensity much lower than the S_{cc} and S_{bb} ones. We will see later that this arises from the action of the Hamiltonian on the states $|j, S_t = \pm 1\rangle$ and $|j, S_\ell = 0\rangle$ (where S_t and S_ℓ denote the transverse and longitudinal modes respectively) making the low energy longitudinal fluctuations evanescent.

4.6.3 Conclusion

We have seen in this section that the numerics were able to reproduce the experimental findings, with a qualitative agreement for exact diagonalization and with a quantitative one for the iTEBD calculations. The philosophy behind the use of numerical techniques is to confirm the Hamiltonian, to determine its various parameters (J, J', ε...) and to understand the relevant terms. Indeed, as shown here, the numerical calculations confirm that the effective staggered field along $\vec{a}$ induced by a uniform field applied along $\vec{b}$ is the key ingredient which drives the rapid lowering of the lowest energy branch and finally triggers this phase transition. Now that the Hamiltonian is confirmed and well established, we can turn to the interpretation of the magnetic excitations to better understand the nature of this quantum phase transition.

4.7 Interpretation: nature of the excitations and of the phase transition

To understand the nature of the excitations, we will see first the action of the Hamiltonian on the zero-field spinon states $|j\ \mathrm{T}\rangle$ and $|j\ \mathrm{L}\rangle$. Then I will expose the quantum field theory approach that the theoretical team has used to understand the low-energy properties of the system, the nature of the transition and more particularly to get a deeper understanding about the nature of the excitations.

4.7.1 Description of the excitations under a transverse magnetic field

To understand the evolution of the excitations throughout the transition occurring under a transverse field applied along the b-axis, it is instructive to rewrite the Hamiltonian given by Eq. (4.6) in the rotating frame $(\vec{\ell}, \vec{b}, \vec{t})$ shown in Fig. 4.13(a). New operators $(\sigma^\ell, \sigma^b, \sigma^t)$ are introduced, along with $\sigma^t = (\sigma^+ + \sigma^-)/2$ and $\sigma^b = (\sigma^+ - \sigma^-)/2i$, the quantization axis $\hat{\ell}$ pointing along the ordered magnetic moment. This yields, for the

intrachain part of the Hamiltonian (XXZ and the Zeeman term of Eq. (4.6)):

$$\begin{aligned}\mathscr{H} &= \sum_n K^{\pm}(\sigma_n^+\sigma_{n+1}^- + \sigma_n^-\sigma_{n+1}^+) \\ &+ K^{\pm\pm}(\sigma_n^+\sigma_{n+1}^+ + \sigma_n^-\sigma_{n+1}^-) \\ &+ K^{\ell\pm}(\sigma_n^\ell\sigma_{n+1}^+ + \sigma_n^\ell\sigma_{n+1}^-) + K^{\ell\ell}\sigma_n^\ell\sigma_{n+1}^\ell \\ &- \mu_B H h^\ell \sigma_n^\ell - \mu_B H(h^+\sigma_n^+ + h^-\sigma_n^-)\end{aligned} \tag{4.17}$$

with

$$\begin{aligned}K^{\ell\ell} &= J(\varepsilon\cos^2\psi + \sin^2\psi) \\ h^\ell &= (-1)^n g_{ba}\cos\psi + g_{bc}\cos\left(\pi\frac{2n-1}{4}\right)\sin\psi \\ K^{\ell\pm} &= J(1-\varepsilon)\sin\psi\cos\psi \\ h^\pm &= \left[-g_{ba}(-1)^n\sin\psi + g_{bc}\cos\left(\pi\frac{2n-1}{4}\right)\cos\psi\right]/2 \pm ig_{bb}/2 \\ K^\pm &= J\frac{\varepsilon(1+\sin^2\psi)+\cos^2\psi}{4} \\ K^{\pm\pm} &= J\left(\frac{1-\varepsilon}{4}\right)\cos^2\psi\end{aligned}$$

In the high field phase, the quantization axis has the same direction as the ordered moments along the a-axis (which means that now $\vec{\hat{\ell}} = \vec{a}$ and $\vec{\hat{t}} = \vec{c}$), and thus the Hamiltonian takes the peculiar form:

$$\begin{aligned}\mathscr{H} = \sum_n J\varepsilon\sigma_n^a\sigma_{n+1}^a + J\frac{(\varepsilon+1)}{4}(\sigma_n^+\sigma_{n+1}^- + \sigma_n^-\sigma_{n+1}^+) + J\frac{(\varepsilon-1)}{4}(\sigma_n^+\sigma_{n+1}^+ + \sigma_n^-\sigma_{n+1}^-) \\ -\mu_B H\left[(-1)^n g_{ba}\sigma_n^a + g_{bc}\sigma_n^c\cos\left(\pi\frac{2n-1}{4}\right) + g_{bb}\sigma_n^b\right]\end{aligned}$$

While complicated at first glance, this form of the Hamiltonian proves meaningful to understand, from a physical point of view, how the confined spinon pairs $|j, S_\ell\rangle$ evolve upon the field. For instance, $K^{\ell\ell}$ renormalizes the energies of the spinons from J to εJ. $K^\pm$ allows each kink forming the bound state to hop (independently) by *two* sites. This term does not mix the $S_\ell = 0, \pm 1$ sectors and plays the role of kinetic energy. It evolves from $\varepsilon J/2$ in zero field up to $(1+\varepsilon)J/4$ above H_c. The staggered field contribution developing with the external field, that enters h^ℓ (but also $h^\pm$), behaves as a confinement potential, in a similar way as the inter-chain interaction J' does in zero field. The remaining terms are more complicated: $K^{\ell\pm}$ and $h^\pm$ move the spinons by *one* site and entangle the $S_\ell = \pm 1$ with the $S_\ell = 0$ sectors. This coupling is responsible for the mixing of the $|1, S_\ell = 0\rangle$ and $|2, S_\ell = \pm 1\rangle$ states.

The most peculiar term (absent in the isotropic Heisenberg case where $\varepsilon = 1$) is $K^{\pm\pm}$. It induces two spin-flips, changing S_ℓ by ± 2, and thus increases the number of spinons. For instance, as shown in Fig. 4.26, when acting on the $|j, S_\ell = 0\rangle$ states, this term essentially gives rise to 4 spinons states carrying a total magnetization $S_\ell^{tot} = \pm 2$. This explains why the low-energy S_{aa} fluctuations are not probed in the high field phase as the neutron selection rule imposes a difference of magnetization $\Delta S = \pm 1$ for the scattering process.

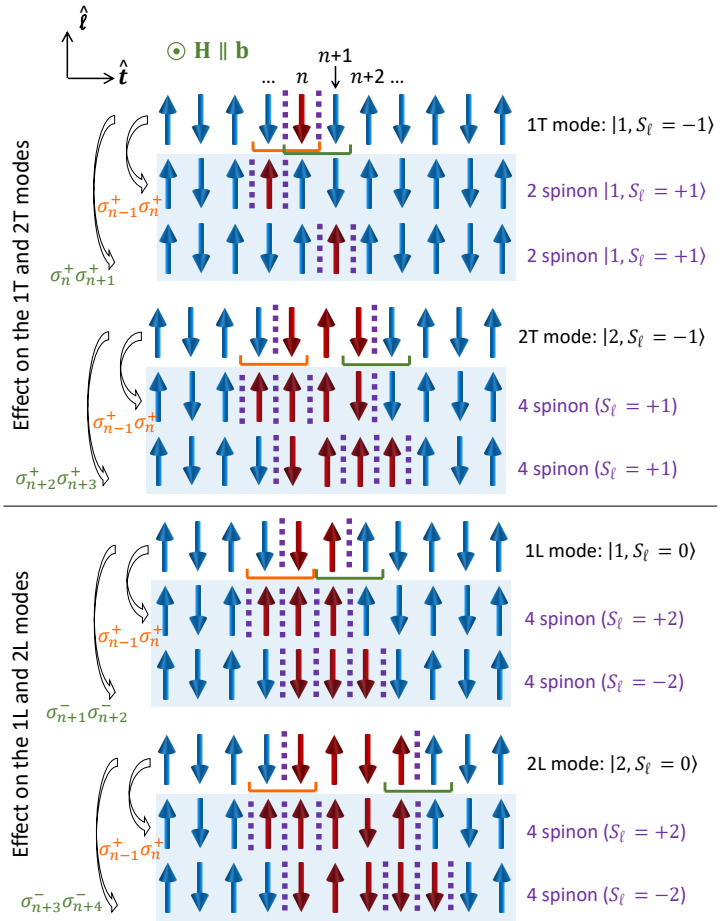

Figure 4.26: **Creation of multi-spinon states.** Cartoons explaining the effect of the $\sigma^\pm_n\sigma^\pm_{n+1}$ operator on the L and T excitations having the two smallest numbers N of flipped spins, with the quantization axis $\vec{\hat{\ell}}$ along the staggered field direction (a-axis).

The cartoon shown in Fig. 4.26 shows further that $K^{\pm\pm}$ also couples the two $|1, S_\ell = \pm 1\rangle$ states with each other, resulting in new eigenstates constructed as:

$$\frac{1}{\sqrt{2}}(|1, S_\ell = +1\rangle + |1, S_\ell = -1\rangle)$$

for the lower branch, and

$$\frac{1}{\sqrt{2}}(|1, S_\ell = +1\rangle + i|1, S_\ell = -1\rangle)$$

for the higher one. Finally, $K^{\pm\pm}$ moves the two spinons by one site. Physically, this means that the new states get an extra kinetic energy provided the two spinons hop simultaneously. Although the physical mechanism is different, these quasiparticles become analogous to the kinetic bound state observed in the Ising-like FM compound $CoNb_2O_6$ [Col+10].

Finally one can see that while at zero-field, the low-energy modes are spinon pairs (which are deconfined for a pure one-dimensional system), in the high field phase, the

lowest energy mode given by the action of $K^{\pm\pm}$ is a linear combination of bound spinons (see the application of $K^{\pm\pm}$ on the $|1\ \mathrm{T}\rangle = |1, S_\ell = -1\rangle$ in Fig. 4.26). Therefore, in the high field phase, the lowest energy mode is not two deconfined spinons carrying a spin $S_\ell = \pm 1/2$ but rather a four spinons state formed by two deconfined pairs of bound spinons, each of them carrying a spin $S_\ell = \pm 1$. Thus, at first sight, the excitations in the low and high field regime have a different nature. It becomes even clearer when we treat this problem by means of quantum field theory as I will explain now.

4.7.2 Quantum field theory: Dual sine-Gordon model and topological excitations

Here, I will expose the quantum field theory approach (bosonization technique) that Thierry Giamarchi and Shintaro Takayoshi developped to understand the low-energy properties in this system.

The validation of the model of Eq. ((4.6)) from the iTEBD calculations allowed them to use field theory to describe the nature of the transition in a more transparent way. Here I would like to emphasize that the field theory technique is not a quantitative approach but a qualitative one, rather used to bring us back to universal and well known equations such as the sine-Gordon model which describes the XXZ model without an external magnetic field. As already exposed in Chap. 1, the sine-Gordon model has the following form:

$$\mathscr{H} = \frac{v}{2\pi}\int dz\left[\frac{1}{K}\left(\frac{d\phi(z)}{dz}\right)^2 + K\left(\frac{d\theta(z)}{dz}\right)^2\right] - \frac{2\lambda}{(2\pi\alpha)^2}\int dz\cos 4\phi(z) \tag{4.18}$$

where 2θ and ϕ are two dual bosonic fields [7] that can be viewed semi-classically through Fig. 4.27(a) as the polar and azimutal angles of a staggered magnetization vector in the real space, $z = nc/4$ with c the lattice constant along the chain direction, α is a non universal constant, v is the spinon velocity, K is the Luttinger parameter, and λ is a contant having a dimension of energy [GP04]. These parameters (v, K, λ) are a function of the anisotropy parameter ε, and they are renormalized when the uniform field along $\vec{b}$ is applied. However, there is no simple analytic form to represent v, K, λ as a function of ε and of the strength of the uniform field. The staggered field along $\vec{a}$ also gives another relevant term which is developped using the bosonization technique [GP04]:

$$\sum_j (-1)^j S_j^x \Rightarrow \frac{1}{\sqrt{2\pi\alpha}}\int dz\cos\theta \tag{4.19}$$

A dual-field double sine-Gordon model is then obtained to describe $BaCo_2V_2O_8$ in an external field along $\vec{b}$:

$$\boxed{\begin{aligned}\mathscr{H}^{\text{eff}} = &\frac{v}{2\pi}\int dz\left[\frac{1}{K}\left(\frac{d\phi(z)}{dz}\right)^2 + K\left(\frac{d\theta(z)}{dz}\right)^2\right]\\ &-\frac{2\lambda}{(2\pi\alpha)^2}\int dz\cos 4\phi(z) - \frac{g_{ba}\mu_B H}{\sqrt{2\pi\alpha}}\int dz\cos\theta(z)\end{aligned}} \tag{4.20}$$

The effect of the Zeeman coupling with the uniform field along the b-axis is renormalized into these parameters [AO99]. Since the Zeeman term of the four-site periodic field

[7] The term "dual" comes from the quantum nature of the spin. Indeed, the precise determination of one of the two angles makes the measurement of the other one imprecise. In other words these two fields do not commute $[\theta, \phi] \neq 0$.

along the c-axis is irrelevant, it does not appear in Eq. (4.20). The effect of this field is actually negligibly small as shown by the numerics.

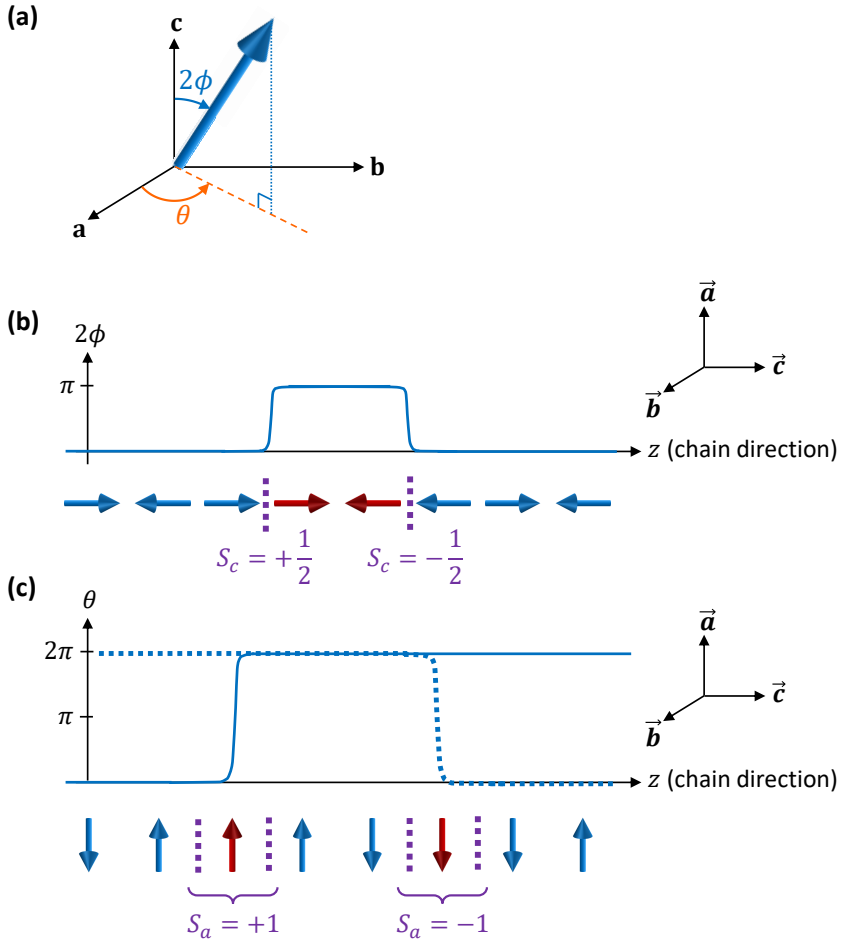

Figure 4.27: **Two dual topological objects.** (a) A qualitative interpretation of the two fields $\phi(z)$ and $\theta(z)$ entering in the field theory description. The quantum nature of a spin 1/2 makes it impossible to determine both angles with an infinite accuracy, the two angles playing a role similar to canonically conjugate variables. (b) Topological excitations in the low field phase (well below the transition). They can be identified with the spinon excitations carrying a topological index $S_c = \pm 1/2$. (c) Topological excitations in the high field phase (far above the transition but still well below the saturation) corresponding to solitons carrying a topological index of $S_a = \pm 1$.

While complicated at first sight, let me explain a bit more qualitatively what this equation means. The first integral, as explained in Chap. 1, is the well known Tomonaga Luttinger Liquid Hamiltonian which describes a Heisenberg chain (and more generally any massless one-dimensional system). The second integral with a $\cos 4\phi(z)$ describes the Ising-like anisotropy of the system and the third one with a $\cos\theta(z)$ describes the effective staggered field along $\vec{a}$. The prefactor of this last integral is proportional to the applied magnetic field H. In the low-field phase, when $H \to 0$, the integral in $\cos 4\phi(z)$ dominates the one in $\cos\theta(z)$. Therefore, to minimize the total energy of the system, $\phi(z) \to 0$, which means that all the spins are along the c-axis. On the contrary, in the

high field phase, i.e. when $\mu_0 H > \mu_0 H_c = 10$ T, the integral in $\cos\theta(z)$ now dominates the other one and thus $\theta(z) \to 0$. Now the spins are along the a-axis. The transition happens when those two terms are equal.

Through this effective Hamiltonian, it became possible to understand the nature of the excitations and their different topological nature (see Fig. 4.27(b-c)). Indeed, the topological excitations in the low field phase (well below the transition) correspond to solitons in the field $4\phi(z)$ linking one of the minima of the $\cos 4\phi(z)$ to the next one. Using the bosonization representation of the spin, they can be identified with the spinon excitations. They carry a spin $S_c = \pm 1/2$ corresponding to the topological index of the excitation. In the high field phase (far above the transition but still well below the saturation), the elementary excitations now correspond to the solitons of the $\cos\theta(z)$, and are thus dual of the low field phase excitations. They carry an index of $S_a = \pm 1$ since $\theta(z)$ changes from 0 to 2π (instead of 0 to π for the field 2θ).

To summarize, two dual excitations compete with each other and the domination of one of them on the other one can be tuned through the value of the applied magnetic field. When the topological excitation carrying an index of $S_a = \pm 1$ fully dominates the spinons ones carrying an index of $S_c = \pm 1/2$, the quantum phase transition occurs. This transition has a topological nature as it comes from the competition between two different topological objects.

4.8 Discussion et conclusions

As already mentioned above, the nature of the excitations in this high field phase has been studied in parallel to our work by other groups in both compounds $SrCo_2V_2O_8$ [Wan+16] and $BaCo_2V_2O_8$ [Mat+17].

In the former study, the excitations were probed by THz spectroscopy at much higher energy and only at the ZC point $\vec{Q}$=(0, 0, 0). As the phase transition was believed to be an order-disorder transition, and thus a paramagnetic phase at high field, it has led to a misunderstanding concerning the nature of the excitations. Indeed the explanation proposed by Wang et *al.* was a deconfinement of the spinons as the interchain interaction would not be effective in the high field phase compared to the applied magnetic field. The problem here was the forgetting of the effective staggered magnetic field which is the key ingredient in this phase transition. In the other study, the excitations were probed by means of neutron scattering experiments. Contrary to the THz study, the staggered field was here taken into account. Both elastic and inelastic neutron scattering experiments have been done and the experimental results are rather similar to ours. However Matsuda et *al.* did not use polarized neutrons and their theoretical analysis was more limited than in our study. Moreover they were focusing essentially on the dispersion spectrum in the high field phase, rather than on the field dependence of the excitations which was the key to understand the topological nature of the transition.

To conclude on this chapter, the analysis of the static and dynamical properties measured experimentally under a transverse field and the agreement with numerics show that the quantum phase transition occuring in $BaCo_2V_2O_8$ is described by the dual field double sine-Gordon model. This provides an explanation of the rather mysterious field-induced transition and enlightens its topological nature. Indeed this transition arises from the competition between two excitations having a different topological nature. This competition (how one excitation dominates the other one) can be tuned through the value of the

applied magnetic field. Let us mention that $BaCo_2V_2O_8$ is the first experimental realization of such kind of topological transition. From a theoretical point of view, the study of the transition itself is a challenging problem. A complete study, in particular taking into account the effective 3D coupling beyond mean-field is still lacking and maybe Quantum Monte Carlo (QMC) calculations could solve this problem.

Chapter 5

$BaCo_2V_2O_8$ under a longitudinal magnetic field

Sommaire

5.1 Summary

5.1.1 Abstract

This chapter is devoted to the study of the $BaCo_2V_2O_8$ compound under a longitudinal magnetic field (i.e. parallel to the easy-axis of magnetization and thus to the *c*-axis). This orientation of the field leads to a totally different behavior compared to the one perpendicular to the easy-axis (see Chap. 4). I will explain first the context and the motivations of this study. Secondly I will recall the state of the art of the studies on $BaCo_2V_2O_8$ under this configuration of the field. I will then show the diffraction experiment carried out up to 25 T. Then I will present our inelastic neutron scattering results showing the spin-dynamics of $BaCo_2V_2O_8$ in the Néel and the Tomonaga-Luttinger liquid (TLL) phases and our related numerical calculations. Finally I will conclude with an interpretation of the data.

5.1.2 Résumé en français

Le cinquième chapitre présente l'étude de $BaCo_2V_2O_8$ sous champ magnétique longitudinal, i.e. parallèle à l'axe Ising. Il a été montré théoriquement que les systèmes 1D de type Ising peuvent être amenés dans une phase non gappée dite de liquide de Tomonaga Luttinger (TLL) en appliquant un champ magnétique longitudinal. Du fait de son paramètre d'anisotropie modéré, la transition de phase quantique entre la phase gappée et non gappée se produit dans ce composé pour une valeur du champ de $\mu_0 H_c \simeq 4$ T, valeur facilement accessible lors d'expériences de diffusion des neutrons.

De plus, il a été prédit que pour des systèmes anisotropes, les corrélations spin-spin longitudinales incommensurables, à la fois statiques et dynamiques, dominent les corrélations transverses commensurables entre $\mu_0 H_c$ et un second champ critique $\mu_0 H^*$. Ainsi, du fait des intéractions interchaînes stabilisant un éventuel ordre magnétique, l'état fondamental observé dans $BaCo_2V_2O_8$ au dessus de 4 T correspond à une phase où l'amplitude des spins est modulée de facon incommensurable, dite phase LSDW (onde de densité de spin longitudinale) en accord avec la théorie TLL. Au dessus de $\mu_0 H^* \simeq 9$ T, l'état fondamental observé correspond à un ordre antiferromagnétique commensurable transverse (perpendiculaire à l'axe Ising) auquel se superpose une composante ferromagnétique parallèle au champ appliqué.

Le travail effectué au cours de cette thèse a été d'étudier la dynamique de spins dans la phase LSDW afin de voir si celle-ci correspond à la dynamique attendue pour un TLL. Pour ce faire, nous sommes allés faire une expérience de diffusion inélastique des neutrons sur un spectromètre au Paul Sherrer Institut en Suisse nous permettant d'atteindre un champ magnétique horizontal de 6.8 T.

Nous avons tout d'abord mesurer la dépendence en champ magnétique des excitations. Nous avons observé que les excitations transverses se scindent en deux branches dans la phase Néel: l'une qui augmente en énergie lorsque le champ augmente et une autre qui diminue pour atteindre un minimum à la transition de phase. Contrairement au champ transverse, la dépendence en champ magnétique est linéaire. Ceci indique que le champ scinde les excitations transverses par l'effet Zeeman. Contrairement aux excitations transverses, les excitations longitudinales n'ont pas de dépendance en champ magnétique dans la phase Néel. Ces observations sont cohérentes avec la nature des excitations. Nous avons ensuite mesuré le spectre des excitations pour différentes valeurs du champ magnétique.

Les spectres dans la phase LSDW sont très différents de celui obtenu à champ nul. En effet, tout le poids spectral est maintenant concentré dans une petite portion de la zone de Brillouin et en énergie. De plus, le maximum du poids spectral et le minimum en énergie sont maintenant au point incommensurable, point qui s'éloigne du point commensurable lorsque le champ magnétique augmente. La dynamique de spins et son évolution sous champ correspondent bien à celles attendues pour un TLL. De plus, la comparaison avec les calculs iTEBD effectués par Shintaro Takayoshi et Thierry Giamarchi nous ont permis de confirmer que la majorité du poids spectral est contenue dans les fluctuations de spins longitudinales. Ce résultat est hautement non trivial car les systèmes magnétiques conventionnels et classiques préfèrent généralement fluctuer perpendiculairement à la fois au champ magnétique et au moment ordonné. Dans le cas de $BaCo_2V_2O_8$, les fluctuations de spins sont préférentiellement dans la direction du champ magnétique et du moment ordonné. Ceci confirme le fort caractère quantique de $BaCo_2V_2O_8$. Alors que la phase TLL a été beaucoup étudié dans des systèmes de type Heisenberg, $BaCo_2V_2O_8$ est le premier composé à chaînes de spins anisotropes où le spectre des excitations a été étudié dans cette phase non gappée.

5.2 Introduction, context and motivations

5.2.1 XXZ AF spin-1/2 chain in a longitudinal magnetic field

XXZ chains with spins 1/2 have been a subject of great interest as no long-range order is expected at zero temperature due to quantum fluctuations. Their ground state belongs to a universality class called a Tomonoga-Luttinger liquid (TLL) under zero and finite magnetic field for the Heisenberg and the XY case or under finite magnetic field applied along z for the Ising-like spin chain, i.e. a longitudinal magnetic field applied along the easy axis. Two types of spin-spin correlation functions $< S^x(\vec{r_i},0)S^x(\vec{r_j},t) >$ (transverse) and $< S^z(\vec{r_i},0)S^z(\vec{r_j},t) >$ (longitudinal) are present in this state. In particular we have for the static correlations $< S_0^x S_r^x > \simeq (-1)^r r^{-\eta_x}$ and $< S_0^z S_r^z > -m^2 \simeq \cos(2k_f r) r^{-\eta_z}$ [BIK86; Mül+81; Hal80]. The first ones can be associated to the staggered correlations and thus to the usual Néel order. The latter have no classical analogue and are typical of quantum spin chains. Here m is the magnetization per spin, r the distance between two spins and $2k_f = \pi(1-m)$ the incommensurate wave number characteristics of the longitudinal spin correlations, which scales with the field-induced ferromagnetic component of the magnetization m. η_z and η_x are the TLL exponents which fulfill the relation $\eta_x\eta_z = 1$. The $(H-\Delta)$ phase diagram of a XXZ spin-1/2 chain is pictured in Fig. 5.1

For $-1 < \Delta < 1$ at zero-field, the transverse correlations dominate. The maximum of the spectral weight for low energy excitations is at $q = \pi$. By applying the magnetic field H, both T and L correlation functions are non-zero at commensurate and incommmensurate positions $q = \pi$ and $2\pi m$ for the transverse correlations and $q = 0$ and $\pi(1-2m)$ for the longitudinal ones [1](I will explain in the next subsection where this incommensurability comes from). However the dominant spectral weight still occurs for the transverse correlation functions at $q = \pi$. In presence of interchain coupling J', an orderering is possible and corresponds to a transverse commensurate ordered state.

For $\Delta > 1$, one can drive Ising-like systems to the TLL phase by applying a sufficiently large longitudinal magnetic field ($H > H_c$ where the gap closes). The dominant correlation function is the longitudinal one $< S^z(\vec{r_i},0)S^z(\vec{r_j},t) >$, which decays the slowest at the incommensurate point $q = \pi(1-2m)$. The ground state in presence of J' is thus an incommensurate spin-density wave (SDW). When H further increases and reaches the value of H^*, the transverse and longitudinal correlations decay at the same rate, and above H^* the transverse correlations $< S^x(\vec{r_i},0)S^x(\vec{r_j},t) >$ dominate again. Hence, the ground state with a finite J' becomes a transverse AF order.

Close to the commensurate-incommensurate transition (i.e. close to H_c), the commensurate correlations of the gapped AF order and the incommensurate longitudinal correlations of the SDW phase compete, resulting in more or less (i.e. rounded) step-like modulation of the magnetic moments amplitude. Qualitatively, the magnetic field forces the spins to align along its direction. It will induce spin-flips in the chain, thus creating pairs of spinons which will spread over a few sites only, to form an incommensurate lattice (i.e. the ratio of the magnetic period to the atomic lattice one is an irrational number). When the field further increases, it will create more and more defects yielding a sinusoidal modulation of the magnetic moments amplitude and thus an incommensurate longitudinal spin density wave (SDW) order in presence of interchain interaction.

[1] This is also true for $\Delta = 1$.

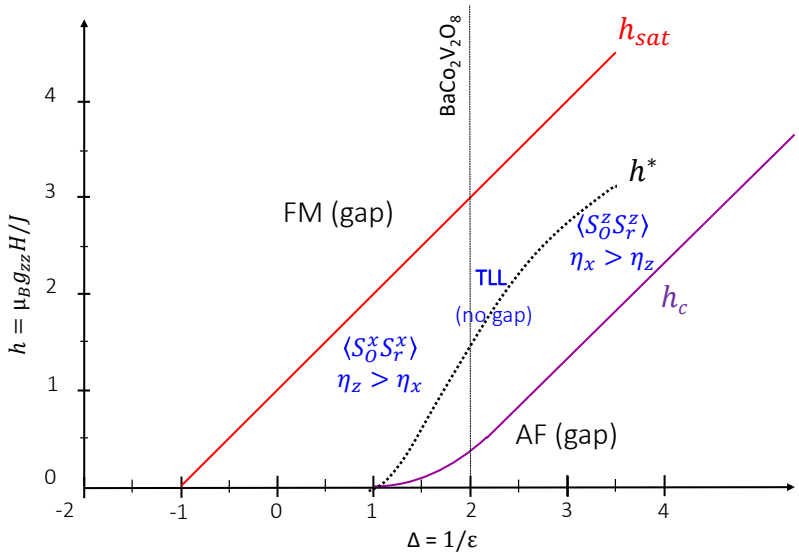

Figure 5.1: **Phase diagram for an XXZ spin 1/2-chain:** Anisotropy $\Delta = 1/\epsilon$ vs magnetic field in reduced units $h = \mu_B g_{zz} H/J$ applied along $\vec{z}$. For $\Delta < -1$, the system is always in a gapped ferromagnetic phase. For $-1 \leq \Delta \leq 1$, the system is already in a TLL phase at zero-field where the static transverse correlations $\langle S_0^x S_r^x \rangle$ are the dominant ones and this holds up to the saturation field h_c. For $\Delta > 1$, i.e. for magnetic systems showing an Ising-like anisotropy along the z-axis, the system enters in a TLL phase above a first critical field h_{sat} when the gap is closed but, contrary to the previous case ($-1 \leq \Delta \leq 1$), the IC static longitudinal correlations $\langle S_0^z S_r^z \rangle$ dominate the transverse ones until a second critical field h^* (pointed out by the black dashed line). This phase has no semi-classical analogue. Above h^*, a spin-flop transition occurs until the saturation field h_{sat}. In this phase, the situation is reversed, i.e. $\langle S_0^x S_r^x \rangle$ dominate. The vertical black dashed line represents the case of $BaCo_2V_2O_8$ where $\Delta = 1/\epsilon \simeq 2$.

The TLL phase has been investigated in some AF spin-1/2 chains, namely in the well known Heisenberg compounds $KCuF_3$ [Lak+05], $CuSO_4 \bullet 5D_2O$ [Mou+13] and $Cu(C_6D_5COO)_2 \bullet 3D_2O$ [Den+97], in the the alternate Heisenberg chain $Cu(NO_3)_2 \bullet 2.5D_2O$ which can be mapped onto an XXZ chain with $\Delta = 1/2$ [Gre+07], and in the XY-like spin-1/2 chain Cs_2CoCl_4 with $\Delta = 0.12$ [Ken+02]. In all these systems, the transverse correlations are always dominant. This phase has been also investigated in two spin-ladder systems, namely $(C_5H_{12}N)_2CuBr_4$ (BPCB) [Kla+08; Rüe+08; Bou+11] and $(C_7H_{10}N)_2CuBr_4$(DIMPY) [Hon+10; Sch+12; Sch+13], which can be mapped onto a spin-1/2 XXZ chain with an easy plane anisotropy [GT99]. Here again, the transverse correlations are always dominant. All these studies have confirmed the different theoretical predictions of the TLL phase, especially the presence of incommensurate fluctuations when a magnetic field is applied.

One may wonder if there is an AF Ising-like spin-1/2 chain which would allow to probe microscopically (by means of neutron scattering for example) this TLL phase where the longitudinal spin-spin correlations dominate? Some Ising-like AF chains such as $CsCoCl_3$ and $CsCoBr_3$ could be at first sight good candidates, but their strong anisotropy $\Delta \simeq 10$ leads to a critical field of $\mu_0 H_c \simeq 75$ T, impossible to reach in neutron scattering

experiments.

Because of its moderate anisotropy ($\epsilon \simeq 0.56 \Leftrightarrow \Delta \simeq 1.8$), $BaCo_2V_2O_8$ allows us to investigate this TLL phase where the longitudinal fluctuations dominate with a convenient critical field of $\mu_0 H_c \simeq 4$ T, easily reachable. As we will see in the next section, this material indeed exhibits interesting physics under a longitudinal magnetic field. Note that because of weak interchain interactions, a long-range order actually appears at finite temperature. The signature of the spin correlations discussed above were shown to be reflected in the nature of the ordered phases stabilized under a magnetic field (applied along the c-axis) and the question is whether the excitations will still reflect the TLL spin-dynamics. $BaCo_2V_2O_8$ is the first realization of such a TLL phase with the longitudinal correlations dominating on the transverse ones in which the spin dynamics can be investigated by neutron scattering.

I will now explain what is expected concerning the excitations of an AF anisotropic spin-1/2 chain for this orientation of the field.

5.2.2 Spin-dynamics of XXZ spin-1/2 chain under a longitudinal magnetic field

The dispersion of the excitations in the TLL phase for an AF Heisenberg spin-1/2 chain has been studied theoretically almost fourty years ago by Müller using Bethe ansatz calculations [Mül+81] and only recently for an AF Ising-like spin-1/2 chain [Yan+17]. It has been predicted that the minima of the 2-spinon continuum (at zero energy) appear both at commensurate and incommensurate points in the reciprocal space, contrary to the zero-field case where they appear at $q = \pi$ and $q = 0$ (for a linear spin 1/2 chain). To understand this incommensurability, let me take the example of an XY spin chain under a field applied along z and do a Jordan-Wigner fermionization (explained in section 1.5.1) to map a spin-1/2 chain onto a spinless fermions representation. The XY-case is considered for more convenience as it leads to a free electron-hole band theory. Indeed, through this transformation, one can go from a spin-1/2 chain to a spinless fermion half filled band system where a spin $S = 1/2$ corresponds to an electron while a spin $S = -1/2$ corresponds to a hole. Using this fermionization for a linear spin-1/2 chain with the constant lattice spacing $a = 1$ under a field applied along the z-direction, the Hamiltonian writes as:

$$\mathscr{H} = \sum_j \frac{J}{2}\left[S_j^+ S_{j+1}^- + S_j^- S_{j+1}^+\right] - \sum_j \mu_B g_{zz} H S_j^z \tag{5.1}$$

$$= \mathscr{H}_{XY} + \mathscr{H}_{field} \tag{5.2}$$

H = 0 case: Let me recall what has been seen in section 1.5.1. Here, we only focus on the XY-Hamiltonian, i.e. $H = 0$. By using the Jordan Wigner transformations, we get:

$$\mathscr{H}_{XY} = -J/2 \sum_j \left(c_j^\dagger c_{j+1} + c_j c_{j+1}^\dagger\right) \tag{5.3}$$

Using the Fourier transform of the c_j operators, one can show that the above Hamiltonian writes as:

$$\begin{aligned} \mathscr{H}_{XY} &= \sum_k \hbar\omega(k) c_k^\dagger c_k \\ \text{with} \quad \hbar\omega(k) &= -J\cos(ka) \end{aligned} \tag{5.4}$$

where a is the lattice spacing.

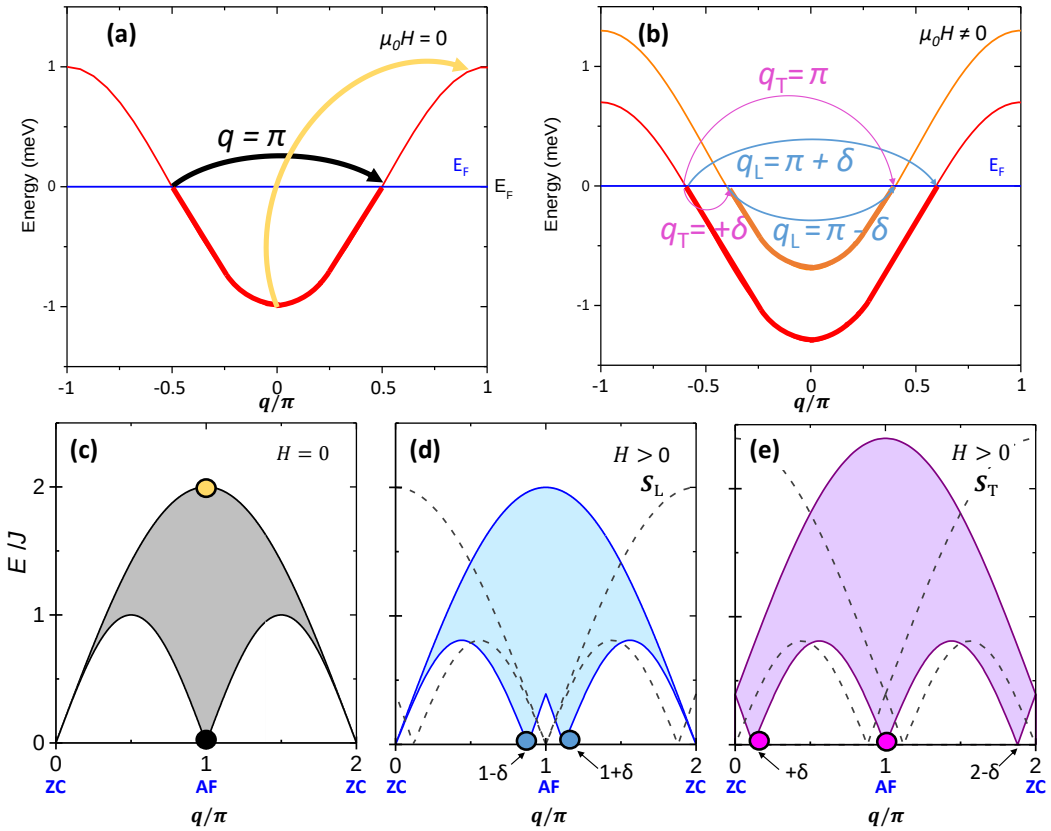

Figure 5.2: **Construction of the dispersions expected for an XY spin-1/2 chain through the Jordan Wigner fermionization**. (a) Particle-hole band obtained through Jordan-Wigner transformations. Two specific particle-hole excitations, at zero-field, are pointed out by black and yellow arrow: they correspond to zero-energy and maximum energy excitations respectively. E_F denotes the Fermi level (set to zero). The fermions are located below E_F (thick line) while the holes are located above (thin line). (b) The applied longitudinal field H can be seen as a chemical potential which splits the degeneracy of the electron-hole bands. The intraband and interband zero-energy excitations (corresponding to longitudinal $S_{\parallel}$ and transverse $S_{\perp}$ fluctuations respectively) are pointed out by the blue and pink arrows. The incommensurability δ arises from the splitting of the bands. (c) 2-spinon continuum expected for an AF XY spin-1/2 chain at zero-field. Black and yellow points are the excitations corresponding to the black and yellows arrows. (d-e) Dispersion spectrum of the longitudinal and transverse fluctuations (S_L and S_T) expected for an AF XY spin-1/2 chain when $H > 0$. Some of the incommensurate positions where the system is gapless are pointed out by the blue and pink points (associated to the blue and pink arrows). The excitation spectra shown in panels (c-e) are the same in all the TLL region and thus in particular for Ising-like spin-1/2 chains with $H_c < H < H_{sat}$, but the energies, which depend on Δ are then renormalized (e.g. multiplied by $\pi/2$ for the Heisenberg case). The black dashed lines in (d) and (e) are showing the effect of the folding in $BaCo_2V_2O_8$.

Hence the XY-model can be mapped exactly to a tight binding Hamiltonian with spinless fermions and it is possible to build the 2-spinons dispersion spectrum from it as

shown in Figs. 5.2(a),(c). However, one has to keep in mind that the degeneracy between the spinons carrying a total magnetization $S^z = \pm 1$ is still present.

$\mathbf{H \neq 0}$ case: The Hamiltonian now writes as:

$$\mathscr{H} = -J/2 \sum_j \left(c_j^\dagger c_{j+1} + c_j c_{j+1}^\dagger \right) - \mu_B g_{zz} H \sum_j c_j^\dagger c_j \tag{5.5}$$

where $c_j^\dagger c_j$ corresponds to the particle density. By using the Fourier transform, this leads to:

$$\begin{aligned} \mathscr{H} &= \sum_k \hbar\omega(k) c_k^\dagger c_k \\ \text{with} \quad \hbar\omega(k) &= -J\cos(ka) - \mu_B g_{zz} H \end{aligned} \tag{5.6}$$

In the case of spins, the magnetic field lifts the degeneracy due to the time reversal symmetry for spins by the Zeeman splitting. In fermionic language, the magnetic field can be viewed as a chemical potential. This spinless Hamiltonian of Eq. (5.5) is written in such a way to obey the particle-hole symmetry which corresponds to the time-reversal symmetry for spins. Hence, the chemical potential will break this symmetry by increasing one of the Fermi levels in one of the two degenerated bands and lowering the other one as represented in Fig. 5.2(b): one band is shifted upward and the other one downwards, with respect to the Fermi level, still located at $E = 0$.

Then the excitations conserving the total number of particles, i.e. the longitudinal excitations (labelled by S_L) or in other words intraband excitations (leading to a difference of magnetization with the ground state of $\Delta S^z = 0$) will give rise to incommensurate and commensurate fluctuations reaching zero-energy at $q = \pi \pm \delta = \arccos(\mu_B g_{zz} H/J)$ with $\delta = 2\pi m$ and $q = 0$ and 2π respectively (see Fig. 5.2(b)). Excitations non conserving the number of particles, i.e. the transverse excitations labelled by S_T, in other words interband excitations (leading to a difference of magnetization of $\Delta S^z = \pm 1$) give rise to fluctuations reaching zero-energy at $q = \pi$ and at the incommensurate points δ and $2\pi - \delta$ (see Fig. 5.2(b)). From all possible intraband and interband excitations, one can, as in the zero-field case, reconstruct the longitudinal S_L and transverse S_T dispersion spectra expected for a spin-1/2 chain in a magnetic field along z (see Fig. 5.2(d-e)).

Let us return to the case of $BaCo_2V_2O_8$ which is an Ising-like antiferromagnet. At zero-field, the system shows discretized energy modes due to the interchain coupling and is gapped at zero-field due both to the Ising anisotropy ($\Delta \simeq 2$) and to the interchain interactions. This means that this gap must be closed by applying the magnetic field until the critical field $\mu_0 H_c$ (see Fig. 5.1).

I recall that there is a folding of the dispersion in $BaCo_2V_2O_8$. One can picture this effect by the dashed black lines plotted in Fig. 5.2(d-e). Before showing my results on the spin-dynamics, let me now present the state of the art of $BaCo_2V_2O_8$ under a longitudinal field established before my PhD, as well as a preliminary neutron diffraction results under very high magnetic field.

5.3 Phase diagram of $BaCo_2V_2O_8$ under a longitudinal magnetic field

5.3.1 State of the art

A lot of studies on $BaCo_2V_2O_8$ under a longitudinal field have been done prior to my PhD. Kimura et *al.* determined the $(H-T)$ phase diagram of $BaCo_2V_2O_8$ under a longitudinal magnetic field by means of high-field magnetization and specific heat measurements [Kim+06; Kim+08b; Kim+08a] (see Fig. 5.3(a-b)). Another interesting study is the work of Okunishi and Suzuki in which they have calculated the TLL exponents η_x and η_z as a function of the applied field [OS07] (see Fig. 5.3(c)). They have shown that an inversion of these exponents occurs for the case of $BaCo_2V_2O_8$ where the longitudinal correlations dominate the transverse ones in the low field region $H_c < H < H^*$ ($\eta_x > \eta_z$ below H^*, $\eta_x < \eta_z$ above).

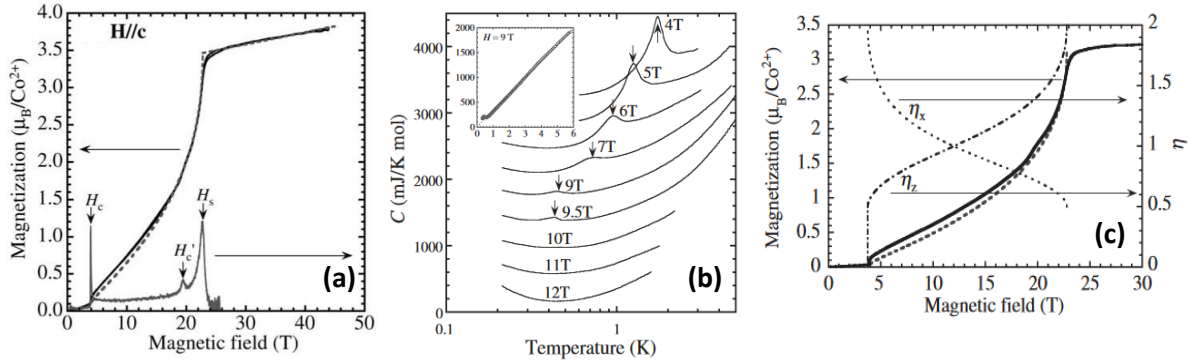

Figure 5.3: **Studies of Kimura et *al.*** (a) Magnetization M versus field H and corresponding field derivative dM/dH of $BaCo_2V_2O_8$ at 1.3 K measured for $\vec{H}||\vec{c}$. Solid and dashed curves are experimental and calculated magnetizations respectively. Figure extracted from [Kim+06]. (b) Temperature dependence of the specific heat of $BaCo_2V_2O_8$ for $\vec{H}||\vec{c}$. The inset shows an extended figure of the specific heat observed at 9 T. (c) Magnetization curve of $BaCo_2V_2O_8$ for $\vec{H} \parallel \vec{c}$ and the calculated TLL exponents. Solid and gray dashed lines are the experimental and theoretical magnetization curves respectively. Figures (b) and (c) extracted from [Kim+08a].

From these calculations and their measurements, Kimura et *al.* proposed that the phase transition occuring at $\mu_0 H \simeq 4$ T corresponds to the change from a Néel phase (commensurate) to a longitudinal incommensurate phase transition, reflecting the quantum nature of the spin-1/2 XXZ chain. However at that point, no microscopic measurements had confirmed this assumption. The first realization of such measurements by neutron scattering experiment on a single crystal was done by Kimura et *al.* [Kim+08a] but because of the setup of the experiment, only the magnetic reflection 4 0 3 could be reached. Nevertheless, by increasing the magnetic field, they have seen magnetic Bragg satellites of the form $4\,0\,3 \pm \delta$ appearing above the critical field confirming that this new phase corresponds to an incommensurate long range order (see Fig. 5.4(a)).

In another single-crystal neutron diffraction study, Canévet et *al.* were able to refine the magnetic structure in this new phase by collecting many reflections above the critical

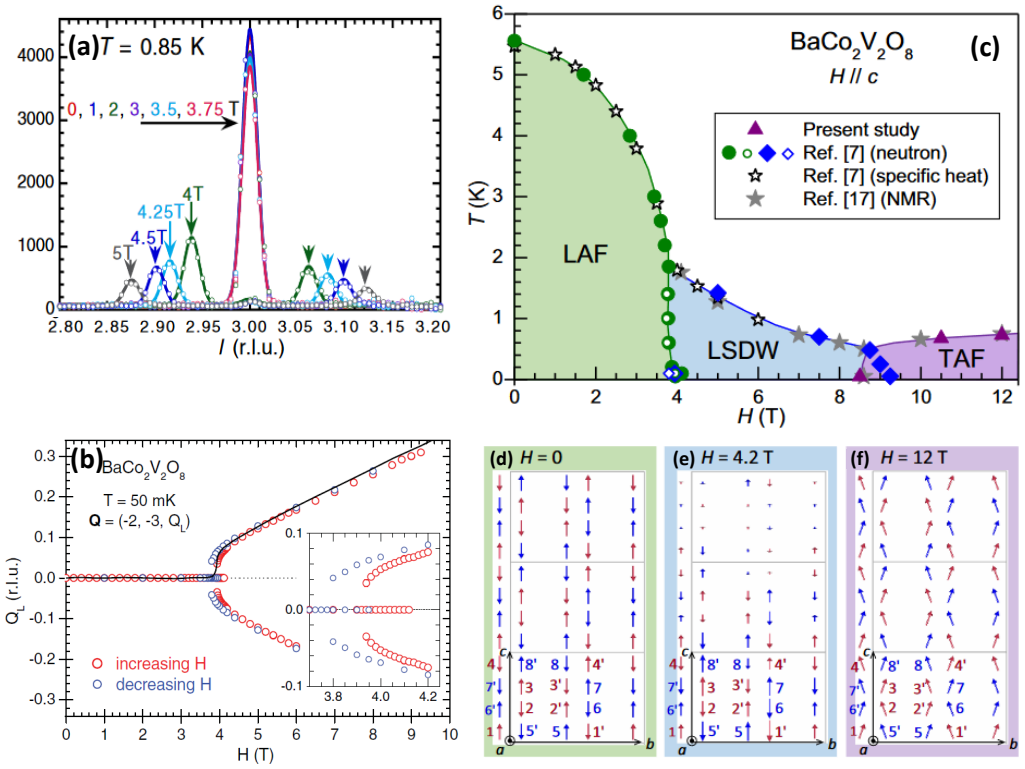

Figure 5.4: $(H-T)$ **phase diagram of $BaCo_2V_2O_8$ in a longitudinal magnetic field** $(\vec{H} \parallel \vec{c})$. (a) Q_L scans across the 4 0 3 magnetic Bragg peak for different values of the magnetic field. The incommensurability growing when increasing the field from $\mu_0 H = 4$ T. Figure extracted from [Kim+08b]. (b) Field dependence of the magnetic reflection $2\,\bar{3}\,Q_L$. (red and blue open circles for increasing and decreasing field respectively). The inset is a zoom of (b). Figure extracted from [Can+13]. This refinement leads to the LSDW structure shown in (e). (c) $(H-T)$ phase diagram obtained by neutron diffraction from [Gre+15b]. From zero-field to $\mu_0 H_c \simeq 4$ T, the magnetic phase corresponds to a Néel phase with the moments along the c-axis (LAF phase with L denoting longitudinal). For $\mu_0 H_c \simeq 4$ T $\leq \mu_0 H \leq \mu_0 H^* \simeq 8.5$ T, the magnetic structure corresponds to a longitudinal spin density wave (LSDW) phase. Above $\mu_0 H^* \simeq 8.5$ T, the system enters in a Néel phase where the moments are now perpendicular to the c-axis (TAF phase with T denoting transverse). (d-f) corresponding magnetic structures refined from the neutron diffraction data. In addition to this TAF component along b, a ferromagnetic one develops parallel to the applied field and thus to the c-axis. Figures extracted from [Gre+15b].

field $\mu_0 H_c \simeq 4$ T where the propagation vector is now $\vec{k}_{\text{LSDW}} = (1, 0, \delta)$ [2] [Can+13] (see Fig. 5.4(b)). Above the critical field, the Néel order is replaced by an ordered phase with an incommensurate modulation of the amplitude of the magnetic moments oriented parallel to the field direction (a longitudinal spin density waves denoted LSDW) as a consequence of the TLL longitudinal correlations. In addition, they could confirm the

[2] The step like modulation should present a Bragg reflection corresponding to a $3\vec{k}_{\text{LSDW}}$ harmonic of the main Bragg reflection characterestic of the incommensurate SDW signal close to the transition. It has not been seen by neutron diffraction, probably because the signal is too weak but it has been observed by NMR experiments [Kla]

first order character of the transition as it exhibits a field hysteresis and the Néel phase and the LSDW phases coexist around H_c as can be seen on the field dependence of δ in Fig. 5.4(b)).

This study was then completed at higher field by Grenier et *al.* (by neutron diffraction experiment) [Gre+15b]. It has been shown that above $H^* = 8.5$ T, this LSDW phase is replaced by another Néel phase. In this high field phase, the magnetic moments are perpendicular to the c-axis in agreement with the TLL transverse correlations which are predicted to dominate above H^*, before the ferromagnetic saturated phase is stabilized at higher field, too high to be reached in this experiment (see Fig. 5.4(c-f)). This second transition was also shown to be of first order, as the LSDW and the transverse AF phase coexist over a wide field region (see Fig. 5.4(c)).

Finally, nuclear magnetic resonance (NMR) measurements have been performed by Klanjšek et *al.* [Kla+15]. This study has led to a complete phase diagram of $BaCo_2V_2O_8$ in a longitudinal field up to the saturation field $\mu_0 H_{sat} \simeq 22.5$ T (see Fig. 5.5).

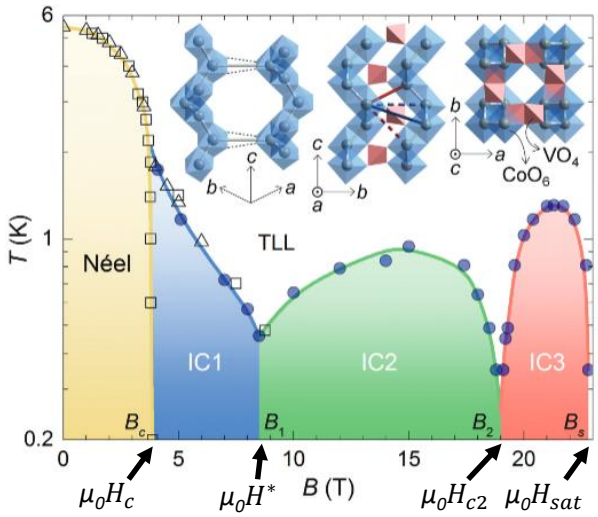

Figure 5.5: $H-T$ **phase diagram of $BaCo_2V_2O_8$ probed by NMR experiments**. From zero field to H^*, this study confirms what has been observed in [Gre+15b; Can+13]. Above H^*, two additional incommensurate phases have been found: IC2 for $H^* \leq H \leq H_{c2}$ and IC3 for $H_{c2} \leq H \leq H_s$.

This work has confirmed the critical fields $\mu_0 H_c \simeq 4$ T and $\mu_0 H^* \simeq 8.5$ T observed in the neutron scattering experiments [Can+13; Gre+15b]. It has also confirmed the inversion of the TLL exponents through the survey of the T_1 relaxation time. However, surprisingly and contrary to the neutron diffraction experiment [Gre+15b], the phase above $\mu_0 H^* \simeq 8.5$ T is found to be also incommensurate (IC2) [Kla+15]. A possible explanation for this discrepancy is that NMR probes the dynamical transverse correlations. As a result, this phase would indeed be a transverse AF phase (as determined by neutron diffraction and as predicted in the TLL theory) but dressed with strong IC fluctuations (seen via the T_1 in NMR), in addition to the expected AF fluctuations. Another scenario could be that there is a true coexistence (not predicted) between the IC order seen by NMR and the AF order seen by neutron diffraction. In this NMR study, a third

incommensurable (IC3) phase has also been found between 19 T and $\mu_0 H_{sat}$. The given explanation for that comes from the huge field dependence of the interchain interaction in this magnetic field range as reported in [Kla+15].

5.3.2 Neutron diffraction experiment under a longitudinal field

To get further insight in the two high field incommensurate phases IC2 and IC3 observed by NMR, I went to perform a neutron diffraction experiment on the time of flight (TOF) diffractometer HFM/EXED [HFM] in the Helmholtz Zentrum of Berlin (HZB) as this instrument allows to reach a static magnetic field of 25 T. But due to some problems with the ^{3}He cryostat, the minimum temperature we could reach was only 0.8 K. As a result, only the IC3 phase could be actually probed as the maximum T_c is about 0.9 K for IC2 and 1.3 K for IC3 (see Fig. 5.5).

After having oriented the c-axis of the sample along the magnetic field, we have collected a set of Bragg reflections. The diffracted neutrons were observed using four PSD detectors. The reflection positions and integrated neutron counts were analyzed with the Mantid software. Because of a small misalignment of the c-axis of the sample with respect to the magnetic field (by about 1.7°), the field was set to 20.75 T instead of the 21 T observed in NMR in order to be at the maximum of the dome of the IC3 phase (see Fig. 5.5). By making the difference between the neutron counts at 20.75 T and at $T = 0.8$ K and the ones at zero-field and at $T = 50$ K, we obtain the results shown in Fig. 5.6.

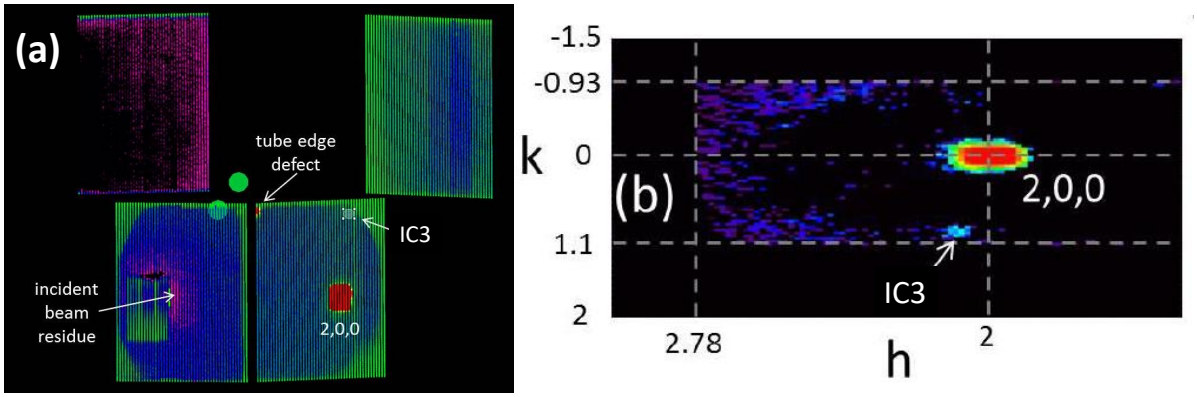

Figure 5.6: **HFM/EXED neutron diffraction experiment.** (a) The observed $BaCo_2V_2O_8$ neutron diffraction result within the four detector panels of HFM/EXED, obtained after subtracting the zero field measurement at 50 K from the 20.75 T one at 0.8 K, using incident λ band of 1.6 - 2.8 Å. The right forward scattering panel includes the 200 reflection (nuclear + ferromagnetic) and the potential observed incommensurate reflection of IC3 phase. (b) Reciprocal difference map in log-scale, where the 200 and (IC3) reflections are shown.

One can see that a strong intensity is found on the 2 0 0 reflection. This corresponds to the superposition of a nuclear and a ferromagnetic Bragg peaks, increasing in intensity with the applied field. Another peak weaker in intensity (see Fig. 5.6(b)) is observed at the incommensurate position $\vec{Q} = (2.04, 0.94, 0.03) = (2, 0, 0) + \vec{k}_{\mathrm{IC3}}$ with

$\vec{k}_{IC3} = (0.04, 0.94, 0.03)$. Unfortunately, it appears close to the edge of the detector (see Fig. 5.6(a)). Moreover, the a-axis of the sample was tilted below the horizontal plane by about 0.2°. This allowed this IC peak to be seen in the detector but the one at $\vec{Q} = (2, 0, 0) - \vec{k}_{IC3}$ which is thus outside the detector (see Fig. 5.6). Note also that due to the restricted Q-range probed here, no other IC peak could be seen. As a result, with a single observation, the incommensurate position of this peak cannot be fully confirmed. This reflection is indeed not so far from the commensurate position 2 1 0, which corresponds to that of an AF peak. Therefore a clear conclusion cannot be given.

We have planned to do another experiment overcoming the problem of the detector's edge and the too limited accessible Q-range and with a better cryogenic environment, allowing us to reach a temperature below 0.5 K and thus to probe also the IC2 phase.

5.4 Tomonaga Luttinger liquid spin-dynamics in the LSDW phase of $BaCo_2V_2O_8$

In this section I will expose our experimental results concerning the spin-dynamics of $BaCo_2V_2O_8$ under a longitudinal magnetic field and show that above the phase transition at $\mu_0 H_c \simeq 4$ T, it corresponds to excitations characteristic of a Tomonaga Luttinger liquid phase.

5.4.1 Experimental details

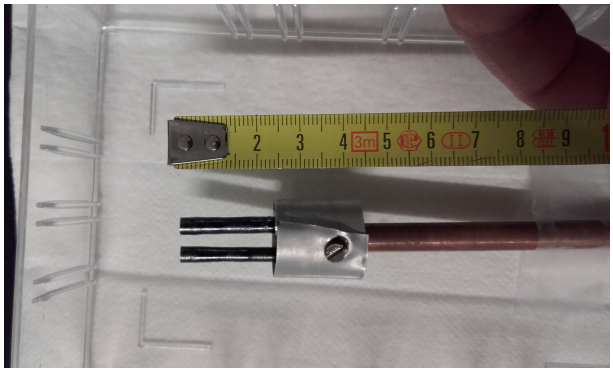

Figure 5.7: **Photograph of the two co-aligned $BaCo_2V_2O_8$ single crystals.** The two crystals were glued on a copper sample holder with black stykast to ensure a good thermal contact. A ring of Cadmium was added to avoid the scattering noise from the glue.

The INS experiments were performed on the cold-neutron TASP triple axis spectrometer at the Paul Scherrer Institute (PSI) [TAS], using a horizontal cryomagnet, that allowed to apply a magnetic field up to 6.8 T. The sample consisted in two $BaCo_2V_2O_8$ single crystals aligned individually with the b-axis vertical, then co-aligned using X-Rays at Institut Néel. The coalignment was checked to be better than 1° around the b-axis. This precision is reasonable enough for an inelastic neutron scattering experiment. The magnetic field was applied along the $c^\star$ axis of the $(a^\star, c^\star)$ scattering plane, hence along

the magnetic moments. The data were measured at the base temperature of 150 mK with a fixed final wave vector of 1.06 $Å^{-1}$, 1.1 $Å^{-1}$, 1.2 $Å^{-1}$ and 1.3 $Å^{-1}$ and the corresponding energy resolutions of 0.06, 0.06, 0.08, and 0.11 meV respectively.

Two experiments with $BaCo_2V_2O_8$ under a longitudinal field had been performed on TASP. The first one had a setup allowing to reach a maximum value of the horizontal field of 4.2 T, i.e. just above the phase transition. Hence the spin-dynamics was essentially probed in the AF phase. A second experiment with a new configuration allowed to perform a study in the LSDW phase (above $\mu_0 H_c$).

5.4.2 Field dependence of the incommensurability δ

In the Néel phase, the magnetic Bragg peaks appear at the AF points $Q = (h+1, k, l)$ with $h+k+l$ even corresponding to the $\vec{k}$=(1, 0, 0) propagation vector. In the LSDW phase, the propagation vector becomes $\vec{k}_{\mathrm{LSDW}}$=(1, 0, δ) where δ is field-dependent and represents the incommensurability of the moment amplitude modulation of the long-range order. δ increases with the field, which means that the period of the modulation of the moments becomes shorter. This manifests itself, as already explained in the previous section (see Fig. 5.4), by a shift of the incommensurate Bragg peak positions in the reciprocal space which should also correspond to a minimum of the dispersion of the excitations, as predicted by the TLL theory when $H > H_c$.

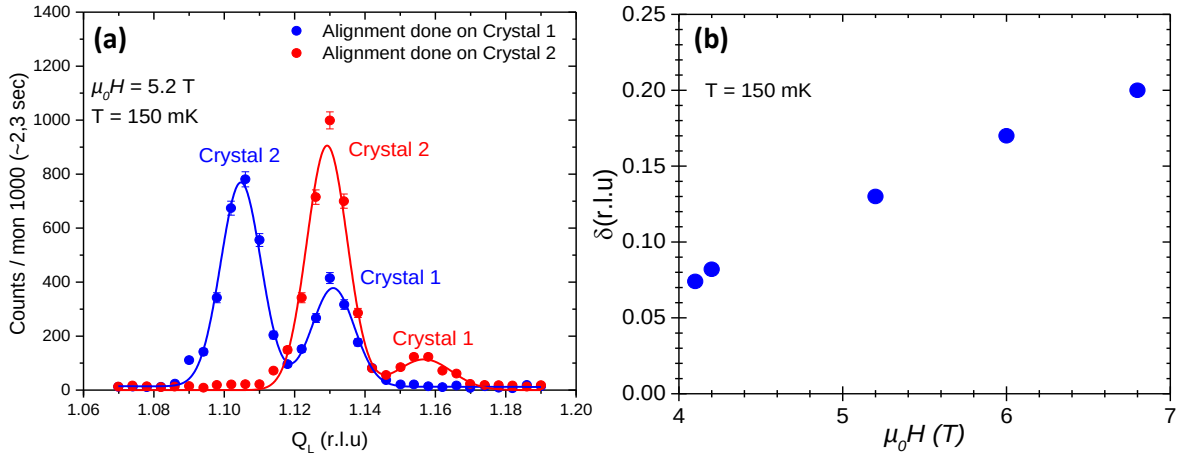

Figure 5.8: **Determination of the incommensurate modulation δ of the propagation vector.** (a) Q_L-scans for the two alignments done on the two crystals. (b) Field dependence of the incommensurability δ determined from Q_L-scans across the Bragg peaks of the LSDW phase $\vec{Q} = (2, 0, 1+\delta)$ for different values of the magnetic field.

In order to determine δ precisely and thus to optimize the inelastic measurements, we have measured Q_L-scans across the magnetic Bragg peak of the LSDW phase $\vec{Q} = (2, 0, 1+\delta)$ for each studied value of the magnetic field. Because of the slight misalignment of about 1° around the vertical direction between the two coaligned crystals, we had to do first the alignment of the first crystal (i.e. a rocking curve) and then a Q_L-scan. The same procedure was done for the second crystal. The corresponding Q_L value was then extracted for each crystal and their average was considered for δ (see an example in Fig. 5.8(a))

where $Q_L = 1.129$ for the first crystal and 1.131 for the second one, yielding $\delta = 1.130$ [3]). Fig. 5.8(b) shows the resulting field dependence of δ, increasing with increasing the field like $\delta = 2\pi m$, in agreement with what was already reported [Can+13].

5.4.3 Magnetic field dependence of the excitations and phase transition

As explained in Chap. 4, probing the magnetic field dependence of the excitations helps us to see and characterize the phase transition occurring under field. Here, we first investigate the field dependence of the excitations, obtained from constant-Q energy scans at $T = 150$ mK (see an example in Fig. 5.9(a)) for different magnetic fields and for four particular points in the reciprocal space: the antiferromagnetic (AF) point $Q = (2, 0, 1)$, the zone center (ZC) point $Q = (3, 0, 1)$, and the two incommensurate positions with respect to these points, $Q = (2, 0, 1+\delta)$ labeled AFIC and $Q = (3, 0, 1+\delta)$ labeled ZCIC.

5.4.3.1 Zeeman splitting in the Néel phase

Fig. 5.9(b) shows the field dependence of the magnetic excitations for $\vec{Q} = (3, 0, 1)$ in the Néel phase, i.e. up to $\mu_0 H_c \simeq 3.8$ T.

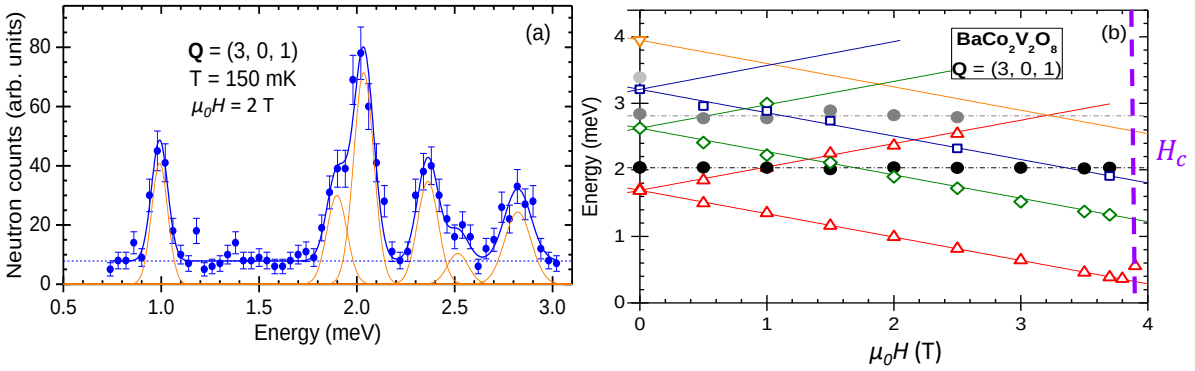

Figure 5.9: **Zeeman splitting in the Néel phase.** (a) Energy scan at $\mu_0 H = 2$ T and $T = 150$ mK for $\vec{Q} = (3, 0, 1)$. Orange dashed lines are individual Gaussian fits of each mode, the blue dashed horizontal line is a fit of the constant background, and the blue solid line is their sum. (b) Field dependence of the magnetic excitations below the transition occurring at $\mu_0 H \simeq 3.8$ T. The Zeeman splitting can be clearly seen for the three first transverse excitations $|j\ \text{T}, S^z = \pm 1\rangle$ with $j = 1, 2, 3$. The solid lines are fit of the Zeeman splitting with the following formula $E_T^j(H) = E_T^j(0) \pm g_{zz}\mu_B H$ yielding $g_{zz} = 6.07$ [Fau+18]. This value of the g_{zz} component of the Landé tensor $\tilde{g}$ is similar to what has been found in [Kim+06]. The thin dashed-dotted lines are a fit to a constant for the two first longitudinal modes: $E_L^j(H) = E_L^j(0)$.

[3] When the alignment is done on the first crystal (blue curve in Fig. 5.8(a)), one can see that the intensity of the first crystal is almost twice weaker than that of crystal 2. The suggested explanation for this is that crystal 2 somehow hides the first one and thus reduces the incident intensity reaching crystal 1 or its scattered intensity. Thus using two coaligned crystals gives only a factor of about 1.5 on the intensity instead of a factor two.

At $H = 0$, the lowest energy excitation at 1.7 meV is the transverse mode $|1\ \mathrm{T}, S^z = \pm 1\rangle$ [Gre+15a]. The field splits the two degenerate states through the Zeeman effect: $\mathscr{H}_{field}\,|1\ \mathrm{T}, S^z = \pm 1\rangle = \pm g_{zz}\mu_B H\,|1\ \mathrm{T}, S^z = \pm 1\rangle$ where $\mathscr{H}_{field} = g_{zz}\mu_B H S^z$. The resulting lowest energy branch (in red in Fig. 5.9) decreases linearly up to the transition that occurs at $\mu_0 H_c = 3.9$ T. The Zeeman splitting acts in the same way on the other transverse energy modes $|j\ \mathrm{T}, S^z = \pm 1\rangle$ with $j = 2, 3$. On the other hand the two first longitudinal excitations at zero-field, corresponding to $|j\ \mathrm{L}, S^z = 0\rangle$ with $j = 1, 2$ do not vary with the field up to $\mu_0 H_c$ which is consistent with the fact that $\mathscr{H}_{field}\,|j\ \mathrm{L}, S^z = 0\rangle = 0$. Hence, the field evolution of the excitations in the Néel phase under a longitudinal field is another evidence of the transverse and longitudinal characters of the excitations at zero-field.

5.4.3.2 Phase transition and magnetic field dependence of the excitations in the LSDW phase

Fig. 5.10 shows the field dependence of the low-energy magnetic excitations for the four different points AF $\vec{Q} = (2, 0, 1)$, ZC $\vec{Q} = (3, 0, 1)$ and their respective incommensurate points AFIC $\vec{Q} = (2, 0, 1 + \delta)$ and ZCIC $\vec{Q} = (2, 0, 1 + \delta)$.

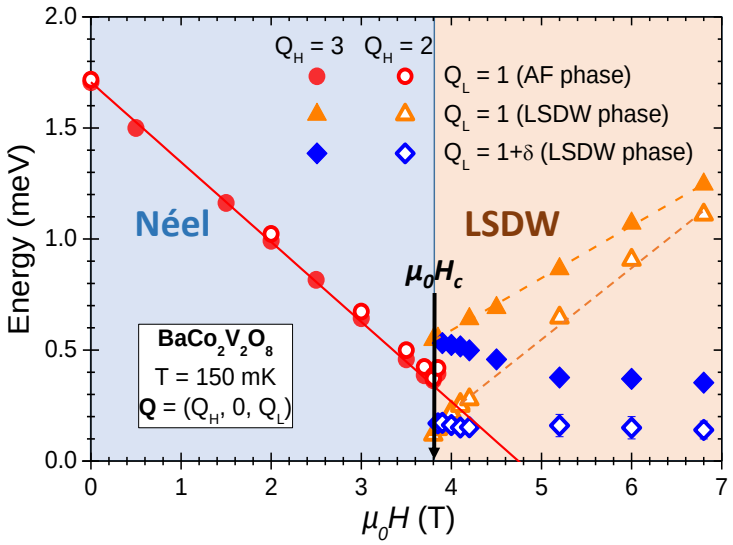

Figure 5.10: **Field dependence of the low-energy magnetic excitations** from energy scans performed in the Néel phase ($0 \leq \mu_0 H \leq \mu_0 H_c = 3.8\ T$) and in the LSDW phase ($\mu_0 H_c \leq H \leq 6.8\ T$) at $T = 150$ mK. Four positions were investigated. In the Néel phase: AF $\vec{Q} = (2, 0, 1)$ (red open circles) and ZC $\vec{Q} = (3, 0, 1)$ (red closed circles). Only the lowest transverse mode in the Néel phase is shown here. In the LSDW phase: AF $\vec{Q} = (2, 0, 1)$ and ZC $\vec{Q} = (3, 0, 1)$ (open and closed orange triangles, respectively) together with the IC positions next to them $\vec{Q} = (2, 0, 1 + \delta)$ and $\vec{Q} = (3, 0, 1 + \delta)$ with δ the IC modulation of the underlying IC ordering (open and closed blue diamonds, respectively). The critical field is indicated by a black arrow. The thick red line in the Néel phase is a fit of the Zeeman splitting as explained above while the dashed orange lines are linear fits in the LSDW phase (see text).

In the Néel phase, only the lowest energy branch arising from the Zeeman splitting of the first transverse mode $|1\ \mathrm{T}, S^z = \pm 1\rangle$ is plotted. The transition between the Néel phase

and the LSDW phase can be clearly seen from the discontinuity in the field dependence of the magnetic excitations and from the minimum of the gap which occurs at $\mu_0 H_c$. Focusing only on the strongest excitations of the LSDW phase, one can see that above the transition, the energy of the modes at the commensurate AF and ZC points increases linearly with the field with a lower energy for the AF point. For the incommensurate AFIC and ZCIC points, the energy of the excitation is almost constant with a minimum energy gap of about 0.15 meV for the former while it slowly decreases while H increases for the latter. The gap at the ZCIC point then reaches a value of about 0.35 meV at $\mu_0 H = 6.8$ T. The fact that we do not close the gap here probably comes from the presence of interchain interactions, as it was the case in a transverse field (see Chap. 4).

5.4.4 Dispersion of the excitations along Q_L in the LSDW phase

5.4.4.1 Overall view of the dispersion spectrum

To probe the dispersion spectrum in the LSDW phase, we have done many energy scans for different values of the scattering vector $\vec{Q} = (Q_H, 0, Q_L)$ for both $Q_H = 2$ and $Q_H = 3$ and by varying Q_L. These dispersion spectra have been investigated for $\mu_0 H = 4.2$ T and 6 T.

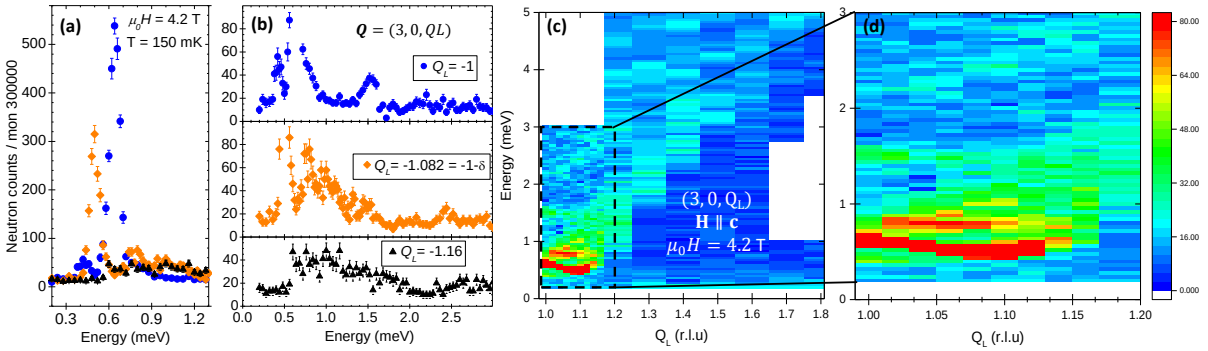

Figure 5.11: **Spin dynamics in the LSDW phase of $BaCo_2V_2O_8$ in the vicinity of a zone center position** at $\mu_0 H = 4.2$ T and $T = 150$ mK. (a,b) Energy scans at three different scattering vectors: the ZC position $(3, 0, 1)$, its IC satellite $(3, 0, 1+\delta)$ with $\delta = 0.082$, and further away along $c^\star$. Panel (a) shows the low energy part of these scans. (c) Inelastic scattering intensity map showing the dispersion spectrum of the magnetic excitations along the $c^\star$ direction, in a longitudinal field at 4.2 T. (d) is a zoom of part of the spectrum delimited by the dashed black box in (c).

Figs. 5.11(a-b) show energy scans performed in the LSDW phase, at $T = 150$ mK and $H = 4.2$ T, at three different scattering vectors at and close to the ZC point. These scans emphasize the presence of a very intense excitation at low energy (typically $E < 1.5$ meV), whose intensity decreases drastically when going further away from the ZC point. It loses a factor of about 2 for $\Delta Q_L \simeq 0.08$ r.l.u. and has completely disappeared for $\Delta Q_L \simeq 0.16$ r.l.u. At this Q_L value remains a broad feature that could correspond to a continuum of excitation or as well to broadened discretized excitations. In all this Q_L-range, in addition to the intense excitation, much weaker ones are also visible, one at a lower energy, and several ones at higher energy.

This is better seen in the intensity map of Fig. 5.11(c) obtained from the constant-Q energy scans and thus showing the overall behavior of the spin dynamics, between the ZC position and 0.8 r.l.u. away from it. One can notice that, as expected for a TLL (see Fig. 5.2), the minimum of the dispersion, with an energy of about $E \simeq 0.35$ meV, occurs at the satellite position of the LSDW phase, $Q_L = 1.082$ r.l.u. at this field value. On the other hand $Q_L = 1$ now corresponds to a (local) maximum of the low energy boundary of the dispersion spectrum. The two positions (AF and ZC on one hand, AFIC and ZCIC on the other hand) plotted in the LSDW phase in Fig. 5.11 thus correspond to the extrema of the dispersion.

5.4.4.2 Field-evolution of the spin-dynamics of the LSDW phase

Fig. 5.12 shows the field-evolution in the spin dynamics of the LSDW phase along Q_L both around AF and ZC positions. Due to the folding of the dispersion in $BaCo_2V_2O_8$, the spin-dynamics across the ZC point $\vec{Q} = (3, 0, 1)$ and the AF point $\vec{Q} = (2, 0, 1)$ are expected to be similar.

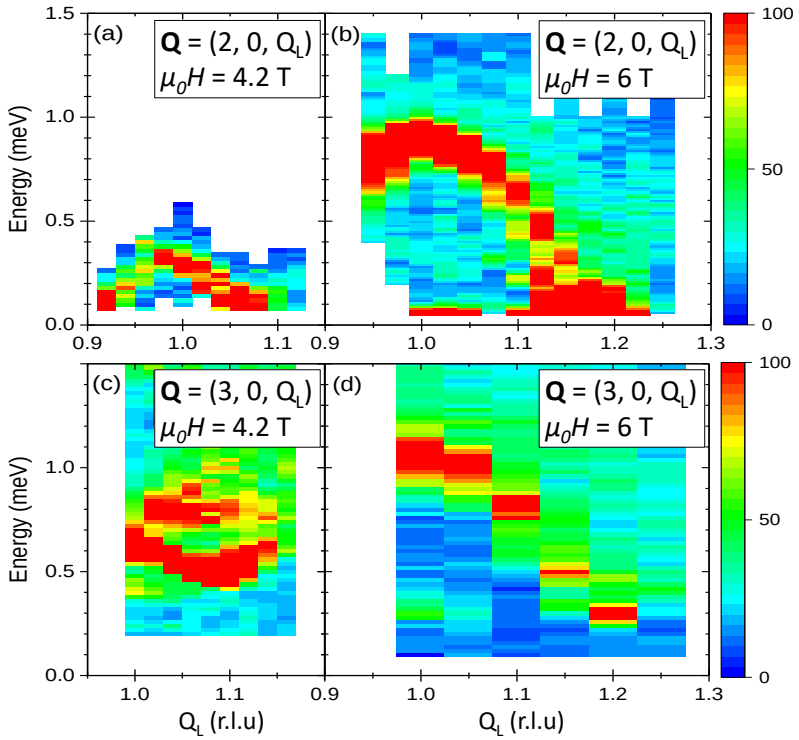

Figure 5.12: **Field dependence of the dispersion spectrum.** (a-b) Inelastic scattering intensity map obtained from a series of Q-constant energy scans around the AF position $\vec{Q} = (2, 0, 1)$ for the two field values $\mu_0 H = 4.2$ T and $\mu_0 H = 6$ T. (c-d) shows the same content, but around the ZC position $\vec{Q} = (3, 0, 1)$. All the Q-constant energy scans were measured at $T = 150$ mK. The intensity is saturated here, especially to emphasize the signal appearing below the arch-bridge at $\mu_0 H = 6$ T and $Q_H = 2$.

At $\mu_0 H = 4$ T, the very intense excitation seen around the ZC position $(3, 0, 1)$ and its incommensurate satellite (see Fig. 5.11(c)) can also be around the AF position $(2, 0, 1)$,

with a comparable intensity (see Fig. 5.12(a)). The dispersion of this excitation along Q_L was studied on both sides of the AF position, up to $\Delta Q_L = \pm 0.1$ r.l.u. Here again, the minima in energy are at the expected incommensurate satellite positions $Q_L = 1 \pm \delta$, and a maximum is observed at $Q_L = 1$. This arch-bridge shape of the dispersion corresponds well to the lower bound of the continuum of excitations in the TLL theory (see Fig. 5.2(d)), except for the residual energy gap of 0.14 meV in the excitations.

Fig. 5.12(b),(d) show the spin dynamics obtained at a higher field of $\mu_0 H = 6$ T across the AF and ZC positions respectively. The minima of the dispersion are still obtained at the incommensurate satellite positions $Q_L = 1 \pm \delta$ and the arch-bridge maximum at the commensurate ones $Q_L = 1$. By increasing the field, the arch bridge dispersion expands. Indeed around both the AF and ZC positions, the amplitude of dispersion is about 0.2 meV at $\mu_0 H = 4.2$ T while it is about 0.8 meV for $\mu_0 H = 6$ T and the IC minimum moves appart from the ZC or AF positions. This seems to be also in agreement with the TLL theory for the incommensurate fluctuations, as their energy increases with increasing the value of δ and thus the value of the magnetic field (see Fig. 5.2(d)).

From Fig. 5.12(b), one can see that a broad very weak signal exists below the arch bridge. This signal seems consistent with the TLL theory where the commensurate fluctuations reach a minimum of energy at the commensurate position $Q_L = 1$ (see Fig. 5.2(c)).

Finally, note that the energy gap is different between the AFIC ($\Delta = 0.14$ meV) and the ZCIC ($\Delta \simeq 0.35$ meV) positions while there is a twice smaller difference in zero-field (the difference is about 0.1 meV). I will explain this difference in the next section.

5.4.5 Dispersion of the excitations along Q_H

We have investigated the dispersion perpendicular to the chain to get an insight about the nature of the interchain interaction in the LSDW phase. Constant-Q energy scans have been performed at 150 mK for different values of the magnetic fields below and above the phase transition up to $\mu_0 H = 6.8\ T$.

Fig. 5.13(a) shows the field evolution of the dispersion along Q_H. Fig 5.13(b) shows the amplitude of dispersion ΔE obtained from the fits of the dispersions. This amplitude increases with the effective interchain coupling J' and with the AF component of the ordered moments involved in the magnetic structure.

While the system is non-dispersive in the Néel phase (see the dispersion in Fig. 5.13 for $\mu_0 H = 3.5$ T and 3.8 T in red and blue dashed lines respectively), a finite dispersion appears in the LSDW phase with a discontinuity in the field dependence of the amplitude of dispersion ΔE at $\mu_0 H_c$. Above the transition $\Delta E = 0.38$ meV for $\mu_0 H = 4.2$ T and then decreases while increasing the magnetic field down to $\Delta E \simeq 0.2$ meV at $\mu_0 H = 6.8$ T.

As we have seen in Chap. 1, the fact that the excitations in the Néel phase at zero-field are almost non-dispersive could be due to the frustration between neighboring chains. In a transverse field (see Chap. 4), the amplitude of dispersion ΔE increases continuously with the transverse field to reach a maximum at the phase transition. This was attributed to the progressive change of magnetic structure imposed by the staggered field and thus to a change in the interchain couplings terms releasing the frustration.

Here the fact that there is a discontinuity of the amplitude of dispersion ΔE between the Néel phase and the LSDW one probably comes from the first order nature of the phase transition (see Fig. 5.4(b)). The change in ΔE can be explained qualitatively by the completely different nature of the two respective ground states. Indeed the fact that the system evolves from a Néel ground state where all the moments have the same amplitude

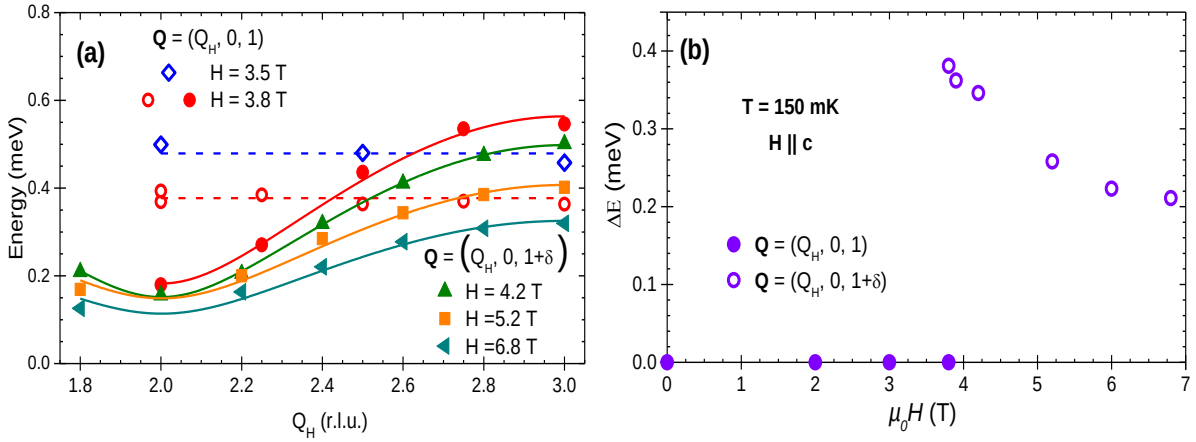

Figure 5.13: **Field evolution of the dispersion along Q_H.** (a) Dispersion along Q_H obtained from constant-Q energy scans measured at $T = 150$ mK for $Q_L = 1$ in the Néel phase and for $Q_L = 1+\delta$ in the LSDW phase for different fields. The dispersive branches (solid symbols) were fitted with the phenomenological law: $E = \sqrt{\Delta^2 + (E_m^2 - \Delta^2)\sin^2[\frac{h\pi}{2}]}$, where $hQ_H + 1$, Δ is the gap and E_m is the maximum of the dispersion. The non-dispersive branches (open symbols) were fitted by a constant $E = E_m = \Delta$ (dashed lines). (b) Field dependence of the amplitude of dispersion $\Delta E = E_m - \Delta$ extracted from the previous fits.

to a longitudinal spin density waves changes drastically the influence of the interchain interactions. This might remove some frustrations in the system as the amplitude of the moments are modulated along the chain in the LSDW phase. The decrease of ΔE with increasing field can be understood by the decrease of the antiferromagnetic component of the magnetic moments at the expense of the ferromagnetic one (which is directly proportional to the incommensurability δ here and logically to the applied magnetic field).

Finally, at zero-field, the fact that the excitations do not disperse perpendicularly to the chain leads almost to the same gap in the dispersion along Q_L for both AF and ZC positions. We have observed on the other hand that the gap Δ is not the same for AFIC and ZCIC positions in the LSDW phase. The difference corresponds to the amplitude of interchain dispersion ΔE which is not zero. Indeed at $\mu_0 H = 4.2$ T, $\Delta(\text{ZCIC}) - \Delta(\text{AFIC}) \simeq 0.36$ meV $\simeq \Delta E$.

5.4.6 Summary of the experimental results

Our experimental results and especially the dispersion along the chain (i.e. along Q_L) seem to comply with the expected TLL spin-dynamics of a spin-1/2 chain as far as the lower bound of the dispersion is concerned. In addition, all the spectral weight seems to be concentrated in the mode which reaches a minimum at the incommensurate position $Q_L = 1 + \delta$ (see the arch bridge in Fig. 5.12(b)). Unfortunately, because of the experimental setup, i.e. the pillars of the cryomagnet, it was impossible for us to discriminate the transverse and longitudinal modes using the geometrical factor of the neutron scattering cross section, in particular the scattering vector $\vec{Q} = (0, 0, 2)$ probing only transverse fluctuations, was not accessible.

Let us recall that in our case, because of the Ising-like anisotropy of $BaCo_2V_2O_8$, the longitudinal correlations $\langle S^z(\vec{r}_i,0)S^z(\vec{r}_j,t)\rangle$ are expected to dominate over the transverse ones up to $\mu_0 H^* \simeq 8.5$ T (as $\eta_x > \eta_z$ in this field region). As the spectral weight is obtained from the double Fourier transform of the spin-spin correlations, this should imply that the main part of the spectral weight is in the S_{zz} fluctuations.

To try to get a deeper insight and to prove the dominance of the longitudinal polarization of these excitations, we used numerical calculations.

5.5 Numerical calculations and interpretation of the results

I will first present the Hamiltonian of the system and my numerical calculations using exact diagonalization as a first attempt to better understand our results. Then I will show the iTEBD results performed by S. Takayoshi and T. Giamarchi.

5.5.1 Hamiltonian of the system

The Hamiltonian of $BaCo_2V_2O_8$ under a longitudinal field is the following [4]:

$$\mathcal{H} = \underbrace{\sum_j J[S^z_j S^z_{j+1} + \frac{\varepsilon}{2}(S^+_j S^-_{j+1} + S^-_j S^+_{j+1})]}_{1} - \underbrace{\sum_j J' < S^z_j > S^z_j}_{2} - \underbrace{\mu_B H g_{zz} \sum_j S^z_j}_{3}$$

with:

1 : XXZ Hamiltonian.

2 : interchain interaction treated in mean field theory.

3 : Zeeman Hamiltonian of the uniform field $\vec{H}$ along the c-axis.

(5.7)

where $g_{zz} = 6.07$ according to the fit of the data in Fig. 5.10. In the following, I will now denote S_{xx} (same as S_{yy} since the symmetry between $\vec{a}$ and $\vec{b}$ is not broken by the field) and S_{zz} the transverse and longitudinal fluctuations of the ordered moments. $S_\perp$ will denote the fluctuations seen through neutron scattering, i.e. perpendicular to the scattering vector $\vec{Q}$.

The interchain interaction is still taken into account even if this term is not relevant in the TLL phase as we will see later. While this part of the Hamiltonian is well defined and can reasonably be treated in mean field theory in the Néel phase, its treatment in the LSDW phase is more questionable. One reason for that is the sinusoidal modulation of the moments. The mean field theory becomes even more critical close to the transition, especially because of the step-like modulation of the amplitude of the magnetic moments. Nevertheless, we made the assumption that the interchain interaction can still be treated in mean field theory.

[4] Note that, as seen in Chap. 4, the Landé tensor $\tilde{g}$ is not diagonal. Hence effective fields along $\vec{a}$ and $\vec{b}$ are induced when a field is applied along $\vec{c}$. However, these effective fields have the same nature than the one along $\vec{c}$ when the field is applied along $\vec{b}$ and thus are non-relevant.

5.5.2 Exact diagonalization

As for the case of the transverse field, I have used my own Mathematica program explained in Chap. 3. Here the Hamiltonian computed is the one of Eq. (5.7) for a simple linear chain. We know that the amplitude of the moments is modulated along the chain in the LSDW phase, therefore the periodic boundary condition was removed (as it has no meaning now). The calculations in the LSDW phase were made with a number $n = 20$ spins and with the 2-spinons basis. The starting point was to compute the field dependence of the excitations in the Néel phase to check that it reproduces qualitatively the features found experimentally.

5.5.2.1 Field-dependence of the excitations

Fig. 5.14 shows the calculated magnetic field dependence of the excitations under a longitudinal field. The scattering intensity is calculated on an AF point $\vec{Q} = (1, 0, 0.5)$.

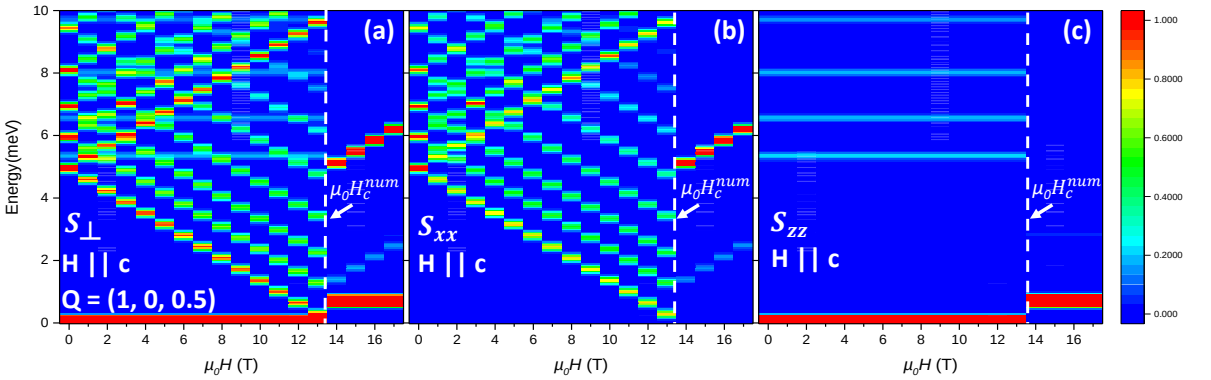

Figure 5.14: **Field dependence of the excitations in the Néel phase calculated by exact diagonalization.** Calculated intensity maps of $S_\perp$ (a), S_{xx} (b) and S_{zz} (c) showing the field-dependence of the magnetic excitations in the Néel phase. $S(Q, \omega)$ is calculated on an antiferromagnetic point (AF) $Q = (1, 0, \frac{1}{2})$ of a linear spin-1/2 XXZ chain. The calculations were made with a 2-spinons basis of $n = 20$ spins. The numerical critical field $\mu_0 H_c^{num}$ is pointed out by the white dashed lines. The step in field (resp. in energy) is taken as 1 T (resp. 0.05 meV).

First, one can see a discontinuity in the field dependence of the excitations across $\mu_0 H_c^{num} \simeq 14$ T marking the occurence of a phase transition. Note that the energies of the modes, and thus also of the critical field, are larger than the experimental one because of the truncation of the Hilbert space. In the following, only the qualitative behavior will thus be considered.

Below this transition, one series of excitations at zero field splits in two branches which exhibit a linear dependence with increasing the field. This corresponds to the Zeeman splitting observed experimentally. A second series of excitations does not vary with increasing the field. This is consistent with the calculated polarization of the modes, i.e. the fact that the first series corresponds to transverse excitations carrying a spin $S = \pm 1$ and the later to longitudinal ones carrying a spin $S = 0$ (see Fig. 5.14(b) and (c) respectively).

Above the transition, the longitudinal fluctuations are the ones observed at the minimum in energy which does not vary when the field further increases, while the transverse ones, higher in energy, increase linearly with increasing the field. At first sight, this seems to reproduce qualitatively what is observed in Fig. 5.10. However one has to keep in mind that the scattering function is calculated at an AF commensurate position for which the energy of the longitudinal mode is supposed to increase with increasing the field (see the open orange triangles in Fig. 5.10).

Here, the calculations reproduce qualitatively well the field dependence of the excitations in the Néel phase. The field dependence in the phase above shows some similar features with our measurements in the LSDW phase. However there are some inconsistencies that I will discuss in the next section, by describing the calculated ground state above the transition.

5.5.2.2 Ground state

The first step before calculating the dispersion spectrum in the phase above the transition is to compute the corresponding ground state and to check that we obtain a longitudinal spin-density wave as expected in the LSDW phase. By calculating the average magnetization on each site, I obtained the ground state shown on Fig. 5.15.

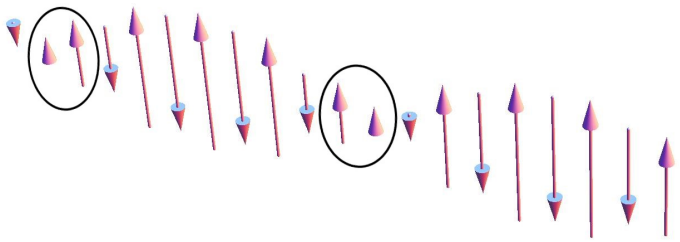

Figure 5.15: **Ground state in the phase above the transition** calculated with $n = 20$ sites at $\mu_0 H = 16$ T. Here the magnetization is plotted perpendicularly to the direction of the chains for more legibility. The black circles show the defects where two moments are aligned ferromagnetically.

One can clearly see a modulation of the amplitude of the ordered moments along the chain. However there are some defects along the chain. Pairs of moments are parallel instead of being antiferromagnetically coupled.

Moreover, I tried to compute the ground state for different values of the magnetic field and different number of sites. In the former case, I have seen that it does not change with increasing the field, which means that the incommensurability remains the same above the phase transition. This probably explains also the fact that the energy of the longitudinal mode does not increases with the field at the AF point since it actually increases with the incommensurability δ. Concerning the influence of the number of sites, I have seen that there are systematically two defects and the incommensurability δ depends on the number of sites. This probably comes from to the huge truncation of the Hilbert space and the highly limited size of the system. Indeed, as explained in section (5.2.1), the LSDW phase

arises from the defects (i.e. the spinons) created by the applied field which spread over a few sites to form a sinusoidal modulation of the magnetic moments amplitude. However, to be able to perform calculations, I needed to truncate the Hilbert space to the 2-spinon basis, thus limiting the number of defaults to 2.

In spite of these limitations, we recover the fact that the ground state corresponds to a modulation of the amplitude of the spins, motivating us to calculate the dispersion spectrum along Q_L.

5.5.2.3 Dispersion spectrum along Q_L

Fig. 5.16 shows the calculated dispersion spectra using exact diagonalization.

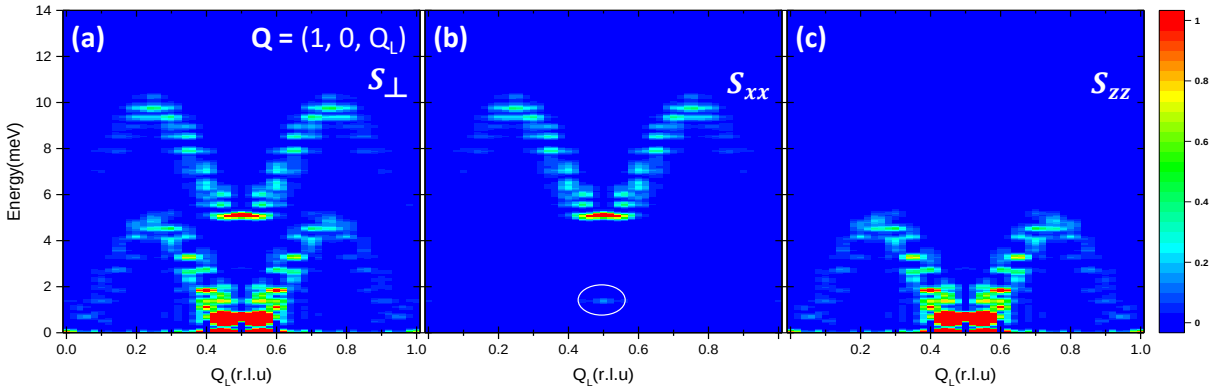

Figure 5.16: **Dispersion spectra along Q_L calculated with exact diagonalization.** (a) $S_\perp$ with $\vec{Q} = (1, 0, Q_L)$. (b-c) the corresponding S_{xx} and S_{zz} calculated polarizations. Here the calculations are performed for a chain with $n = 20$ sites. The scale in intensity is in arbitrary units. The step in Q_L is taken as 0.02 r.l.u (resp. 0.05 meV). The white round in (b) shows the very weak intensity of the commensurate transverse at $Q_L = 0.5$.

One can see that compared to the results at zero-field (see section. 3.4.3), the system is now ungapped. Moreover an incommensurability has developed around the AF point for the lowest energy branch (see Fig. 5.16(a)) which corresponds to longitudinal fluctuations (see Fig. 5.16(c)). Two energy branches higher in energy and corresponding to the transverse fluctuations S_{xx} also appear in the calculated spectrum: a first one at low energy around 2 meV, very weak in intensity (pointed out by the white circle in Fig. 5.16(b)) at the commensurate AF position $Q_L = 0.5$ and a second one at higher energy (around 5 meV at $Q_L = 0.5$) which seems to have minima of energy at incommensurate positions around the AF position $Q_L = 0.5$. Those results are qualitatively consistent with what is expected for an AF chain in a longitudinal field at the AF position [Mül+81] and some features are reproduced if we compare to [Yan+17]. Note that the spectral weight is almost zero at ZC positions $Q_L = 0$ and $Q_L = 1$.

However, the absence of gap expected for the transverse excitations at the AF point is not reproduced here. This is again supposedly due to the huge truncation of the Hilbert space and the limited size of the chain. Nevertheless we can show by these calculations that the majority of the spectral weight is contained in the lowest energy mode which corresponds to longitudinal fluctuations S_{zz}. In order to fully confirm this hypothesis and

to have a better accuracy for the comparison with the experimental data, let us now turn to iTEBD calculations.

5.5.3 iTEBD calculations

I will show here the iTEBD calculations done by Shintaro Takayoshi and Thierry Giamarchi for a screw chain as $BaCo_2V_2O_8$. They have computed the Hamiltonian of Eq. 5.7 by taking $g_{zz} = 6.07$ and by treating the interchain interaction by means of mean-field theory. The other parameters are the ones found from the fit of the dispersion spectrum at zero-field (see section 4.6.2.1), i.e. $J = 5.8$ meV and $\epsilon = 0.53$. As we will see later in this section, the mean field treatment of the interchain interaction does not work well near the critical point and, moreover, the interchain interaction does not seem to play a crucial role in the dynamics. Thus, in order to reproduce correctly the data in the LSDW phase, J' was taken as 0.03 meV (while $J' = 0.17$ meV for the zero-field and the transverse field cases). The number of sites is taken as $n = 200$ in order to reproduce well the incommensurability of the system. As in my calculations, there is no periodic boundary conditions.

I would like to emphasize that while the profile in energy was well known for years [Mül+81], no calculations of the dynamical structure factors were done until our study and the recent paper of Yang et *al.* [Yan+17] in which they study the spin dynamics of the similar compound $SrCo_2V_2O_8$. I will discuss this work in the conclusion of this chapter.

5.5.3.1 Calculated magnetic field dependence of δ

The first step before calculating the dispersion spectra for different values of the magnetic field was to calculate the magnetic field dependence of the incommensurability of the ground state from the static spin-spin correlation function $\left\langle S^z(\vec{0},0)S^z(\vec{r},t)\right\rangle$ to compare with the experimental findings.

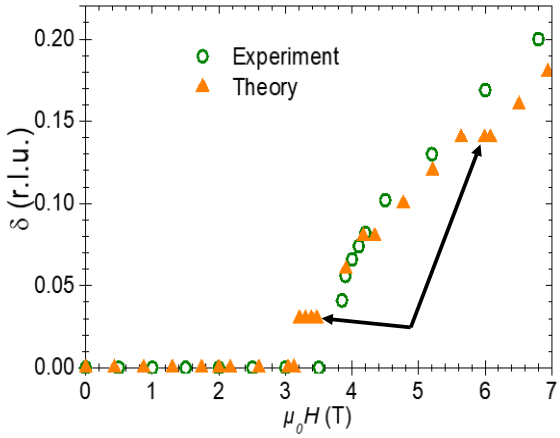

Figure 5.17: **Calculated field dependence of the incommensurability** δ to compare with the experimental ones obtained from neutron scattering experiments on D23 at ILL and on TASP at PSI. The black arrows point out the step-like tendencies in the field dependence of δ.

Fig. 5.17 shows the calculated magnetic field dependence of the incommensurability using iTEBD for $J' = 0.17$ meV. One can see that the calculations reproduce well the experimental data. However the incommensurability starts to develop slightly before the experimental critical field of $\mu_0 H_c \simeq 3.8$ T. This is due to the influence of the interchain interaction and its incorrect treatment. Moreover step like tendencies appear in the calculated field dependence of δ. This might be due to the finite size of the system.

5.5.3.2 Overall view of the calculated dispersion spectrum in the LSDW phase

Let us first see an overall view of the calculated dispersion spectra along Q_L.

Figs. 5.18((a),(d)) show the dispersion spectra calculated using iTEBD along $(Q_H, 0, Q_L)$ for the two values $Q_H = 3$ and 2 at $\mu_0 H = 6$ T.

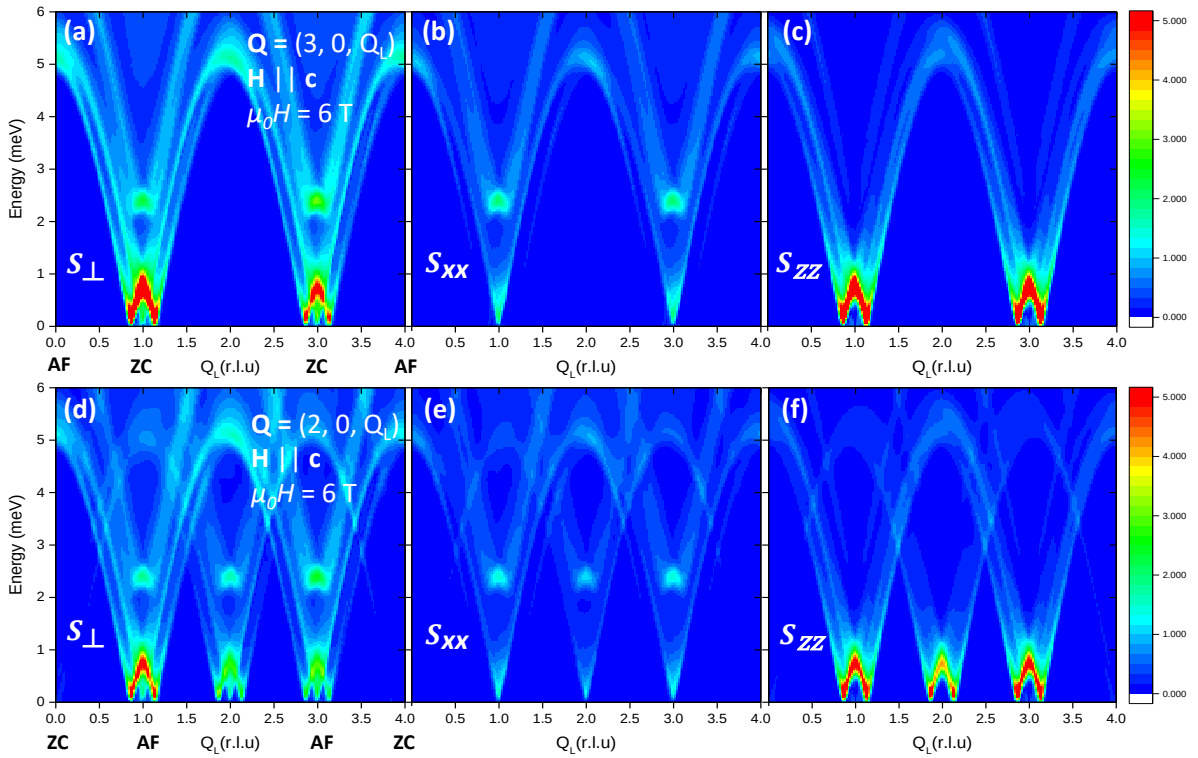

Figure 5.18: **Calculated dispersion spectrum** along Q_L at $\mu_0 H = 6$ T for $\vec{Q} = (Q_H, 0, Q_L)$ with the two values $Q_H = 3$ (a-c) and $Q_H = 2$ (d-f). The calculated transverse and longitudinal excitations S_{xx} and S_{zz} are also shown: for $Q_H = 3$ (b-c) and for $Q_H = 2$ (e-f). The intensity is in arbitrary units.

One can see that an incommensurability develops in both cases as we can clearly see minima of energy on IC positions, for example around $Q_L = 1$ which corresponds to an AF position for $Q_H = 2$ and to a ZC position for $Q_H = 3$. These incommensurate excitations correspond to longitudinal fluctuations S_{zz} (see Fig. 5.18((c),(f))). The fact that it is seen similarly at the ZC and AF points is due to the folding of the dispersion due to the screw structure of the chain. However in theory an incommensurability should also develop around the ZC point for the transverse excitations S_{xx} at zero energy. This

is not seen here which means that the associated spectral weight must be vanishing small (as in the case of exact diagonalization).

Instead, the transverse fluctuations S_{xx} exhibit the minima of energy only at AF commensurate positions where the system is gapless (for example at $Q_L = 1$ in Fig. 5.18(e)). A second incommensurate energy mode higher in energy is also present. This one is similar to the one I have found with exact diagonalization.

Finally, concerning the spectral weight, one can see that the maxima of intensity correspond to longitudinal fluctuations S_{zz} in all cases.

5.5.3.3 Comparison with the experiments

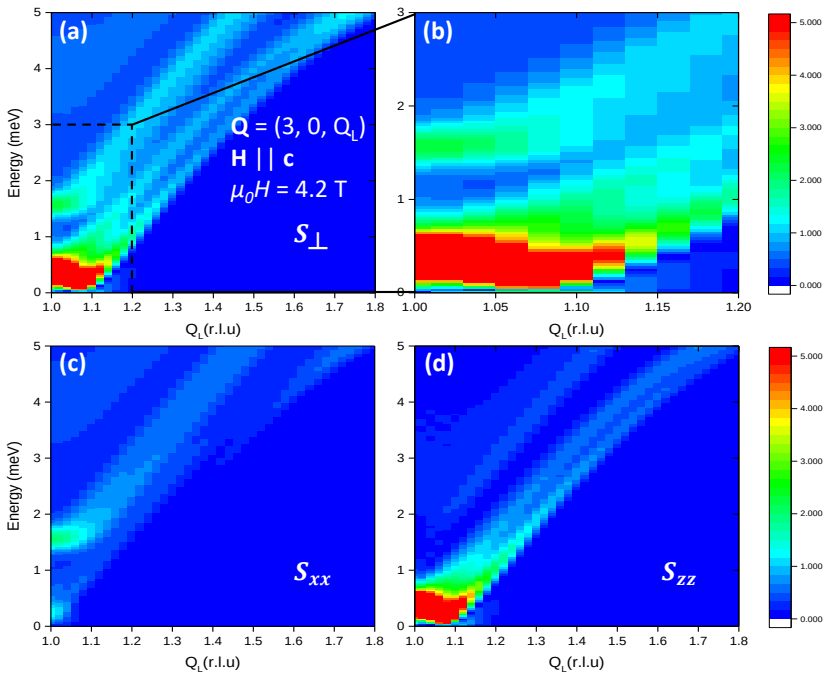

Figure 5.19: **Calculated dispersion spectrum around the ZC point** along Q_L at $\mu_0 H = 4.2$ T for $\vec{Q} = (3, 0, Q_L)$ (a). (b) is a zoom of the spectrum (a). (c-d) Calculated transverse and longitudinal fluctuations S_{xx} and S_{zz} respectively. The intensity is in arbitrary units.

Fig. 5.19 shows the calculated dispersion spectrum along Q_L for $\vec{Q} = (3, 0, Q_L)$ at $\mu_0 H = 4.2$ T. Fig. 5.19(a) and its zoom Fig. 5.19(b) have to be compared with Fig. 5.11(c-d). One can see a good agreement with the experimental data. All the spectral weight is concentrated in the low energy range extending from the ZC to the incommensurate position and slightly above. These calculations further confirm that the majority of the spectral weight is carried by the longitudinal fluctuations S_{zz} (see Fig. 5.19(c-d)).

However there are few differences with the experimental data. First, there is almost no gap at the incommensurate position in the calculations ($\simeq 0.2$ meV) while there is one of about 0.5 meV in the experiment. This gap is explained by the fact that the system becomes clearly dispersive perpendicularly to the chain in the LSDW phase. Unfortunately, the treatment of the interchain interaction in mean field theory is one of the limitation

of the calculations. In addition, the intensity of the two main calculated longitudinal branches (starting at about 0.4 and 1.6 meV at $Q_L = 1$) are a bit different in the calculations, possibly due to an anticrossing as the one observed in zero-field. This could also explain why the additional intermediate excitation seen experimentally around 0.8 meV (see Fig. 5.11(d)) is not well reproduced by the calculation.

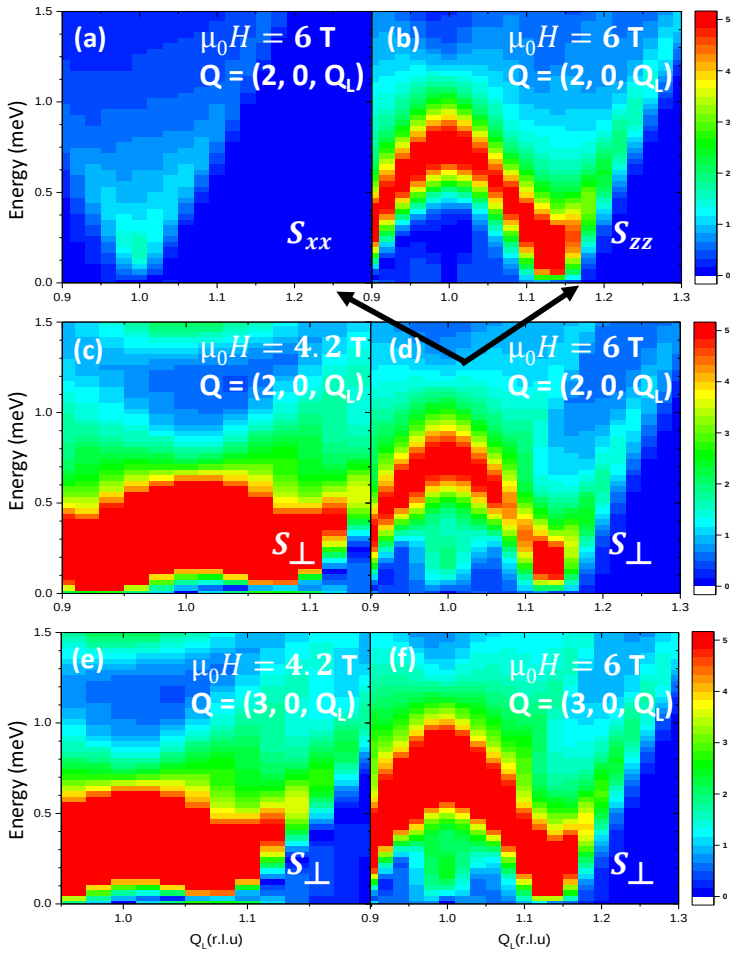

Figure 5.20: **Calculated field dependence of the dispersion spectrum along Q_L.** (a-b) calculated dispersion spectrum of the transverse and longitudinal fluctuations S_{xx} and S_{zz} at $\mu_0 H = 6$ T. (c-d) calculated dispersion spectrum for $\vec{Q} = (2, 0, Q_L)$ at $\mu_0 H = 4.2$ T and $\mu_0 H = 6$ T respectively. (e-f) show the same calculations for $\vec{Q} = (3, 0, Q_L)$.

Fig. 5.20 shows the field evolution of the dispersion spectra along $\vec{Q} = (2, 0, Q_L)$ and $\vec{Q} = (3, 0, Q_L)$. This figure has to be compared with Fig. 5.12. Once again, one can observe a rather good agreement between the calculations and the experimental results. Indeed the arch bridge expands with increasing the magnetic field as seen in the experiment. The calculations for $Q_H = 2$ (see Fig. 5.20(c-d)) reproduce better the experiment than for $Q_H = 3$ as the gap of the interchain dispersion is almost null around the AFIC position (contrary to the ZCIC one for the reasons explained before). The arch bridge corresponds to S_{zz} fluctuations (see Fig. 5.20(b)) while the weak spectral weight, reaching a minimum in energy at the commensurate point $Q_L = 1$, corresponds to S_{xx} fluctuations

(see Fig. 5.20(a)).

To summarize, the calculations reproduce qualitatively well the experimental results. The arch bridge corresponds to longitudinal fluctuations while the transverse ones correspond to the ones having a minimum in energy at the commensurate position. Moreover it has been confirmed numerically that the majority of the spectral weight is contained in the longitudinal fluctuations. This is in agreement with the theory which predicts that for Ising-like spin-1/2 chains, the longitudinal correlations should dominate in this low field region of the TLL phase ($H_c < H < H^*$).

5.5.3.4 Influence of the interchain interaction on the dispersion spectrum

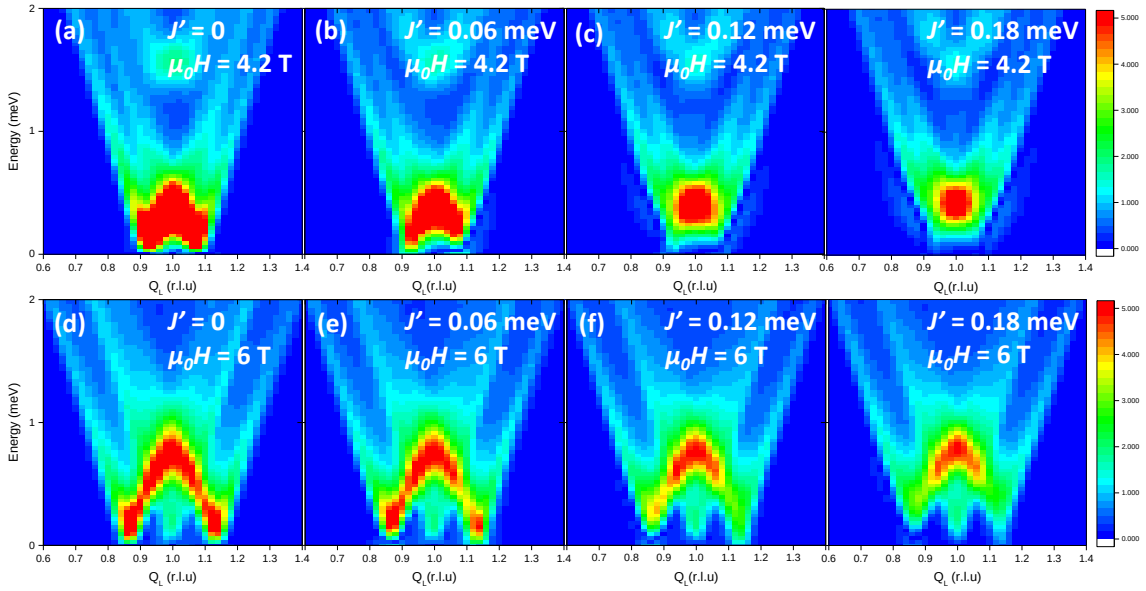

Figure 5.21: **Influence of the interchain interaction on the dispersion spectrum** along Q_L. (a-c) Calculated Dispersion spectra around the AF position ($Q_H = 2$) at $\mu_0 = 4.2$ T and for $J' = 0, 0.06$, 0.12 and 0.18 meV respectively. (d-f) shows the same spectra at $\mu_0 H = 6$ T.

Fig. 5.21 shows the calculated dispersion spectra along Q_L for different values of the interchain interaction treated in a mean-field theory. Close to the transition (see Fig. 5.21(a-c)), the interchain interaction strongly affects the spin-dynamics. Indeed for $J' = 0$ (see Fig. 5.21(a)), the incommensurability is well developed. However, if we increase the interchain interaction up to $J' = 0.12$ meV (see Fig. 5.21(c)), the spectral weight shrinks at the commensurate position. This must be due to the limitation of the mean field treatment of the interchain interaction to capture a step-like modulation of the amplitude of the moments expected close to the transition.

However, further away from the critical field, for example at $\mu_0 H = 6$ T (see Fig. 5.21(d-f)), the interchain interaction has less influence with only moderate changes in the spectral weight. But still, $J' = 0$ or eventually 0.06 meV allows to reproduce better the experiment.

Thus, the interchain interaction treated in mean field theory does not alter too much

the spin-dynamics, except close to the transition. THis shows mainly that it is not a crucial parameter for the spin dynamics of $BaCo_2V_2O_8$ in the LSDW phase.

5.6 Conclusion

Before concluding, I would like to discuss a study on $SrCo_2V_2O_8$ under a longitudinal field has been done in parallel to our work [Wan+18; Yan+17]. In their paper, Wang et *al.* did not use neutron scattering experiments but terahertz spectroscopy and thus they were only sensitive to the ZC point $(0, 0, 0)$. They have mainly focused on the field dependence of the excitations in the paramagnetic phase and have shown that they correspond to Bethe strings, quasiparticles that have been predicted a long time ago from the Bethe ansatz [Bet31; Gau71; TS72]. In our case, we probed the spin-dynamics of $BaCo_2V_2O_8$ for several points of the Brillouin zone, and we focused on the dispersion spectra along the chain in the ordered phase.

In our work, the spin-dynamics of $BaCo_2V_2O_8$ under a longitudinal field has been investigated both experimentally and numerically. We have shown that it corresponds to the one of a Tomonoga Luttinger liquid. This is expected to occur by applying the field along the easy-axis of anisotropy which changes the system from a gapped Néel phase to an incommensurate gapless phase [Mül+81]. The good agreement between the experiment and the numerical calculations allows us to confirm the fact that the majority of the spectral weight is contained in the longitudinal fluctuations. This result, consistent with the fact that the longitudinal correlations are predicted to dominate in this material because of its anisotropy, is highly non-trivial. Indeed it enlightens the very strong quantum character of $BaCo_2V_2O_8$ since classical systems prefer to fluctuate both perpendicularly to the magnetic field and to the ordered moments. While the TLL spin-dynamics has been studied in many Heisenberg materials, $BaCo_2V_2O_8$ is the first anisotropic spin-chain where the dispersion spectrum is probed in the gapless phase.

We have shown here that $BaCo_2V_2O_8$ is a remarkable material showing many quantum features. In particular, we have proven that the longitudinal fluctuations, usually rather elusive, are in our case enhanced by the application of a magnetic field along the c-axis.

Chapter 6

Pressure and doping effect on $BaCo_2V_2O_8$: preliminary results

Sommaire

6.1 Summary

6.1.1 Abstract

In this chapter, I will first present the study of $BaCo_2V_2O_8$ under high pressure and longitudinal field where a commensurate-incommensurate transition from a Néel state to a longitudinal spin-density waves (LSDW) phase occurs as explained in Chap. 5. I will show and discuss the specific heat results which has led to the (H, P, T) phase diagram of $BaCo_2V_2O_8$.

Second, I will present very briefly the study of $BaCo_2V_2O_8$ under the substitution of the magnetic ions Co^{2+} by non-magnetic impurities Mg^{2+}. I will show the static and dynamical properties of $Ba(Co_{1-x}Mg_x)_2V_2O_8$ measured by neutron scattering. Then I will present my numerical calculations which reproduce some of the experimental features. Finally I will give a conclusion and the perspectives of this study. Both studies are ongoing studies and the results and conclusions are still preliminary.

6.1.2 Résumé en français

Le sixième chapitre est consacré à deux études toujours en cours. La première concerne $BaCo_2V_2O_8$ sous pression hydrostatique et sous champ longitudinal. Afin de déterminer le diagramme de phase (H, P, T) de $BaCo_2V_2O_8$ des mesures de chaleur spécifique sous champ magnétique et sous pression hydrostatique ont été faites. Pour cela, $BaCo_2V_2O_8$ a été préalablement placé dans une cellule à enclumes diamant, dispositif permettant d'atteindre des pressions de l'ordre de 10 GPa. Les résultats ont montré que la température critique et le champ critique augmentent lorsque la pression augmente. La température critique augmente néanmoins très légèrement dans la phase LSDW en comparaison avec la phase Néel, ce qui nous a permis de conclure que l'interaction intrachaîne est la quantité la plus affectée lorsque la pression augmente.

La deuxième étude concerne la substitution des ions magnétiques de Co^{2+} par des ions non magnétiques Mg^{2+}. Nous avons pour cela étudié les propriétés statiques et dynamiques de $Ba(Co_{1-x}Mg_x)_2V_2O_8$ pour les deux concentrations $x = 2\%$ et $x = 5\%$.

L'étude des propriétés statiques par diffraction des neutrons montre que la structure magnétique à champ nul est essentiellement conservée en présence des impuretés. La température critique décroît linéairement lorsque la concentration magnétique augmente jusqu'à $x = 5\%$. La phase LSDW n'a pas été observée pour $x = 5\%$ dans la gamme de températures étudiée et une autre expérience est planifiée afin de voir si celle-ci existe pour le cas $x = 2\%$.

Concernant les propriétés dynamiques, les mesures par diffusion inélastique dans les deux composés de neutrons ont montré que les impuretés affectent beaucoup le spectre des excitations. En effet, en plus des excitations discrètes dispersives dues au confinement des spinons par l'interaction interchaîne qui se retrouvent élargis, des modes non dispersifs existent dans la partie des basses énergies du spectre. Ces derniers doivent provenir des effets de taille finie du système et pourraient être vus comme excitations locales oú les spinons sont liés aux impuretés non magnétiques. Mes calculs de diagonalisations exactes semblent confirmer ce qui est observé expérimentalement. D'autres expériences de diffusion neutronique sont prévues afin d'aller plus loin dans l'analyse de ces échantillons dopés. De plus des calculs iTEBD et Monte Carlo quantique pourraient nous aider à mieux comprendre l'effet de ces impuretés non magnétiques.

6.2 $BaCo_2V_2O_8$ under a hydrostatic pressure

6.2.1 Context and motivations

A quantum phase transition is defined as a transition due to quantum fluctuations at zero temperature by varying a physical parameter such as a magnetic field. This is what we have seen in the previous chapters (see Chap. (4) and Chap. (5)), where we have studied two different quantum phase transitions in $BaCo_2V_2O_8$ for different orientations of the magnetic field.

The idea to probe phase transitions in magnetic systems by means of magnetic fields comes to mind naturally. However, another physical parameter that we can play with is the pressure. Studies with pressure are commonly done with superconductors, for example the study of Drozdov et *al.* where they have found a conventional superconductivity at ambiant temperature in the sulfure hybride system H_2S at high pressure (around 200 GPa which is almost the gravitational pressure of the sun...) [Dro+15]. Another example is the investigation of phase transitions in heavy fermion compounds, for instance the well known compound URu_2Si_2, where a mysterious hidden order phase[1] occurs [Has+08]. Concerning magnetic systems, the effect of the application of a hydrostatic pressure has been investigated in some compounds such as the spin-1/2 ladder system $SrCuO_3$ [Weh+18], the spin-Peierls chain TiOCl [Rot+18] or in the quantum dimer material $TiCuCl_3$ where quantum phase transitions are controlled by high pressure and probed by inelastic neutron scattering experiments [Mer+14].

Some theoretical studies have been carried out in order to relate the critical field $\mu_0 H_c$ and the critical temperature T_c to the anisotropy Δ, the interchain interaction J' and intrachain interaction J of quasi-1D spin systems. Steiner et *al.* proposed the following formula for the critical temperature T_N between the paramagnetic phase and the Néel phase [SVW76]: $k_B T_N \simeq S^2\sqrt{|J'||J|}$. This experession is modified in the quantum case where quantum fluctuations decrease the critical temperature [SIP75]. The anisotropy also plays a role since the ordering is easier in the Ising case than in the Heisenberg case [SIP75; SVW76]. To model the Néel to LSDW phase transition obtained in a longitudinal field in $BaCo_2V_2O_8$, Okunishi et *al.* [OS07] have studied numerically a linear spin chain by treating the interchain interaction by mean field theory. They have shown that both the critical temperature T_c^{ic} between the incommensurate longitudinal spin-density waves (LSDW phase) state and the paramagnetic phase and the critical field $\mu_0 H_c$ between the Néel phase and the LSDW phase increase with increasing Δ. Moreover they proposed the following formula relating T_c^{ic} and the interchain interaction: $T_c^{ic} \propto J(J'/J)^{\eta_x(2\eta_x-1)}$ where $\eta_x = \eta_x(H,\Delta)$ is the Luttinger exponent with $\eta_x > 1$ in the LSDW phase.

Experimentally, Niesen et *al.* investigated the effect of a chemical pressure in $BaCo_2V_2O_8$ by substituting the atoms of barium by lighter atoms of strontium. They have shown that the lattice parameter a strongly decreases while c increases slightly when increasing strontium concentration (see Fig. 6.1(a)). The main effect of the chemical pressure is thus to bring the chains closer to each other. Therefore, the interchain interaction is expected to be stronger. However they have investigated the $(H-T)$ phase diagram of $Ba_{1-x}Sr_xCo_2V_2O_8$ by macroscopic measurements for different values of the Sr concen-

[1] The name of "hidden order" comes from the fact that despite 20 years of experimental and theoritical work, the order parameter which leads the system to this phase is still unknown.

tration and they have shown that the critical temperature T_N decreases with increasing the concentration of strontium (see Fig. 6.1(b)). This result is counter intuitive but is probably due to the enhancement of the frustration of the interchain interactions between neighboring chains. In contrast, the critical magnetic field $\mu_0 H_c$ at zero-temperature is not affected with increasing the concentration of Strontium.

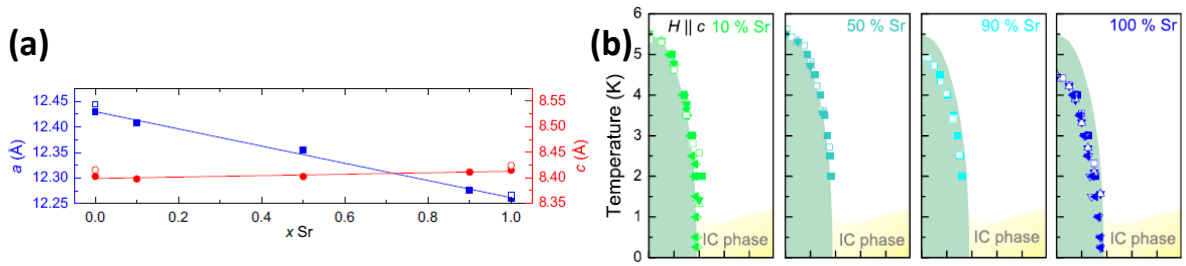

Figure 6.1: **$BaCo_2V_2O_8$ under chemical pressure.** (a) lattice parameters a (in blue) and c (in red) as a function of the concentration of Strontium. (b) $(H-T)$ phase diagram of $Ba_{1-x}Sr_xCo_2V_2O_8$ under a longitudinal magnetic field for differents concentration x of strontium. Figures extracted from [Nie+14]

In our case, the idea is to study the effect of an hydrostatic pressure on $BaCo_2V_2O_8$ under a longitudinal field (i.e. $\vec{H} \parallel \vec{c}$) to obtain its phase diagram (H, P, T). Indeed, one can imagine intuitively that the uniform pressure will induce changes of the interchain J' and intrachain J couplings. The fact that the pressure is applied in an isotropic way does not necessary imply however that the two exchange couplings will vary by the same amount. Finally, the anisotropy can also be affected if the oxygen octahedra surrounding the Co^{2+} are distorted.

To probe the (H, P, T) phase diagram of $BaCo_2V_2O_8$, we have done specific heat measurements (AC-calorimetry) under high pressure using the diamong anvil cells (DACs) described in Chap. (2.3).

6.2.2 AC-calorimetry measurements

6.2.2.1 Experimental setup

This experiment has been carried out in the CEA-Grenoble with the help of Daniel Braithwaite. When the DACs cells are ready, they are loaded on the stick of the orange cryostat shown in Fig. 6.2 allowing to reach a temperature of ~ 2.8 K. A magnetic coil allows to apply a magnetic field up to 9 T.

We have then performed AC-calorimetry measurements (for more details see section 2.3.2.1). The working frequency was determined by measuring the frequency dependence of the signal at constant temperature. Then the frequency multiplied by the measured signal V_{AC} as a function of the frequency is plotted in a log-log scale. At low frequency, a linear dependence is observed. This indicates that the sample is still thermally coupled to the bath: in one period, the heat can propagate in the sample and in its environment. Then a flat dependence (frequency-independent) is observed. This is where the quasi-adiabatic conditions hold and thus where the sample is thermally decoupled

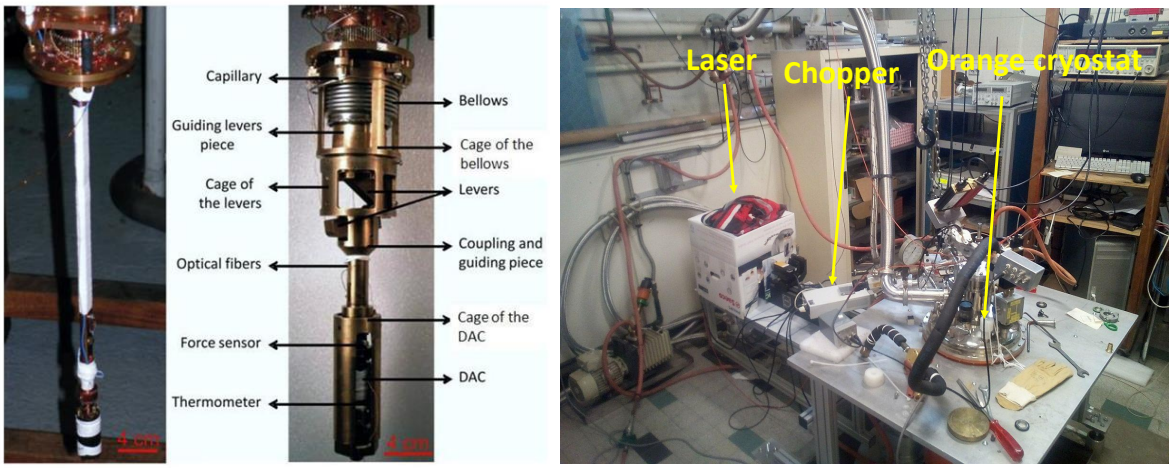

Figure 6.2: **Experimental setup of specific heat measurements under high pressure, magnetic field and low-temperature**. Left: The stick of the orange cryostat where the DAC is inserted. The stick is equipped of levers which allow to apply a force (and thus a pressure) on the DAC. Right: Picture of the experimental setup. The stick is now inside the orange cryostat which is surrounded by a magnetic coil. The laser and the chopper are also shown.

from the bath. We chose to work in this regime at $f = 615$ Hz.

Two kinds of calorimetric measurements have been done:

- by varying the temperature at a fixed value of the magnetic field. These measurements were done with a step of 1 T.
- by varying the magnetic field at a fixed value of the temperature. All these measurements were done with a temperature of 3 K.

In the following, $P = 0$ is associated to the ambient pressure ($\simeq 1$ bar).

6.2.2.2 Criterion for the data treatment

AC-calorimetry measurements allow to probe phase transitions for small samples in a semi-quantitative way. With this method, both the amplitude of the oscillating signal V_{AC} proportional to the alternative part of the temperature T_{AC} of the sample (and thus inversely proportional to the heat capacity C) and the phase shift θ between the applied heat and the resulting thermal oscillation are measured.

Fig. 6.3 shows the criterion that we have used to identify transitions for the two different calorimetric measurements (in temperature and in magnetic field). Here the calorimetry curves are expressed as C/T_{AC}.

Fig. 6.3(a-b) show calorimetry measurements in amplitude and in phase shift respectively versus temperature at $\mu_0 H = 1$ T for $P = 5$ kbars and $P = 65$ kbars. Note that the background is temperature and pressure dependent. The anomaly peak in the amplitude

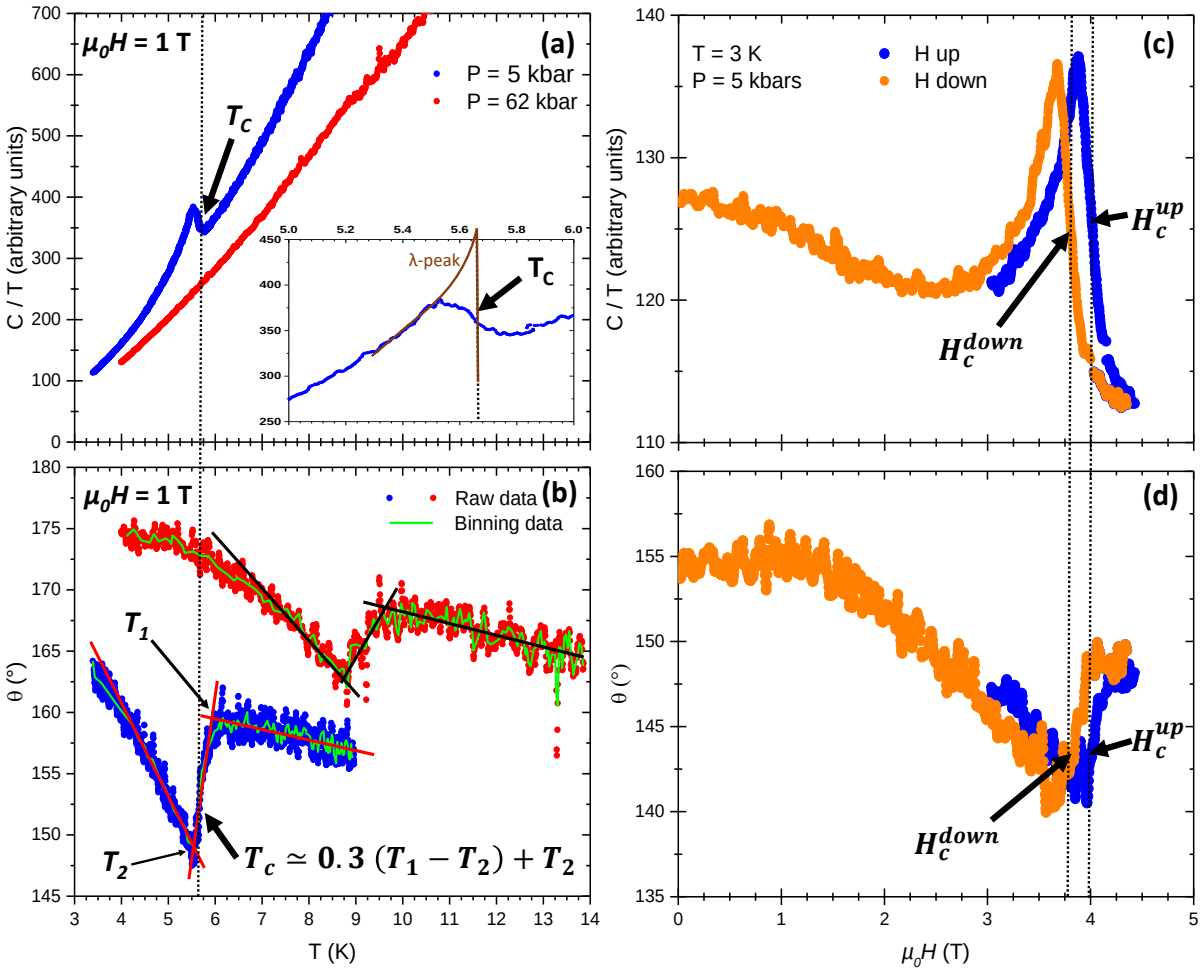

Figure 6.3: **Criterion for data treatment**. (a) Calorimetry measurements versus temperature at $\mu_0 H = 1$ T for selected pressures: 5 kbars in blue and 62 kbars in red. The inset is a zoom of the anomaly rounded peak seen at $P = 5$ kbars. The brown solid line shows the fictitious λ-peak expected. One can see that the temperature at the inflection point of the rounded curve corresponds to the value given by the λ-anomaly. (b) Corresponding phase shift θ. The points and the green solid lines are the raw and binned data respectively. The black dashed line shows the critical temperature. The black and red solid lines are an approximation of the binned data curve. (c) Calorimetry measurements with increasing and decreasing the magnetic field measured at $T = 3$ K. (d) Corresponding phase shift θ. The black dashed lines point out the critical field for increasing and decreasing field.

signal V_{AC} becomes rapidly undetectable with increasing the pressure (see Fig. 6.3(a)). However it is still observable in the phase shift for any values of the pressure. This is why I have mainly focused on the phase shift rather than the amplitude.

Fig. 6.3(c-d) shows calorimetry scans in amplitude and in phase shift respectively versus magnetic field at $T = 3$ K for $P = 5$ kbars only. One can see that an hysteresis is present when ramping up and down. Here also, when increasing the pressure, the anomaly in C/T becomes rapidly undetectable but still observable in the phase shift (curves not shown).

The criterion that I chose to extract the critical temperature T_c is the following: from the low pressure results (i.e. $P < 40$ kbars where the anomaly in the C/T signal is still observable), the critical temperature marking the transition is extracted by taking the inflection point of the anomaly in the C/T signal corresponding to the temperature that would give a λ sharp peak (see the inset in Fig. 6.3(a)). From that, the obtained value is reported on the phase shift data. In our example $T_N \simeq 5.6$ K. Then I have binned the raw data in order to reduce the duplicate data and also to deal with the fact that the noise increases with increasing the pressure (see the green lines in Fig. 6.3(b)). The curve is then approximated by three straight lines (red and black lines in Fig. 6.3(b)) and two temperatures T_1 and T_2 can be extracted at their intersection. It turns out that the calculation of the ratio $(T_c - T_2)/(T_1 - T_2)$ for different magnetic fields and different pressures (where the anomaly in the amplitude signal is still observable) gives systematically $\simeq 0.3$. Therefore, for each calorimetric measurement, I did the same procedure consisting of:

1. binning the data of the phase shift θ
2. plotting the solid lines and extracting the intersection points T_1 and T_2
3. calculating the critical temperature through the formula $T_c = 0.3(T_1 - T_2) + T_2$

The same procedure was used on the measurements in magnetic fields. For more convenience, I have systematically performed measurements while ramping down the field to be in the same conditions given the hysteretical nature of the Néel-LSDW transition.

6.2.3 Experimental results

From the data treatment described above, we extracted the critical temperatures T_N and T_c^{ic} and the critical field $\mu_0 H_c$. Example of (H, T) phase diagram at different pressures are shown in Fig. 6.4.

Note first that the data at ambiant pressure reproduces well what has been observed in $BaCo_2V_2O_8$, both with neutrons and heat capacity measurements [Can+13].

Fig. 6.5 shows the pressure dependence of the critical temperatures T_N and T_c^{ic} for different values of the magnetic field. The extraction of $\mu_0 H_c$ with calorimetric measurements performed by varying the magnetic field at $T = 3$ K was limited by the fact that $\mu_0 H_c$ becomes too high to be probed above 50 GPa. Moreover the extraction of the critical temperatures T_N and T_c^{ic} at high values of pressure and high values of magnetic field (typically 8 T and 9 T) was impossible due to the very strong noise in the data increasing both with the pressure and the temperature.

We can observe that, in the Néel phase, the critical temperature T_N increases with increasing the pressure for any value of the magnetic field. Moreover the behavior is similar for all the values of the magnetic field. For one value of the pressure and by increasing the magnetic field, T_N decreases smoothly at low-field values (below 2 or 3 T) and starts to decrease faster afterwards following the expected dependence of an order parameter.

Surprisingly, T_N increases strongly in the Néel phase while T_c^{ic} increases very slightly in the LSDW phase. For example, between $P = 30$ kbars and $P = 46$ kbars, T_c^{ic} has

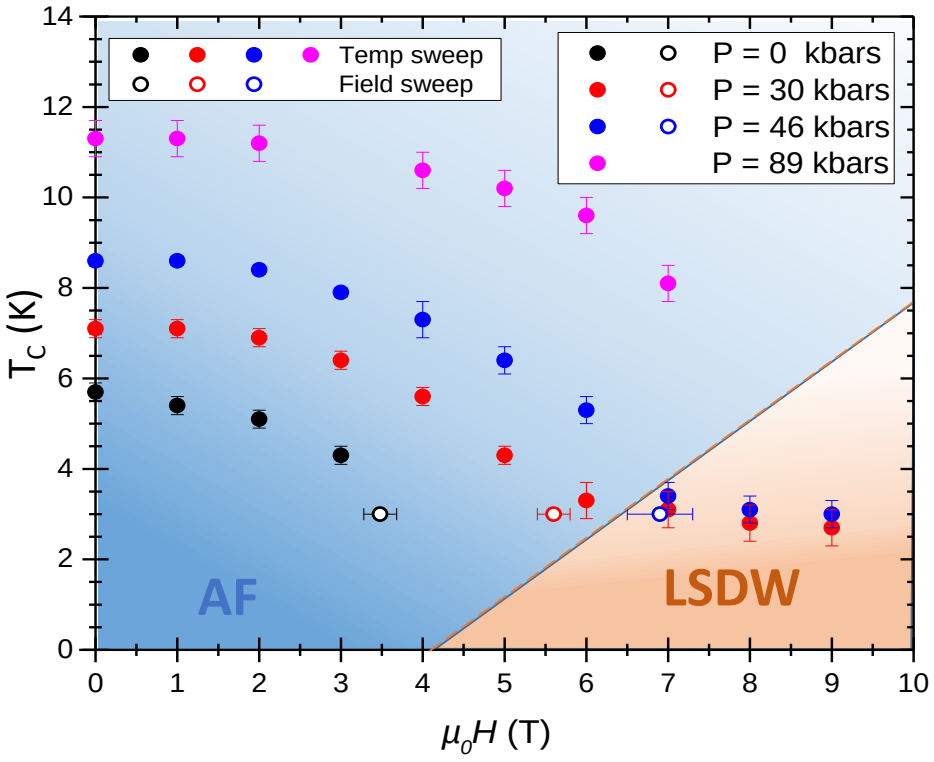

Figure 6.4: (H,T) **phase diagrams** obtained from the temperature and magnetic field calorimetric measurements (full and open symbols respectively) for selected pressures. The error bars correspond to the width of the anomaly seen in the phase shift.

increased only by about 0.1 K at $\mu_0 H = 7$ T while T_N increases by about 1.5 K at zero field in the Néel phase (see Fig. 6.4).

Another result that we can extract is the pressure dependence of the critical field $\mu_0 H_c$ at $T = 3$ K (see the inset in Fig. 6.5). Interestingly, $\mu_0 H_c$ increases linearly with the pressure. From the linear fit of the data, we obtain the following formula: $\mu_0 H_c = 0.07\ P + \mu_0 H_c^0$ (where P is expressed in kbars, and $\mu_0 H_c$ in T) with $\mu_0 H_c^0 = 3.6 \pm 0.2$ T, the intercept value of the linear fit. This value is consistent with the one found equal to 3.5 T at about 3 K at ambiant pressure in [Can+13].

6.2.4 Interpretation and perspectives

Our study by means of heat capacity measurements under pressure using DACs leads to the global (H,P,T) phase diagram of $BaCo_2V_2O_8$ (see Fig. 6.6).

Let us discuss our results with respect to the different experimental and theoretical studies recalled in section 6.2.1. We have the two formulas: $k_B T_N \simeq S^2\sqrt{|J'||J|}$ for an Heisenberg chain and $T_c^{ic} \propto J(J'/J)^{\eta_x(2\eta_x-1)}$ in the context of $BaCo_2V_2O_8$. Moreover H_c, T_N and T_c^{ic} increase with increasing the anisotropy Δ. In the study of Niesen et *al.*, T_N was shown to decrease by the substitution of the barium atoms by strontium atoms (lighter element) and this was ascribed to a complex change of the interchain interactions

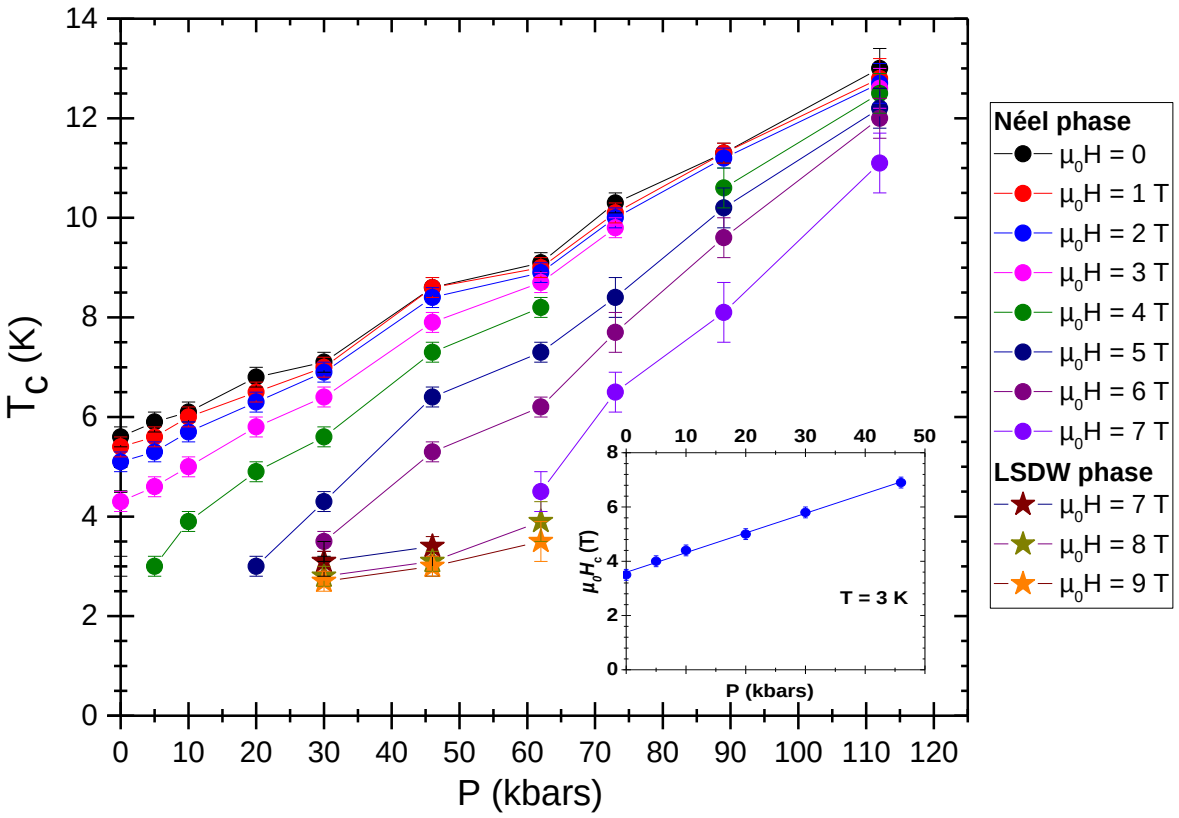

Figure 6.5: **Pressure dependence of T_N and T_c^{ic}** of the Néel phase (circles) and of the LSDW phase (stars) respectively for different values of the magnetic field. Solid lines are guide for the eyes. The inset shows the pressure dependence of the critical field $\mu_0 H_c$ at $T = 3$ K between the Néel phase and the LSDW phases. The solid line is a linear fit of the data.

and to the enhancement of the frustration between neighboring chains. In our study, the critical temperature T_c and the critical magnetic field $\mu_0 H_c$ between the Néel phase and the LSDW phase both increase with the pressure. Interestingly, T_c^{ic} increases very slightly in the LSDW phase. This is due to the fact that $\eta_x \to 1$ in the LSDW phase, leading to $T_c^{ic} \propto J'$. By comparing these results with all the considerations above, our study suggests that the intrachain interaction J increases by the application of a hydrostatic pressure and has the strongest effect on the critical temperature and magnetic field.

Our study does not allow us to extract individually J, J' and Δ since they all contribute to the critical quantities and to determine their pressure dependence through heat capacity measurements as there is no exact analytic formulas for quasi-1D systems. To go further, one possible idea would be to perform an inelastic neutron scattering experiment on $BaCo_2V_2O_8$ under pressure. Indeed through the dispersion spectrum and the iTEBD calculations, one could be able to extract the 3 parameters for each value of the pressure. A diffraction experiment under pressure would also be useful to probe the distortion of the structure of $BaCo_2V_2O_8$ under pressure. The problem is essentially that the DACs are impossible to use for neutron measurements, mainly because it requires really small

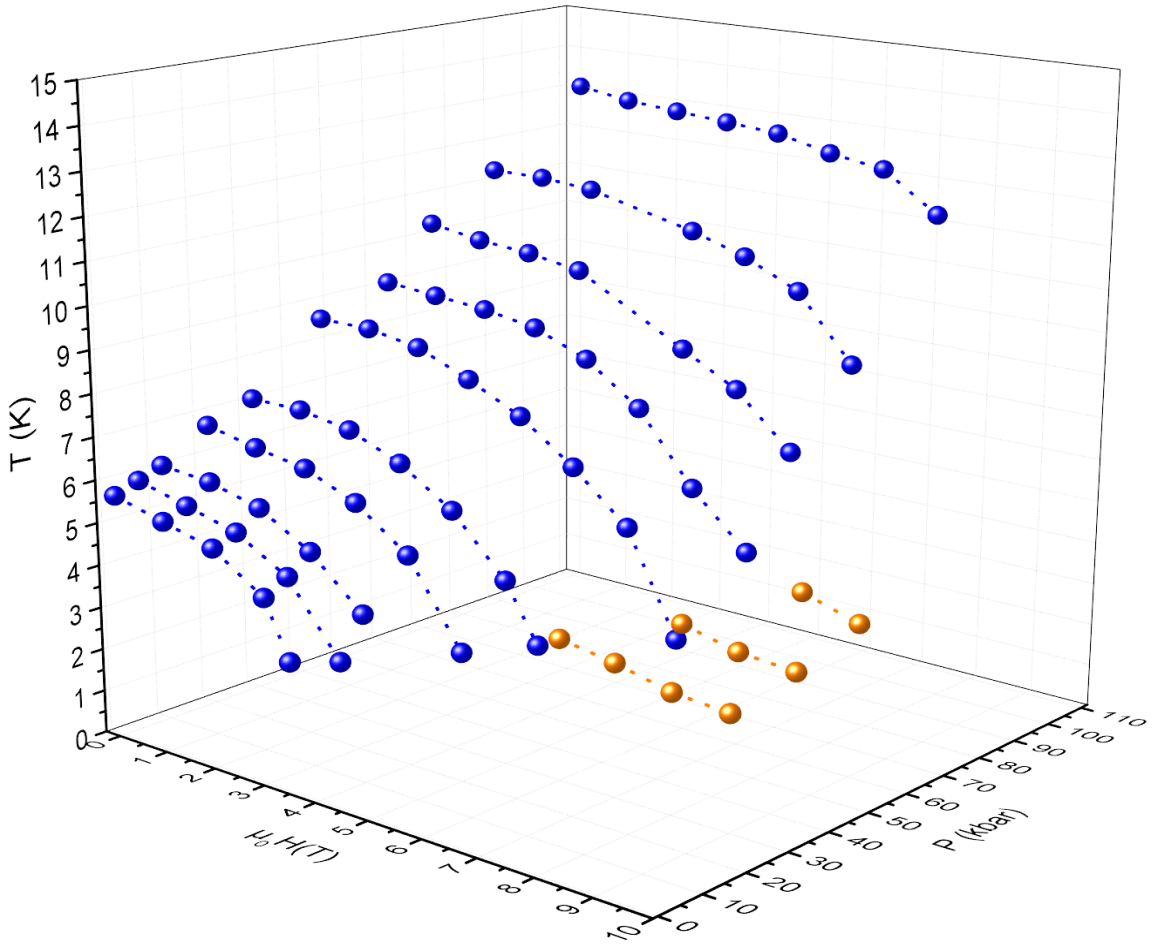

Figure 6.6: (H, P, T) **phase diagram of $BaCo_2V_2O_8$.** The blue and orange circles point out the critical temperatures of the Néel phase and the LSDW phase respectively. Dashed lines are guide for the eyes.

samples (about 0.2 mm^2 square) while inelastic measurements need large single crystals. This therefore limits the maximum pressure that can be applied. Using other pressure devices, diffraction experiments can be done on powder up to $\simeq$ 11 GPa but inelastic neutron scattering experiments on single crystal are still challenging under pressure.

What could be interesting is to do the same measurements but with the magnetic field applied perpendicularly to $\vec{c}$, along the b-axis. Indeed, as explained in Chap. 4, the origin of the staggered field along $\vec{a}$ induced by the uniform field along $\vec{b}$ is the small tilt between the c-axis and the local easy-axis of anisotropy. Niesen et *al.* have shown that for this configuration of the field, the critical field strongly decreases when increasing the concentration of strontium [Nie+14] implying that the tilt of the octahedron, hence the staggered field, is affected by the chemical pressure. The question is then: what happens when a hydrostatic pressure is applied on $BaCo_2V_2O_8$?

Finally it is also interesting to study the influence of the substitution of the Co^{2+} magnetic ions by non-magnetic impurities Mg^{2+}. This is what I am going to expose

briefly below.

6.3 Doping effect on $BaCo_2V_2O_8$

6.3.1 Context and motivations

The aim of this study is to understand the effect of cutting the chains by non-magnetic impurities. How are modified the static and dynamical properties of segments of chains with respect to infinite ones?

1D systems are known to be much more sensitive to doping effects than to 3D non frustrated systems [All+09; Son+15], in particular for the intra chain doping where a magnetic atom is replaced by another magnetic specie or by a non-magnetic impurity. This can be understood through Fig. 6.7. Whatever the case, the doping with impurities is expected to strongly affect the magnetic static properties, as well as the dynamics ones.

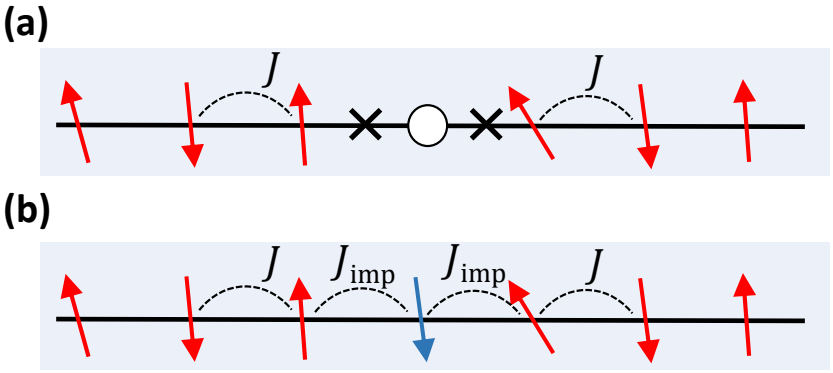

Figure 6.7: **Doping effect in spins chains.** (a) One magnetic atom is substituted by a non-magnetic impurity, leading to a cut of the chain. (b) One magnetic atom is replaced by another magnetic specie, leading to a local change of the intrachain interaction J to J_{imp}.

Theoritical studies have been done on the effect of impurities on quantum spin chains [EAH02; EA95; WH00a]. Exotic physics emerges from the disorder such as the Kondo effect in spin chains [LSA08], or the fact that segmented chains with an odd or an even number of spins behave differently [EA92].

Experimentally, many studies have also investigated the effect of in-chain impurities in spin ladder systems such as $SrCu_2O_3$ [Azu+97; Fuj+98; Ohs+99] and in spin-chains such as the spin-Peierls compound $CuGeO_3$ [Has+93; Mas+98; Gre+98; Gre+02]. This compound consists in spin-1/2 chains which spontaneously form spin-dimers (thus singlets carrying a spin $S = 0$) when decreasing the temperature, because of the distortion of the lattice. In $CuGeO_3$, it has been shown that the in-chain doping of the Cu^{2+} magnetic ions carrying a spin-1/2 by impurities (magnetic or not) strongly affects the spin-Peierls transition [Gre+02]. The critical temperature strongly decreases while increasing the concentration of impurities. Whatever the nature of the impurities, the singlets including an impurity are broken, yielding a free spin-1/2. Moreover, an AF order appears by an order by disorder effect and the associated Néel temperature increases while increasing

the concentration of impurities. Finally, the influence of the doping was also investigated on the incommensurate phase of $CuGe_{1-x}Si_xO_3$ appearing under magnetic field [Kir+96; Gre+98]. It was shown that this phase completely disappears for $x = 0.7\%$ which shows that the IC phase is much more fragile and sensitive to the long-range correlations than the AF phase. The nature of the excitations of such segmented chains have also been studied [Aug+99; Ken+03].

In addition to this, our main motivation is based on the work by S. Niesen et *al.* who studied through macroscopic measurements the effect of in-chain substitutions by replacing the magnetic ions of Co^{2+} by other transition metal ions with different spin quantum numbers (Cu^{2+}, Ni^{2+} and Mn^{2+}) and by non-magnetic ions Mg^{2+}. The latter subsitution strongly affects both the crystallographic and the magnetic properties of $BaCo_2V_2O_8$. Indeed the lattice parameter a is strongly reduced by the Mg^{2+} substitution (see Fig. 6.8(a)), as well as the critical temperature between the Néel phase and the paramagnetic phase and the critical field between the AF phase and the LSDW one (see Fig. 6.8(b)). Hovewer Niesen et *al.* concluded from their study that the anisotropy is not much affected by the substitution [Nie+14].

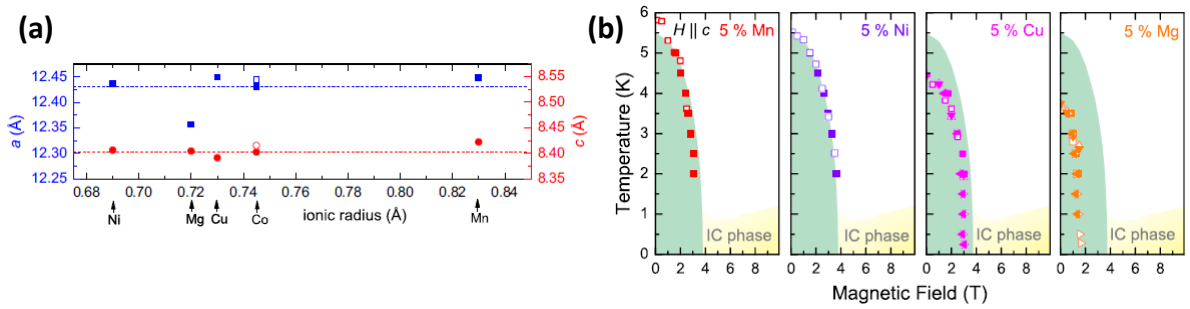

Figure 6.8: **In-chain subsitution of $BaCo_2V_2O_8$.** (a) Lattice parameters a and c as a function of the ionic radius of the element of substitution. (b) $(H-T)$ phase diagrams of $Ba(Co_{1-x}M_x)_2V_2O_8$ for a longitudinal field. Figures extracted from [Nie+14].

The first goal of our study was to check by neutron diffraction if the LSDW phase of $BaCo_2V_2O_8$ still exists when substituting the Co^{2+} magnetic ions by non-magnetic impurities Mg^{2+}. This could have allowed the investigation of both the static and dynamical properties of $BaCo_2V_2O_8$ at much lower values of the magnetic field. While we did not found a LSDW phase, it turns out that the dynamical properties of the doped $Ba(Co_{1-x}Mg_x)_2V_2O_8$ for the two concentrations of Mg^{2+} $x = 2\%$ and $x = 5\%$ nevertheless show a very interesting behavior as explained below. As the data are still under treatment and the results are not yet well understood, I will only show briefly what we obtained.

6.3.2 Static properties

Two single-crystal diffraction experiments have been carried out on 6T2 (LLB) for $x = 5\%$ and on D23 (ILL) for $x = 2\%$. These experiments were performed with a 6 T and a 12 T cryomagnet respectively, and with a dilution insert allowing to reach temperatures down to 50 mK.

After the refinement of the crystalline structure using the same structure as in the pure compound, we have found that it is essentially unaffected by the Mg^{2+} impurities. The quality of the refinement is illustrated by the standard plot showing the calculated vs observed Bragg intensities displayed in Fig. 6.9(a).

The same conclusion holds for the magnetic structure in zero-field (see Fig. 6.9(b)), yet the Néel temperature is slightly reduced from 5.5 K in the pure compound down to $T_N = 4.9$ K and 3.8 K for $x = 2\%$ and $x = 5\%$ respectively (see Figs 6.9(c-d)). The later value is consistent with what was observed in [Nie+14] (see Fig. 6.8(b)). The ordered magnetic moment is also reduced from 2.2 μ_B down to 1.8 μ_B and 1.3 μ_B for $x = 2\%$ and $x = 5\%$ respectively (see Fig. 6.9(d)). At zero-field, the ordered magnetic moment and the Néel temperature T_N then follow a linear dependence as a function of the concentration of impurities Mg^{2+} as shown in Fig. 6.9(d).

Finally, we have looked for the IC signal that would reveal the presence of the LSDW phase under longitudinal magnetic field. While in pure $BaCo_2V_2O_8$ the LSDW phase is observed above $\mu_0 H_c \simeq 4.0$ T [Can+13; Gre+15b], no such phase has been detected in $Ba(Co_{1-x}Mg_x)_2V_2O_8$ with $x = 5\%$ where a large reduction of the critical field $\mu_0 H_c \simeq 2$ T occurs [2]. This reduction is actually consistent with what was observed in [Nie+14] (see Fig. 6.8(b)).

The strong reduction of the Néel temperature T_N and of the critical field $\mu_0 H_c$, and the absence of an IC ordered phase above $\mu_0 H_c$ can be attributed to the decrease of the spin-spin correlations by the non magnetic impurities. This is in contrast with the case of $CuGeO_3$ where the AF order is enhanced by impurities. However, as for the incommensurate phase in $CuGeO_3$, the LSDW phase in $BaCo_2V_2O_8$ must be more fragile than the staggered one upon doping since it has a long periodicity. Qualitatively, the Mg impurities cut the chains and induce pinning of the magnetic moments in the chains thus leading to the destruction of the 3D ordering. We have started to study a smaller doping $x = 2\%$, to test if the LSDW phase resists to this amount of impurities.

6.3.3 Dynamical properties

One may wonder how do the impurities modify the dispersion spectrum of $BaCo_2V_2O_8$ at zero-field and what is the spin-dynamics of a segmented spin-chain.

To answer this, we have performed two inelastic neutron scattering experiments at zero-field on $Ba(Co_{1-x}Mg_x)_2V_2O_8$ for the two concentrations $x = 2\%$ and $x = 5\%$ on IN12 (ILL) using an orange cryostat allowing us to go down to 1.5 K.

We have determined the dispersion spectra at zero-field both for $\vec{Q} = (0, 0, Q_L)$ (for which only the transverse fluctuations S_{aa} and S_{bb} are probed) and $\vec{Q} = (2, 0, Q_L)$ (for which both longitudinal S_{cc} and transverse fluctuations are probed) and for the two concentrations $x = 2\%$ and $x = 5\%$. The INS experiments need to be completed and I show in the following only preliminary results.

Figs 6.10(a-b) show an example of such a spectrum for $x = 2\%$ (non-saturated and saturated in intensity respectively) measured at $T = 1.5$ K along $\vec{Q} = (0, 0, Q_L)$. This spectrum is very peculiar, since the intensity is nicely distributed in (Q, ω) space along a curve carrying the majority of the spectral weight that looks like the dispersion of the Zeeman ladder typical of the pure $BaCo_2V_2O_8$ case. These Zeeman Ladders [Gre+15a],

[2] Unfortunately, we have not been able to study yet the static properties of the 2% compound under field, due to cryogenic problems. An experiment is planned to finish this study.

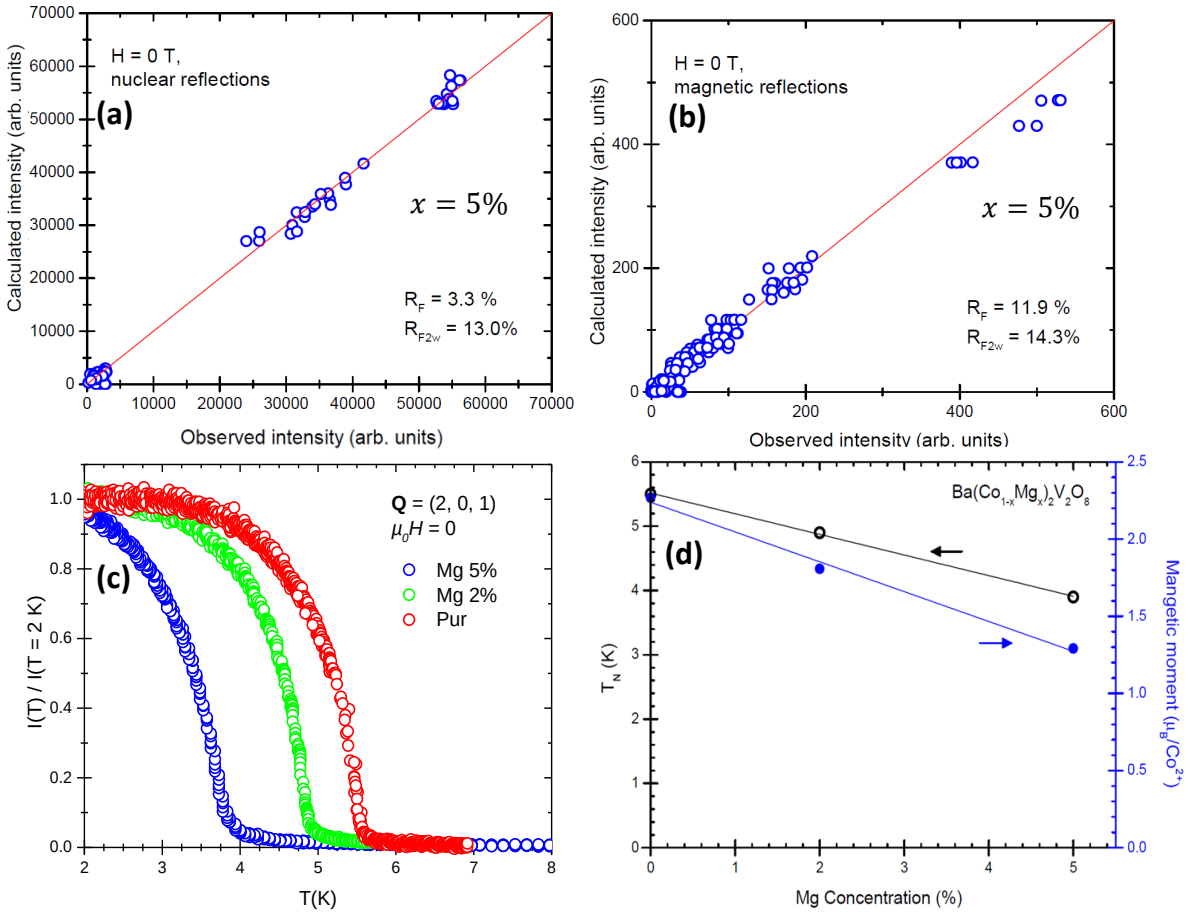

Figure 6.9: **Static properties of $Ba(Co_{1-x}Mg_x)_2V_2O_8$.** (a-b) Refinement of the nuclear and magnetic structures of $Ba(Co_{1-x}Mg_x)_2V_2O_8$ for $x = 5\%$ at zero-field. The agreement factors are reported on the figures. (c) Temperature dependence of the normalized neutron counts $I(T)/I(T = 1.5\ \mathrm{K})$ at the maximum of the magnetic Bragg peak 2 0 1 (which is proportional to $|m_c|^2$) at zero-field for $x = 0\%$ (pure compound), $x = 2\%$, and $x = 5\%$. (d) Value of the Néel temperature T_N (left scale) and of the ordered magnetic moment (right scale) as a function of the concentration of the non-magnetic impurities Mg^{2+}. The blue and black lines are linear fits of T_N and the ordered moment respectively.

i.e. a serie of discrete modes confined by the inter-chain interaction, still probably exist in the doped compound but much broader. Moreover in the low-energy part of the spectrum, i.e. below the curve carrying the majority of the spectral weight, non-dispersive modes are visible as shown in Figs. 6.10(c-d) for $x = 2\%$ at $\vec{Q} = (0, 0, Q_L)$ and $x = 5\%$ at $\vec{Q} = (2, 0, Q_L)$ respectively. These modes do not exist in the pure compound and thus should come from finite size effects due to the confinement of the excitations around the ends of the chain, i.e. the impurities [DV09]. Indeed it is easily understood that it costs less energy to flip a spin next to the impurity (as it is proportional to $\propto J$) than elsewhere in the chain ($\propto 2J$). To try to reproduce these non-dispersive modes, I have performed numerical calculations using my code.

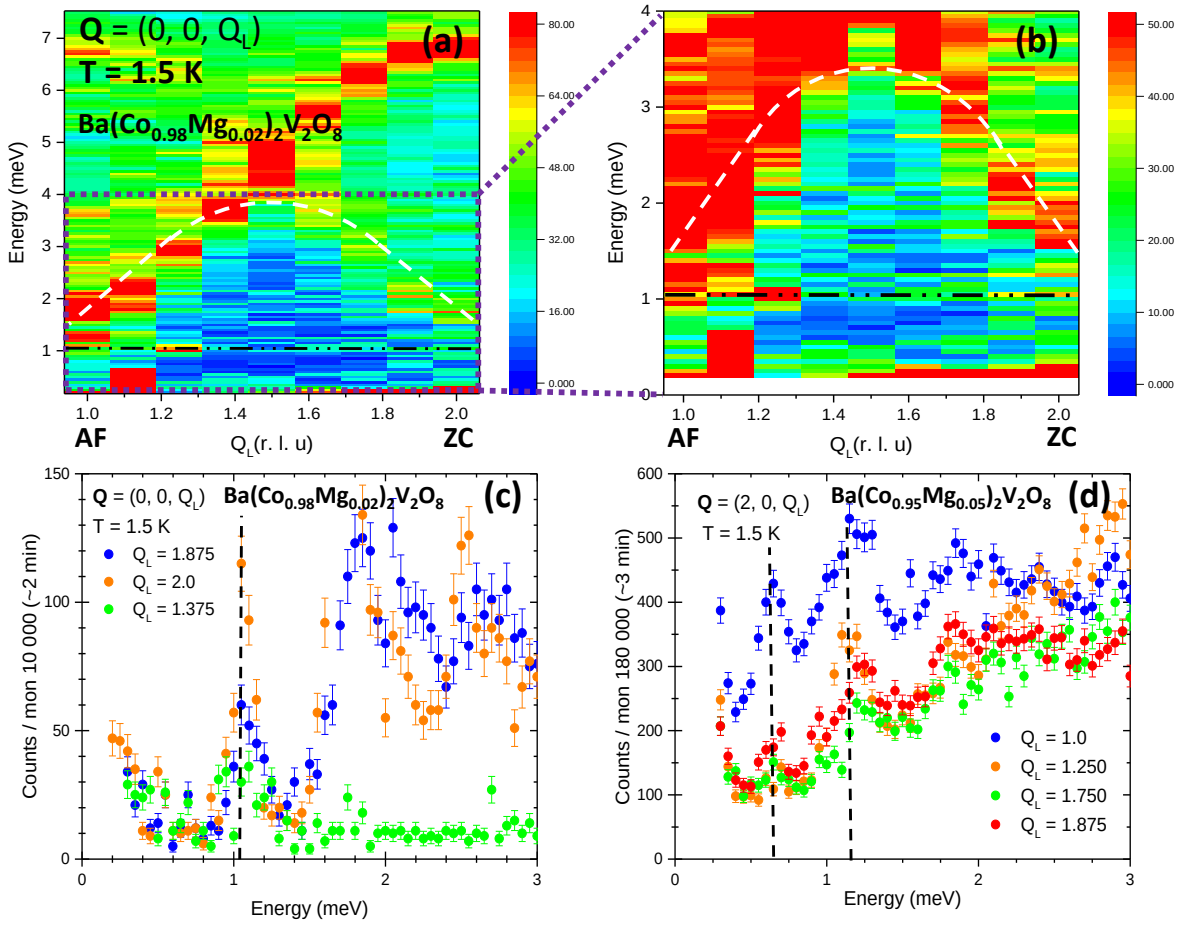

Figure 6.10: **Dynamical properties of $Ba(Co_{1-x}Mg_x)_2V_2O_8$ and non-dispersive excitations.** (a) Dispersion spectrum along $\vec{Q} = (0, 0, Q_L)$ for $x = 2\%$ measured at $T = 1.5$ K by gathering several energy scans obtained for different Q_L. The white dashed line delimits the part where no spectral weight is observed in the pure compound. The black dashed line points out the lowest non-dispersive energy mode observed in this system. (b) Zoom of (a) with a saturated intensity scale. (c-d) Energy scans for $x = 2\%$ and $x = 5\%$ at different Q_L. The black dashed lines point out non-dispersive modes.

6.3.4 Numerical calculations using exact diagonalization

If we suppose that the distribution of the magnetic impurities is homogeneous and thus that they are equally distributed in the chain, then the chain segments have a finite size and contain a number of spins $n \simeq 1/x$. To model these chain segments and the finite size effects, I removed the periodic boundary conditions in the calculations.

I chose to use at first step $n = 20 \leftrightarrow x = 5\%$, $J = 5$ meV, $\epsilon = 0.5$ and a slighter smaller value $J' = 0.1$ meV than in the previous calculations (where I took $J' = 0.3$ meV) in order to minimize the confinement of the spinons due to the interchain interactions.

Fig 6.11(a) shows the dispersion spectrum calculated along $\vec{Q} = (1, 0, Q_L)$ for $n = 20 \leftrightarrow x = 5\%$. One can see that we still have Zeeman ladders, but broaded in intensity. This may be due to both the finite size of the chain and/or the low interchain value $J' = 0.1$ meV. Interestingly, if we saturate the intensity of the dynamical structure factor

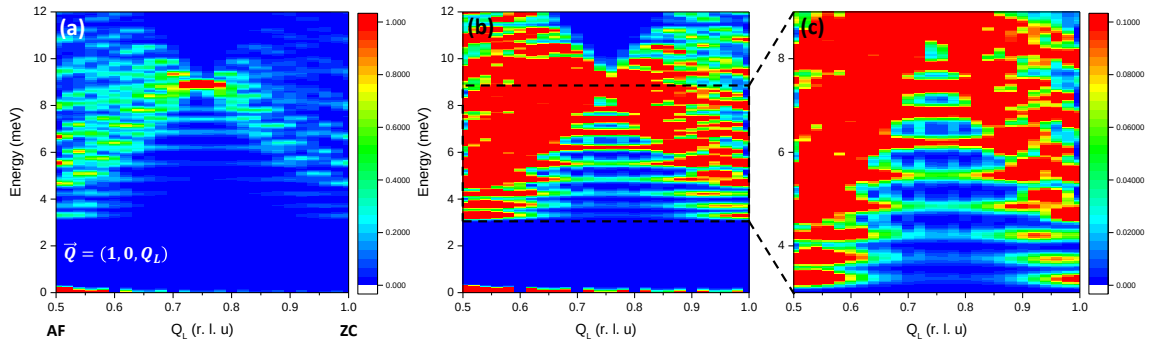

Figure 6.11: **Calculated dispersion spectrum of a chain segment** (a) along $\vec{Q} = (1, 0, Q_L)$ with $n = 20$. (b) Same than (a) with the intensity scale saturated in order to see the non-dispersive excitations. (c) Zoom of (b).

as shown in Fig. 6.11(b-c), non-dispersive modes appear in the $(\vec{Q}, \omega)$ zone delimited by the black-dashed rectangle, with a maximum of intensity at the AF point ($Q_L = 0.5$ numerically instead of $Q_L = 1$ experimentally as I consider a linear spin-chain in the calculation) and minimum between the AF point and the ZC point, i.e. $Q_L = 0.75$. This is consistent with what is observed experimentally (see at $Q_L = 1$ and $Q_L = 1.5$ in Figs. 6.10(a-b)).

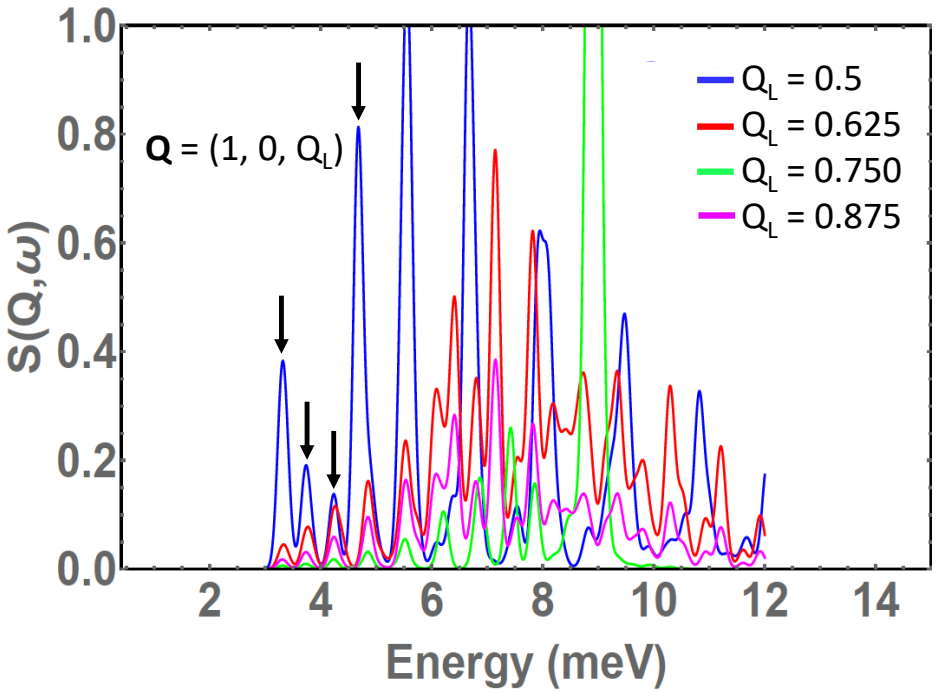

Figure 6.12: **Calculated energy scans** for different values of Q_L. The black arrows point out the four first non-dispersive modes, also shown in Fig. 6.11(c).

Fig. 6.12 shows the superposition of calculated energy-scans for various scattering vectors $Q = (1, 0, QL)$. At low-energy values, typically the ones in Fig. 6.11(c), one can clearly observe that the position in energy of the peaks does not move by varying Q_L (or very slightly). Moreover, we can also observe that the difference in energy $\Delta\omega$ between two successive non-dispersive mode is roughly constant as long as it is not mixed with the Zeeman ladders. The difference in energy between two successive excitations is given by $\Delta\omega = 2J/n$ [Boh+18; EA92; WH00a]. This yields $\Delta\omega)_{theory} = 0.5$ meV in agreement with the numerical value $(\Delta\omega)_{num} \simeq 0.5$ meV obtained in my calculations.

Here I want to emphasize the fact that these calculations are done for a segment of chain. However in $Ba(Co_{1-x}Mg_x)_2V_2O_8$, we rather have a Poisson distribution of size of the chains. Then a perfect simulation should be the sum over all sizes taking into account the different probability of having a chain of size n.

6.3.5 Preliminary conclusion and perspectives

We have seen that the substitution of Co^{2+} by non-magnetic impurities changes both the static and dynamical properties of $BaCo_2V_2O_8$. At zero-field, the nuclear and magnetic structures are essentially unaffected by the Mg impurities. Both the values of the ordered moment and of the Néel temperature T_N decrease linearly with increasing the concentration of impurities up to $x = 5\%$. The LSDW phase was not observed in $Ba(Co_{1-x}Mg_x)_2V_2O_8$ for $x = 5\%$ in the investigated temperature range and another experiment is planned to check if this phase is preserved in the case of $x = 2\%$. Concerning the dynamical properties, we have seen that the dispersion spectrum of $BaCo_2V_2O_8$ is strongly affected by the impurities. In addition to broadened Zeeman ladders, non-dispersive modes exist especially visible in the low energy part of the spectrum. They should come from the finite size effects of the system. This study is still in progress as both neutron diffraction and inelastic neutron scattering experiments are planned to complete these results. My calculations using exact diagonalization seem to confirms qualitatively what has been observed experimentally. Quantum Monte Carlo and iTEBD calculations would be helpful to understand deeper the effect of the non-magnetic impurities.

CONCLUSION

In this thesis, we have focused on the study of quantum phase transitions in the quasi-1D Ising-like antiferromagnet $BaCo_2V_2O_8$. This compound consists in chains of magnetic ions Co^{2+} carrying an effective spin $S = 1/2$ displaying a moderate anisotropy along the c-axis, hence parallel to the chains. This compound has revealed many quantum signatures as summarized in the following.

The first study was devoted to $BaCo_2V_2O_8$ under a transverse field, i.e. a field applied perpendicularly to the Ising-axis. While the Ising chain in a transverse field is a paradigm of quantum phase transition, we have found a new kind of phase transition. We performed both elastic and inelastic neutron scattering on a single crystal of $BaCo_2V_2O_8$ to better understand its static and dynamical properties under a transverse field. We have observed in the diffraction and inelastic neutron scattering experiments signatures of a quantum phase transition between 2 ordered phases. Indeed, because of the slight tilt of about 5° between the local Ising-axis of the magnetic moments and the c-axis, the application of a uniform transverse field induces a staggered magnetic field both perpendicular to the Ising axis and to the applied field. This local field competes with the Ising anisotropy and causes a quantum phase transition while increasing the field. To go further in the analysis, we have used numerical simulations, from my own code and by iTEBD calculations through a collaboration with Shintaro Takayoshi and Thierry Giamarchi. By combining the neutron scattering experiments and the numerical calculations, we were able to confirm the Hamiltonian of the system and the key role of the staggered field. Furthermore, it has been shown that this system can be mapped into quantum field theory model called double sine-Gordon model. The single sine-Gordon model is known to describe Ising-like spin chains and Heisenberg chain in a staggered field but so far, no experimental realization of a compound presenting these two aspects had been found until our study. The identification of the dual field double sine-Gordon model for $BaCo_2V_2O_8$ has allowed us to show that the quantum phase transition is topological in nature. Indeed, it has shown that this transition can be tuned through the applied magnetic field and comes from the competition between two dual topological excitations carrying a different topological index. In the low-field phase, the excitations consist in spinons carrying a topological index $S^z = \pm 1/2$ while in the high field phase, the excitations are pairs of bounded spinons carrying a topological index $S^x = \pm 1$. This work has led to the first experimental realization of such kind of topological phase transition [Fau+18].

The second study was dedicated to $BaCo_2V_2O_8$ under a longitudinal field, i.e. a field applied parallel to the Ising-axis. It has been theoretically predicted that it is possible to drive Ising-like spin-1/2 chains into a gapless Tomonaga Luttinger liquid (TLL) phase by applying a field parallel to the Ising-axis and thus closing the anisotropy gap. Moreover, because of the anisotropy, the longitudinal correlations are expected to dominate

the transverse ones just above the critical field and thus an exotic physics is expected. Because $BaCo_2V_2O_8$ presents a moderate anisotropy compared to previous studied compounds such as $CsCoCl_3$ or $CsCoBr_3$, the critical field in our case is $\mu_0 H_c \simeq 4$ T, thus easily reachable for the study by neutron scattering. We have thus performed an inelastic neutron scattering to probe the spin-dynamics along the chain across the commensurate-incommensurate phase transition. By combining experimental results and numerical calculations as in the previous study, we were able to show that the spin-dynamics of $BaCo_2V_2O_8$ above the critical field is compatible with the TLL theory. This is the first time that the dispersion spectrum for an anisotropic spin-1/2 chain is probed in this gapless phase. We have shown that the majority of the spectral weight is carried by the longitudinal fluctuations, i.e. fluctuations parallel both to the Ising-axis and to the applied magnetic field. We have therefore shown that $BaCo_2V_2O_8$ is a remarkable material where both the static and dynamical properties are dominated by quantum longitudinal fluctuations in the TLL phase enhanced by a longitudinal magnetic field.

A study of $BaCo_2V_2O_8$ under a hydrostatic pressure has also been carried out. We have probed $BaCo_2V_2O_8$ under both pressure and a magnetic fields up to 9 T parallel to the chain-axis to establish its (H, P, T) phase diagram. To do so, we have used diamond anvil cells allowing us to reach a pressure of about 10 GPa. The pressure cell containing the sample was then placed into an orange cryostat with a magnetic coil. Then, we have performed specific heat measurements using the AC-calorimetry principle. The analysis of the data has shown that both the critical temperature T_c and the critical field H_c increase with increasing the pressure. Curiously, the critical temperature of the LSDW phase of $BaCo_2V_2O_8$ seems to be very slightly dependent on the pressure compared to the Néel phase. From our results and the comparison of other theoretical and experimental studies, we proposed that the intrachain interaction J increases and has the strongest effect on the critical temperature and critical magnetic field. This should be confirmed by doing inelastic neutron scattering experiment under pressure. What could be interesting would be to do the same study with a magnetic field applied perpendicularly to the chain. In this case, the effective staggered field induced by the uniform field comes from the slight tilt between the local Ising-axis of the magnetic moments and the c-axis. One could expect to modify and to control the Landé tensor $\tilde{g}$ by applying a hydrostatic pressure and thus to tune the topological quantum phase transition that we evidenced at ambient pressure.

A study of $Ba(Co_{1-x}Mg_x)_2V_2O_8$ has also been initiated with the two different Mg concentrations $x = 2\%$ and $x = 5\%$ in order to understand the effect of the substitution of the magnetic ions Co^{2+} by non-magnetic impurities Mg^{2+}. Indeed, the impurities cut the chains into segmented chains and a drastic change in the static and the dynamical properties of doped compounds is expected compared to the pure compound $BaCo_2V_2O_8$. We have then started to perform elastic and inelastic neutron scattering experiments. Concerning the static properties, we have shown that both the critical temperature and the critical field $\mu_0 H_c$ decrease linearly with the non-magnetic impurities concentration x, i.e. a signature of the reduction of the correlations in the system. The more surprising result comes from the spin-dynamics measurements where non-dispersive modes seem to be present in the dispersion spectrum at zero-field. These modes could arise from the finite size effects of the system and could be seen as localized excitations where the spinons are bounded to the impurities. This work is still in progress. Indeed other neutron scattering experiments are planned to go further in the analysis and numerical calculations such as

quantum Monte Carlo and iTEBD should help us to get a deeper understanding of the effect of the non-magnetic impurities.

Finally, this work has shown a very nice example of the complementary between experimental work, numerical calculations and theory. Indeed the systematic comparison between the neutron scattering results and the iTBED calculations have revealed the nature of two exotic quantum phase transitions and many quantum signatures of this original quasi-1D Ising-like antiferromagnet $BaCo_2V_2O_8$ model system. To go further in our understanding of the 3D couplings in this system, Monte Carlo calculations could be performed.

En conclusion, lors de cette thèse, nous nous sommes concentrés sur l'étude de transitions de phases quantiques dans le composé quasi-1D antiferromagnétique à anisotropie de type Ising $BaCo_2V_2O_8$. Ce composé consiste en des chaînes d'ions magnétiques Co^{2+}, portant un spin effectif 1/2. Les moments magnétiques présentent une anisotropie le long de l'axe c, i.e. le long des chaînes. Ce composé a révélé de nombreuses signatures quantiques, comme résumé dans ce qui suit.

La première étude est dédiée à $BaCo_2V_2O_8$ sous un champ magnétique transverse, i.e. un champ magnétique perpendiculaire à l'axe Ising. Alors que la chaîne Ising en champ transverse est un paradigme de transition de phase quantique, nous avons trouvé une transition de phase d'une toute nouvelle nature dans $BaCo_2V_2O_8$ en champ transverse. Nous avons effectué des mesures de diffusions élastiques et inélastiques de neutrons sur un cristal de $BaCo_2V_2O_8$ afin de mieux comprendre ses propriétés statiques et dynamiques sous champ transverse. Nous avons observé au travers de ces expériences la signature d'une transition de phase quantique entre deux phases ordonnées. En effet, à cause d'une légère inclinaison d'environ 5° de l'axe d'anisotropie avec l'axe c, le tenseur de Landé est non-diagonal. En d'autres termes, l'application d'un champ uniforme transverse induit un champ effectif alterné perpendiculaire à la fois à l'axe Ising et au champ uniforme appliqué. Ce champ local entre en compétition avec l'anisotropie de type Ising. Il en résulte une transition de phase quantique lorsque le champ magnétique augmente. Afin d'aller plus loin, nous avons utilisé des techniques numériques, à la fois des diagonalisations exactes de mon côté, et des calculs iTEBD au travers d'une collaboration avec Thierry Giamarchi et Shintaro Takayoshi. En combinant les expériences de diffusion de neutrons et les calculs numériques, nous avons été capables de confirmer l'Hamiltonien du système et le rôle clé du champ alterné dans la transition de phase quantique. De plus, nous avons montré que ce système peut être décrit par une théorie des champs dite de "Double sine Gordon". Le simple "sine Gordon model" est connu pour décrire des chaînes de type Ising et des chaînes de type Heisenberg soumises à un champ local alterné, mais jusqu'à maintenant aucun système ne présentait à la fois ces deux ingrédients. L'identification du modèle Double sine Gordon pour $BaCo_2V_2O_8$ nous a permis de montrer que la transition de phase est de nature topologique. En effet, cette transition peut être contrôlée par le champ magnétique et provient de la compétition entre deux excitations topologiques de natures différentes. Dans la phase à bas champ, les excitations consistent en des spinons ayant un index topologique $S_z = \pm 1/2$ alors que dans la phase à haut champ, les excitations sont des paires de spinons confinés portant un index topologique $S_x = \pm 1$. Ce travail a mené à la première réalisation d'une telle sorte de transition de phase quantique.

La seconde étude a été dédiée à $BaCo_2V_2O_8$ sous champ longitudinal, i.e. un champ parallèle à l'axe d'anisotropie de type Ising. Il a été théoriquement prédit qu'il est possible d'amener un système de chaînes de spins 1/2 de type Ising à une phase non gappée dite liquide de Tomonage Luttinger (TLL) en appliquant un champ magnétique parallèle à l'axe Ising et par conséquent en fermant le gap d'anisotropie. De plus, à cause de cette anisotropie, les corrélations longitudinales, à la fois statiques et dynamiques, dominent les corrélations transverses juste au dessus de la transition. Du fait de son anisotropie modérée comparé aux précédents composés tels que $CsCoCl_3$ et $CsCoBr_3$, $BaCo_2V_2O_8$ a un champ critique de $\mu_0 H_c \simeq 4$ T, facilement accessible au moyen de la diffusion des neutrons. Nous avons effectué une expérience de diffusion inélastique de neutrons afin de mesurer la dynamique de spins le long des chaînes au dessus de la transition de

phase commensurable-incommensurable. En combinant les résultats expérimentaux et numériques comme dans l'étude précédente, nous avons pu montrer que la dynamique de spins dans $BaCo_2V_2O_8$ au-dessus du champ critique correspond à celle attendue pour un TLL. Nous avons montré que la majorité du poids spectral est portée par les fluctuations longitudinales, i.e. fluctuations parallèle à la fois au champ magnétique et à l'axe Ising. Nous avons donc montré que $BaCo_2V_2O_8$ est un composé remarquable où les propriétés statiques et dynamiques sont dominées par des corrélations longitudinales dans la phase à bas champ du TLL, celles-ci étant renforcées par le champ magnétique appliqué. C'est la première fois que le spectre des excitations pour une chaîne de spins 1/2 anisotrope est mesuré dans cette phase non gappée.

Une étude de $BaCo_2V_2O_8$ sous pression hydrostatique a été entreprise. Nous avons réalisé des mesures de chaleur spécifique dans $BaCo_2V_2O_8$ sous champ magnétique longitudinal et sous pression hydrostatique afin d'établir le diagramme de phase (H, P, T) de celui-ci. L'analyse des données a montré que la température critique T_c et le champ critique H_c augmentent lorsque la pression augmente. Curieusement, la température critique de la phase LSDW semble être très peu dépendante de la pression, comparativement à celle de la phase Néel. À partir de nos résultats et de la comparaison avec d'autres études théoriques, nous proposons que la quantité la plus affectée par l'effet de la pression est l'interaction intrachaîne J, celle-ci ayant le plus gros effet sur T_c et H_c. Cette hypothèse pourrait être confirmée en faisant des expériences de diffusion inélastique de neutrons sous pression hydrostatique. Une autre expérience qui pourrait être intérressante serait de faire la même étude sous champ transverse. En effet, dans ce cas précis, le champ effectif alterné provient de la légère inclinaison entre l'axe c et l'axe Ising. On pourrait alors s'attendre à modifier et donc contrôler le tenseur de Landé en appliquant une pression hydrostatique, et donc contrôler la transition de phase topologique que nous avons mise en évidence à pression ambiante.

Une étude de $Ba(Co_{1-x}Mg_x)_2V_2O_8$ a aussi été initiée pour les deux différentes concentrations de Mg $x = 2\%$ et $x = 5\%$ afin de mieux comprendre l'effet de substitution des ions magnétiques de Co^{2+} par des impuretés non magnétiques Mg^{2+}. En effet les impuretés coupent les chaînes en des segments de chaînes et un changement drastique dans les propriétés statiques et dynamiques des composés dopés est attendu en comparaison avec le composé pur $BaCo_2V_2O_8$. Nous avons donc effectué des mesures de diffusion élastique et inélastique des neutrons. Concernant les propriétés statiques, nous avons montré que le champ critique et la température critique décroient linéairement avec la concentration en impuretés non magnétiques x: ceci consiste à une signature de la réduction des corrélations dans le système. Le plus surprenant des résultats provient des mesures de la dynamique de spins où des modes non-dispersifs semblent être présents dans le spectre des excitations à champ nul. Ces modes pourraient provenir des effets de taille finie du système et pourraient être vus comme des excitations locales où les spinons sont liés aux impuretés. Ces travaux sont toujours en cours. En effet d'autres expériences de diffusion des neutrons sont prévues afin d'aller plus loin dans l'analyse et des calculs numériques tels que des calculs Monte Carlo quantique et iTEBD devraient nous aider à avoir une meilleure compréhension de l'effet de ces impuretés non-magnétiques.

Enfin, cette thèse a montré un très bel exemple de la complémentarité entre travail

expérimental, numérique et théorique. En effet, la comparaison systématique entre les résultats de diffusion des neutrons et les calculs iTEBD ont permis de révéler deux transitions de phases exotiques et beaucoup de signatures quantiques du composé modèle quasi-1D antiferromagnetique de type Ising $BaCo_2V_2O_8$. Des calculs Monte Carlo quantique nous permettraient d'aller plus loin dans notre compréhension des couplages 3D dans ce système.

Bibliography

[A F+72] Richard A. Forman et al. “Pressure Measurement Made by the Utilization of Ruby Sharp-Line Luminescence”. In: 176 (May 1972), pp. 284–5.

[Aff+87] Ian Affleck et al. “Rigorous results on valence-bond ground states in antiferromagnets”. In: *Phys. Rev. Lett.* 59 (7 Aug. 1987), pp. 799–802. DOI: 10.1103/PhysRevLett.59.799. URL: https://link.aps.org/doi/10.1103/PhysRevLett.59.799.

[All+09] H. Alloul et al. “Defects in correlated metals and superconductors”. In: *Rev. Mod. Phys.* 81 (1 Jan. 2009), pp. 45–108. DOI: 10.1103/RevModPhys.81.45. URL: https://link.aps.org/doi/10.1103/RevModPhys.81.45.

[Ama+90] Kiichi Amaya et al. “High Field Magnetization of Quasi One Dimensional Ising Antiferromagnet CsCoCl3”. In: *Journal of the Physical Society of Japan* 59.5 (1990), pp. 1810–1816. DOI: 10.1143/JPSJ.59.1810. eprint: https://doi.org/10.1143/JPSJ.59.1810. URL: https://doi.org/10.1143/JPSJ.59.1810.

[AO99] Ian Affleck and Masaki Oshikawa. “Field-induced gap in Cu benzoate and other $S = \frac{1}{2}$ antiferromagnetic chains”. In: *Phys. Rev. B* 60 (2 July 1999), pp. 1038–1056. DOI: 10.1103/PhysRevB.60.1038. URL: https://link.aps.org/doi/10.1103/PhysRevB.60.1038.

[AP51] A. Abragam and M. H. L. Pryce. “The theory of paramagnetic resonance in hydrated cobalt salts”. In: *Proceedings of the Royal Society of London A: Mathematical, Physical and Engineering Sciences* 206.1085 (1951), pp. 173–191. ISSN: 0080-4630. DOI: 10.1098/rspa.1951.0063. eprint: http://rspa.royalsocietypublishing.org/content/206/1085/173.full.pdf. URL: http://rspa.royalsocietypublishing.org/content/206/1085/173.

[Aue94] Assa Auerbach. “Spin Wave Theory”. In: *Interacting Electrons and Quantum Magnetism*. New York, NY: Springer New York, 1994, pp. 113–127. ISBN: 978-1-4612-0869-3. DOI: 10.1007/978-1-4612-0869-3_11. URL: https://doi.org/10.1007/978-1-4612-0869-3_11.

[Aug+99] D. Augier et al. “Soliton bound states in the Raman spectrum of pure and doped spin-Peierls chains”. In: *Phys. Rev. B* 60 (2 July 1999), pp. 1075–1081. DOI: 10.1103/PhysRevB.60.1075. URL: https://link.aps.org/doi/10.1103/PhysRevB.60.1075.

[Azu+97] M. Azuma et al. “Switching of the gapped singlet spin-liquid state to an antiferromagnetically ordered state in $Sr(Cu_{1-x}Zn_x)_2O_3$”. In: *Phys. Rev. B* 55 (14 Apr. 1997), R8658–R8661. DOI: 10.1103/PhysRevB.55.R8658. URL: https://link.aps.org/doi/10.1103/PhysRevB.55.R8658.

[Ber71] V. L Berezinskii. "Destruction of long-range order in one-dimensional and two-dimensional systems having a continuous symmetry group I. Classical systems." In: *Sov. Phys. JETP* (1971).

[Bet31] H. Bethe. "Zur Theorie der Metalle". In: *Zeitschrift für Physik* 71.3 (Mar. 1931), pp. 205–226. ISSN: 0044-3328. DOI: 10.1007/BF01341708. URL: https://doi.org/10.1007/BF01341708.

[BIK86] N.M. Bogoliubov, A.G. Izergin, and V.E. Korepin. "Critical exponents for integrable models". In: *Nuclear Physics B* 275.4 (1986), pp. 687–705. ISSN: 0550-3213. DOI: https://doi.org/10.1016/0550-3213(86)90579-1. URL: http://www.sciencedirect.com/science/article/pii/0550321386905791.

[BKM98] A. Hamid Bougourzi, Michael Karbach, and Gerhard Müller. "Exact two-spinon dynamic structure factor of the one-dimensional $s = \frac{1}{2}$ Heisenberg-Ising antiferromagnet". In: *Phys. Rev. B* 57 (18 May 1998), pp. 11429–11438. DOI: 10.1103/PhysRevB.57.11429. URL: https://link.aps.org/doi/10.1103/PhysRevB.57.11429.

[Blu63] M. Blume. "Polarization Effects in the Magnetic Elastic Scattering of Slow Neutrons". In: *Phys. Rev.* 130 (5 June 1963), pp. 1670–1676. DOI: 10.1103/PhysRev.130.1670. URL: https://link.aps.org/doi/10.1103/PhysRev.130.1670.

[Boh+18] Annabelle Bohrdt et al. "Dynamic structure factor in impurity-doped spin chains". In: *Phys. Rev. B* 98 (2 July 2018), p. 020402. DOI: 10.1103/PhysRevB.98.020402. URL: https://link.aps.org/doi/10.1103/PhysRevB.98.020402.

[Bou+11] Pierre Bouillot et al. "Statics and dynamics of weakly coupled antiferromagnetic spin-$\frac{1}{2}$ ladders in a magnetic field". In: *Phys. Rev. B* 83 (5 Feb. 2011), p. 054407. DOI: 10.1103/PhysRevB.83.054407. URL: https://link.aps.org/doi/10.1103/PhysRevB.83.054407.

[Cab+14] I. Cabrera et al. "Excitations in the quantum paramagnetic phase of the quasi-one-dimensional Ising magnet $CoNb_2O_6$ in a transverse field: Geometric frustration and quantum renormalization effects". In: *Phys. Rev. B* 90 (1 July 2014), p. 014418. DOI: 10.1103/PhysRevB.90.014418. URL: https://link.aps.org/doi/10.1103/PhysRevB.90.014418.

[Can+13] E. Canévet et al. "Field-induced magnetic behavior in quasi-one-dimensional Ising-like antiferromagnet $BaCo_2V_2O_8$: A single-crystal neutron diffraction study". In: *Phys. Rev. B* 87 (5 Feb. 2013), p. 054408. DOI: 10.1103/PhysRevB.87.054408. URL: https://link.aps.org/doi/10.1103/PhysRevB.87.054408.

[Can10] Emmanuel Canevet. "Magnetic phase transitions in low dimensional quantum spin systems". Theses. Université Joseph-Fourier - Grenoble I, Dec. 2010. URL: https://tel.archives-ouvertes.fr/tel-00712631.

[Col+10] R. Coldea et al. "Quantum Criticality in an Ising Chain: Experimental Evidence for Emergent E8 Symmetry". In: *Science* 327.5962 (2010), pp. 177–180. ISSN: 0036-8075. DOI: 10.1126/science.1180085. eprint: http://science.sciencemag.org/content/327/5962/177.full.pdf. URL: http://science.sciencemag.org/content/327/5962/177.

[CP62] Jacques des Cloizeaux and J. J. Pearson. "Spin-Wave Spectrum of the Antiferromagnetic Linear Chain". In: *Phys. Rev.* 128 (5 Dec. 1962), pp. 2131–2135. DOI: 10.1103/PhysRev.128.2131. URL: https://link.aps.org/doi/10.1103/PhysRev.128.2131.

[D23] D23. URL: %5Curl%7Bhttps://www.ill.eu/users/instruments/instruments-list/d23/description/instrument-layout/%7D.

[Den+97] D. C. Dender et al. "Direct Observation of Field-Induced Incommensurate Fluctuations in a One-Dimensional $S = 1/2$ Antiferromagnet". In: *Phys. Rev. Lett.* 79 (9 Sept. 1997), pp. 1750–1753. DOI: 10.1103/PhysRevLett.79.1750. URL: https://link.aps.org/doi/10.1103/PhysRevLett.79.1750.

[DKO02] D. V. Dmitriev, V. Ya. Krivnov, and A. A. Ovchinnikov. "Gap generation in the XXZ model in a transverse magnetic field". In: *Phys. Rev. B* 65 (17 Apr. 2002), p. 172409. DOI: 10.1103/PhysRevB.65.172409. URL: https://link.aps.org/doi/10.1103/PhysRevB.65.172409.

[Dro+15] A. P. Drozdov et al. "Conventional superconductivity at 203 kelvin at high pressures in the sulfur hydride system". In: *Nature* 525 (Aug. 2015), 73 EP -. URL: http://dx.doi.org/10.1038/nature14964.

[DS98] Jan von Delft and Herbert Schoeller. "Bosonization for beginners — refermionization for experts". In: *Annalen der Physik* 7.4 (1998), pp. 225–305. DOI: 10.1002/(SICI)1521-3889(199811)7:4<225::AID-ANDP225>3.0.CO;2-L. eprint: https://onlinelibrary.wiley.com/doi/pdf/10.1002/%28SICI%291521-3889%28199811%297%3A4%3C225%3A%3AAID-ANDP225%3E3.0.CO%3B2-L. URL: https://onlinelibrary.wiley.com/doi/abs/10.1002/%28SICI%291521-3889%28199811%297%3A4%3C225%3A%3AAID-ANDP225%3E3.0.CO%3B2-L.

[DV09] R. L. Doretto and Matthias Vojta. "Quantum magnets with weakly confined spinons: Multiple length scales and quantum impurities". In: *Phys. Rev. B* 80 (2 July 2009), p. 024411. DOI: 10.1103/PhysRevB.80.024411. URL: https://link.aps.org/doi/10.1103/PhysRevB.80.024411.

[EA92] Sebastian Eggert and Ian Affleck. "Magnetic impurities in half-integer-spin Heisenberg antiferromagnetic chains". In: *Phys. Rev. B* 46 (17 Nov. 1992), pp. 10866–10883. DOI: 10.1103/PhysRevB.46.10866. URL: https://link.aps.org/doi/10.1103/PhysRevB.46.10866.

[EA95] Sebastian Eggert and Ian Affleck. "Impurities in $S = 1/2$ Heisenberg Antiferromagnetic Chains: Consequences for Neutron Scattering and Knight Shift". In: *Phys. Rev. Lett.* 75 (5 July 1995), pp. 934–937. DOI: 10.1103/PhysRevLett.75.934. URL: https://link.aps.org/doi/10.1103/PhysRevLett.75.934.

[EAH02] Sebastian Eggert, Ian Affleck, and Matthew D. P. Horton. "Néel Order in Doped Quasi-One-Dimensional Antiferromagnets". In: *Phys. Rev. Lett.* 89 (4 July 2002), p. 047202. DOI: 10.1103/PhysRevLett.89.047202. URL: https://link.aps.org/doi/10.1103/PhysRevLett.89.047202.

[ETH] ETH. URL: %5Curl%7Bhttp://www.neutron.ethz.ch/research/resources/graphite-filter-transmission.html%7D.

[Fau+18] Quentin Faure et al. “Topological quantum phase transition in the Ising-like antiferromagnetic spin chain BaCo2V2O8”. In: *Nature Physics* 14.7 (2018), pp. 716–722. ISSN: 1745-2481. DOI: 10.1038/s41567-018-0126-8. URL: https://doi.org/10.1038/s41567-018-0126-8.

[Fei13] Adrian E. Feiguin. *The Density Matrix Renormalization Group*. Ed. by Adolfo Avella and Ferdinando Mancini. Berlin, Heidelberg: Springer Berlin Heidelberg, 2013, pp. 31–65. ISBN: 978-3-642-35106-8. DOI: 10.1007/978-3-642-35106-8_2. URL: https://doi.org/10.1007/978-3-642-35106-8_2.

[Fer12] Amalia Fernandez-Panyella. “Ytterbium-based heavy-fermion compounds under extreme conditions : new instrumentation to tackle fundamental questions.” Theses. Université de Grenoble, Dec. 2012. URL: https://tel.archives-ouvertes.fr/tel-00858322.

[FN17] Michael E. Fisher and Naoto Nagaosa. “Profile of David J. Thouless, J. Michael Kosterlitz, and F. Duncan M. Haldane, 2016 Nobel Laureates in Physics”. In: *Proceedings of the National Academy of Sciences* 114.4 (2017), pp. 626–628. ISSN: 0027-8424. DOI: 10.1073/pnas.1620134114. eprint: http://www.pnas.org/content/114/4/626.full.pdf. URL: http://www.pnas.org/content/114/4/626.

[FT81] L.D. Faddeev and L.A. Takhtajan. “What is the spin of a spin wave?” In: *Physics Letters A* 85.6 (1981), pp. 375–377. ISSN: 0375-9601. DOI: https://doi.org/10.1016/0375-9601(81)90335-2. URL: http://www.sciencedirect.com/science/article/pii/0375960181903352.

[Fuj+98] N. Fujiwara et al. “NMR Study of Zn Doping Effect in Spin Ladder System $SrCu_2O_3$”. In: *Phys. Rev. Lett.* 80 (3 Jan. 1998), pp. 604–607. DOI: 10.1103/PhysRevLett.80.604. URL: https://link.aps.org/doi/10.1103/PhysRevLett.80.604.

[Gau71] M. Gaudin. “Thermodynamics of the Heisenberg-Ising Ring for $\Delta > 1$”. In: *Phys. Rev. Lett.* 26 (21 May 1971), pp. 1301–1304. DOI: 10.1103/PhysRevLett.26.1301. URL: https://link.aps.org/doi/10.1103/PhysRevLett.26.1301.

[Goo68] John B. Goodenough. “Spin-Orbit-Coupling Effects in Transition-Metal Compounds”. In: *Phys. Rev.* 171 (2 July 1968), pp. 466–479. DOI: 10.1103/PhysRev.171.466. URL: https://link.aps.org/doi/10.1103/PhysRev.171.466.

[GP04] T. Giamarchi and Oxford University Press. *Quantum Physics in One Dimension*. International Series of Monogr. Clarendon Press, 2004. ISBN: 9780198525004. URL: https://books.google.fr/books?id=1MwTDAAAQBAJ.

[Gre+02] B. Grenier et al. “Electron spin resonance of Ni-doped $CuGeO_3$ in the paramagnetic, spin-Peierls, and antiferromagnetic states: Comparison with nonmagnetic impurities”. In: *Phys. Rev. B* 65 (9 Feb. 2002), p. 094425. DOI: 10.1103/PhysRevB.65.094425. URL: https://link.aps.org/doi/10.1103/PhysRevB.65.094425.

[Gre+07] B. Grenier et al. “Spin excitations throughout the field-induced magnetic phase of the spin 1/2 alternating chain compound Cu(NO3)2Â·2.5D20”. In: *Journal of Magnetism and Magnetic Materials* 310.2, Part 2 (2007). Proceedings of the 17th International Conference on Magnetism, pp. 1269–1271. ISSN: 0304-8853. DOI: https://doi.org/10.1016/j.jmmm.2006.10.434. URL: http://www.sciencedirect.com/science/article/pii/S0304885306016428.

[Gre+15a] B. Grenier et al. “Longitudinal and Transverse Zeeman Ladders in the Ising-Like Chain Antiferromagnet $BaCo_2V_2O_8$”. In: *Phys. Rev. Lett.* 114 (1 Jan. 2015), p. 017201. DOI: 10.1103/PhysRevLett.114.017201. URL: https://link.aps.org/doi/10.1103/PhysRevLett.114.017201. Erattum. In: *Phys. Rev. Lett.* 115 (11 Sept 2015) https://link.aps.org/doi/10.1103/PhysRevLett.115.119902.

[Gre+15b] B. Grenier et al. “Neutron diffraction investigation of the $H-T$ phase diagram above the longitudinal incommensurate phase of $BaCo_2V_2O_8$”. In: *Phys. Rev. B* 92 (13 Oct. 2015), p. 134416. DOI: 10.1103/PhysRevB.92.134416. URL: https://link.aps.org/doi/10.1103/PhysRevB.92.134416.

[Gre+98] Grenier, B. et al. “Neutron-scattering study of the commensurate-incommensurate transition under field in Si-doped $CuGeO_3$ spin-Peierls systems”. In: *Europhys. Lett.* 44.4 (1998), pp. 511–517. DOI: 10.1209/epl/i1998-00503-6. URL: https://doi.org/10.1209/epl/i1998-00503-6.

[Gre11] B. Grenier. *Cours neutrons Master 2 PMCR, Grenoble*. 2011.

[GS88] Giamarchi, T. and Schulz, H.J. “Theory of spin-anisotropic electron-electron interactions in quasi-one-dimensional metals”. In: *J. Phys. France* 49.5 (1988), pp. 819–835. DOI: 10.1051/jphys:01988004905081900. URL: https://doi.org/10.1051/jphys:01988004905081900.

[GT99] T. Giamarchi and A. M. Tsvelik. “Coupled ladders in a magnetic field”. In: *Phys. Rev. B* 59 (17 May 1999), pp. 11398–11407. DOI: 10.1103/PhysRevB.59.11398. URL: https://link.aps.org/doi/10.1103/PhysRevB.59.11398.

[Hal80] F. D. M. Haldane. “General Relation of Correlation Exponents and Spectral Properties of One-Dimensional Fermi Systems: Application to the Anisotropic $S=\frac{1}{2}$ Heisenberg Chain”. In: *Phys. Rev. Lett.* 45 (16 Oct. 1980), pp. 1358–1362. DOI: 10.1103/PhysRevLett.45.1358. URL: https://link.aps.org/doi/10.1103/PhysRevLett.45.1358.

[Hal83a] F. D. M. Haldane. “Nonlinear Field Theory of Large-Spin Heisenberg Antiferromagnets: Semiclassically Quantized Solitons of the One-Dimensional Easy-Axis Néel State”. In: *Phys. Rev. Lett.* 50 (15 Apr. 1983), pp. 1153–1156. DOI: 10.1103/PhysRevLett.50.1153. URL: https://link.aps.org/doi/10.1103/PhysRevLett.50.1153.

[Hal83b] F.D.M. Haldane. “Continuum dynamics of the 1-D Heisenberg antiferromagnet: Identification with the O(3) nonlinear sigma model”. In: *Physics Letters A* 93.9 (1983), pp. 464–468. ISSN: 0375-9601. DOI: https://doi.org/10.1016/0375-9601(83)90631-X. URL: http://www.sciencedirect.com/science/article/pii/037596018390631X.

[Has+08] E. Hassinger et al. "Temperature-pressure phase diagram of URu_2Si_2 from resistivity measurements and ac calorimetry: Hidden order and Fermi-surface nesting". In: *Phys. Rev. B* 77 (11 Mar. 2008), p. 115117. DOI: 10.1103/PhysRevB.77.115117. URL: https://link.aps.org/doi/10.1103/PhysRevB.77.115117.

[Has+93] M. Hase et al. "Effects of substitution of Zn for Cu in the spin-Peierls cuprate, $CuGeO_3$: The suppression of the spin-Peierls transition and the occurrence of a new spin-glass state". In: *Phys. Rev. Lett.* 71 (24 Dec. 1993), pp. 4059–4062. DOI: 10.1103/PhysRevLett.71.4059. URL: https://link.aps.org/doi/10.1103/PhysRevLett.71.4059.

[He+05a] Zhangzhen He et al. "Crystal Growth and Magnetic Properties of BaCo2V2O8". In: *Chemistry of Materials* 17.11 (2005), pp. 2924–2926. DOI: 10.1021/cm050760e.

[He+05b] Zhangzhen He et al. "Field-induced order-disorder transition in the quasi-one-dimensional anisotropic antiferromagnet $BaCo_2V_2O_8$". In: *Phys. Rev. B* 72 (17 Nov. 2005), p. 172403. DOI: 10.1103/PhysRevB.72.172403. URL: https://link.aps.org/doi/10.1103/PhysRevB.72.172403.

[HFM] HFMEXED. URL: %5Ctext%7B%5Curl%7Bhttps://www.helmholtz-berlin.de/pubbin/igama_output?modus=einzel&gid=1939&sprache=en%7D%7D.

[HOA01] Yasuhiro Hieida, Kouichi Okunishi, and Yasuhiro Akutsu. "Anisotropic antiferromagnetic spin chains in a transverse field: Reentrant behavior of the staggered magnetization". In: *Phys. Rev. B* 64 (22 Nov. 2001), p. 224422. DOI: 10.1103/PhysRevB.64.224422. URL: https://link.aps.org/doi/10.1103/PhysRevB.64.224422.

[Hon+10] Tao Hong et al. "Field-Induced Tomonaga-Luttinger Liquid Phase of a Two-Leg Spin-1/2 Ladder with Strong Leg Interactions". In: *Phys. Rev. Lett.* 105 (13 Sept. 2010), p. 137207. DOI: 10.1103/PhysRevLett.105.137207. URL: https://link.aps.org/doi/10.1103/PhysRevLett.105.137207.

[HS06] Riccardo Hertel and Claus M. Schneider. "Exchange Explosions: Magnetization Dynamics during Vortex-Antivortex Annihilation". In: *Phys. Rev. Lett.* 97 (17 Oct. 2006), p. 177202. DOI: 10.1103/PhysRevLett.97.177202. URL: https://link.aps.org/doi/10.1103/PhysRevLett.97.177202.

[HY79] Kinshiro Hirakawa and Hideki Yoshizawa. "Neutron Scattering Study of a One-Dimensional Ising-Like Antiferromagnet CsCoCl3. II. Spin Dynamics". In: *Journal of the Physical Society of Japan* 46.2 (1979), pp. 455–461. DOI: 10.1143/JPSJ.46.455. eprint: https://doi.org/10.1143/JPSJ.46.455. URL: https://doi.org/10.1143/JPSJ.46.455.

[IN1] IN12. URL: %5Curl%7Bhttps://www.ill.eu/users/instruments/instruments-list/in12/description/instrument-layout/%7D.

[IS80] Norikazu Ishimura and Hiroyuki Shiba. "Dynamical Correlation Functions of One-Dimensional Anisotropic Heisenberg Model with Spin 1/2. IIsing-Like Antiferromagnets". In: *Progress of Theoretical Physics* 63.3 (1980), pp. 743–758. DOI: 10.1143/PTP.63.743. eprint: /oup/backfile/content_public/journal/ptp/63/3/10.1143/ptp.63.743/2/63-3-743.pdf. URL: +%20http://dx.doi.org/10.1143/PTP.63.743.

[Jae98] Gregg Jaeger. "The Ehrenfest Classification of Phase Transitions: Introduction and Evolution". In: *Archive for History of Exact Sciences* 53.1 (May 1998), pp. 51–81. DOI: 10.1007/s004070050021. URL: https://doi.org/10.1007/s004070050021.

[Joh+00] D. C. Johnston et al. "Thermodynamics of spin $S = 1/2$ antiferromagnetic uniform and alternating-exchange Heisenberg chains". In: *Phys. Rev. B* 61 (14 Apr. 2000), pp. 9558–9606. DOI: 10.1103/PhysRevB.61.9558. URL: https://link.aps.org/doi/10.1103/PhysRevB.61.9558.

[Jos13] José. "J. V. 40 years of Berezinskii-Kosterlitz-Thouless theory". In: *World Scientific* (2013).

[JT37] H. A. Jahn and E. Teller. "Stability of polyatomic molecules in degenerate electronic states - I—Orbital degeneracy". In: *Proceedings of the Royal Society of London A: Mathematical, Physical and Engineering Sciences* 161.905 (1937), pp. 220–235. ISSN: 0080-4630. DOI: 10.1098/rspa.1937.0142. eprint: http://rspa.royalsocietypublishing.org/content/161/905/220.full.pdf. URL: http://rspa.royalsocietypublishing.org/content/161/905/220.

[JW28] P. Jordan and E. Wigner. "Über das Paulische Äquivalenzverbot". In: *Zeitschrift für Physik* 47.9 (Sept. 1928), pp. 631–651. ISSN: 0044-3328. DOI: 10.1007/BF01331938. URL: https://doi.org/10.1007/BF01331938.

[Kaw+11] Yu Kawasaki et al. "Magnetic structure and spin dynamics of the quasi-one-dimensional spin-chain antiferromagnet $BaCo_2V_2O_8$". In: *Phys. Rev. B* 83 (6 Feb. 2011), p. 064421. DOI: 10.1103/PhysRevB.83.064421. URL: https://link.aps.org/doi/10.1103/PhysRevB.83.064421.

[Ken+02] M. Kenzelmann et al. "Order-to-disorder transition in the XY-like quantum magnet Cs_2CoCl_4 induced by noncommuting applied fields". In: *Phys. Rev. B* 65 (14 Apr. 2002), p. 144432. DOI: 10.1103/PhysRevB.65.144432. URL: https://link.aps.org/doi/10.1103/PhysRevB.65.144432.

[Ken+03] M. Kenzelmann et al. "Structure of End States for a Haldane Spin Chain". In: *Phys. Rev. Lett.* 90 (8 Feb. 2003), p. 087202. DOI: 10.1103/PhysRevLett.90.087202. URL: https://link.aps.org/doi/10.1103/PhysRevLett.90.087202.

[Ken+05] M. Kenzelmann et al. "$S = \frac{1}{2}$ chain in a staggered field: High-energy bound-spinon state and the effects of a discrete lattice". In: *Phys. Rev. B* 71 (9 Mar. 2005), p. 094411. DOI: 10.1103/PhysRevB.71.094411. URL: https://link.aps.org/doi/10.1103/PhysRevB.71.094411.

[Kim+05] S. Kimura et al. "High Field Magnetization and High Frequency ESR of the Quasi One-Dimensional Ising-Like Antiferromagnet $CsCoCl_3$ in Transverse Field". In: *Progress of Theoretical Physics Supplement* 159 (2005), pp. 153–157. DOI: 10.1143/PTPS.159.153.

[Kim+06] S Kimura et al. "High field magnetism of the quasi one-dimensional anisotropic antiferromagnet BaCo 2 V 2 O 8". In: *Journal of Physics: Conference Series* 51.1 (2006), p. 99. URL: http://stacks.iop.org/1742-6596/51/i=1/a=021.

[Kim+07] S. Kimura et al. "Field-Induced Order-Disorder Transition in Antiferromagnetic $BaCo_2V_2O_8$ Driven by a Softening of Spinon Excitation". In: *Phys. Rev. Lett.* 99 (8 Aug. 2007), p. 087602. DOI: 10.1103/PhysRevLett.99.087602. URL: https://link.aps.org/doi/10.1103/PhysRevLett.99.087602.

[Kim+08a] S. Kimura et al. "Longitudinal Spin Density Wave Order in a Quasi-1D Ising-like Quantum Antiferromagnet". In: *Phys. Rev. Lett.* 101 (20 Nov. 2008), p. 207201. DOI: 10.1103/PhysRevLett.101.207201. URL: https://link.aps.org/doi/10.1103/PhysRevLett.101.207201.

[Kim+08b] S. Kimura et al. "Novel Ordering of an $S = 1/2$ Quasi-1d Ising-Like Antiferromagnet in Magnetic Field". In: *Phys. Rev. Lett.* 100 (5 Feb. 2008), p. 057202.

[Kim+13] Shojiro Kimura et al. "Collapse of Magnetic Order of the Quasi One-Dimensional Ising-Like Antiferromagnet BaCo2V2O8 in Transverse Fields". In: *Journal of the Physical Society of Japan* 82.3 (2013), p. 033706. DOI: 10.7566/JPSJ.82.033706. eprint: https://doi.org/10.7566/JPSJ.82.033706. URL: https://doi.org/10.7566/JPSJ.82.033706.

[Kir+96] V. Kiryukhin et al. "Synchrotron x-ray-scattering study of magnetic-field-induced transitions in $Cu_{1-x}(Zn, Ni)_xGeO_3$". In: *Phys. Rev. B* 54 (10 Sept. 1996), pp. 7269–7278. DOI: 10.1103/PhysRevB.54.7269. URL: https://link.aps.org/doi/10.1103/PhysRevB.54.7269.

[Kla] M. Klanjšek. *Private Communication.*

[Kla+08] M. Klanjšek et al. "Controlling Luttinger Liquid Physics in Spin Ladders under a Magnetic Field". In: *Phys. Rev. Lett.* 101 (13 Sept. 2008), p. 137207. DOI: 10.1103/PhysRevLett.101.137207. URL: https://link.aps.org/doi/10.1103/PhysRevLett.101.137207.

[Kla+15] M. Klanjšek et al. "Giant magnetic field dependence of the coupling between spin chains in $BaCo_2V_2O_8$". In: *Phys. Rev. B* 92 (6 Aug. 2015), p. 060408. DOI: 10.1103/PhysRevB.92.060408. URL: https://link.aps.org/doi/10.1103/PhysRevB.92.060408.

[Koh+01] Masahumi Kohgi et al. "Staggered Field Effect on the One-Dimensional $S = \frac{1}{2}$ Antiferromagnet Yb_4As_3". In: *Phys. Rev. Lett.* 86 (11 Mar. 2001), pp. 2439–2442. DOI: 10.1103/PhysRevLett.86.2439. URL: https://link.aps.org/doi/10.1103/PhysRevLett.86.2439.

[KT73] J M Kosterlitz and D J Thouless. "Ordering, metastability and phase transitions in two-dimensional systems". In: *Journal of Physics C: Solid State Physics* 6.7 (1973), p. 1181. URL: http://stacks.iop.org/0022-3719/6/i=7/a=010.

[Lak+05] Bella Lake et al. “Quantum criticality and universal scaling of a quantum antiferromagnet”. In: *Nature Materials* 4 (Mar. 2005). Article, 329 EP -. URL: http://dx.doi.org/10.1038/nmat1327.

[Lan+80] L.D. Landau et al. *Statistical Physics*. Course of Theoretical Physics ptie. 1. Elsevier Science, 1980. ISBN: 9780750633727. URL: https://books.google.fr/books?id=SCPtuAEACAAJ.

[Lej+11] P. Lejay et al. “Crystal growth and magnetic property of MCo2V2O8 (M=Sr and Ba)”. English. In: *Journal of Crystal Growth* 317.1 (2011), pp. 128–131. DOI: 10.1016/j.jcrysgro.2011.01.016.

[LGN02] P. Lecheminant, Alexander O. Gogolin, and Alexander A. Nersesyan. “Criticality in self-dual sine-Gordon models”. In: *Nuclear Physics B* 639.3 (2002), pp. 502–523. ISSN: 0550-3213. DOI: https://doi.org/10.1016/S0550-3213(02)00474-1. URL: http://www.sciencedirect.com/science/article/pii/S0550321302004741.

[Lin63] M. E. Lines. “Magnetic Properties of $CoCl_2$ and $NiCl_2$”. In: *Phys. Rev.* 131 (2 July 1963), pp. 546–555. DOI: 10.1103/PhysRev.131.546. URL: https://link.aps.org/doi/10.1103/PhysRev.131.546.

[Lov84] S.W. Lovesey. *Theory of neutron scattering from condensed matter*. International series of monographs on physics vol. 2. Clarendon Press, 1984. ISBN: 9780198520177. URL: https://books.google.fr/books?id=8%5C_LvAAAAMAAJ.

[LRS09] L. Liang, R. Rinaldi, and H. Schober. “Neutrons applications in Earth, Energy and Environmental Sciences”. In: (2009).

[LSA08] Nicolas Laflorencie, Erik Sørensen, and Ian Affleck. “The Kondo effect in spin chains”. In: *Journal of Statistical Mechanics: Theory and Experiment* 2008.02 (2008), P02007. URL: http://stacks.iop.org/1742-5468/2008/i=02/a=P02007.

[LSM61] Elliott Lieb, Theodore Schultz, and Daniel Mattis. “Two soluble models of an antiferromagnetic chain”. In: *Annals of Physics* 16.3 (1961), pp. 407–466. ISSN: 0003-4916. DOI: https://doi.org/10.1016/0003-4916(61)90115-4. URL: http://www.sciencedirect.com/science/article/pii/0003491661901154.

[Mal61] S. V. Maleyev. “Polarized neutron scattering in magnets”. In: *Phys. Usp.* 45.6 (1961), pp. 569–596. DOI: 10.1070/PU2002v045n06ABEH001017. URL: https://ufn.ru/en/articles/2002/6/a/.

[Mas+98] T. Masuda et al. “Phase Transition between Dimerized-Antiferromagnetic and Uniform-Antiferromagnetic Phases in the Impurity-Doped Spin-Peierls Cuprate $CuGeO_3$”. In: *Phys. Rev. Lett.* 80 (20 May 1998), pp. 4566–4569. DOI: 10.1103/PhysRevLett.80.4566. URL: https://link.aps.org/doi/10.1103/PhysRevLett.80.4566.

[Mat+17] M. Matsuda et al. “Magnetic structure and dispersion relation of the $S = \frac{1}{2}$ quasi-one-dimensional Ising-like antiferromagnet $BaCo_2V_2O_8$ in a transverse magnetic field”. In: *Phys. Rev. B* 96 (2 July 2017), p. 024439. DOI: 10.1103/PhysRevB.96.024439. URL: https://link.aps.org/doi/10.1103/PhysRevB.96.024439.

[Mer+14] P. Merchant et al. “Quantum and classical criticality in a dimerized quantum antiferromagnet”. In: *Nature Physics* 10 (Apr. 2014). Article, 373 EP -. URL: http://dx.doi.org/10.1038/nphys2902.

[Mir03] E. Miranda. “Introduction to bosonization”. en. In: *Brazilian Journal of Physics* 33 (Mar. 2003), pp. 3–35. ISSN: 0103-9733. URL: http://www.scielo.br/scielo.php?script=sci_arttext&pid=S0103-97332003000100002&nrm=iso.

[MK04] Hans-Jürgen Mikeska and Alexei K. Kolezhuk. “One-dimensional magnetism”. In: *Quantum Magnetism*. Ed. by Ulrich Schollwöck et al. Berlin, Heidelberg: Springer Berlin Heidelberg, 2004, pp. 1–83. ISBN: 978-3-540-40066-0. DOI: 10.1007/BFb0119591. URL: https://doi.org/10.1007/BFb0119591.

[ML94] Daniel C. Mattis and Elliott H. Lieb. “Exact Solution of a Many-Fermion System and Its Associated Boson Field”. In: *Bosonization*. 1994, pp. 98–106. DOI: 10.1142/9789812812650_0008. eprint: https://www.worldscientific.com/doi/pdf/10.1142/9789812812650_0008. URL: https://www.worldscientific.com/doi/abs/10.1142/9789812812650_0008.

[Mou+13] Martin Mourigal et al. “Fractional spinon excitations in the quantum Heisenberg antiferromagnetic chain”. In: *Nature Physics* 9 (June 2013). Article, 435 EP -. URL: http://dx.doi.org/10.1038/nphys2652.

[MRK69] R. M. Moon, T. Riste, and W. C. Koehler. “Polarization Analysis of Thermal-Neutron Scattering”. In: *Phys. Rev.* 181 (2 May 1969), pp. 920–931. DOI: 10.1103/PhysRev.181.920. URL: https://link.aps.org/doi/10.1103/PhysRev.181.920.

[MRM00] Jamie L. Manson, Eric Ressouche, and Joel S. Miller. “Spin Frustration in MII[C(CN)3]2 (M = V, Cr). A Magnetism and Neutron Diffraction Study”. In: *Inorganic Chemistry* 39.6 (Mar. 2000), pp. 1135–1141. ISSN: 0020-1669. DOI: 10.1021/ic991231d. URL: https://doi.org/10.1021/ic991231d.

[Mül+81] Gerhard Müller et al. “Quantum spin dynamics of the antiferromagnetic linear chain in zero and nonzero magnetic field”. In: *Phys. Rev. B* 24 (3 Aug. 1981), pp. 1429–1467. DOI: 10.1103/PhysRevB.24.1429. URL: https://link.aps.org/doi/10.1103/PhysRevB.24.1429.

[Nag+82] S. E. Nagler et al. “Propagating Domain Walls in $CsCoBr_3$”. In: *Phys. Rev. Lett.* 49 (8 Aug. 1982), pp. 590–592. DOI: 10.1103/PhysRevLett.49.590. URL: https://link.aps.org/doi/10.1103/PhysRevLett.49.590.

[Nag+91] S. E. Nagler et al. “Spin dynamics in the quantum antiferromagnetic chain compound $KCuF_3$”. In: *Phys. Rev. B* 44 (22 Dec. 1991), pp. 12361–12368. DOI: 10.1103/PhysRevB.44.12361. URL: https://link.aps.org/doi/10.1103/PhysRevB.44.12361.

[Nie+13] S. K. Niesen et al. “Magnetic phase diagrams, domain switching, and quantum phase transition of the quasi-one-dimensional Ising-like antiferromagnet $BaCo_2V_2O_8$”. In: *Phys. Rev. B* 87 (22 June 2013), p. 224413. DOI: 10.1103/PhysRevB.87.224413. URL: https://link.aps.org/doi/10.1103/PhysRevB.87.224413.

[Nie+14] S. K. Niesen et al. “Substitution effects on the temperature versus magnetic field phase diagrams of the quasi-one-dimensional effective Ising spin-$\frac{1}{2}$ chain system $BaCo_2V_2O_8$”. In: *Phys. Rev. B* 90 (10 Sept. 2014), p. 104419. DOI: 10.1103/PhysRevB.90.104419. URL: https://link.aps.org/doi/10.1103/PhysRevB.90.104419.

[OA97] Masaki Oshikawa and Ian Affleck. “Field-Induced Gap in $S = 1/2$ Antiferromagnetic Chains”. In: *Phys. Rev. Lett.* 79 (15 Oct. 1997), pp. 2883–2886. DOI: 10.1103/PhysRevLett.79.2883. URL: https://link.aps.org/doi/10.1103/PhysRevLett.79.2883.

[Ohs+99] S. Ohsugi et al. “Impurity-induced staggered polarization and antiferromagnetic order in spin-$\frac{1}{2}$ Heisenberg two-leg ladder compound $SrCu_2O_3$: Extensive Cu NMR and NQR studies”. In: *Phys. Rev. B* 60 (6 Aug. 1999), pp. 4181–4190. DOI: 10.1103/PhysRevB.60.4181. URL: https://link.aps.org/doi/10.1103/PhysRevB.60.4181.

[Oku+15] A. Okutani et al. “High-Field Multi-Frequency ESR in the Quasi-1D SÂ =Â 1/2 Ising-Like Antiferromagnet BaCo2V2O8 in a Transverse Field”. In: *Applied Magnetic Resonance* 46.9 (Sept. 2015), pp. 1003–1006. ISSN: 1613-7507. DOI: 10.1007/s00723-015-0655-6. URL: https://doi.org/10.1007/s00723-015-0655-6.

[OS07] Kouichi Okunishi and Takahumi Suzuki. “Field-induced incommensurate order for the quasi-one-dimensional XXZ model in a magnetic field”. In: *Phys. Rev. B* 76 (22 Dec. 2007), p. 224411. DOI: 10.1103/PhysRevB.76.224411. URL: https://link.aps.org/doi/10.1103/PhysRevB.76.224411.

[Pfe70] Pierre Pfeuty. “The one-dimensional Ising model with a transverse field”. In: *Annals of Physics* 57.1 (1970), pp. 79–90. ISSN: 0003-4916. DOI: https://doi.org/10.1016/0003-4916(70)90270-8. URL: http://www.sciencedirect.com/science/article/pii/0003491670902708.

[PVM12] Ho N. Phien, Guifré Vidal, and Ian P. McCulloch. “Infinite boundary conditions for matrix product state calculations”. In: *Phys. Rev. B* 86 (24 Dec. 2012), p. 245107. DOI: 10.1103/PhysRevB.86.245107. URL: https://link.aps.org/doi/10.1103/PhysRevB.86.245107.

[Raj82] R. Rajaraman. *Solitons and Instantons: An Introduction to Solitons and Instantons in Quantum Field Theory*. North-Holland personal library. North-Holland Publishing Company, 1982. ISBN: 9780444862297. URL: https://books.google.fr/books?id=1XucQgAACAAJ.

[Reg07] L. P. Regnault. “Polarimétrie neutronique longitudinale et sphérique en diffusion inélastique”. In: *Collection SFN* 7 (2007).

[RH86] Wichmann R. and Müller-Buschbaum Hk. “Neue Verbindungen mit SrNi2V2O8-Struktur: BaCo2V2O8 und BaMg2V2O8”. In: *Zeitschrift für anorganische und allgemeine Chemie* 534.3 (1986), pp. 153–158. DOI: 10.1002/zaac.19865340320. eprint: https://onlinelibrary.wiley.com/doi/pdf/10.1002/zaac.19865340320. URL: https://onlinelibrary.wiley.com/doi/abs/10.1002/zaac.19865340320.

[Rod93] Juan Rodríguez-Carvajal. "Recent advances in magnetic structure determination by neutron powder diffraction". In: *Physica B: Condensed Matter* 192.1 (1993), pp. 55–69. ISSN: 0921-4526. DOI: https://doi.org/10.1016/0921-4526(93)90108-I. URL: http://www.sciencedirect.com/science/article/pii/092145269390108I.

[Ros87] J. Rossat-Mignod. "19. Magnetic Structures". In: Methods in Experimental Physics 23 (1987). Ed. by Kurt SkÃ¶ld and David L. Price, pp. 69–157. ISSN: 0076-695X. DOI: https://doi.org/10.1016/S0076-695X(08)60770-X. URL: http://www.sciencedirect.com/science/article/pii/S0076695X0860770X.

[Rot+18] Costel R. Rotundu et al. "Enhancement and destruction of spin-Peierls physics in a one-dimensional quantum magnet under pressure". In: *Phys. Rev. B* 97 (5 Feb. 2018), p. 054415. DOI: 10.1103/PhysRevB.97.054415. URL: https://link.aps.org/doi/10.1103/PhysRevB.97.054415.

[Rüe+08] Ch. Rüegg et al. "Thermodynamics of the Spin Luttinger Liquid in a Model Ladder Material". In: *Phys. Rev. Lett.* 101 (24 Dec. 2008), p. 247202. DOI: 10.1103/PhysRevLett.101.247202. URL: https://link.aps.org/doi/10.1103/PhysRevLett.101.247202.

[Rut18] Rutkevich, Sergei B. "Kink confinement in the antiferromagnetic XXZ spin-(1/2) chain in a weak staggered magnetic field". In: *EPL* 121.3 (2018), p. 37001. DOI: 10.1209/0295-5075/121/37001. URL: https://doi.org/10.1209/0295-5075/121/37001.

[Sac11] Subir Sachdev. *Quantum Phase Transitions*. 2nd ed. Cambridge University Press, 2011. DOI: 10.1017/CBO9780511973765.

[Sch+12] D. Schmidiger et al. "Spectral and Thermodynamic Properties of a Strong-Leg Quantum Spin Ladder". In: *Phys. Rev. Lett.* 108 (16 Apr. 2012), p. 167201. DOI: 10.1103/PhysRevLett.108.167201. URL: https://link.aps.org/doi/10.1103/PhysRevLett.108.167201.

[Sch+13] D. Schmidiger et al. "Spectrum of a Magnetized Strong-Leg Quantum Spin Ladder". In: *Phys. Rev. Lett.* 111 (10 Sept. 2013), p. 107202. DOI: 10.1103/PhysRevLett.111.107202. URL: https://link.aps.org/doi/10.1103/PhysRevLett.111.107202.

[Sch05] U. Schollwöck. "The density-matrix renormalization group". In: *Rev. Mod. Phys.* 77 (1 Apr. 2005), pp. 259–315. DOI: 10.1103/RevModPhys.77.259. URL: https://link.aps.org/doi/10.1103/RevModPhys.77.259.

[Sch11] Ulrich Schollwöck. "The density-matrix renormalization group in the age of matrix product states". English. In: *Annals of Physics* 326.1 (2011), pp. 96–192. DOI: 10.1016/j.aop.2010.09.012.

[Shi80] Hiroyuki Shiba. "Quantization of Magnetic Excitation Continuum Due to Interchain Coupling in Nearly One-Dimensional Ising-Like Antiferromagnets". In: *Progress of Theoretical Physics* 64.2 (1980), pp. 466–478. DOI: 10.1143/PTP.64.466. eprint: /oup/backfile/content_public/journal/ptp/64/2/10.1143/ptp.64.466/2/64-2-466.pdf. URL: +%20http://dx.doi.org/10.1143/PTP.64.466.

[Shu95] Clifford G. Shull. "Early development of neutron scattering". In: *Rev. Mod. Phys.* 67 (4 Oct. 1995), pp. 753–757. DOI: 10.1103/RevModPhys.67.753. URL: https://link.aps.org/doi/10.1103/RevModPhys.67.753.

[SIP75] D. J. Scalapino, Y. Imry, and P. Pincus. "Generalized Ginzburg-Landau theory of pseudo-one-dimensional systems". In: *Phys. Rev. B* 11 (5 Mar. 1975), pp. 2042–2048. DOI: 10.1103/PhysRevB.11.2042. URL: https://link.aps.org/doi/10.1103/PhysRevB.11.2042.

[SO04] Masahiro Sato and Masaki Oshikawa. "Coupled $S = \frac{1}{2}$ Heisenberg antiferromagnetic chains in an effective staggered field". In: *Phys. Rev. B* 69 (5 Feb. 2004), p. 054406. DOI: 10.1103/PhysRevB.69.054406. URL: https://link.aps.org/doi/10.1103/PhysRevB.69.054406.

[Son+15] M. Songvilay et al. "Random dilution effects in the frustrated spin chain $\beta-CaCr_{2-x}Sc_xO_4$". In: *Phys. Rev. B* 91 (5 Feb. 2015), p. 054408. DOI: 10.1103/PhysRevB.91.054408. URL: https://link.aps.org/doi/10.1103/PhysRevB.91.054408.

[Son16] Manila Songvilay. "Structures et propriétés d'oxydes magnétiques à topologie frustrée et de basse dimension". In: (2016). URL: http://www.theses.fr/2016SACLS403.

[SS68] Paul F. Sullivan and G. Seidel. "Steady-State, ac-Temperature Calorimetry". In: *Phys. Rev.* 173 (3 Sept. 1968), pp. 679–685. DOI: 10.1103/PhysRev.173.679. URL: https://link.aps.org/doi/10.1103/PhysRev.173.679.

[Sto+03] M. B. Stone et al. "Extended Quantum Critical Phase in a Magnetized Spin-$\frac{1}{2}$ Antiferromagnetic Chain". In: *Phys. Rev. Lett.* 91 (3 July 2003), p. 037205. DOI: 10.1103/PhysRevLett.91.037205. URL: https://link.aps.org/doi/10.1103/PhysRevLett.91.037205.

[SVW76] M. Steiner, J. Villain, and C.G. Windsor. "Theoretical and experimental studies on one-dimensional magnetic systems". In: *Advances in Physics* 25.2 (1976), pp. 87–209. DOI: 10.1080/00018737600101372. eprint: https://doi.org/10.1080/00018737600101372. URL: https://doi.org/10.1080/00018737600101372.

[TAS] TASP. URL: %5Curl%7Bhttps://www.helmholtz-berlin.de/pubbin/igama_output?modus=einzel&gid=1939&sprache=en%7D.

[TFG18] Shintaro Takayoshi, Shunsuke C. Furuya, and Thierry Giamarchi. "Topological transition between competing orders in quantum spin chains". In: *Phys. Rev. B* 98 (18 Nov. 2018), p. 184429. DOI: 10.1103/PhysRevB.98.184429. URL: https://link.aps.org/doi/10.1103/PhysRevB.98.184429.

[TS72] Minoru Takahashi and Masuo Suzuki. "One-Dimensional Anisotropic Heisenberg Model at Finite Temperatures". In: *Progress of Theoretical Physics* 48.6 (1972), pp. 2187–2209. DOI: 10.1143/PTP.48.2187. eprint: /oup/backfile/content_public/journal/ptp/48/6/10.1143/ptp.48.2187/2/48-6-2187.pdf. URL: http://dx.doi.org/10.1143/PTP.48.2187.

[Vid07] G. Vidal. "Classical Simulation of Infinite-Size Quantum Lattice Systems in One Spatial Dimension". In: *Phys. Rev. Lett.* 98 (7 Feb. 2007), p. 070201. DOI: 10.1103/PhysRevLett.98.070201. URL: https://link.aps.org/doi/10.1103/PhysRevLett.98.070201.

[WA08] Steven R. White and Ian Affleck. "Spectral function for the $S = 1$ Heisenberg antiferromagetic chain". In: *Phys. Rev. B* 77 (13 Apr. 2008), p. 134437. DOI: 10.1103/PhysRevB.77.134437. URL: https://link.aps.org/doi/10.1103/PhysRevB.77.134437.

[Wae12] Naemi Waeselmann. "Structural transformations in complex perovskite-type relaxor and relaxor-based ferroelectrics at high pressures and temperatures". In: (May 2012).

[Wan+16] Zhe Wang et al. "From confined spinons to emergent fermions: Observation of elementary magnetic excitations in a transverse-field Ising chain". In: *Phys. Rev. B* 94 (12 Sept. 2016), p. 125130. DOI: 10.1103/PhysRevB.94.125130. URL: https://link.aps.org/doi/10.1103/PhysRevB.94.125130.

[Wan+18] Zhe Wang et al. "Experimental observation of Bethe strings". In: *Nature* 554 (Feb. 2018), 219 EP -. URL: http://dx.doi.org/10.1038/nature25466.

[WC09] B. T. M. (Bertram Terence Martin) Willis and C. J Carlile. *Experimental neutron scattering*. English. Formerly CIP. Oxford ; New York : Oxford University Press, 2009. ISBN: 9780198519706 (hbk.)

[Weh+18] B. Wehinger et al. "Giant Pressure Dependence and Dimensionality Switching in a Metal-Organic Quantum Antiferromagnet". In: *Phys. Rev. Lett.* 121 (11 Sept. 2018), p. 117201. DOI: 10.1103/PhysRevLett.121.117201. URL: https://link.aps.org/doi/10.1103/PhysRevLett.121.117201.

[WH00a] Stefan Wessel and Stephan Haas. "Excitation spectra and thermodynamic response of segmented Heisenberg spin chains". In: *Phys. Rev. B* 61 (22 June 2000), pp. 15262–15268. DOI: 10.1103/PhysRevB.61.15262. URL: https://link.aps.org/doi/10.1103/PhysRevB.61.15262.

[WH00b] Stefan Wessel and Stephan Haas. "Three-dimensional ordering in weakly coupled antiferromagnetic ladders and chains". In: *Phys. Rev. B* 62 (1 July 2000), pp. 316–323. DOI: 10.1103/PhysRevB.62.316. URL: https://link.aps.org/doi/10.1103/PhysRevB.62.316.

[WH93] Steven R. White and David A. Huse. "Numerical renormalization-group study of low-lying eigenstates of the antiferromagnetic S=1 Heisenberg chain". In: *Phys. Rev. B* 48 (6 Aug. 1993), pp. 3844–3852. DOI: 10.1103/PhysRevB.48.3844. URL: https://link.aps.org/doi/10.1103/PhysRevB.48.3844.

[Whi92] Steven R. White. "Density matrix formulation for quantum renormalization groups". In: *Phys. Rev. Lett.* 69 (19 Nov. 1992), pp. 2863–2866. DOI: 10.1103/PhysRevLett.69.2863. URL: https://link.aps.org/doi/10.1103/PhysRevLett.69.2863.

[Wil03] Heribert Wilhelm. "AC-Calorimetry at High Pressure and Low Temperature". In: *Advances in Solid State Physics*. Ed. by Bernhard Kramer. Berlin, Heidelberg: Springer Berlin Heidelberg, 2003, pp. 889–913. ISBN: 978-3-540-44838-9. DOI: 10.1007/978-3-540-44838-9_63. URL: https://doi.org/10.1007/978-3-540-44838-9_63.

[Xu+00] Guangyong Xu et al. “Holes in a Quantum Spin Liquid”. In: *Science* 289.5478 (2000), pp. 419–422. ISSN: 0036-8075. DOI: 10.1126/science.289.5478.419. eprint: http://science.sciencemag.org/content/289/5478/419.full.pdf. URL: http://science.sciencemag.org/content/289/5478/419.

[Yan+17] W. Yang et al. “Quantum spin dynamics of the axial antiferromagnetic spin-$\frac{1}{2}$ XXZ chain in a longitudinal magnetic field”. In: *ArXiv e-prints* (Feb. 2017). arXiv: 1702.01854 [cond-mat.str-el].

[Zha+12] Z. Y. Zhao et al. “Heat transport of the quasi-one-dimensional Ising-like antiferromagnet $BaCo_2V_2O_8$ in longitudinal and transverse fields”. In: *Phys. Rev. B* 85 (13 Apr. 2012), p. 134412. DOI: 10.1103/PhysRevB.85.134412. URL: https://link.aps.org/doi/10.1103/PhysRevB.85.134412.

Résumé

Ce manuscrit présente l'étude de transitions de phase quantiques dans l'oxyde $BaCo_2V_2O_8$, un système antiferromagnétique quasi-unidimensionnel constitué de chaînes d'ions cobalt portant un spin effectif $S = 1/2$ caractérisé par une forte anisotropie de type Ising. Lors de ce travail, nous avons étudié les propriétés statiques et dynamiques de $BaCo_2V_2O_8$ sous l'effet de différents paramètres physiques.

Notre première étude a porté sur l'effet d'un champ magnétique transverse, i.e. appliqué perpendiculairement à l'axe Ising. Il a été proposé que lors de l'application d'un tel champ, un champ magnétique alterné effectif est induit perpendiculairement à l'axe d'anisotropie et au champ uniforme appliqué. La comparaison d'expériences de diffusion (élastique et inélastique) de neutrons et de calculs numériques nous a permis de montrer que ce champ alterné entre en compétition avec l'anisotropie. Ceci aboutit à une transition de phase originale, dite topologique, que l'on peut modéliser par une théorie quantique des champs nommée « modèle de double sine-Gordon » qui décrit la compétition entre deux excitations topologiques duales. Nous avons pu montrer que $BaCo_2V_2O_8$ sous champ magnétique transverse était la première réalisation d'une telle théorie.

La seconde étude était consacrée à $BaCo_2V_2O_8$ sous champ magnétique longitudinal, i.e. un champ appliqué parallèlement à l'axe Ising. La dynamique de spins a été sondée grâce à la diffusion inélastique de neutrons et nous avons montré qu'au-dessus d'un champ critique de 4 T, celle-ci semble en accord avec le spectre des fluctuations de spin attendu pour un liquide de Tomonaga Luttinger (TLL). De plus, les calculs numériques ont confirmé que, du fait de l'anisotropie de type Ising dans ce système, la majorité du poids spectral du spectre en énergie est porté par les fluctuations de spins de type longitudinales. Ce résultat est la signature d'un comportement quantique sans analogue classique avec des fluctuations de basses énergies essentiellement longitudinales pilotant la physique du système. Enfin, c'est la première fois que la dynamique de spin dans des chaînes de type Ising a pu être sondée dans cette phase TLL.

Les deux dernières études sont préliminaires. Le diagramme de phase de $BaCo_2V_2O_8$ a été sondé par des mesures calorimétriques sous l'application d'une pression hydrostatique et d'un champ magnétique longitudinal. Afin d'obtenir des pressions allant jusqu'à 10 GPa, nous avons utilisé une cellule à enclumes de diamant. Nous avons effectué des mesures de chaleur spécifique qui nous ont permis de sonder l'effet de la pression sur le Hamiltonien de $BaCo_2V_2O_8$ au travers de son diagramme de phase (H, P, T). Enfin, nous avons étudié l'effet de la substitution des ions magnétiques Co^{2+} par des impuretés non-magnétiques Mg^{2+}. Les expériences de diffraction neutronique sous champ longitudinal ont montré que la température et le champ critiques diminuent proportionnellement à la concentration en impuretés. La dynamique de spins à champ magnétique nul a aussi été sondée et révèle l'apparition de modes non-dispersifs, provenant possiblement de l'effet de segmentation des chaînes par les impuretés.

En conclusion, nos études expèrimentales couplées à des calculs numériques nous ont permis de dévoiler une physique extrêmement riche dans ce composé modèle pour l'étude du magnétisme quantique et des transitions de phase quantiques.

Mots-clefs : Magnétisme quantique, Ordre et excitations, Transitions de phases quantiques, Diffusion neutronique, chaînes de spins.

Abstract

This manuscript is devoted to the study of quantum phase transitions in the $BaCo_2V_2O_8$ oxide, a quasi-one dimensional antiferromagnet consisting of spin chains of cobalt magnetic ions carrying an effective spin $S = 1/2$ showing a strong Ising-like anisotropy. To achieve this, we have studied $BaCo_2V_2O_8$ under the effect of different physical parameters. Our first study concerned the effect of a transverse magnetic field, i.e. applied perpendicularly to the Ising axis. It has been shown that when $BaCo_2V_2O_8$ is subjected to such a field, an effective staggered magnetic field is induced perpendicularly to both the Ising-axis and the uniform applied field. Using neutron scattering experiments (both elastic and inelastic) compared to numerical calculations, we have proved that this staggered field competes with the Ising-like anisotropy. This leads to a very original quantum phase transition. Our system can actually be mapped onto a quantum field theory called "double sine-Gordon model", describing the competition between two dual topological excitations. We have thus shown that $BaCo_2V_2O_8$ under a transverse magnetic field is the first experimental realization of such a theory.

The second study was devoted to the effect of a longitudinal magnetic field, i.e. a field applied parallel to the Ising-axis. The spin-dynamics have been investigated by means of inelastic neutron scattering experiments and it has been shown that above a critical field of 4 T, it corresponds to the one expected for a Tomonaga Luttinger liquid phase (TLL). Moreover, numerical calculations have shown that, because of the Ising-like anisotropy in this system, the majority of the spectral weight in the energy spectrum is carried by longitudinal spin fluctuations. This result is the signature of a quantum behavior without classical analogous with low energy longitudinal fluctuations driving the physics of the system. Finally, this is the first time that the dispersion spectrum for an Ising-like spin $\frac{1}{2}$ chain could be probed in this TLL phase.

The last two studies are preliminary work. The phase diagram of BaCo2V2O8 has been probed by calorimetric measurements under pressure and under a longitudinal magnetic field. Pressures up to 10 GPa have been obtained using a diamond anvil cell. We have then performed specific heat measurements allowing us to investigate the effect of pressure on the Hamiltonian of $BaCo_2V_2O_8$ through its (H, P, T) phase diagram. Finally, we have also started to study the effect of the substitution of magnetic ions Co^{2+} by non-magnetic impurities Mg^{2+}. The neutron diffraction experiments under a longitudinal magnetic field have shown that the critical temperature and critical field decrease proportionally to the concentration of impurities. The spin-dynamics at zero-field has also been investigated and reveals the appearance of non-dispersive magnetic modes, which possibly comes from the finite size effect of the spin chains segmented by the non-magnetic impurities.

In conclusion, our experimental studies associated to numerical calculations allowed us to unveil a very rich physics in this model compound for the study of quantum magnetism and quantum phase transitions.

Keywords: Quantum magnetism, Order and excitations, Quantum phase transitions, neutron scattering, spin chains.